



**University of
Leicester**

**BALQSOs in SDSS: On the absence of
Observational Evidence for Ly- α -N V
line-locking and a discussion of the physical
conditions within BAL outflows**

Chris Cottis

Supervisor:

Michael Goad

A thesis submitted for the degree of
Doctor of Philosophy
at the University of Leicester

X-ray & Observational Astronomy Group
Department of Physics & Astronomy
University of Leicester

May 2010

BALQSOs in SDSS: On the absence of Observational Evidence for Ly- α –N V line-locking and a discussion of the physical conditions within BAL outflows

Chris Cottis

ABSTRACT

Broad absorption line quasars show broad blue shifted absorption indicative of high velocity outflowing material. The mechanism responsible for accelerating these outflows is a matter of much debate. In this thesis I investigate the possibility that radiative line driving is responsible for driving the outflows in some objects.

Various metrics have been proposed to compile homogeneous samples of BALQSOs. Using a new hybrid algorithm we have compiled a sample of 3552 BALQSOs representing approximately 12.5% of the quasars for which SDSS spectra (from DR5) covering the C IV broad absorption line region are available.

From this BALQSO catalogue we have selected the largest sample of objects exhibiting evidence for radiative line driving (the ghost of Ly- α), a feature observed in the BAL troughs of around 1% of BALQSOs. Using this sample we test the criteria purported necessary for ghost-formation in order to confirm whether the identified feature is in fact a ghost. This investigation suggests that the feature observed in the majority of objects arises from the superposition of multiple absorption components, which mimic the appearance of a ghost and unrelated to interactions between N V and Ly- α .

Follow up spectroscopic observations of some of the ghost candidate objects taken using the William Herschel Telescope and the Gemini North telescope are presented. The reduction of these data is described in detail. The criteria for ghost formation are tested on the new spectra with similar results.

One object whose absorption has undergone significant changes is identified and photo-ionisation models used to provide constraints on the physical conditions within the absorber. These models suggest that the changes are due to an increase in the ionisation parameter and not due to changes in the gas covering fraction. The location and mass outflow rate in this object is consistent with previous estimates in similar systems.

The work presented within this thesis does not preclude radiative line driving as a mechanism responsible for high velocity quasar outflows. It does however suggest that the ghost of Ly- α , previously considered the strongest evidence for radiative line driving is rarely observed.

Publications

A significant amount of work contained in this thesis has been published in the following papers:

Knigge, C. and Scaringi, S. and Goad, M. and Cottis, C., "The intrinsic fraction of broad-absorption line quasars", MNRAS, 2008, 386, 1426

Scaringi, S. and Cottis, C. and Knigge, C. and Goad, M., "Classifying broad absorption line quasars: metrics, issues and a new catalogue constructed from SDSS DR5", MNRAS, 2009, 399, 2231

Cottis, C. and Goad, M. and Knigge, C. and Scaringi, S., "Searching for the signature of radiative line driving: On the absence of Ly α -N V line-locking features in a large sample of BALQSOs", submitted to MNRAS, 2010, arXiv:1004.2145

Acknowledgements

Thanks must go first and foremost to my supervisor, Mike Goad for his help and guidance throughout the creation of this thesis. To my parents for their excellence and their financial support. Also thanks to the Sloan Digital Sky Survey. Funding for the SDSS and SDSS-II has been provided by the Alfred P. Sloan Foundation, the Participating Institutions, the National Science Foundation, the U.S. Department of Energy, the National Aeronautics and Space Administration, the Japanese Monbukagakusho, the Max Planck Society, and the Higher Education Funding Council for England. The SDSS Web Site is <http://www.sdss.org/>. STFC for their funding of my research and the Gemini collaboration for the data they collected. Thanks to the Isaac Newton Group for letting me play with the WHT. To my collaborators Christian Knigge and Simone Scaringi. Thanks to all of my fellow PhD students in Leicester for the many fun times (and the black madness) I have had both in Leicester and at NAM. Good luck to the Leicester Longhorns and University Staff Cricket team in future years and thanks to all the coaches and players for the excellent season(s) spent together. Thanks to the wonderful Sophie for her support. Finally thanks to those poor souls who have to read this!

Contents

References	1
1 Introduction	1
1.1 Quasar SED	2
1.1.1 Radio	2
1.1.2 Optical/UV	3
1.1.3 X-ray	4
1.1.4 Gamma-Rays	4
1.2 History, Sub-types and Classification	6
1.3 The Standard Model: Unifying AGN	8
1.3.1 Black Holes	9
1.3.2 The broad line region	10
1.3.3 The narrow line region	11
1.3.4 A dusty obscuring torus	11
1.3.5 Evidence for the standard model	12
1.4 AGN feedback	13
1.5 Broad Absorption Lines	14
1.5.1 How do BALQSOs fit into unification schemes	15
1.5.2 Driving Mechanisms	18

1.6	The Sloan Digital Sky Survey	22
1.7	This Thesis	23
2	Identifying Broad Absorption Line Quasars	25
2.1	Continuum fitting	26
2.2	The SDSS DR5 Quasar Catalogue	30
2.3	The AI and BI	30
2.3.1	The Balnicity Index	30
2.3.2	The Intrinsic Absorption Index	31
2.4	The AI and BI distributions	32
2.5	BALQSOs and Intrinsic absorbers	37
2.6	Composite Spectra	42
2.7	LVQ- Learning Vector Quantisation	45
2.8	The BALQSO Fraction	45
2.9	Summary	48
3	Identifying objects exhibiting the ghost of Lyman-α	49
3.1	The ghost of Ly- α	49
3.2	Selection of ghost-candidate spectra	51
3.3	Selecting a Comparison Sample	57
3.4	Testing the criteria for the formation of observable ghost features	60
3.4.1	Significant C IV broad absorption line	60
3.4.2	Strong Intrinsic Ly- α emission	60
3.4.3	Narrow emission-lines	62

3.4.4	Strong N v broad absorption line	63
3.4.5	Little far-UV flux	64
3.4.6	The width of the ghost feature	67
3.5	Summary of the results of testing Arav's criteria	68
3.6	SDSS J101056.68+355833.3: Si IV ghost?	77
3.7	On the reality of the ghost phenomenon	78
3.7.1	Fake Ghost zones	78
3.7.2	Random sampling	80
3.7.3	A preferred velocity for peaks?	81
3.7.4	Appearance of double-troughs at other velocities	82
3.7.5	K-S test	85
3.7.6	A Monte Carlo test for ghosts	86
3.8	Summary	87
4	Observations of ghost-candidate spectra with GMOS and WHT	88
4.1	The William Herschel Telescope and Intermediate Dispersion Spectrograph and Imaging System	89
4.1.1	ISIS	89
4.2	WHT Observations and Data reduction	90
4.2.1	WHT Sample Selection	90
4.2.2	Instrumental Set Up	90
4.2.3	WHT Observations	92
4.2.4	Data Reduction	95
4.2.5	Extracting 1-d spectra	98

4.2.6	SDSS Flux Calibration	103
4.2.7	Object Spectra	103
4.3	Gemini Observations and Data Reduction	130
4.3.1	The Gemini Observatory	130
4.3.2	Sample Selection	130
4.3.3	Instrumental Set Up	131
4.3.4	Observed data	131
4.3.5	Data Reduction	131
4.3.6	Extracting 1-d spectra	136
4.3.7	Object Spectra	139
4.4	Ghosts and Arav's Criteria	149
4.5	Summary	150
5	SDSS J1138+3517	153
5.1	Observations	155
5.2	Constraining ionic column densities	155
5.2.1	Fitting the underlying continuum and line emission	156
5.2.2	The Curve of Growth	163
5.2.3	Multi-component fitting	164
5.2.4	Estimating the Column Density using analysis of apparent optical depth profiles	171
5.2.5	Partial Coverage	176
5.2.6	An inhomogeneous absorber model	179
5.2.7	Column Density Estimates	182
5.3	Changes between the SDSS and WHT observations	184

5.4	Photo-Ionisation Models	184
5.4.1	Models	186
5.4.2	Constraints on the physical conditions within the absorbing clouds	193
5.5	Mass of the outflow	197
5.6	Summary	199
6	Conclusions and Future Work	201
6.1	Conclusions	201
6.1.1	BALQSOs	201
6.1.2	The ghost of Lyman- α	202
6.1.3	SDSS 1138+3517	203
6.1.4	Summary	203
6.2	Future Work	204
6.2.1	Constraining the physical conditions in BAL outflows	204
6.2.2	The importance of N v absorption in complex C IV BALs	205

List of Figures

1.1	A typical quasar spectrum	3
1.2	The X-ray reflection model.	5
1.3	Example spectra of Seyfert 1 and 2 galaxies.	6
1.4	The unification model.	12
1.5	Elvis' proposed structure for outflows in quasars.	17
1.6	Schematic illustration of the creation of the ghost of Lyman- α	21
2.1	Geometric QSO Composite	28
2.2	An example of a composite fit to a quasar spectrum.	29
2.3	An example of a linear fit to a quasar spectrum.	29
2.4	Comparison of BI values calculated by the author and Trump et al. 2006	33
2.5	AI distribution of DR5 of the SDSS.	33
2.6	AI distribution for all objects, objects with BI>0 and objects with BI=0	34
2.7	BI distribution from DR5 of the SDSS	35
2.8	Modified AI distribution	35
2.9	Modified AI distribution for all objects, objects with BI>0 and objects with BI=0	36
2.10	Example spectra with low AI and BI=0.	38
2.11	Example spectra with low AI and BI>0.	39

2.12	Example spectra with fairly high AI and BI=0.	40
2.13	Example spectra with fairly high AI and BI>0.	41
2.14	Composite spectra of quasars with BI>0	43
2.15	Composite spectra of quasars with AI>0	43
2.16	Composite spectra of quasars with AI>0 and BI=0	44
2.17	BALQSO Fraction as a function of S/N in the g',r' and i' band for the AI, BI and LVQ	47
3.1	Composite spectrum of objects rejected due to having multiple trough features.	53
3.2	Composite spectrum of objects rejected due to having double-trough, ghost-like features, that appear outside of the ghost zone.	54
3.3	Composite spectrum of objects rejected due to having insufficient absorption either side of the ghost feature.	54
3.4	Composite spectrum of the ghost-candidate sample of 43 objects.	55
3.5	Flow diagram of the ghost selection algorithm.	56
3.6	Flow diagram of the comparison sample selection.	59
3.7	Composites of the high-z ghost candidates, comparison sample and all non-BALQSOs from DR5 of the SDSS.	61
3.8	An illustration of our method for estimating the He II strength.	66
3.9	FWHM of the C IV emission-line and the ghost feature.	68
3.10	Spectra of 11 ghost candidates for which Arav's criteria can be tested.	70
3.11	Spectra of 10 ghost candidates for which Arav's criteria can be tested.	71
3.12	Composite ghost-candidate spectra and comparison spectra and the ratio of the two.	72
3.13	11 Ghost candidates for which only some of Arav's criteria can be tested.	75
3.14	Another 11 Ghost candidates for which only some of Arav's criteria can be tested.	76

3.15	SDSS J101056.68+355833.3: A possible Si IV ghost.	77
3.16	Composite residual intensity spectra of two randomly selected BALQSO samples.	80
3.17	Distribution functions showing the incidence of peaks as a function of velocity blue-ward of C IV rest wavelength.	82
3.18	Residual intensity composite spectrum compiled after aligning all spectra to the initial absorption.	83
3.19	The frequency distribution of velocities of the first absorption trough.	84
3.20	Residual intensity spectra of the multi-trough sample, single peak sample, and ghost- candidate sample.	84
4.1	5700 dichroic response	92
4.2	Fringing modulation using the RED+ detector and R158 grating	93
4.3	WHT bias image	96
4.4	WHT flat-field image	96
4.5	Example response fit to a WHT flat-field image	96
4.6	A cross-section of a flat-field corrected image	97
4.7	Example WHT aperture and background	97
4.8	Example WHT aperture trace	99
4.9	WHT arc image	99
4.10	WHT arc spectra	100
4.11	A WHT standard star spectrum	101
4.12	An example WHT sensitivity function	101
4.13	WHT spectrum of SDSS J101844.45+544015.6	106
4.14	Continuum normalised spectra of SDSS J101844.45+544015.6.	107

4.15 C IV and Si IV absorption troughs of SDSS J101844.45+544015.6.	107
4.16 WHT spectrum of SDSS J113831.42+351725.3	109
4.17 Continuum normalised spectra of SDSS J113831.42+351725.3.	110
4.18 C IV and Si IV absorption in velocity space for SDSS J113831.42+351725.3.	110
4.19 WHT spectrum of SDSS J114704.47+153243.3	112
4.20 Continuum normalised spectra of SDSS J114704.47+153243.3.	113
4.21 C IV and Si IV absorption troughs of SDSS J114704.47+153243.3.	113
4.22 WHT spectrum of SDSS J134458.82+483457.5	116
4.23 Continuum normalised spectra of SDSS J134458.82+483457.5.	117
4.24 C IV and Si IV absorption in velocity space for SDSS J134458.82+483457.5.	117
4.25 WHT spectrum of SDSS J162657.47+405848.0	119
4.26 Continuum normalised spectra of SDSS J162657.47+405848.0.	120
4.27 C IV and Si IV absorption troughs of SDSS J162657.47+405848.0.	120
4.28 WHT spectrum of SDSS J170056.85+602639.7	122
4.29 Continuum normalised spectra of SDSS J170056.85+602639.7.	123
4.30 C IV and Si IV absorption troughs of SDSS J170056.85+602639.7.	123
4.31 WHT spectrum of SDSS J164152.30+305851.7	125
4.32 Continuum normalised spectra of SDSS J164152.30+305851.7.	126
4.33 C IV and Si IV absorption troughs of SDSS J164152.30+305851.7.	126
4.34 WHT spectrum of SDSS J212412.60+095923.3	128
4.35 Continuum normalised spectra of SDSS J212412.60+095923.3.	129
4.36 C IV and Si IV absorption troughs of SDSS J212412.60+095923.3.	129
4.37 The first section of the Gemini bias image	134

4.38	The second section of the Gemini bias image	134
4.39	The third section of the Gemini bias image	134
4.40	A Gemini flat-field image	135
4.41	A Gemini flat-field response image	135
4.42	Arc Lamp Spectrum.	137
4.43	GMOS sensitivity function using the R400 grating and OG515 filter	138
4.44	GMOS sensitivity function using the B600 grating and GG455 filter	138
4.45	Gemini spectrum of SDSS J085104.05+051539.8	141
4.46	Continuum normalised Gemini and SDSS DR5 spectra of SDSS J085104.05+051539.8	142
4.47	C IV and Si IV absorption in velocity space for SDSS J085104.05+051539.8	142
4.48	Gemini spectrum of SDSS J115007.65+542737.1	144
4.49	Continuum normalised Gemini and SDSS DR5 spectra of SDSS J115007.65+542737.1	145
4.50	C IV and Si IV absorption in velocity space for SDSS J115007.65+542737.1	145
4.51	Gemini spectrum of SDSS J142244.45+352330.6	147
4.52	Continuum normalised Gemini and SDSS DR5 spectra of SDSS J142244.45+352330.6	148
4.53	C IV and Si IV absorption in velocity space for SDSS J142244.45+352330.6	148
5.1	Continuum scaling the SDSS and WHT observations of SDSS J1138+3517.	154
5.2	12 composites composed of the four quartiles of C IV EW, peak flux and FWHM.	158
5.3	Continuum and emission line fits to the C IV emission and absorption region of the SDSS spectrum of SDSS1138+3517.	159
5.4	Continuum and emission line fits to the Si IV emission and absorption region of the SDSS spectrum of SDSS1138+3517.	160
5.5	Continuum and emission line fits to the C IV emission and absorption region of the WHT spectrum of SDSS1138+3517.	161

5.6	Continuum and emission line fits to the Si IV emission and absorption region of the WHT spectrum of SDSS1138+3517.	162
5.7	Curve of growth for the Si IV absorption in SDSS1138+3517.	165
5.8	Four component Gaussian fit to the Si IV absorption in the SDSS spectrum of SDSS J1138+3517169	
5.9	Single component Gaussian fit to the Si IV absorption in the WHT spectrum of SDSS J1138+3517170	
5.10	Two component Gaussian fit to the high velocity C IV absorption in the SDSS spectrum of SDSS J1138+3517	172
5.11	Five component Gaussian fit to the C IV absorption in the WHT spectrum of SDSS J1138+3517173	
5.12	Si IV ionised column density as a function of velocity in the WHT spectrum.	175
5.13	Covering fractions calculated from the data.	177
5.14	Residual Intensity fits using a partial coverage model.	178
5.15	Residual Intensity fits using a power law inhomogeneous absorber model.	180
5.16	Variation in the results obtained by an inhomogeneous absorber to those of partial or complete coverage by a homogeneous absorber.	181
5.17	Variation in the results obtained by an inhomogeneous absorber to those of partial or complete coverage by a homogeneous absorber.	181
5.18	SED of the Ionising continuum used by Cloudy.	186
5.19	Ionised Column density as a function of ionisation parameter with $n_H=10^5 \text{ cm}^{-3}$ and $N_H=10^{20} \text{ cm}^{-2}$	187
5.20	Ionised Column density as a function of ionisation parameter with $n_H=10^{11} \text{ cm}^{-3}$ and $N_H=10^{20} \text{ cm}^{-2}$	188
5.21	Ionised Column density as a function of ionisation parameter with $n_H=10^7 \text{ cm}^{-3}$ and $N_H=10^{21} \text{ cm}^{-2}$	189
5.22	Ionised Column density as a function of ionisation parameter with $n_H=10^9 \text{ cm}^{-3}$ and $N_H=10^{21} \text{ cm}^{-2}$	189

5.23 Ionised Column density as a function of ionisation parameter with $n_H=10^7 \text{ cm}^{-3}$ and $N_H=10^{22} \text{ cm}^{-2}$	190
5.24 Ionised Column density as a function of ionisation parameter with $n_H=10^9 \text{ cm}^{-3}$ and $N_H=10^{22} \text{ cm}^{-2}$	190
5.25 Ionised Column density as a function of ionisation parameter with $n_H=10^7 \text{ cm}^{-3}$ and $N_H=10^{23} \text{ cm}^{-2}$	191
5.26 Ionised Column density as a function of ionisation parameter with $n_H=10^9 \text{ cm}^{-3}$ and $N_H=10^{23} \text{ cm}^{-2}$	191
5.27 Ionised Column density as a function of ionisation parameter with $n_H=10^7 \text{ cm}^{-3}$ and $N_H=10^{24} \text{ cm}^{-2}$	192
5.28 Ionised Column density as a function of ionisation parameter with $n_H=10^9 \text{ cm}^{-3}$ and $N_H=10^{24} \text{ cm}^{-2}$	192
5.29 Carbon Silicon ratio computed from the C IV and Si IV ionised columns using $N_H=10^7$, $n_H=10^{21}$ for both SDSS and WHT observations.	196
5.30 Carbon Silicon ratio computed from the C IV and Si IV ionised columns using $N_H=10^9$, $n_H=10^{22}$ for both SDSS and WHT observations.	196

List of Tables

3.1	The results of testing Arav's criteria on our ghost sample.	73
3.2	The results of testing Arav's criteria on our comparison sample.	74
3.3	K-S tests on the multi-trough phenomenon	85
3.4	Monte Carlo simulations of the double trough phenomenon	86
4.1	WHT observation targets, filters and exposure times.	91
4.2	GMOS observations	132
4.3	Tests of Arav's Criteria for the Gemini and WHT observations	152
5.1	Wavelength boundaries used to scale the composite emission lines	159
5.2	Details of the components used to fit the absorption in the SDSS and WHT spectra of SDSS J1138+3517	167
5.3	Column densities calculated using the apparent optical depth method	175
5.4	A summary of column density estimates produced by the different methods.	183

Chapter 1

Introduction

Active Galaxies contain a central source less than a few parsecs across (Filippenko et al. 1993) that outshines the whole of the rest of the galaxy, sometimes by factors greater than a thousand. These objects represent the most luminous continuous radiation sources in the universe and are present in around one percent of galaxies.

AGN are important in cosmological studies as their extreme Luminosities (10^{41} - 10^{48} erg s^{-1}) ensure that they are more easily observed at high redshift than ordinary galaxies. AGN can be used to probe the composition and spatial distribution of the universe to greater depths than ordinary galaxies. Indeed, absorption lines from intervening systems can be seen in many quasar spectra (York et al. 1986, Sargent et al. 1988, York et al. 1991), enabling investigation of material that would otherwise be undetectable. There may be a limit to the redshift at which AGN are observed due to the time needed to grow black holes of the size required to power these objects.

The close relationship between the mass of the central black hole believed to power these systems and the galaxy mass (Wandel 1999, Ferrarese & Merritt 2000, Gebhardt et al. 2000) suggest that black hole growth is closely linked with galaxy growth. This link suggests that accretion onto the central black hole may be an important part of the evolution of galaxies. AGN may also play a role in regulating star formation within their host galaxy, either by accreting a significant amount of the potential star forming gas and dust or by

blowing this material away in the powerful winds that are evident in a number of objects showing broad blue-shifted absorption believed to be from material outflowing at extremely high velocities ($>0.1c$ see Turnshek 1984, Pounds et al. 2003a, Pounds et al. 2003b, King 2010). There is also considerable evidence for blue shifts in some of the broad emission lines, especially C IV (Espey & Junkkarinen 1993).

1.1 Quasar SED

AGN emit copious amounts of energy across the whole of the electromagnetic spectrum. In this section I discuss the main features of a typical quasar spectral energy distribution over a wide range of energies and the possible mechanisms responsible for the observed features.

1.1.1 Radio

Whilst the radio morphology and brightnesses of quasars differs considerably between objects the spectrum can almost always be accurately described by a synchrotron mechanism. Compact radio sources are typically optically thick to their own synchrotron emission resulting in more complex spectra due to absorption. The power law spectra observed require power law distributions in electron energy, assuming a constant magnetic field, such that the number of electrons with energy E , $N(E)$ is given by equation 1.1.1.

$$N(E)dE = N_0 E^{-s} dE \quad (1.1.1)$$

α , the power law slope of the spectrum is given by $\alpha = (s - 1)/2$ so for a typical power-law index of 0.7 $s = 2.4$ (Peterson 1997).

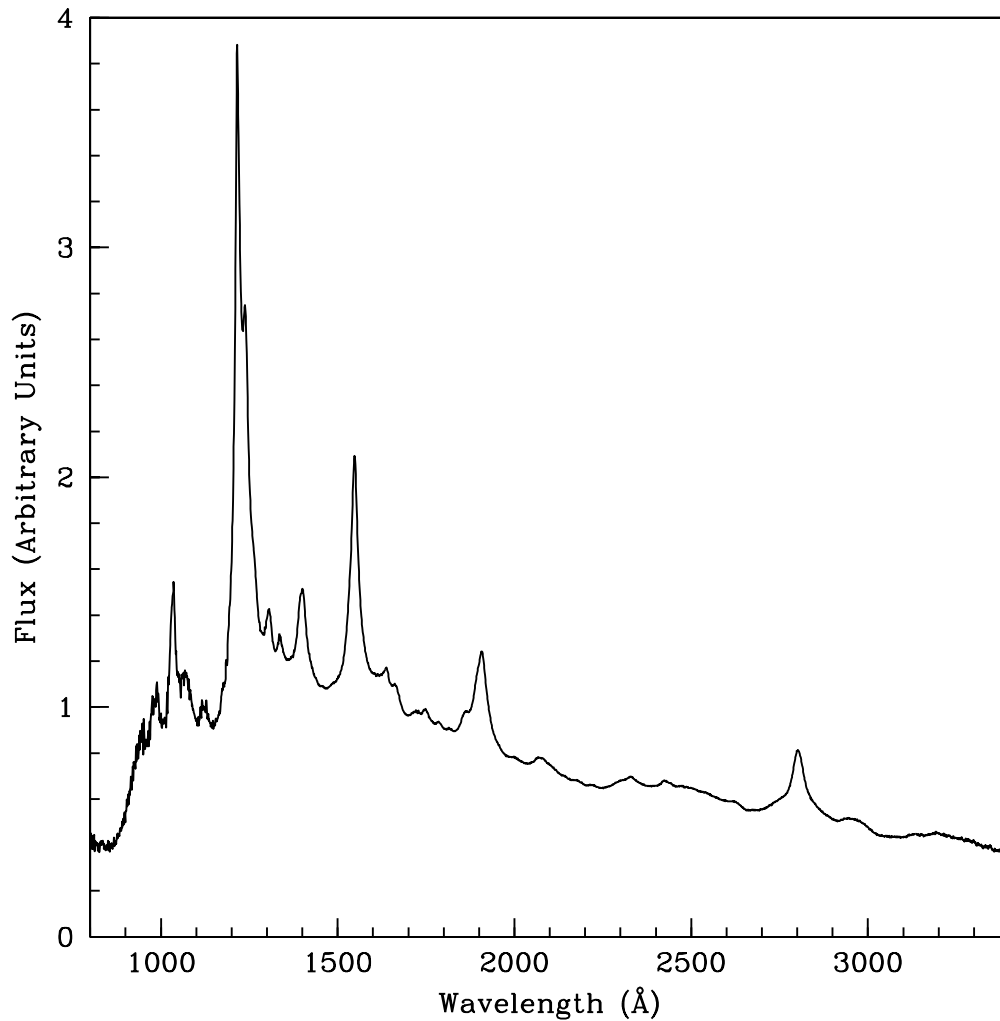


FIGURE 1.1: A geometric composite of all QSOs with redshifts between 1.7 and 4.2 in DR5 of the SDSS.

1.1.2 Optical/UV

Figure 1.1 shows a geometric composite spectrum of the UV emission of quasars at redshift 1.7 to 4.2. This figure shows the strong broad emission lines that are typical of these objects. Typical widths (FWHM) for these broad lines are between 1000 and 5000 km s^{-1} and are due to the bulk motion of the emitting gas around the central black hole.

The underlying continuum is often described as a reddened power law although there is typically some curvature, as well as the big blue bump (Sanders et al. 1989; Elvis et al. 1994). At wavelengths bluer than

the Ly- α emission line at 1215 Å the spectrum is strongly effected by absorption and little of the emitted spectrum remains.

1.1.3 X-ray

The accretion disc within AGN is expected to produce the majority of its' continuum emission in the UV/optical regime as a result of its temperature ($\sim 10^5$ K). In order to produce the bright, usually power law ($f(E) \sim E^{-\Gamma}$ where $\Gamma \approx 2$), hard X-ray emission observed some other mechanism is required. It is believed that this mechanism is Compton up scattering of the UV photons by a very hot corona above (and below) the accretion disc. This corona is thought to be heated by interactions, possibly through magnetic fields, with the accretion disc and can have a thermal (Haardt & Maraschi 1991) or non-thermal (Zdziarski et al. 1990) electron distribution. This power-law continuum illuminates the accretion disc and some fraction is Compton 'reflected' (Lightman & White 1988; Guilbert & Rees 1988; George & Fabian 1991). The lower energy X-rays are rarely reflected as photoelectric absorption dominates whereas hard photons tend to be Compton scattered and are rarely absorbed. After photoelectric absorption some fluorescent line emission will be produced, the most prominent line is the Fe K_α line at 6.4 keV. Figure 1.2 shows a Monte Carlo simulation by Reynolds 1996 of the reflected X-ray spectrum when an incident power-law illuminates a gaseous slab which has cosmic abundances.

1.1.4 Gamma-Rays

Not very much is known about quasar emission at these extremely high (TeV) energies. Kniffen et al. 1993 discuss the gamma-ray emission in 3C 279 and it's considerable variability although observations are consistent with a power law spectrum other forms are not ruled out. Blazars are typically observed to be Gamma-ray sources and AGN/Blazars have been suggested as possible sources of the gamma-ray background (Padovani et al. 1993). Blazar spectra in the TeV regime are typically explained by relatively low energy synchrotron radiation boosted to considerably higher energy by inverse Compton scattering within a jet moving towards the observer (Abdo et al. 2010). This mechanism is known as synchrotron

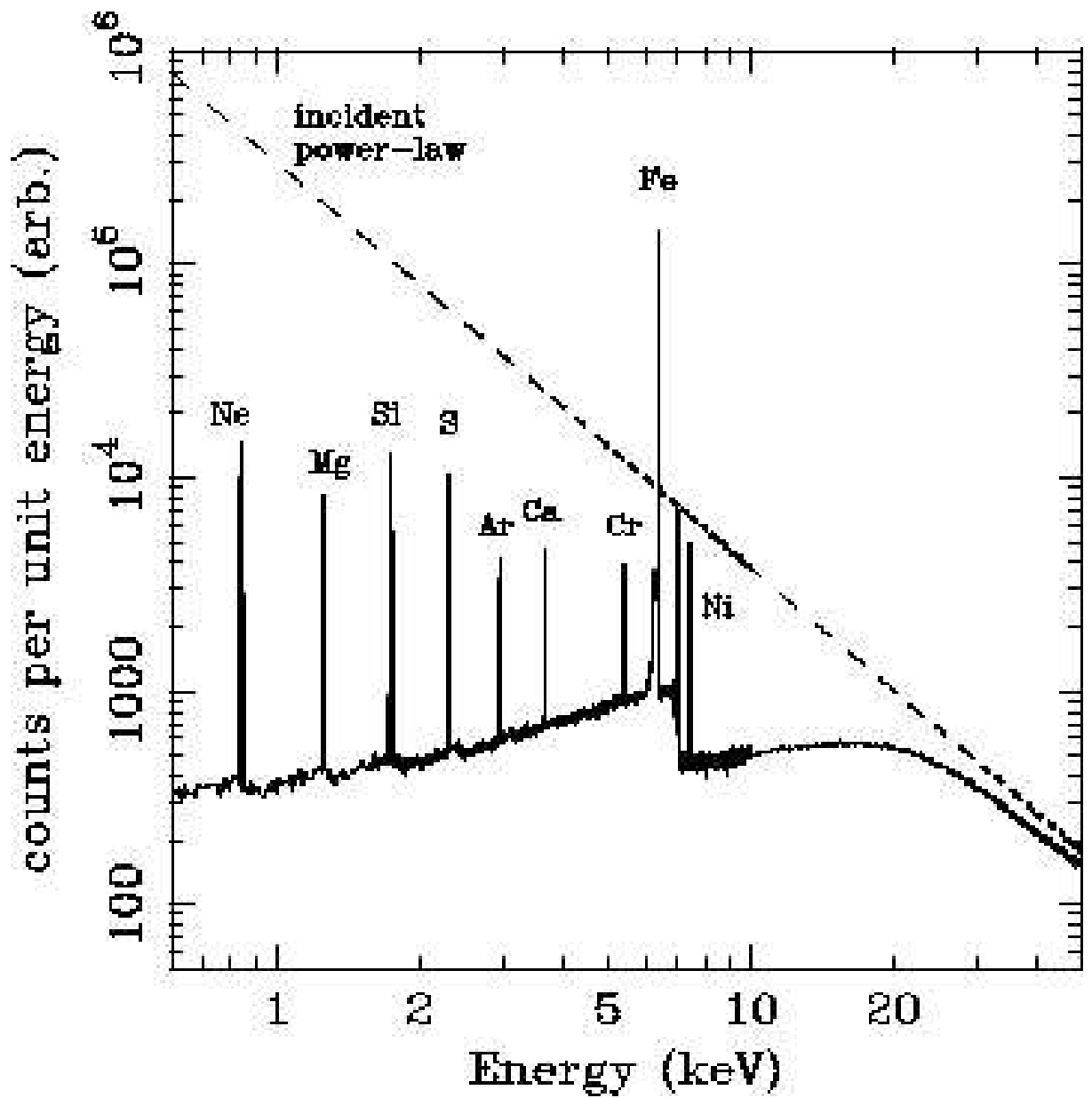


FIGURE 1.2: The X-ray reflection model based on a Monte Carlo simulation of scattering of a power-law from a gaseous slab (Reynolds 1996).

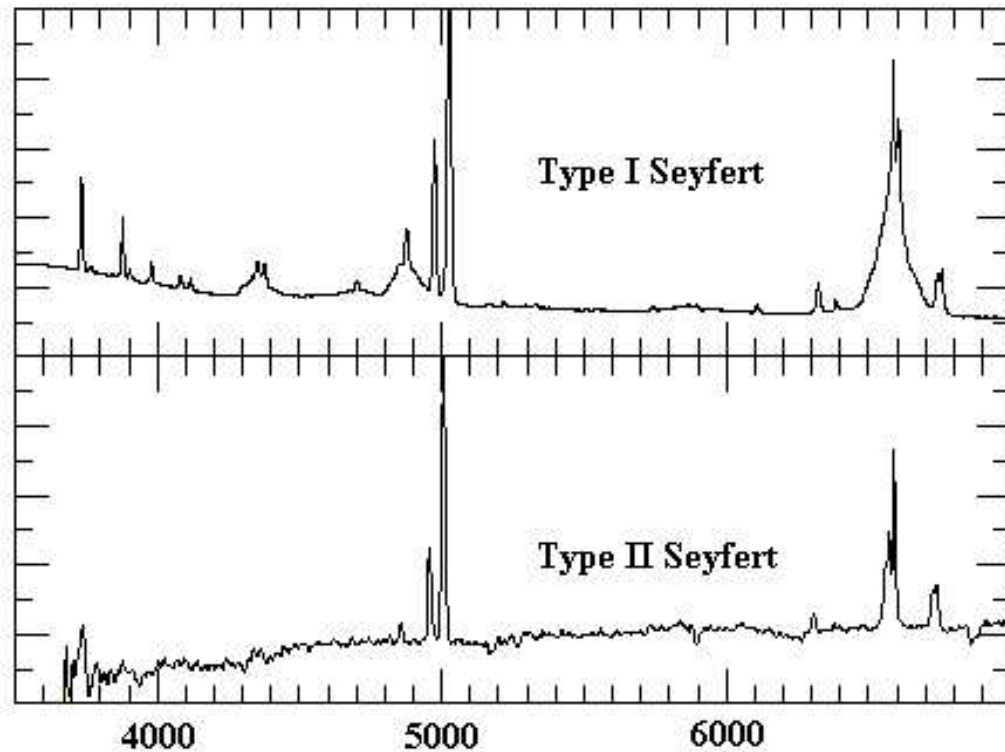


FIGURE 1.3: Example spectra of Seyfert 1 (top-NGC 4151) and 2 (bottom-NGC 4941) galaxies (Keel 1983). The wavelength is given in \AA at the bottom of the diagram.

self-Compton (SSC).

1.2 History, Sub-types and Classification

Due to the extremely large range of luminosity and redshift amongst active galactic nuclei their discovery was made in a number of different stages, via numerous methods and the connections between the different classes of object took in some cases many years to be made.

Extreme nuclear luminosities were first observed by Seyfert 1943 in what we now know as Seyfert galaxies. These objects are relatively low luminosity, by AGN standards, such that the central emission source is comparable in luminosity to the rest of the galaxy. The first sample of such objects were selected as galaxies showing high central surface brightness. UV/optical spectra of these galaxies show two distinct classes. Seyfert 1 galaxies show extremely broad permitted emission-lines along with narrower lines which

include forbidden lines (Khachikian & Weedman 1974). Seyfert 1 galaxies also show strong UV and X-ray continuum emission. Seyfert 2 galaxies show only the relatively narrow (several 100 km s^{-1}) emission-lines in both permitted and forbidden lines, they also tend to be significantly weaker at UV and X-ray wavelengths (Lawrence & Elvis 1982). The differences in the widths of the emission lines can be clearly seen in Figure 1.3 which shows as example of both classes. The reasons behind these differences are discussed in section 1.3.

Quasars or 'quasi-stellar radio sources' were first identified in the late 1950s when the angular resolution of large area radio surveys, such as the 3C catalogue (Edge et al. 1959), became high enough to allow radio sources to be matched to their optical counterparts. These objects are at such high distances that the galaxies in which the AGN reside appear as point sources in optical observations. The vast majority of other radio sources appear to be from galaxies so these radio emitting point sources caused much confusion. This confusion was enhanced by the optical spectra of these sources which showed strong ($EW > 10 \text{ \AA}$ in some of the stronger lines) very broad ($FWHM \approx 1000 \text{ km s}^{-1}$) emission-lines at wavelengths uncharacteristic of emission lines in stellar sources. Schmidt (1963) noted that in one object, 3C 273, these lines appeared to line up with the hydrogen Balmer-series if the object is red shifted by $z=0.158$. This redshift was, at the time, one of the largest ever recorded and only matched by a few rich galaxy clusters. If this redshift is due to the universal expansion then it implies an extremely large distance and a disturbingly large luminosity. With improvements in optical astronomy similar objects have been found which show weak or undetected radio emission. Whilst these objects are technically known as QSOs (quasi-stellar objects) the terms quasar and QSO are often used interchangeably to refer to all high luminosity AGN irrespective of the strength of their radio emission. Indeed, only around 10 % of AGN are radio loud, the majority show only weak radio emission.

Fanaroff & Riley 1974 split radio galaxies into two classes based upon their radio brightness and morphology. Most radio galaxies show a central source and significantly extended radio lobes extending away from the source. These radio lobes usually occur in pairs in opposite directions and can extend as far as Mpc

from the central source. FR I sources are typically weaker radio emitters and tend to have bright central sources co-incident with the optical emission. Due to the weaker radio emission FR I galaxies are not technically quasars but can be QSOs. FR II galaxies show brighter radio emission and tend to be brighter in the lobes, perhaps as a result of a powerful outflowing jet.

The extreme luminosities seen in AGN became even harder to explain when coupled with the relatively common and rapid variation, especially in X-ray emission (Pounds et al. 1986, Green et al. 1993). A few sources were found to vary significantly over timescales of days. Using light travel time arguments this suggests the majority of the emission is coming from a region no more than a few light days across. Thus these objects emit more light than an entire galaxy from a source comparable in size to the solar system. These extremely bright objects are indicative of physical extremes that had not been previously observed and require an extremely efficient method of producing light, significantly more efficient than even nuclear fusion, the power source responsible for starlight.

Blazars are another class of object contained within the AGN family. They can be sub-classified into BL-Lacertae objects (BL-Lacs) and Optical Violent Variables (OVVs). BL-Lacs show much weaker emission-lines than other AGN and extremely highly variable continuum emission at all wavelengths (factors >100 over timescales of months). OVVs are essentially type I AGN showing broad emission lines and large UV and X-ray luminosities but with highly variable luminosity ($\sim 50\%$) on short timescales (days). The currently accepted explanation for the bright highly variable continuum in these objects is that we are viewing them as a jet pouring towards us resulting in the continuum emission from this jet being doppler boosted to much higher luminosity than would be seen from other viewing angles.

1.3 The Standard Model: Unifying AGN

In this section I describe the main physical features that form the standard model of AGN.

1.3.1 Black Holes

It is widely believed that the mechanism responsible for the extremely high nuclear luminosities in AGN is accretion onto a compact object. Accretion can release energy much more efficiently than nuclear fusion and this is required to produce such large luminosities from relatively small regions (<a few light days across). Accretion processes are important in powering many other astrophysical phenomena such as X-ray binaries (Pringle & Rees 1972). Through simply balancing the inward force of gravity with the outward radiation pressure it is possible to produce a theoretical upper limit on the luminosity that can be maintained through accretion onto an object of a given mass, M . This limit is known as the Eddington luminosity, L_{ED} , and combined with the Luminosities observed in AGN can provide a lower limit on the mass of the compact object responsible for powering an AGN. If an object were to consistently exceed this luminosity it would blow away the remaining material resulting in a decrease in the accretion rate and therefore the luminosity.

$$L_{ED} = \frac{4\pi Gcm_p}{\sigma_e} M = 1.26 \times 10^{38} \frac{M}{M_{\odot}} \text{ergs s}^{-1} \quad (1.3.1)$$

Using equation 1.3.1 for a typical quasar luminosities of 10^{47} ergs s^{-1} assuming the source is at the Eddington Luminosity, requires a mass of approximately $10^9 M_{\odot}$. If this compact object is a black hole it would be a few AU across based on the Schwarzschild radius. This is consistent with the rapid variability observed in some quasars.

Observations of the orbits of stars around the centre of our own galaxy reveal an extremely massive compact object (see Reid et al. 2003, Shen et al. 2005). This object is so massive and so compact that it is almost certainly a black hole. There is now mounting evidence that such super massive black holes are common or perhaps even ubiquitous in the centre of galaxies. Accretion onto a super massive black hole is therefore the most likely explanation for the extreme nuclear luminosities seen in AGN.

In order to maintain angular momentum as material is accreted onto the black hole it is likely the in-

falling material will take the form of an accretion disc (Pringle & Rees 1972, Bardeen 1974). Shlosman et al. 1990 argue that a thin accretion disc is not a viable method of transporting in-falling material over distances greater than parsecs so such discs are unlikely to be larger than this.

1.3.2 The broad line region

Near to the central black hole (<few 100 light days) there are high density, high velocity clouds, which are photo-ionised by the central continuum source giving rise to the broad emission lines. The strongest lines are the UV resonance and optical recombination lines. These broad emission lines are dominated by the permitted and meta stable lines suggesting the density in this region is high.

Observations of variability in the continuum and Balmer lines of several quasars show these broad lines lagging continuum variability by around 100 days. Assuming this correlation is indicative of a causal relationship it provides an estimate of the size of the broad line region (BLR) from light travel time arguments (Peterson 1993; Kaspi et al. 2000). Reverberation mapping studies also show no difference in the time-lag between the red and blue sides of the broad emission lines. This strongly suggests that there is no bulk radial motion in the broad line emitting gas as if the gas was moving inwards/outwards we would see the red/blue side of the line vary first. As there is no bulk radial motion the gas in the broad line region is likely to be virialised. This is not true for those emission lines which show blue-shifts such as C IV. If the ionisation parameter of the BLR is constant between objects its size can be expected to scale as the square root of the Luminosity of the central source (Peterson 1993). This simple assumption works relatively well for nearby AGN (Kaspi et al. 2005).

A lower limit on the density of the broad line region can be inferred by the absence of [O III] $\lambda\lambda 4363 \text{ \AA}$ since this line is collisionally de-excited above 10^8 cm^{-3} . Reverberation mapping has shown that much of the C III] $\lambda\lambda 1909 \text{ \AA}$ emission, believed to originate from the BLR and place an upper limit of 10^{10} cm^{-3} on the density of this region, actually arises from a different, lower density ($\rho \approx 10^{9.5} \text{ cm}^{-3}$) region to the C IV and Ly- α emission. There is clear evidence for both density and ionisation stratification such that the

higher ionisation lines respond more rapidly (and are therefore thought to be produced from closer to the AGN) than lower ionisation lines (Netzer & Peterson 1997). The density of the part of the BLR responsible for the C IV emission is likely to be closer to 10^{11} cm^{-3} (Ferland et al. 1992).

1.3.3 The narrow line region

At larger distances (\approx pc) we find the narrow-line clouds. These clouds are made up of lower density, lower velocity gas and give rise to the narrow emission-lines. The presence of strong narrow lines from forbidden transitions suggests that the narrow emission lines are formed in a different region with a lower density than the BLR. The ratio of various forbidden lines can be used as a diagnostic of the density in this narrow line region (NLR). The electron density in this region is typically found to be $n_e \approx 10^3$ to 10^6 cm^{-3} . If we assume that the velocity width of these lines is due to Keplerian rotation then this implies that the NLR is considerably further from the central black hole than the broad line region. This is backed up by observations of nearby Seyfert galaxies (Cecil et al. 1990; Kaiser et al. 2000). Due to its lower density the NLR can remain at similar ionisation to the closer, denser BLR.

1.3.4 A dusty obscuring torus

One relatively simple model proposed by Osterbrock 1978 attempts to explain the observed differences between Seyfert 1 and 2 galaxies by invoking a dust and gas torus which blocks the line of sight to the central regions from some observing angles. In this way all Seyfert galaxies can possess both a broad line region and narrow line region. If the broad lines are emitted from much closer to the nucleus and formed within the dust and gas torus they will not be visible from all angles. Thus Seyfert galaxies viewed from an angle such that the broad line region and central source are exposed will show broad emission-lines along with bright ultraviolet and X-ray fluxes and be classified as type 1. Seyfert 2 galaxies by contrast are viewed through the dusty torus which absorbs significant amounts of UV and X-ray flux as well as the emission from the broad line region leaving only narrow lines. Figure 1.4 is taken from Urry & Padovani 1995 and shows a schematic of this unification model. The dusty torus is shown in orange with

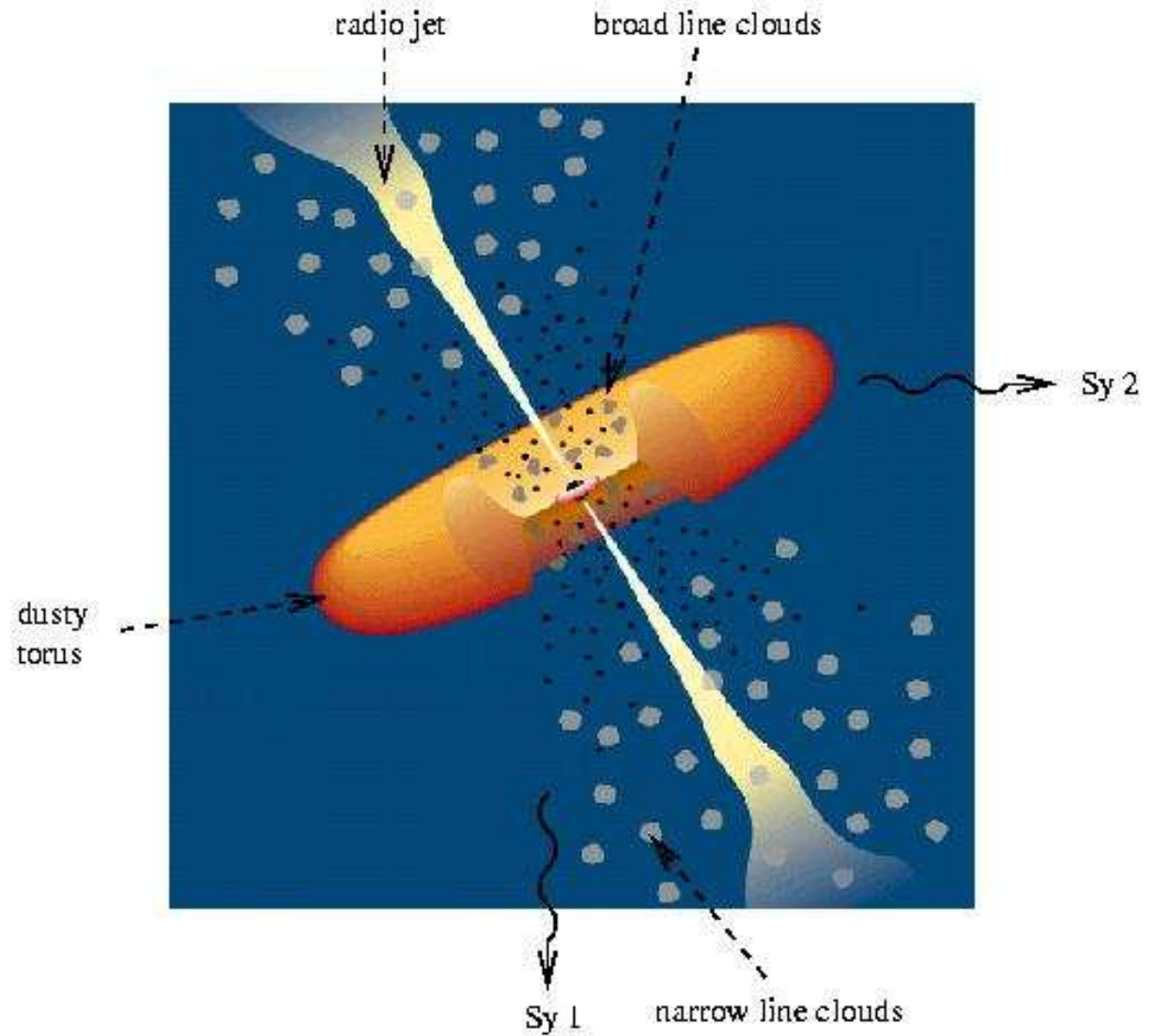


FIGURE 1.4: A diagram of a unification model set out by Urry and Padovani 1995.

the BLR clouds in black and the NLR clouds represented by the lighter colour. This dusty torus is likely to form as the temperature drops allowing dust grains to form. Such a feature may have been observed (at a temperature of ≈ 1350 K) by Riffel et al. 2009.

1.3.5 Evidence for the standard model

Observations of weak broad emission-lines in the polarised spectra of Seyfert 2 galaxies (Antonucci & Miller 1985, Miller et al. 1991) along with the similar UV continuum shapes in Seyfert 1 and 2 galaxies

require an additional component to this model. This component scatters the continuum into the line of sight from above the obscuring torus and is required by observations of the polarised continuum of NGC 1068 (Code et al. 1993) to scatter in a way that is wavelength independent. Scattering from electrons is the most likely mechanism. NGC 1068 shows evidence of increased polarisation in the UV continuum which is polarised by 16%, while the narrow line region is less than 1% polarised. This suggests the narrow line region is viewed directly and is in a different location to that responsible for the scattered continuum emission. Evidence for a further scattering element is provided by the polarisation of the H- α line in some Seyfert 1 galaxies. Robinson et al. 2003 suggest that Seyfert galaxies contain a scattering ring in the same plane as the proposed torus as well as a polar scattering component previously proposed. As well as the considerable evidence of a hidden BLR in type 2 Seyferts Riffel et al. 2009 present observations of what might be emission from the heated inner wall of the dusty torus.

The much more luminous central source in quasars suggests that either the AGN is powered by a significantly larger black hole and/or that the accretion rate is higher. Higher accretion rates are much more likely to drive outflow jets in order to conserve angular momentum and the higher luminosities will also provide more power for any radiatively driven outflows. Outflows in quasars are an important phenomenon, they may be responsible for the radio lobes seen in FR II galaxies, while blazars may be the result of viewing a quasar down an outflowing jet resulting in very large Doppler boosting of the continuum emission from the jet swamping the emission-lines. Outflows are also seen as absorption lines and this is discussed in Section 1.5.

1.4 AGN feedback

The vast energies produced by AGN may have a significant impact on the evolution of the galaxy in which the AGN resides. This energy may also be important on even larger scales effecting both the formation and growth of galaxy clusters.

One way in which the AGN can effect galaxy growth is by preventing cooling-flows (see Brüggén &

Kaiser 2002, Ruszkowski & Begelman 2002). A cooling flow occurs when the intra-cluster medium (ICM) is allowed to cool, this results in the cooler gas falling under gravity to the centre of the cluster. Unless this process is regulated it will result in extremely large and bright galaxies ($M > 10^{12} M_{\odot}$, $L > 10^{45} \text{ ergs s}^{-1}$) in the centre of galaxy clusters. Such galaxies are considerably less common than predicted by numerical simulations which do not take AGN feedback into account (Kauffmann et al. 1999, Cole et al. 2000, Cole et al. 2001, Bower et al. 2006). AGN provide large amounts of energy both in the form of luminosity and kinetic energy in outflows (Di Matteo et al. 2005) that may be capable of preventing the gas from cooling explaining the lack of extremely high mass galaxies if galaxies become active as they grow rapidly.

In recent years interest in BALQSOs outflows has risen sharply, principally because of the realisation that such high velocity outflows carry a substantial amount of energy and momentum into the ISM, and may therefore be important in driving AGN feedback as well as providing a mechanism for quenching star formation (Scannapieco et al. 2005). Indeed, the discovery of highly ionised, very high-velocity X-ray outflows (e.g. Pounds et al. 2003a, Pounds et al. 2003b, Pounds & Reeves 2009), for which the energy transport (in terms of mechanical energy) is large enough to interrupt the growth of the host galaxy, may provide the causal link behind the well-known correlation between the mass of the central black hole and the mass of the bulge (e.g. Ferrarese & Merritt 2000, Gebhardt et al. 2000, Tremaine et al. 2002).

1.5 Broad Absorption Lines

Broad absorption line quasars (BALQSOs) as their name suggests, show strong broad blue-shifted absorption lines in their spectra believed to be indicative of high velocity ($\sim 0.1c$) out-flowing winds. BALQSOs represent approximately 15% of quasars in general (Turnshek 1984, Reichard et al. 2003a, Trump et al. 2006, Knigge et al. 2008, Scaringi et al. 2009). The majority ($\sim 85\%$, Sprayberry & Foltz 1992, Reichard et al. 2003b) of BALQSOs are known as HiBALs, displaying absorption in lines of high ionisation only (e.g. N V, Si IV, and C IV). The remainder are classified as LoBals and show in addition broad absorption in lines of lower ionisation species, most notably Al III and Mg II. LoBALs are further sub-classified according to the presence of Fe absorption, as Fe LoBals. Since the spectra of LoBals are in

general redder than HiBals, Becker et al. 2000 suggests that BALQSOs and in particular Fe LoBALs may be an early phase in the development of emerging or re-fuelled quasars.

Observations of objects in which the broad absorption absorbs significant amounts of flux from the broad emission line provide strong evidence that the absorption is located outside of the broad line region. X-ray observations suggest that the hydrogen columns in BALQSOs are extremely large ($N_H > 10^{22} \text{ cm}^{-2}$) as the majority of BALQSOs are barely detected even in relatively long X-ray observations (Green & Mathur 1996, Giustini et al. 2008). Bautista et al. 2010 suggest that the hydrogen density in the outflow responsible for two FeLoBALs is likely to be in the region of 10^4 cm^{-3} , this density allows the outflow to remain relatively highly ionised up to quite large distances from the ionising source (compared to the broad line region).

1.5.1 How do BALQSOs fit into unification schemes

There has been much debate about the relationship between BALQSOs and the general quasar population as a whole. Simple unification schemes, suggest that BALQSOs and non-BALQSOs are similar objects and that any observed differences in their spectra arise due to orientation effects (Ogle et al. 1999, Weymann et al. 1991, Schmidt & Hines 1999, Elvis 2000).

Elvis 2000 proposed the structure shown in Figure 1.5 as a way of explaining BALQSOs as well as the various narrow absorption lines seen in quasars. In this picture all AGN contain a highly ionised high-velocity outflow. Initially this outflow rises vertically off of the accretion disc before being radiatively accelerated. When the AGN is viewed from above the outflow no absorption is seen. Viewed along the outflow AGN will show extremely deep broad absorption lines with high column densities, these are the BALQSOs. At angles such that the AGN is viewed through but not along the outflow narrow lower velocity (as the material is not moving directly towards the observer) material is seen. This is consistent with observations of persistent relatively low velocity narrow absorption in NGC 5548 (Shull & Sachs 1993;

Mathur et al. 1999). If this absorption was due to a radial flow then the material would have moved far enough from the ionising continuum to significantly alter its ionisation. As this is not seen viewing the material through an outflow moving at an angle to the observer may be a much better model for this source. However, if the density of the flow decreases as it moves further from the ionising continuum it may be possible to maintain constant ionisation.

Several instances of outflows varying (Barlow 1993;Lundgren et al. 2007), appearing (Hamann et al. 2008) or disappearing (see Chapter 5) suggest that the relationship between BALs and non-BALs is more complex than a simple change in observing angle. Barlow 1993 saw significant changes in the strength of absorption in several BALQSOs and suggested that these changes are best explained by changes in the ionisation of the outflow rather than its covering fraction. In order to significantly change the depth of absorption in a BAL outflow in any given line one could imagine a change in the ionisation of the gas drastically reducing the ionised column density for that line. In instances where several absorption lines are seen to appear or disappear together a change in the covering fraction appears unlikely whereas ionisation changes will occur at the same time for all absorbers as to absorb the continuum they must be in the line of sight.

There has been much debate on the radio properties of BALQSOs and what they imply about the orientation of the outflows. Initially all the BALQSOs found were radio quiet (Stocke et al. 1992;Brotherton et al. 1998) discovered the first radio loud BALQSO but it remains the case that the majority of BALQSOs are not radio loud. Shankar et al. 2008 have suggested that this is due to a bias created by beaming of radio emission produced in jets. They have suggested that the intrinsic radio properties of BALQSOs and non-BALQSOs are the same but that the outflow responsible for the broad absorption is at a different angle to that responsible for the radio jet. If this is the case then those objects whose radio emission is Doppler boosted will be much less likely to show broad absorption lines and this may explain the dependence of the fraction of objects showing BALs with radio luminosity.

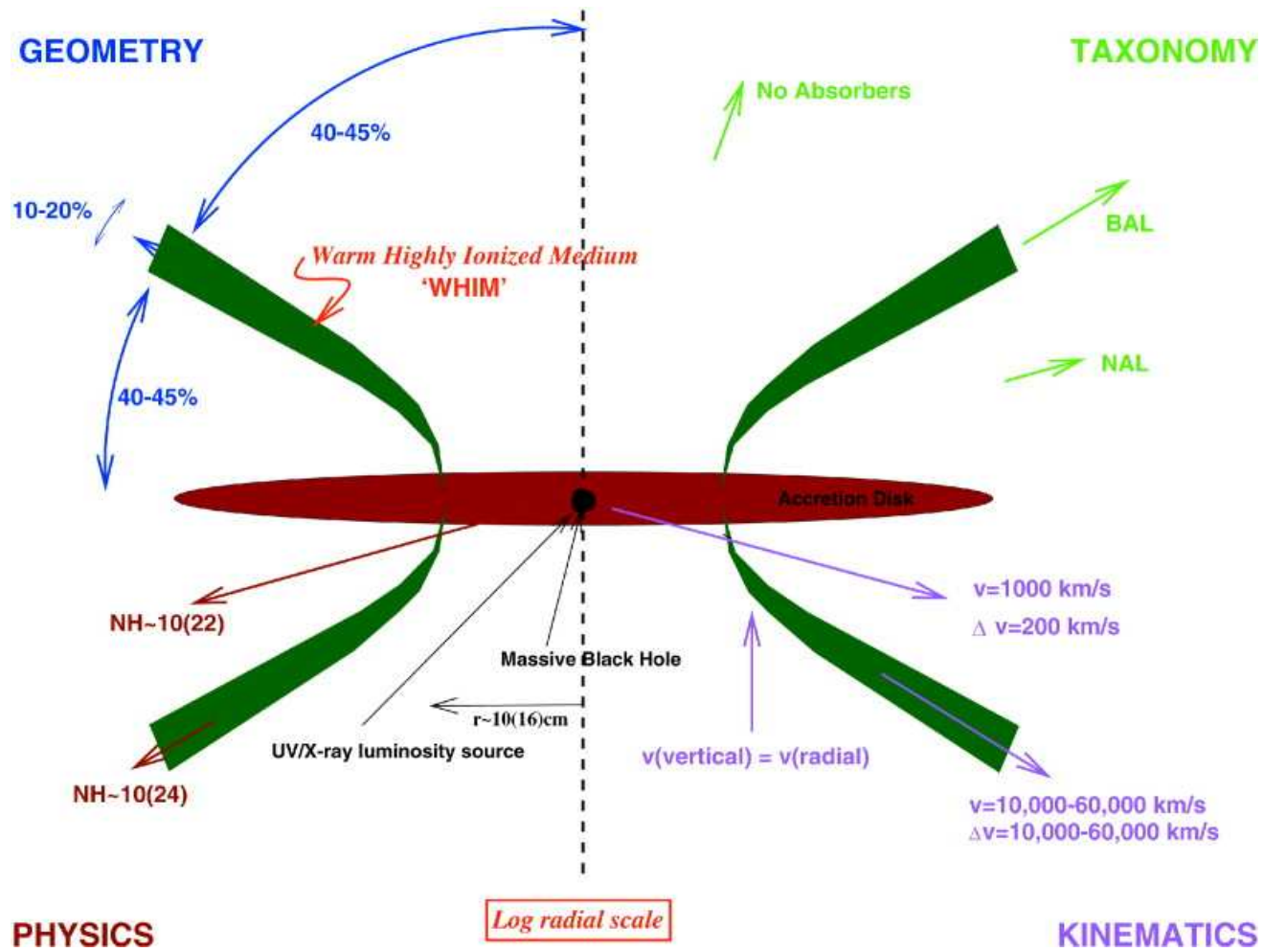


FIGURE 1.5: Elvis' proposed structure for quasars. The top left quadrant shows the geometry of the structure. The top right quadrant shows what type of object would be viewed from a variety of observing angles. The bottom left quadrant shows the column densities which would be observed. The bottom right quadrant shows the outflow velocities which would be observed.

1.5.2 Driving Mechanisms

Despite the increasing importance of quasar outflows the precise mechanism responsible for accelerating them to high velocity remains uncertain. Radiative acceleration (Shlosman et al. 1985, Arav & Li 1994, Murray et al. 1995, Proga et al. 2000, Chelouche & Netzer 2001), Magneto Hydro Dynamic (MHD) driven winds (Blandford & Payne 1982, Emmering et al. 1992, Konigl & Kartje 1994, Bottorff et al. 1997) and thermally driven winds are seen as the main contenders (see e.g. Proga 2007 for a review). A major hindrance to progress in this area is the absence of a clean discriminatory observational signature of what are essentially orthogonal wind geometries. For radio-quiet objects, AGN unification schemes tend to favour equatorial wind geometries (e.g. Elvis 2000). By contrast, observations of radio-loud BALQSOs (Becker et al. 1997, Becker et al. 2000, Brotherton et al. 1998) and in particular polarisation observations of PKS 0040-005 indicate a non-equatorial BAL outflow (Brotherton et al. 2006). One possible explanation for the apparent difference in wind geometry between radio-loud and radio-quiet objects, is that different acceleration mechanisms operate in these two classes of objects.

Magneto-Hydro-Dynamic driving

Blandford & Payne 1982 show that it is at least theoretically possible to extract energy and angular momentum from an accretion disc by interactions with magnetic fields and that such interactions are capable of producing high velocity collimated outflows. This mechanism enables accretion to take place independent of viscosity as these magnetic interactions take the place of viscosity in allowing angular momentum to be transferred away from the accretor. Emmering et al. 1992 suggest a combination of magnetic and radiative driving where the dusty gas is radiatively accelerated and flows along magnetic field lines.

Thermally Driven Winds

Equation 1.5.1 is the equation of motion for gas surrounding the AGN, ρ, P, B, ϕ and F^{rad} are the gas density, pressure, magnetic field, gravitational potential and radiation force per unit mass respectively. Magnetic driving is explained by the second components of the left hand side of equation 1.5.1. The first component, ∇P , is the pressure gradient and can be described as a thermal gradient in a region where the gas is of constant density, as the gas pressure depends on the temperature. As the gas closer to the AGN will be hotter the gas will tend to be accelerated away from the black hole by the pressure gradient. If this force is large enough it may be capable of playing a significant role in the acceleration of BAL outflows.

$$\rho \frac{Dv}{Dt} + \rho \nabla \phi = -\nabla P + \frac{1}{4\pi} (\nabla \times B) \times B + \rho F^{rad} \quad (1.5.1)$$

Radiative Line Driving

The final component of equation 1.5.1 allows the possibility of radiative driving. In highly ionised gas the effect of radiative line driving is much reduced. This suggests that in order to produce high velocity outflows a shielding component is required to prevent the outflowing gas from being ionised (Murray et al. 1994).

Perhaps the strongest indicator that radiative driving is responsible for accelerating at least some of the high velocity flows, is the appearance of line-locking features in the spectra of a small fraction of BAL quasars (e.g. Weymann et al. 1991, Korista et al. 1993, Arav 1996, Vilkoviskij & Irwin 2001). The most well-studied of these is the so-called ghost of Ly- α , a small hump seen in the absorption troughs of a small fraction (less than a few percent) of BALQSOs believed to be formed via the interaction between Ly- α photons and N v ions.

The ghost of Ly- α is a peak seen in the absorption trough of less than 5% (Arav 1996, North et al. 2006)

of BALQSOs. It is seen 5900 km s^{-1} blue-ward of the centre of the emission line associated with the absorption. The feature was identified by Korista et al. 1993 after being seen in a difference spectrum of BALQSO and non-BALQSO spectral composites produced by Weymann et al. 1991 who pointed out that the difference between the two absorption troughs was approximately equal to the velocity separation of N v and Ly- α . In a series of papers in the mid 90's (Arav & Li 1994, Arav et al. 1994, Arav & Begelman 1994, Arav et al. 1995, Arav 1996) Arav suggested that the feature seen at this velocity was a result of the increased radiative pressure on N v ions at this velocity within the outflow. In this picture N v ions moving at 5900 km s^{-1} 'see' the Ly- α emission from the AGN at the energy of their own emission resulting in a large increase in the scattering cross section of the Ly- α photons. Consequently, out-flowing N v ions receive an increase in radiation pressure leading to a large injection of momentum into the outflow. The out-flowing ions of other species are dragged to higher velocities by electromagnetic interactions with the N v ions, leading to a deficit of material at this velocity (because each out-flowing ion spends very little time at this velocity before being accelerated to greater velocities). In turn this causes a decrease in the opacity at this velocity which manifests as a peak within the absorption troughs of the out-flowing species. A schematic of this mechanism is given in Figure 1.6 which is taken from Arav 1996.

This simple mechanism explains both the presence of the feature and why its position is linked to the rest frame of the source. This is not the case for shadowing of N v by Ly- α (Korista et al. 1993) where the separation of the troughs is constant but their velocities are determined by the velocity of the first trough. Arav 1996 suggested that the reason for the feature being most prominent in C IV absorption rather than in other species, is that the doublet separation of C IV is far smaller (498 km s^{-1}). By comparison the larger doublet separations of Si IV (1933 km s^{-1}) and O VI (1647 km s^{-1}) result in the feature being blurred over several thousand km s^{-1} , producing a low contrast feature which is difficult to detect in low S/N data.

Previous studies have been limited to small samples of relatively low quality spectra, with strong ghosts often only becoming apparent in composite spectra (Arav et al. 1995, North et al. 2006). Moreover, distinguishing between line-locking features and similar features caused by the chance alignment of multiple absorption systems is difficult with relatively small samples. Indeed, Korista et al. 1993, showed that in a

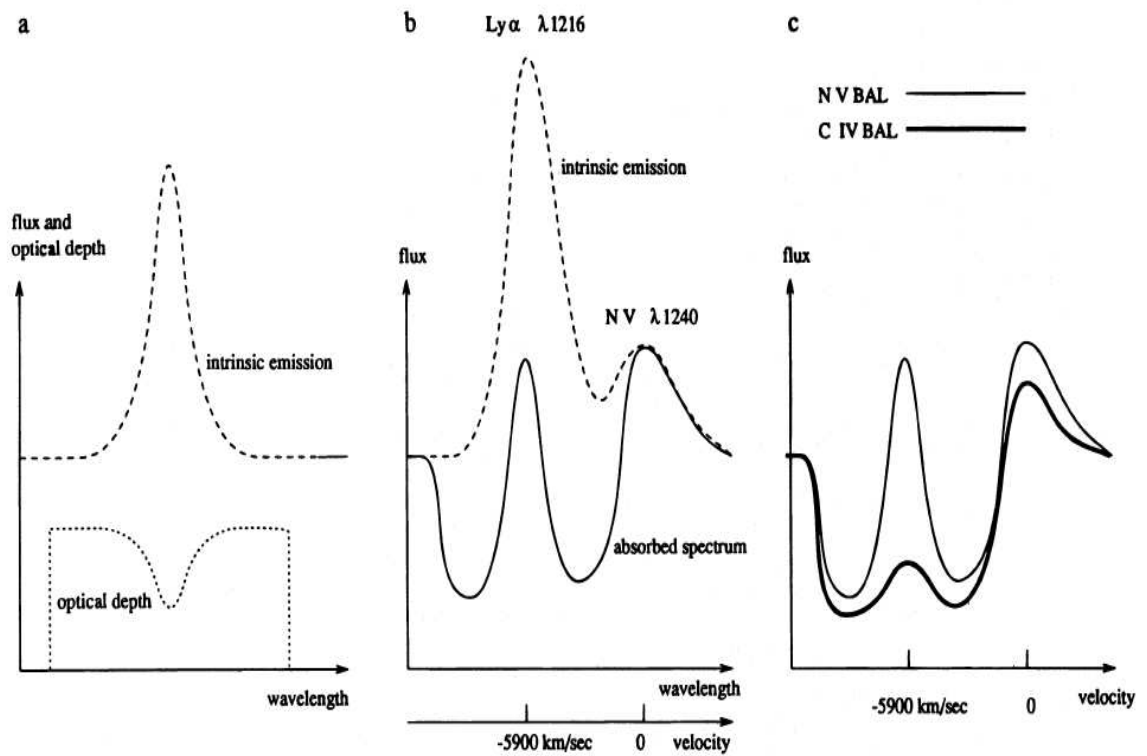


FIGURE 1.6: Schematic illustration of the creation of the ghost of Lyman- α . Panel (a) shows how the optical depth of a radiatively driven flow changes when the outflowing material encounters a strong emission line. Panel (b) shows the region around the strongest quasar emission line Ly- α . The N v ions encounter this line at 5900 km S^{-1} and this effect is transferred to other lines dragged along by this increased acceleration on the N v ions.

sample 72 objects, evidence for line-locking features was merely suggestive rather than convincing. The Sloan Digital Sky Survey provides a vast quantity of quasar spectra allowing an unprecedented number of BALQSOs and ghost candidates to be identified.

A decelerating flow?

It may also be possible to explain the observations of outflowing gas in these objects by way of a decelerating flow. In this picture the outflow is thrown off the accretion disc at a very high velocity before decelerating due to a combination of gravity and collisions with the low velocity gas and dust it must travel through.

1.6 The Sloan Digital Sky Survey

The Sloan Digital Sky Survey or SDSS (Castander 1998, York et al. 2000) covers π sr of the sky at high galactic latitude ($>30^\circ$) and at its 7th data release (Abazajian et al. 2009) contained photometric information on over 200 million distinct objects as well as optical spectra of nearly 10^6 galaxies and over 10^5 quasars. The survey was designed primarily to provide information on the large scale structure of the universe by providing photometric (and spectroscopic) redshifts for a very large number of galaxies and quasars and has been hugely influential in cosmological studies (for example Percival et al. 2010, Sánchez et al. 2009). Interesting objects such as AGN were then photometrically selected (see Richards et.al 2002 for details on the target selection algorithm) for spectroscopic follow up. The photometric data are taken in 5 specially designed filters these are named u' (centred on 3560 Å), g' (4680 Å), r' (6180 Å), i' (7500 Å) and z' (8870 Å) and the wavelengths given are the effective wavelengths given by York et al. 2000. The SDSS telescope is a 2.5m wide-field telescope located at Apache Point Observatory (APO) in New Mexico. The telescope uses a large secondary mirror along with correcting lenses in order to obtain a 3° field without distortion. In spectrographic mode the telescope uses two fiber-fed spectrographs and is able to simultaneously observe up to 640 objects. The fibers are placed into a fiber plug plate, these plates are individually drilled for each field to observe the objects selected for spectroscopic follow up. Photometric

and spectroscopic calibration are performed using data from the USNO 1m telescope and the photometric telescope (PT) a 0.5m telescope equipped with the SDSS filter set in order to calibrate the photometry. Most of the work in this thesis draws on data from the 5th data release (DR5) of the SDSS (Adelman-McCarthy et al. 2007). Schneider et al. 2007 have produced a quasar catalogue from DR5 of the SDSS containing spectra of 77429 spectroscopically confirmed quasars. With such a large sample of quasars to start from it is possible to produce relatively large samples of even extremely rare objects such as those exhibiting evidence of the ghost of Lyman- α .

1.7 This Thesis

This thesis investigates the outflows seen in BALQSOs.

Chapter 2 highlights the issues involved in selecting clean samples of BALQSOs. This chapter addresses the problems of using mathematical metrics and identifies the different types of object selected by the 'balnicity' index (BI:Weymann et al. 1991) and the absorption index (AI:Hall et al. 2002, Trump et al. 2006). The use of learning algorithms (Knigge et al. 2008, Scaringi et al. 2009) is introduced and the advantages and disadvantages considered. Finally a sample of 3552 BALQSOs selected from the fifth data release of the SDSS(Adelman-McCarthy et al. 2007) is presented (more detail on this sample can be found in Scaringi et al. 2009)

Chapter 3 is largely based on Cottis et al. 2010 and describes an attempt to determine whether the ghost of Lyman- α is really the result of radiative line driving. The largest sample of ghost candidate objects to date is identified and the method used to identify them discussed. Arav et al. 1995 set out criteria required for the formation of a visible ghost feature and these criteria are discussed and tested on this sample. The results of these tests are inconclusive and raise questions about the reality of the ghost phenomenon. A series of investigations into the presence or absence of an excess of peaks at the ghost velocity is presented.

Chapter 4 describes the observation and reduction of follow up spectra of some of the ghost candidates

presented in Chapter 3 taken with the William Herschel Telescope and Gemini North. There is some discussion of the differences between the SDSS spectra and the follow up observations and Arav's criteria are tested on these follow up spectra.

One of the objects observed with the WHT showed considerable changes to the C IV and Si IV absorption. These changes along with what they can tell us about the physical conditions and location of the absorbing gas are discussed in Chapter 5.

Finally a summary of this thesis and the conclusions drawn from this research, along with ideas for future research in this area are presented in Chapter 6.

Chapter 2

Identifying Broad Absorption Line Quasars

In order to search for evidence of radiative line driving we require a large sample of objects exhibiting evidence for the ghost of Lyman- α . As these objects are rare we require a large homogenous sample of objects showing broad absorption lines.

This chapter addresses the problem of searching the huge quantities of data produced by astronomical surveys, such as the Sloan Digital Sky Survey (SDSS: Castander 1998) for broad absorption line quasars. Historically large data sets such as those produced by the COSMOS survey (Scoville et al. 2007) were classified by eye. This method produced results biased by time of the day, who classified which objects and many other factors which would not effect automated classification. We therefore require a robust automated system for identifying BALQSOs in large QSO samples. There are several issues to address, firstly in order to identify absorption features it is necessary to define a 'continuum' with respect to which absorption can be measured. Once the continuum has been characterised we need to specify a significance level below which the spectra can be considered to be absorbed, which is particularly important for noisy data. Next it is necessary to produce a set of criteria by which the amount of absorption can be characterised. The intrinsic Absorption Index (AI:Hall et al. 2002, Trump et al. 2006) and Balnicity Index (BI:Weymann et al. 1991) are introduced and their definitions and distributions discussed. The bimodal nature of the log(AI) distribution is considered and the possibility that it is due to the intricacies of the

definition discussed and ruled out. The prospect that this feature is due to the AI selecting two different classes of object and not just BALQSOs is suggested as evidence that the Balnicity Index is a more reliable method of selecting BALQSOs. We also note that the BI does not give a complete sample of objects with broad blue-shifted absorption and discuss the use of learning vector quantisation algorithms in defining BALQSO samples (see e.g. Knigge et al. 2008).

2.1 Continuum fitting

Fitting the continuum can be performed in numerous ways, the simplest and most obvious method being to pick regions on either side of the absorption, that are not contaminated by line emission or absorption, and simply join the two with a straight line. This method has the advantage of being simple, reproducible and robust.

A more sophisticated method is to create a template spectrum with which to compare the object. Various templates and methods for producing them can be found in the literature (eg. Vanden Berk et al. 2001, Zheng et al. 1997). In order to create a composite spectrum that retains the average spectral shape a geometric rather than arithmetic mean is used. The geometric mean is given by $(\prod_i^n x_i)^{1/n}$ in each wavelength bin where n is the number of objects and x_i is the flux of object i in the appropriate wavelength bin. This method of creating the composite is useful for quasar spectra as they tend to follow a power law, for which the geometric mean gives a composite with the average power law slope whilst the arithmetic mean will give a composite that is, in general, not a power law. For this reason the geometric mean allows the composite to be modified and fit to individual spectra in a much simpler way as well as giving a better fit to the majority of spectra.

The composite that I have created contains 28421 spectra from the Sloan Digital Sky Survey (SDSS) 5th data release (DR5) quasar catalogue (Schneider et al. 2007) in the redshift range 1.7 to 4.2, selected to ensure each spectrum is visible over the normalisation region as well as to include only those objects in the redshift range of our potential BALQSOs. Each spectrum is converted to the rest frame of the object

using the redshift given in the quasar catalogue, it is then re-binned into 1 Å bins. The SDSS spectra have a resolution of 69 kms^{-1} , at redshift zero this corresponds to of the order 1 Å/pixel but in the rest frame of the source depends on the wavelength and redshift. The spectrum is then normalised so that the average flux between 1700 Å and 1750 Å is equal to unity. This ensures that the composite is not biased by changes in the spectral slope of, or features present in, high luminosity or nearby sources. Due to the large number of spectra used in the creation of the composite it will have a very high signal to noise ratio allowing many emission lines to be seen. The geometric composite along with the number of spectra contributing to each bin can be seen in Figure 2.1. Due to the redshift requirements the composite spectrum covers the rest-frame wavelength range 734 Å to 3418 Å.

In order to use the geometric composite to isolate continuum regions for an individual object one must modify the composite to take into account differences in spectral slope and the amount of internal reddening due to dust. This is done using equation 2.1.1

$$f'_c(\lambda, \alpha, E(B - V)) = f_c(\lambda, \alpha_c, E(B - V)_c) \lambda^{(\alpha - \alpha_c)} \times 10^{-(E(B - V) - E(B - V)_c) \zeta(\lambda)} \quad (2.1.1)$$

where $f'_c(\lambda, \alpha, E(B - V))$ is the modified template that is normalised and fit to the input spectrum, $f_c(\lambda, \alpha_c, E(B - V)_c)$ is the composite spectrum, λ is wavelength, $E(B - V)$ is a measure of the degree of reddening based on the SMC extinction curve as a function of wavelength, $\zeta(\lambda)$, given by Pei 1992 and α is the spectral slope. The spectra are normalised so that their flux in the region between 1700 and 1750 Å are equal. A modified χ^2 value is calculated using equation 2.1.2

$$\chi^2(\alpha, E(B - V)) = \sum_{\lambda} \frac{1}{w(\lambda)} \sum_{\lambda} [f'_c(\lambda, \alpha, E(B - V)) - f_i(\lambda)]^2 \frac{w(\lambda)}{\sigma(\lambda)} \quad (2.1.2)$$

where $f_i(\lambda)$ is the input spectrum, $\sigma(\lambda)$ is the error on the input spectrum, $f'_c(\lambda, \alpha, E(B - V))$ is the modified composite and $w(\lambda)$ is the weighting function used to remove prominent emission line regions as given by Reichard et al. 2003a. The weighting function gives a weighting of zero between the lower and upper wavelength limits of the Lyman- α and N v blend, Si IV, C IV, C III] and Mg II emission line regions as given by Vanden Berk et al. 2001 as well as giving a zero weighting to anything blueward of

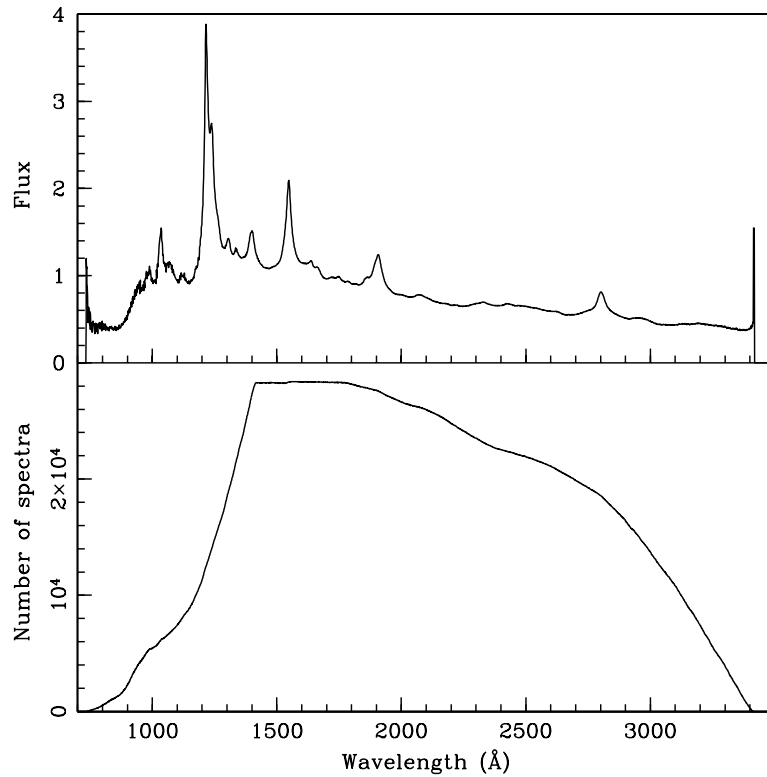


FIGURE 2.1: Geometric QSO Composite (top) in arbitrary flux units (as the fluxes of all of the contributing objects are normalised) and the number of spectra contributing to each bin as a function of wavelength (bottom).

1050 Å or redward of 3418 Å (as the composite does not cover this region). The BAL regions are given a weighting of 0.5 and are defined as being between the Si IV upper limit and C IV lower limit from Vanden Berk et al. 2001 for the C IV BAL and between 2575 and 2686 Å for the Mg II BAL. This calculation is performed for various values of α and $E(B - V)$ and the value of $\chi^2(\alpha, E(B - V))$ minimised.

In the C IV emission line region as defined by Vanden Berk et al. 2001 linear interpolation between points on either side of the region is used to produce the model continuum value although this region is not used for the fitting process. An example of a composite fit is shown in Figure 2.2 along with the weighting function. The composite fitting was unable to provide a good fit for 91 spectra, mostly due to the presence of very red and/or extremely absorbed spectra. For these, a linear fit across the BAL region is used (see e.g. Figure 2.3). The regions used to produce the linear fits are between 1290 to 1310 Å on the blue side and between 1720 to 1740 Å on the red side.

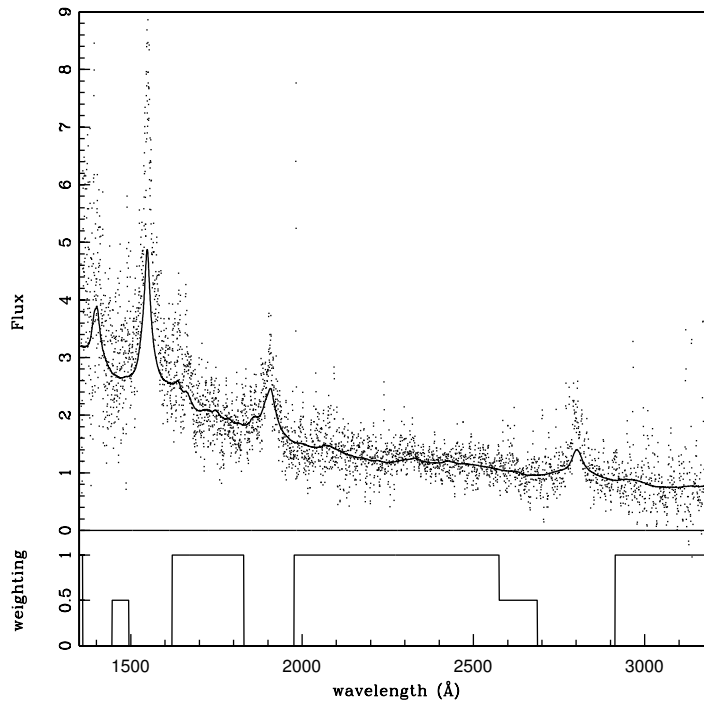


FIGURE 2.2: Modified composite fit to a quasar spectrum shown with the weighting used to calculate the modified χ^2 value for each wavelength region in the bottom panel. The emission lines have a weighting of 0 and are not fit, it is therefore not surprising that the spectra is poorly fit in these regions. The solid line in the top panel is the modified quasar composite, the points are the flux measurements for the fit object.

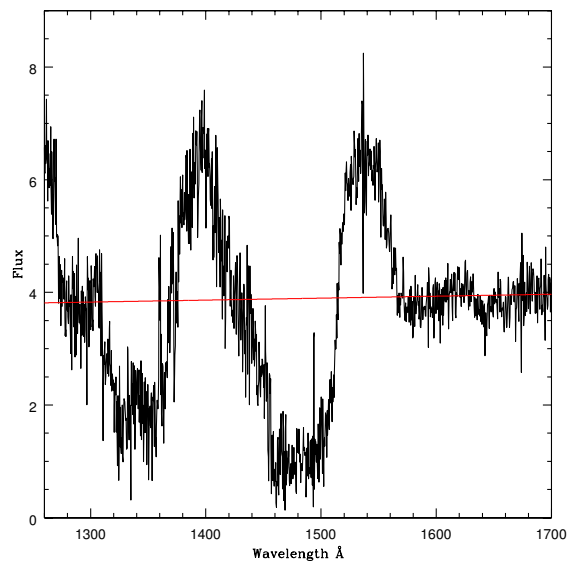


FIGURE 2.3: Example of a linear fit, shown in red, across the C IV and Si IV emission and absorption region of a quasar spectrum. The spectrum fit is that of SDSS J015921.53+141043.1 shown in black.

2.2 The SDSS DR5 Quasar Catalogue

The Sloan Digital Sky Survey fifth data release contains over a million spectra. The DR5 quasar catalogue contains spectra of 77429 quasars, of these 28421 have redshifts between 1.7 and 4.2 and thus show C IV emission in their SDSS spectrum. Sloan spectra are available to download from their web page in 1 dimensional form and have been sky subtracted, corrected for telluric absorption and spectrophotometrically calibrated by the pipeline. Each spectrum is presented in 69 km s^{-1} bins giving a resolution, $\frac{\lambda}{\delta\lambda}$, per two pixel element of approximately 2000 over the whole wavelength range.

2.3 The AI and BI

The traditional method of quantifying the depth and broadness of absorption in a quasar spectrum has been to use the Balnicity index (Weymann et al. 1991). Recently there has been much debate regarding the completeness of this metric leading some authors to introduce a new metric for BAL classification known as the absorption index, AI (Trump et al. 2006), which they claim produces a more complete sample of BAL objects. Below we define the two metrics and discuss the merits of each.

2.3.1 The Balnicity Index

Weymann et al. 1991 introduced the Balnicity Index (BI) as a quantitative measure of 'BALness'. The BI can take values between 0 and 20000 km s^{-1} and is given by equation 2.3.1

$$BI = \int_{3000}^{25000} C[1 - f(v)/0.9]dv \quad (2.3.1)$$

where C is 1 for those parts of a trough below 90% of the continuum after the trough has been below 90% of the continuum for 2000 km s^{-1} and zero elsewhere. The integral is in velocity space with blue shifted velocities being positive. Calculation of the BI starts at 3000 km s^{-1} in order to avoid confusion between the continuum and line emission and to avoid including absorption caused by gas within the host galaxy

that will typically have low velocity relative to the AGN. The BI of a completely black trough spanning the entire region would be 20000 km s^{-1} . A BI value greater than zero was, until recently, the usually accepted empirical definition of a BALQSO. Trump et al. 2006 suggested that the BI will miss many genuine BAL objects whose absorption does not extend beyond 5000 km s^{-1} (the integral starts at 3000 km s^{-1} and the absorption must extend for at least 2000 km s^{-1}).

2.3.2 The Intrinsic Absorption Index

Hall et al. 2002 defined the intrinsic absorption index or AI as a tool to investigate unusual BAL objects.

The AI is given by equation 2.3.2

$$AI = \int_0^{29000} C' [1 - f(v)/0.9] dv \quad (2.3.2)$$

where in this case C' is 1 for all of regions in which the spectrum is below 90% of the continuum for more than 450 km s^{-1} and zero otherwise. This definition will clearly give non zero values for a significantly larger number of objects than the BI (c.f. equation 2.3.1) as it will include absorption close to the line centre as well as not requiring the absorption to be as broad as the BI. Trump et al. 2006 extended this work using a modified version of the AI, that has just $f(v)$ in place of $f(v)/0.9$ (meaning Trump et al. 2006's AI is a true measure of EW) as well as requiring that the width of the absorption exceed 1000 km s^{-1} rather than 450 km s^{-1} , as a method of defining BALQSOs in order to include those objects whose absorption does not extend beyond 5000 km s^{-1} or whose troughs are between 1000 and 2000 km s^{-1} wide.

Trump et al.'s AI produces a much larger sample of BAL candidates representing a BAL fraction of 26%. This value is significantly larger than the 12% found by Weymann et al. 1991. However Knigge et al. 2008 along with work presented here show that Trump et al.'s distribution of AIs has a low AI peak occupied almost exclusively by those objects with BI=0 suggesting that the AI while efficient at finding absorption systems may include two distinct classes of object and therefore may not be a good method of defining BALQSOs.

2.4 The AI and BI distributions

Previous studies indicate that the derived values of BI are sensitive to the continuum placement. In order to look at the variations introduced to the BI based on the continuum placement the BI values given to objects by Trump et al. 2006 and the author are presented in Figure 2.4. This figure shows that at high values of BI the value calculated by the author is consistent with that from Trump et al. 2006 whilst at low values the two diverge. This is to be expected as troughs which are close to 2000 km s^{-1} in width may contribute significantly to one value but not at all to the other. This could occur when a point close to the edge of the trough is slightly above 90% of one of the fit continua whilst remaining below 90% of the other resulting in one value of the BI being considerably larger than the other. A similar effect could occur in broad shallow troughs where a point within the trough may be above 90% of one of the continuum fits but not the other. Troughs contributing to large values of the BI are likely to be much deeper than 0.9 times the continua throughout the trough and considerably wider than 2000 km s^{-1} and are therefore unlikely to only contribute to one value because of variations in the continuum fit.

All AI and BI values discussed, with the exception of those shown in Figure 2.4 have been calculated by the author. The $\log(\text{AI})$ distribution (Figure 2.5 calculated using equation 2.3.2) appears to be bimodal with one group centred around a few hundred km s^{-1} and the other around a few thousand (see Knigge et al. 2008). When it is split up into those objects with BI of zero and those with non-zero BIs (see Figure 2.6) it becomes clear that the majority of objects in the low end of this distribution would not classically be considered BALQSOs. This bimodality may be an effect of the exclusion of the $f(v)/0.9$ as it is not present in the AI distribution resulting in a minimum non zero AI value of 100 km/s which may result in bunching together objects at the low end of the distribution. In order to test this theory a new AI distribution is calculated using $f(v)/0.9$ instead of $f(v)$. This distribution is shown in Figure 2.8 and does remove some of the bimodality however when the new distribution is split up into those objects with $\text{BI}=0$ and those with $\text{BI}>0$ (see Figure 2.9) it is clear that the two different populations remain.

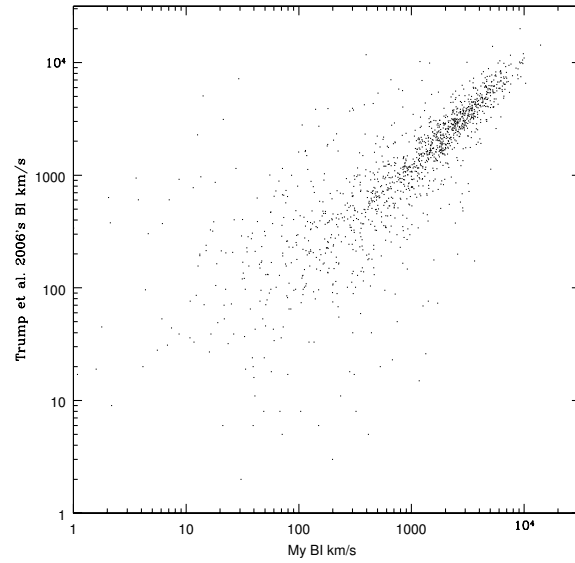


FIGURE 2.4: Values of the BI calculated by the author plotted against values of the BI calculated by Trump et al. 2006 for the same objects.

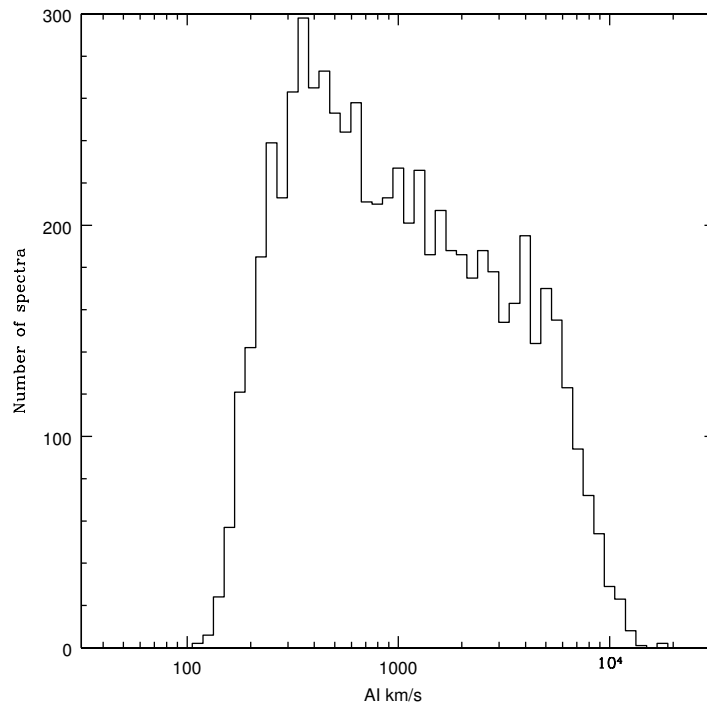


FIGURE 2.5: The distribution of the absorption index as calculated by the author using equation 2.3.2 from DR5 of the SDSS plotted in log space.

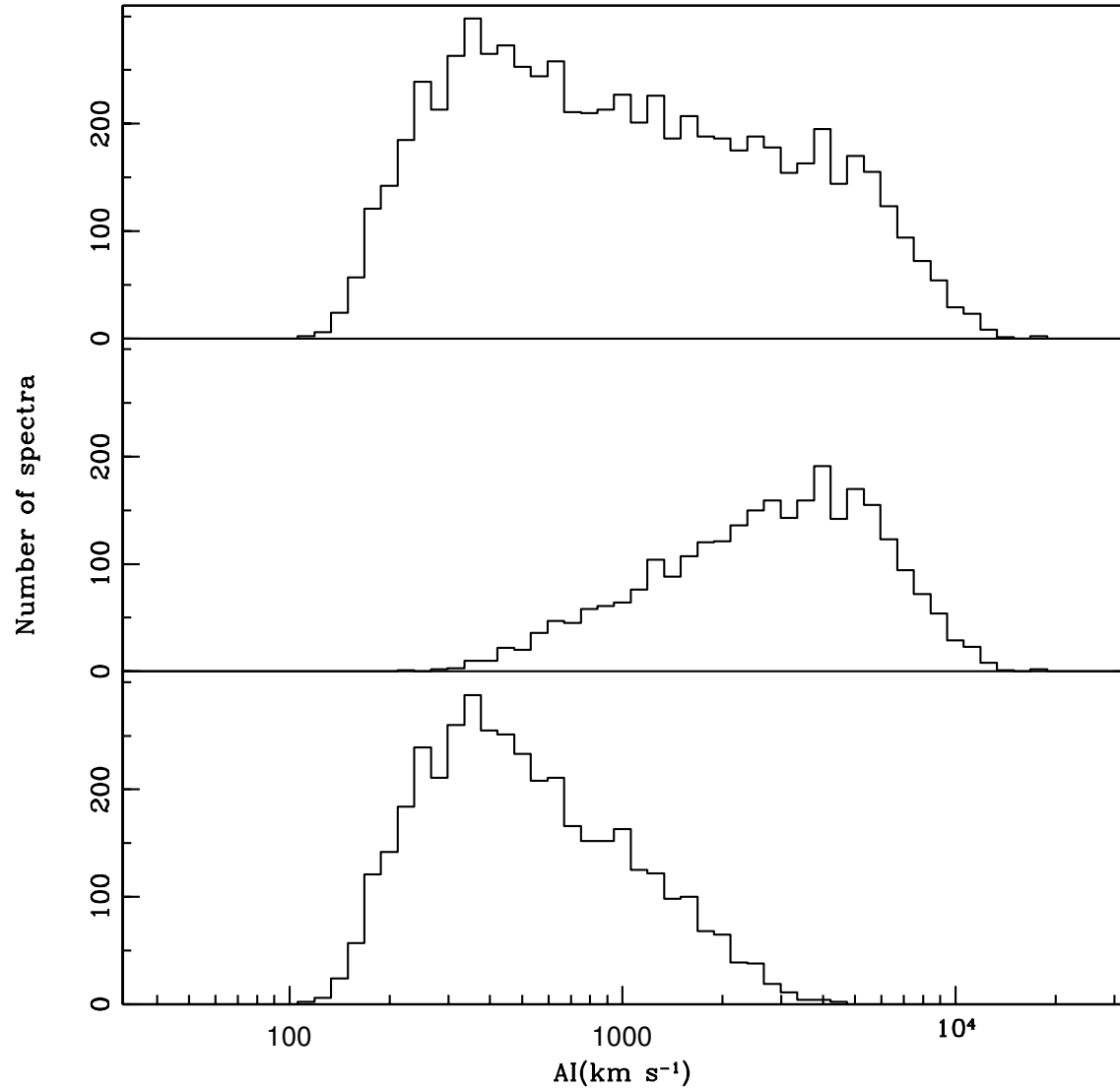


FIGURE 2.6: Top, AI distribution calculated using equation 2.3.2 by the author for all objects in DR5. Middle, AI distribution calculated by the author for those objects with non-zero BIs. Lower panel, AI distribution for those objects with BI=0.

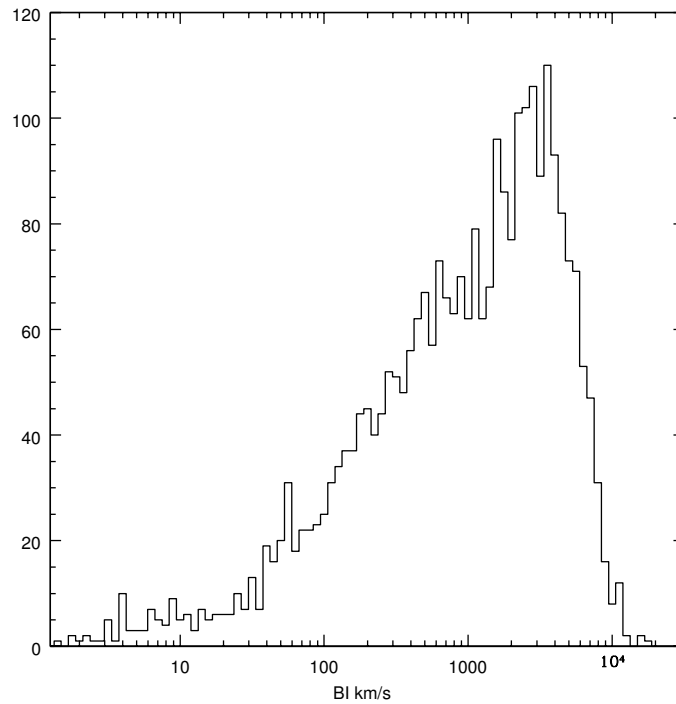


FIGURE 2.7: The distribution of the balnicity index as calculated using equation 2.3.1 from DR5 of the SDSS plotted in log space.

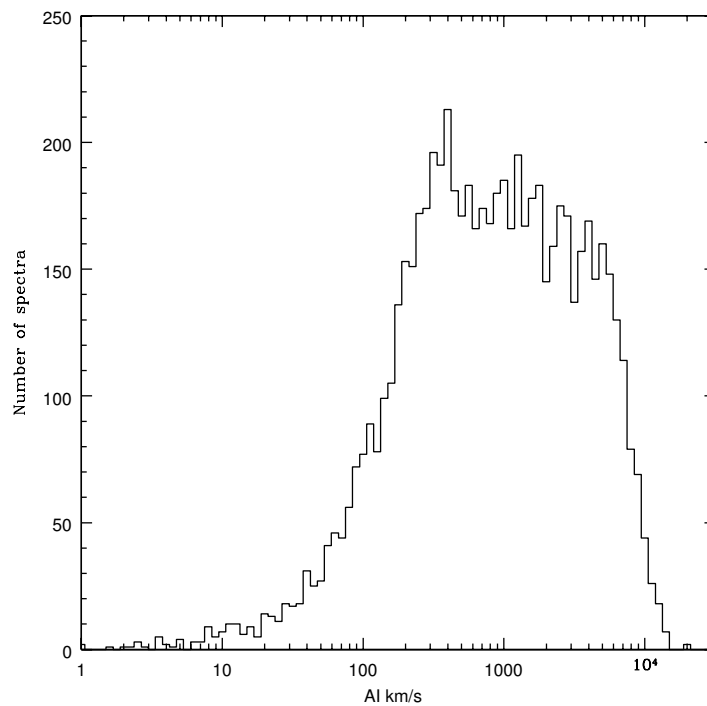


FIGURE 2.8: Modified AI distribution calculated using equation 2.3.2 with $f(v)/0.9$ replacing $f(v)$ for all objects in DR5 of the SDSS.

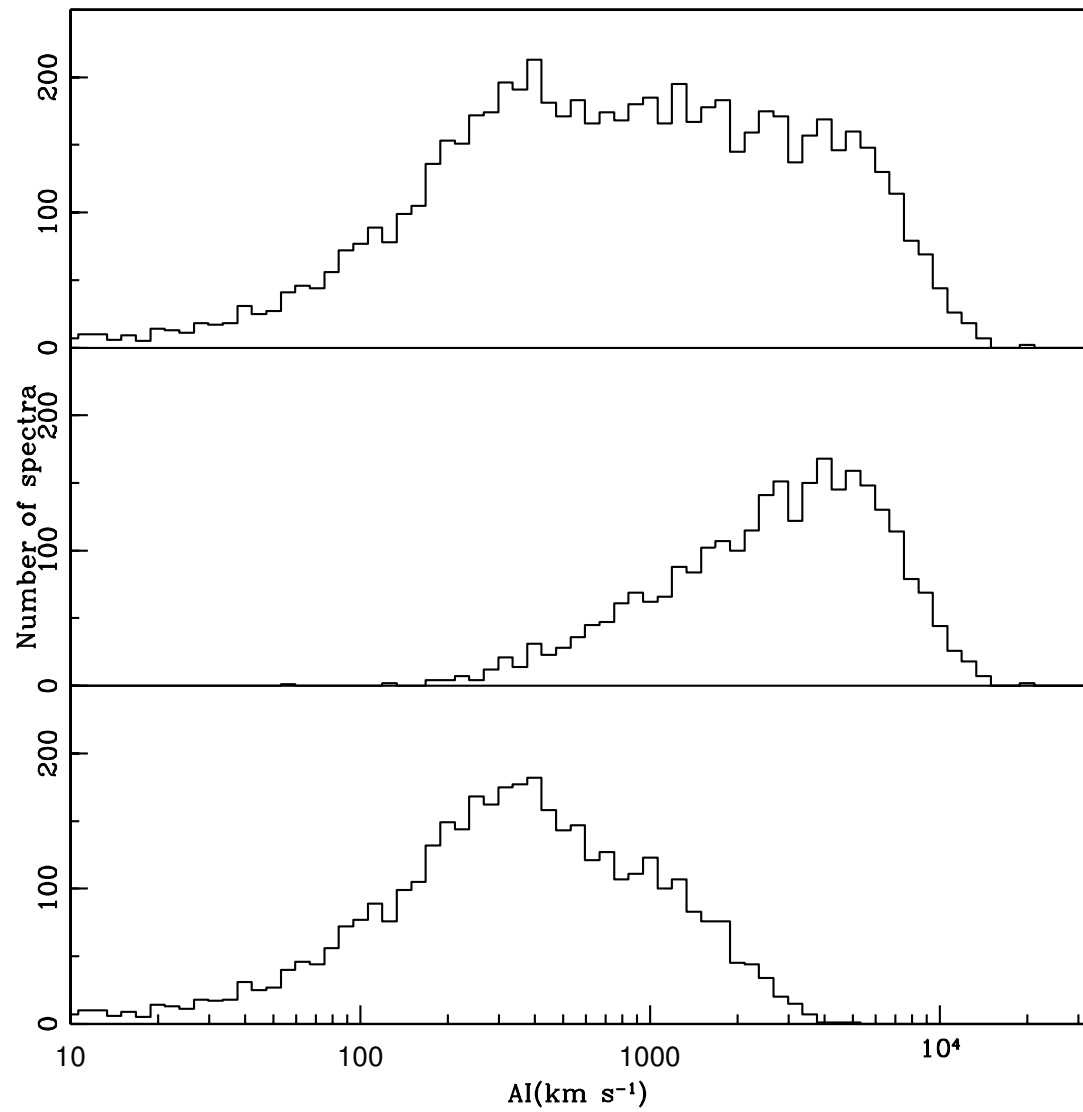


FIGURE 2.9: Modified AI distribution using equation 2.3.2 with $f(v)/0.9$ replacing $f(v)$. Calculated from DR5 of the SDSS for all objects (top), objects with $BI > 0$ (middle) and $BI = 0$ (bottom).

2.5 BALQSOs and Intrinsic absorbers

Whilst many of the objects with $AI > 0$ would not be selected as BALQSOs by the BI this does not necessarily mean that they are physically distinct as they may simply be slightly narrower or lower velocity outflows produced via the same underlying mechanism as the objects selected by the BI. A selection of spectra with a variety of AI and BI values are shown in Figures 2.10 to 2.13 to highlight differences between objects from the low and high end of the AI distribution. Figure 2.10 shows that these objects do not show broad blue-shifted absorption features suggesting that using $AI > 0$ as a definition for BALQSOs will result in significant contamination from objects that are not genuine BALQSOs. However in Figure 2.11 one can see that those objects which have non-zero values for the BI and low AI values also show no obvious broad absorption suggesting that a sample of BALQSOs selected purely on the basis of the BI may also contain some incorrect identifications (probably due to poor continuum fits). Figures 2.12 and 2.13 show objects with fairly large values for the AI with objects in Figure 2.12 having a zero BI. These two figures show that the majority of objects with high AI values do show broad absorption lines irrespective of their BI values. The objects in Figure 2.12 are precisely those that the AI was designed to find.

These figures highlight the problems inherent in using fixed metrics to identify BAL features. Metrics designed to include all of the true BALs tend also to identify a significant number of objects whose absorption may be produced via a different mechanism for example: (1) by absorption within the host galaxy, which typically occurs at low velocity relative to the AGN; (2) intervening absorption systems at different redshift to the host galaxy that will generally occur at random velocity shifts and may be due to absorption by different species.

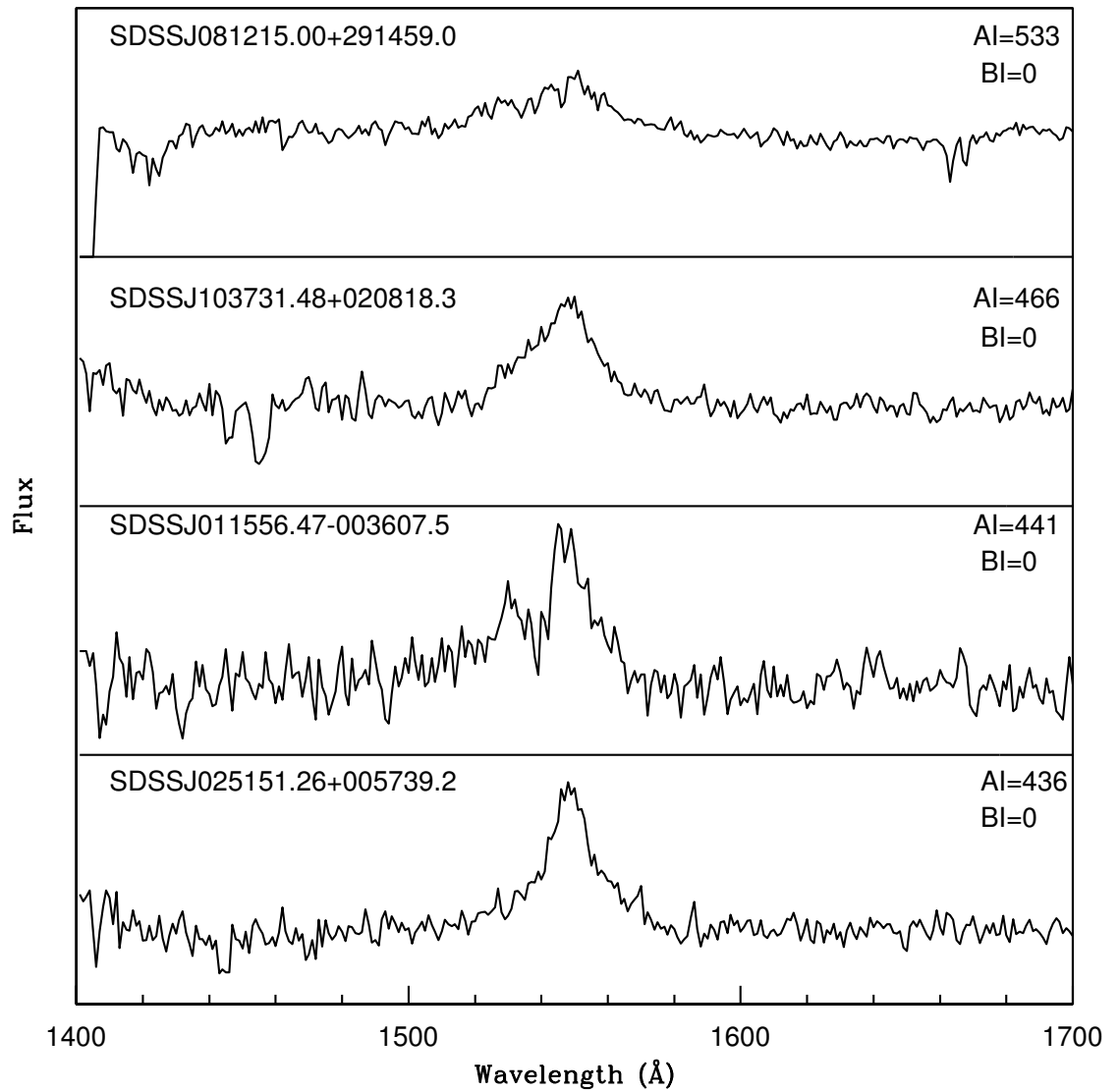


FIGURE 2.10: Example spectra of objects with AI values, calculated by the author, of between 300 and 600 kms^{-1} and BI=0.

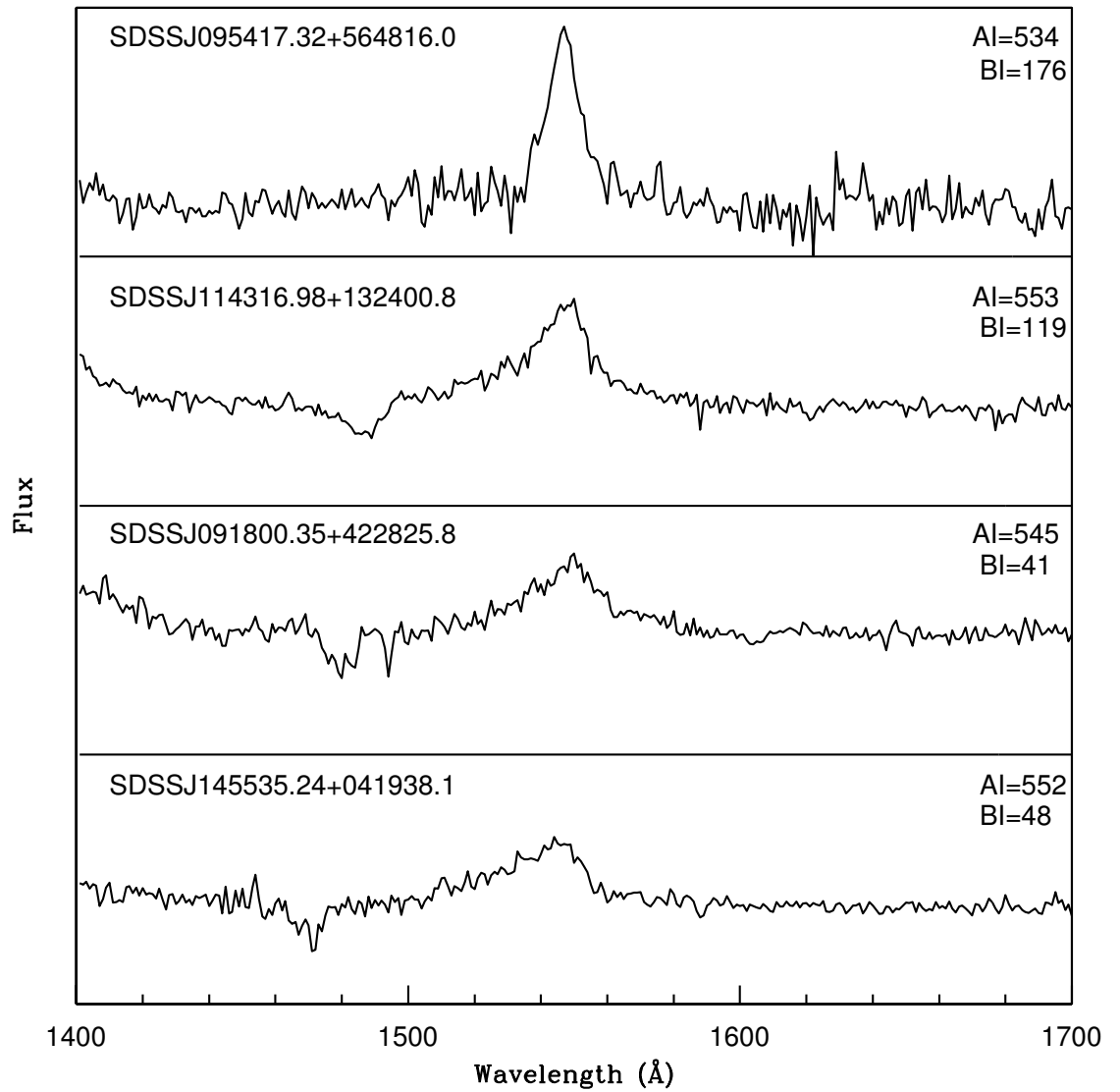


FIGURE 2.11: Example spectra of objects with AI values, calculated by the author, of between 300 and 600 kms^{-1} and $\text{BI} > 0$.

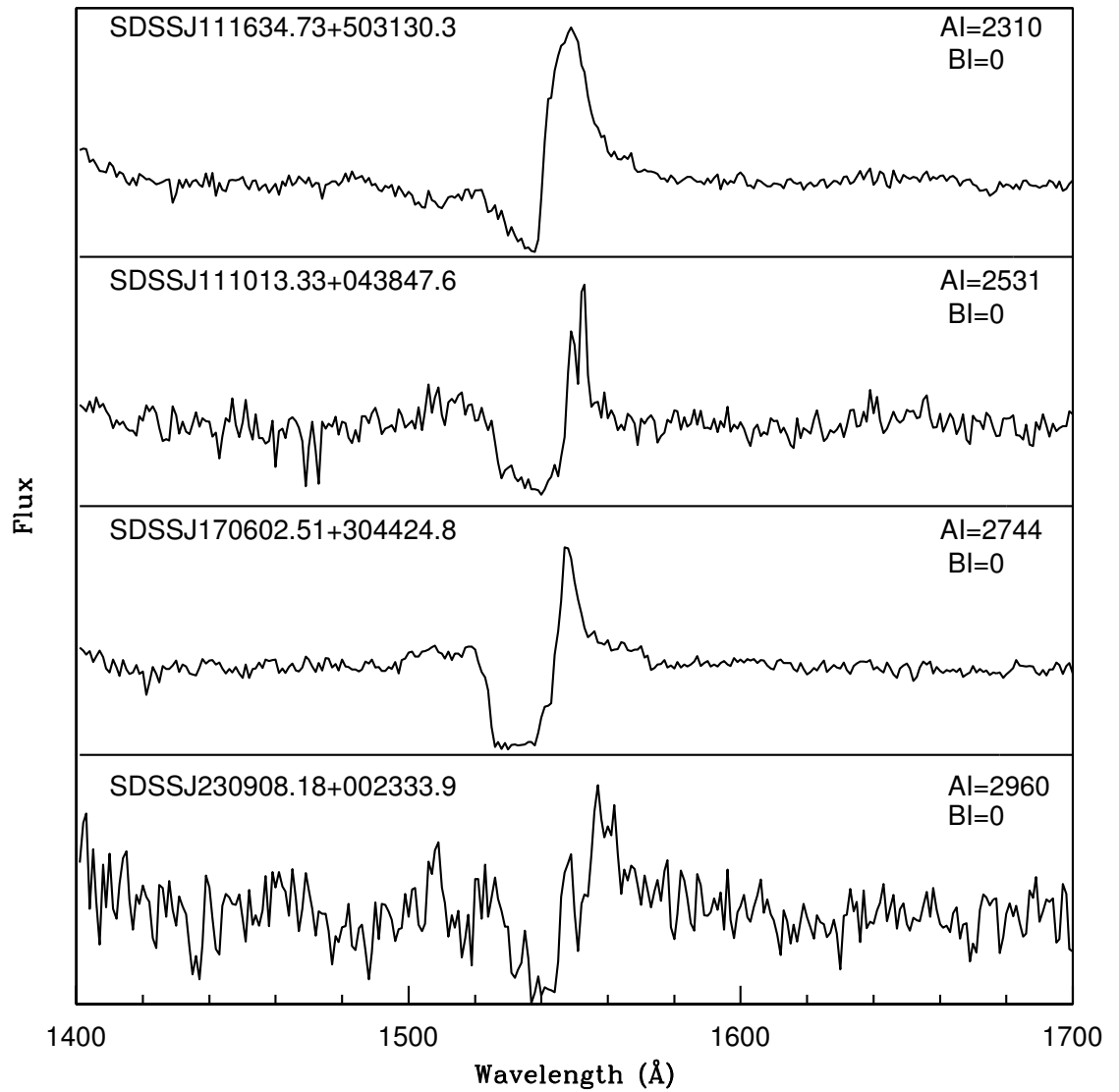


FIGURE 2.12: Example spectra of objects with AI, calculated by the author, of between 1500 and 3000 kms^{-1} and BI=0.

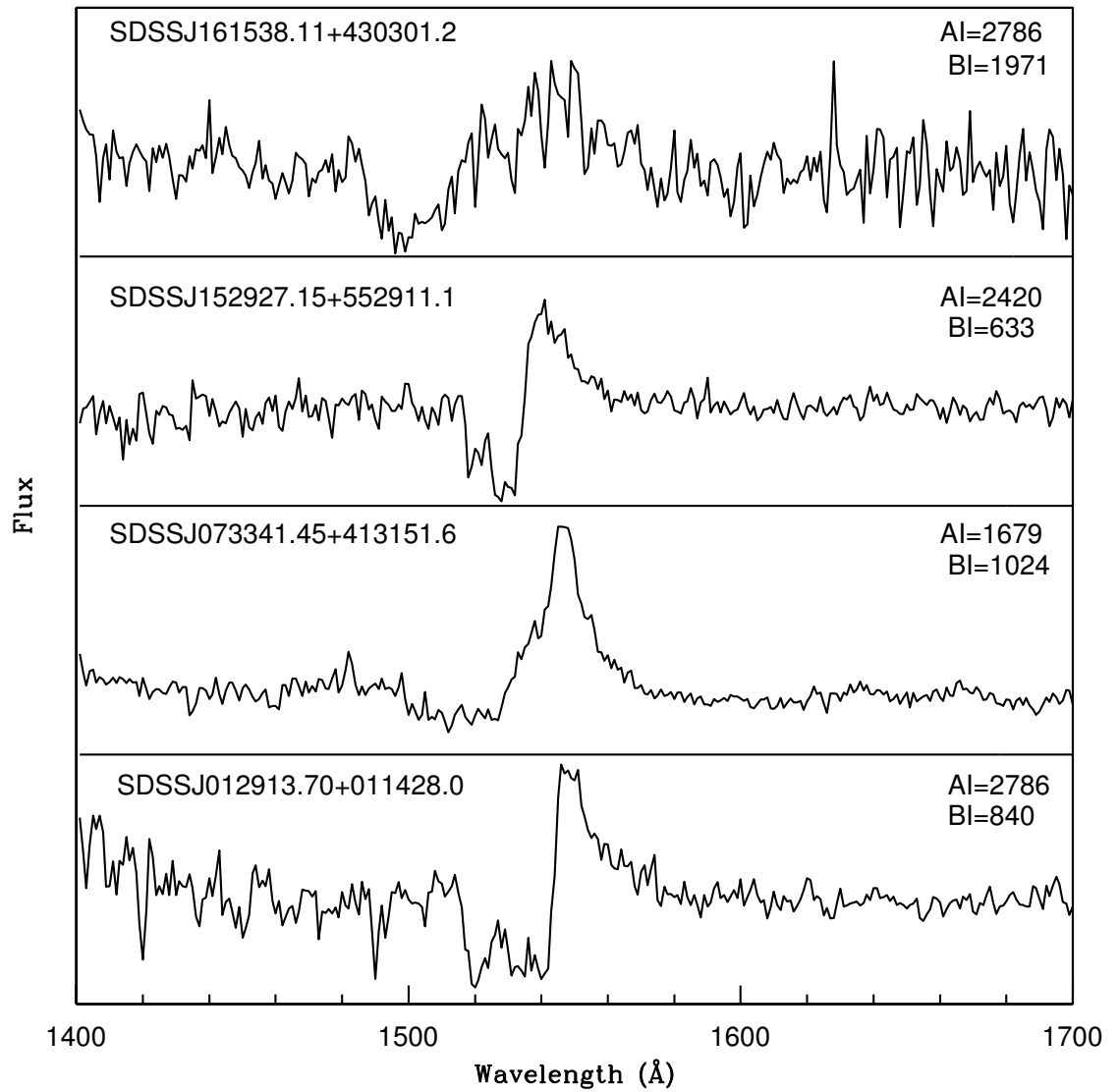


FIGURE 2.13: Example spectra of objects with AI, calculated by the author, of between 1500 and 3000 kms^{-1} and $\text{BI} > 0$.

2.6 Composite Spectra

Another way to look at the different types of object selected by the metrics is to create composite spectra of those objects selected by the different methods. These composites are created using the same method used to create the quasar composite used in the continuum fitting process. The quasar spectra are put into the rest frame using the SDSS quasar catalogue redshift, re-binned into 1 Å bins and normalised to an average flux of unity between 1700 and 1750 Å. The composites are all geometric means.

Figure 2.14 shows the composite of all objects selected by the BI (dashed line) in addition to the composite of all DR5 quasars between redshifts 1.7 and 4.2 (solid line). This composite shows that the objects selected by the BI show significantly redder spectra in the UV. This is expected because BALQSOs are generally viewed through more dust contained in the outflow than non-BALQSOs (Reichard et al. 2003b). The BI composite also shows that the emission lines are somewhat weaker although this is likely to be due to absorption in some objects rather than a genuine relationship between blue shifted absorption and line strength.

The AI composite is shown in Figure 2.15 and is again shown along with the quasar composite. This spectrum is similar to the BI composite but is less red and almost identical to the general quasar composite beyond 1700 Å. The absorption in C IV also appears to be spread more evenly across the trough compared to the BI composite which shows very deep absorption close to the emission line which drops off as you go further from the line.

Figure 2.16 shows the composite spectra of those objects with $AI > 0$ and $BI = 0$. This spectrum is the most revealing as it shows that there is very little difference in the overall spectral shape of these objects compared to the general quasar population. The absorption in these objects appears to be randomly spread throughout the trough suggesting that a significant portion of this absorption occurs in regions unconnected to the AGN emission. If this is the case then such objects are clearly physically distinct from the BALQSO population which is produced by outflows from close to the central engine.

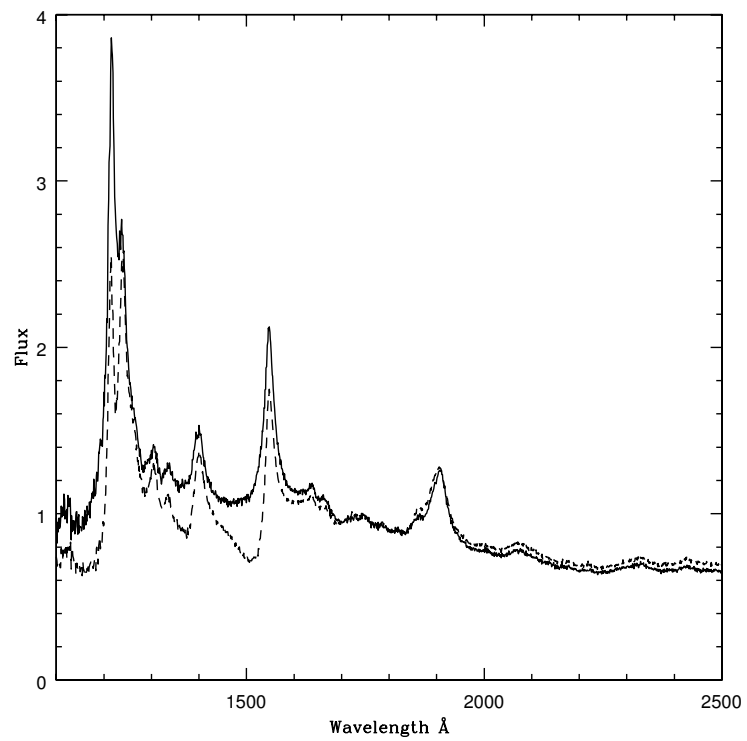


FIGURE 2.14: Composite spectra for all quasars (solid line) and quasars with $BI > 0$ (dashed line).

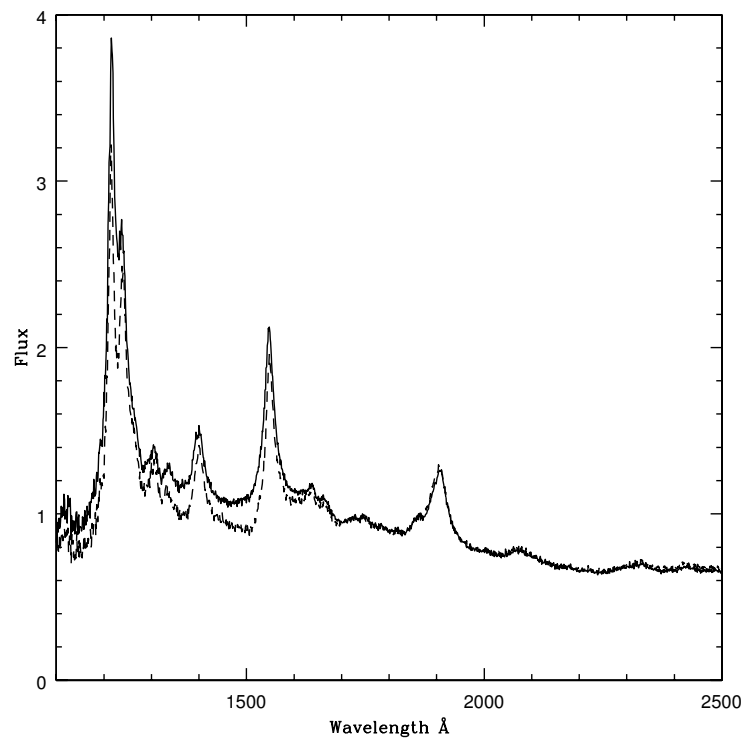


FIGURE 2.15: Composite spectra of all quasars (solid line) and quasars with $AI > 0$ (dashed line).

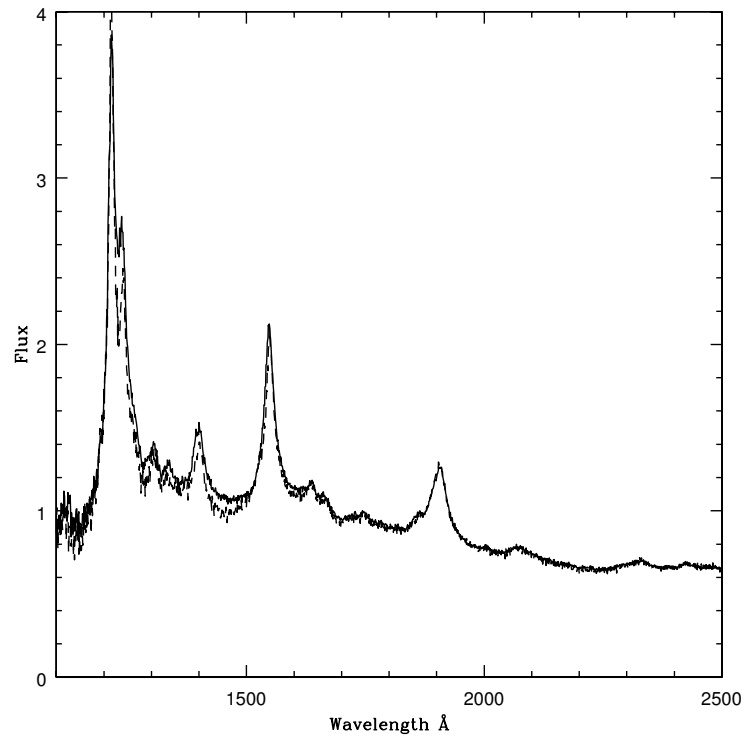


FIGURE 2.16: Composite spectra of all quasars (solid line) and quasars with $AI > 0$ and $BI = 0$ (dashed line).

2.7 LVQ- Learning Vector Quantisation

In an attempt to circumvent the problems of using inflexible metrics Knigge et al. 2008 used a learning vector quantisation algorithm to identify BALQSOs from the quasar catalogue from DR3 of the SDSS (Schneider et al. 2005) which contains 46420 quasars compared to the 77429 in DR5 (Adelman-McCarthy et al. 2007). The algorithm employed is essentially a neural network that learns how to recognise BALQSOs and non-BALQSOs when given a sufficiently large set of training objects tagged by the authors. The details of the network training can be found in Knigge et al. 2008 and do not form part of this thesis. In addition to the LVQ network those objects for which the network and the BI disagree (i.e. the network classes a $BI=0$ object as a BALQSO or a $BI>0$ object as a non-BALQSO) are visually inspected and classified by the authors, this step is necessary as the majority of these objects with $BI>0$ are visually classified as BALQSOs. This method is applied to the DR5 catalogue by Scaringi et al. 2009 and we find 3552 BALQSOs. The LVQ alone would miss-classify 710 of these objects as non-BALQSOs as well as including another 440 objects which have been visually classified as non-BALQSOs.

2.8 The BALQSO Fraction

The fraction of objects identified as BALQSOs obviously depends upon the method used to identify objects as BALQSOs. The fractions found by the various metrics and the LVQ network of Knigge et al. 2008 and Scaringi et al. 2009 are discussed here. There are 28421 quasars between redshift 1.7 and 4.2 which allow the C IV BAL region to be seen. Of these, 2880 ($10.1\pm 0.2\%$) have $BI>0$ and 6778 ($23.9\pm 0.3\%$) have $AI>0$, the LVQ network based method of Scaringi et al. 2009 gives 3552 ($12.5\pm 0.2\%$). The errors given are statistical errors only and do not include systematic errors.

There are several causes of systematic error in the derived BAL fraction. For example, the algorithm used by the SDSS to select quasars is based upon non-BALQSO colours which are different to BALQSO colours so a BALQSO is more likely to appear in a region in 4D colour space that will not be flagged as a possible

quasar. In addition, the absorption will reduce the luminosity of a source such that at a given redshift and intrinsic AGN luminosity a BALQSO will be fainter so non-BALQSOs close to the magnitude limit of the sample would not be included if they were significantly absorbed (and therefore less bright). These systematic errors are difficult to quantify and their importance varies with redshift. Knigge et al. 2008 treat this problem in some detail and conclude that there is no evidence for any evolution of the BAL fraction with redshift. For this reason I have chosen not to investigate any variation in the BAL fraction with redshift for the DR5 samples. The sources of systematic error given in this section will lead to an underestimate of the intrinsic BALQSO fraction which Knigge et al. 2008 suggest is $17\pm 4\%$ based on an observed fraction of approximately 13.5% from DR3.

The fraction of objects identified as BALQSOs is also dependent on the signal-to-noise ratio (see e.g. Figure 2.17). This figure shows that the dependence of BAL fraction on S/N is complex and depends on the band used to measure the S/N ratio for low values of S/N and that there is essentially no change in fraction by any of the methods above S/N of 10. The fraction of objects identified as BALQSOs by the AI decreases with increasing S/N in all bands suggesting that at low S/N the AI incorrectly selects objects due to noise in their spectra more often than it fails to select objects showing absorption. The BI and LVQ methods select a fraction of objects that appears to be independent of the S/N in the r' band but increases with S/N in the i' band and decreases with S/N in the g' band. The increase in BALQSO fraction at low S/N in the g' band may be due to the redshift of these objects as for the majority of our sample the C IV BAL would appear within the g' band this may result in BALQSOs showing lower g' band S/N than they would if they did not show absorption. The i' band is least likely to be effected by absorption and the increase in BALQSO fraction with S/N suggests that some BALQSOs are being missed due to their poor S/N ratio while very few non-BALQSOs are miss classified by the BI or LVQ due to low S/N.

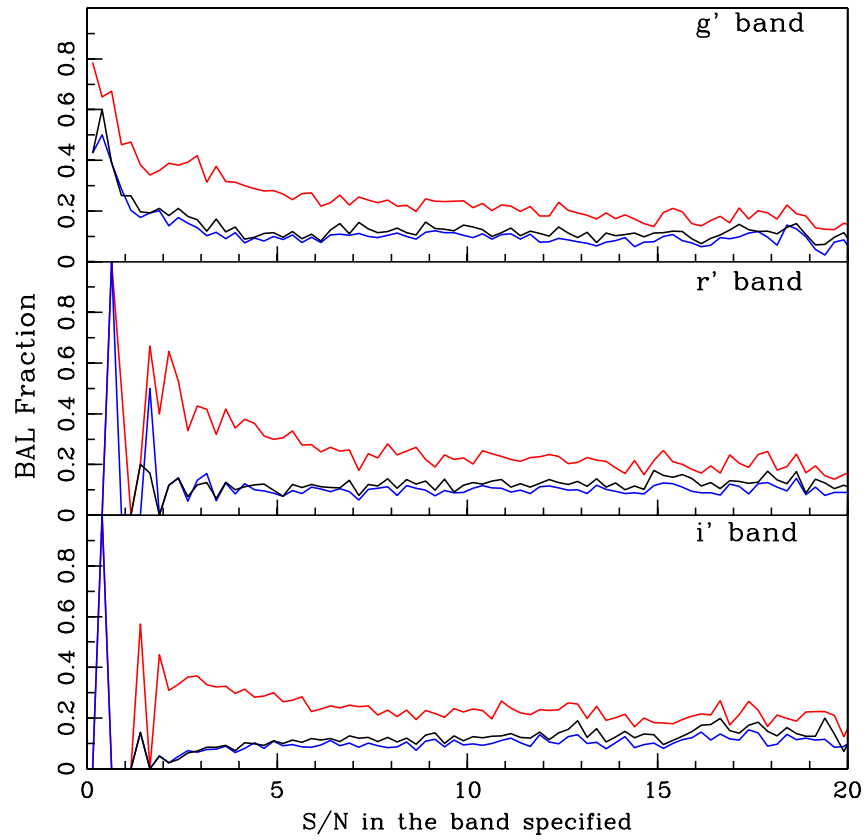


FIGURE 2.17: BALQSO fraction as a function of S/N for the AI (red), BI (blue) and LVQ (black) methods. The top panel is for the S/N in the g' band, the middle panel the S/N in the r' band and the lower panel the S/N in the i' band.

2.9 Summary

Having used three different methods to identify BALQSOs in DR5 of the SDSS it is clear that all three methods have drawbacks. This is partly due to problems with defining what a BALQSO is as well as difficulties pinpointing where absorption comes from in a given object. Metrics are inherently inflexible and this is a major weakness when attempting to identify objects which are not well defined. Thus whether the difference between a mini-BAL and a BAL is a physical one or an arbitrary line in the sand is not clear.

However it is clear that the BI is incapable of identifying objects whose absorption does not extend beyond 5000 km s^{-1} blueward of the emission-line or those objects with absorption lines narrower than 2000 km s^{-1} . The BI does not produce very many false positive identifications except in situations where the continuum is poorly estimated.

The AI is unlikely to miss any significant broad absorption but will identify far more absorption systems, many of which may be intervening absorbers within the host galaxy which are unrelated to the broad absorption outflows. The bi-modality within the $\log(\text{AI})$ distribution may be evidence of two separate mechanisms responsible for the absorption identified by the AI. Inspecting examples of objects with $\text{AI} > 0$ and $\text{BI} = 0$ (Figure 2.10) shows that the AI does select objects other than those which show clear broad absorption troughs.

The LVQ-based method of Scaringi et al. 2009 is a robust hybrid method based on a combination of a neural network and visual inspection of outliers. This method requires visual classification of those objects for which the network and the BI disagree as without this stage the network will miss-classify a significant number of objects. It is this LVQ-based method that is used to provide a BALQSO catalogue from DR5 of the SDSS throughout the rest of this thesis.

Chapter 3

Identifying objects exhibiting the ghost of Lyman- α

This chapter discusses the line-locking feature known as the ghost of Ly- α . The proposed mechanism responsible for the formation of this feature is described in section 3.1, along with the criteria set out by Arav et al. 1995 required for the feature to be observable. Section 3.2 describes the method used to select objects which show evidence of this feature, the selection of a comparison sample is described in section 3.3. The methods used to test Arav's criteria along with the results of these tests are presented in section 3.4. A summary of these results is presented in section 3.5 and as these results appear to show little correlation between meeting the criteria and the presence of a feature within the ghost zone, we have performed a series of tests to establish the reality of the ghost feature are presented in section 3.7 after discussion of a potential Si IV ghost in section 3.6. This work draws largely from our paper (Cottis et al. 2010) published in MNRAS.

3.1 The ghost of Ly- α

The feature that is poetically known as the ghost of Ly- α is a hump seen in the absorption trough of a small fraction (less than 5%, Arav 1996, North et al. 2006) of BALQSOs located 5900 km s⁻¹ blue-ward of the centre of the line to which the absorption is attributed. The feature was first investigated by Korista

et al. 1993 after being seen in a difference spectrum of BALQSO and non-BALQSO spectral composites produced by Weymann et al. 1991 who pointed out that the difference between the two absorption troughs was approximately equal to the velocity separation of N V and Ly- α . In a series of papers in the mid 90's (Arav & Li 1994, Arav et al. 1994, Arav & Begelman 1994, Arav et al. 1995, Arav 1996) Arav suggested that the feature seen at this velocity was a result of the increased radiative pressure on N V ions at this velocity within the outflow. In this picture N V ions moving at 5900 km s^{-1} 'see' the Ly- α emission from the AGN at the energy of their own emission resulting in a large increase in the scattering cross section of the Ly- α photons. Consequently, out-flowing N V ions receive an increase in radiation pressure leading to a large injection of momentum into the outflow. The out-flowing ions of other species are dragged to higher velocities by electromagnetic interactions with the N V ions, leading to a deficit of material at this velocity (because each out-flowing ion spends very little time at this velocity before being accelerated to greater velocities). In turn this causes a decrease in the opacity at this velocity which manifests as a peak within the absorption troughs of the out-flowing species.

This simple mechanism explains both the presence of the feature and why its position is linked to the rest frame of the source.¹ Arav 1996 suggested that the reason for the feature being most prominent in C IV absorption rather than in other species, is that the doublet separation of C IV is far smaller (498 km s^{-1}). By comparison the larger doublet separations of Si IV (1933 km s^{-1}) and O VI (1647 km s^{-1}) result in the feature being blurred over several thousand km s^{-1} , producing a low contrast feature which is difficult to detect in low S/N data. For this reason, in this study we confine our search for ghost features to the C IV broad absorption line only.

¹This is not the case for shadowing of N V by Ly- α (Korista et al. 1993) where the separation of the troughs is constant but their velocities are determined by the velocity of the first trough.

Since Ly- α and N v are amongst the strongest UV lines in AGN spectra, an obvious question to ask is why aren't ghost-features ubiquitous amongst the general BALQSO population? To answer this, Arav proposed a set of physically motivated criteria which had to be met before ghost features would be observable. These are:

1. Significant broad absorption in the region between 3000 and 9000 km s⁻¹ blue-ward of line centre,
2. Strong intrinsic Ly- α emission,
3. Narrow Ly- α emission,
4. Strong broad N v absorption,
5. Little far-UV flux between between $\lambda 200\text{\AA}$ and $\lambda 1000\text{\AA}$.

The first criterion is simply a statement that ghost-features can only be observed if significant photon scattering is occurring. The second criterion implies that there must be a significant flux of Ly- α photons, while the third requires that the line-emitting gas has a relatively narrow spread in velocities so that the resulting feature is not spread over a large range of velocity reducing the contrast. Since the dominant scattering ion is N v, strong N v absorption is also needed. The final requirement, and the most difficult to measure, recognises that in order for Ly- α -N v line-locking to dominate the dynamics of the flow, there cannot be significant far-UV line driving (see e.g. Korista et al. 1993).

3.2 Selection of ghost-candidate spectra

BALQSOs represent $\sim 15\%$ of the quasar population (see e.g. Knigge et al. 2008 and references therein), of these, between $\sim 20\text{-}25\%$ show evidence for multiple troughs (Korista et al. 1993, North et al. 2006). Amongst the multi-trough objects, ghost candidates are likely rare representing less than a few per cent of BALQSOs (Arav 1996) because of the stringent requirements for ghost observability. Thus in order to find significant numbers of ghost-candidates, large quasar samples are required.

All previous ghost candidate samples have been limited to just a handful of objects (North et al. 2006, Arav 1996). The largest previous sample was that compiled by North et al. 2006 from the EDR of SDSS with 7 ghost-candidates. By comparison, Data Release 5 (DR5) of the Sloan Digital Sky Survey (SDSS) contains 77,429 quasars of which 28,421 have redshifts between 1.7 and 4.2 allowing C IV and any associated absorption to be seen in their optical spectra. We require a visible C IV BAL because although radiative line driving will produce a feature in all absorption troughs, the resultant hump will be most easily observed in the C IV absorption trough because of the small doublet separation of this line. Several BALQSO samples have been compiled from the various data releases of the SDSS (Reichard et al. 2003a; Trump et al. 2006; Knigge et al. 2008) and from DR5 (Gibson et al. 2009a, Scaringi et al. 2009). Here, as discussed in Chapter 2, we adopt the BALQSO catalogue of Scaringi et al. 2009, containing 3,552 BALQSOs.

To identify strong ghost candidates we have performed five cuts on this BALQSO sample. The first cut eliminates noisy spectra ($S/N < 4$ per pixel), estimated in two line-free continuum bands from $\lambda\lambda 1650\text{--}1700\text{\AA}$ and $\lambda\lambda 1700\text{--}1750\text{\AA}$. To reduce contamination from emission, absorption and cosmic rays that may be present in either bin we take the greater of the two values as our S/N estimate. The second cut removes all objects which show an apparently single smooth absorption trough. Following this cut we are left with only those objects which display multiple absorption trough features (1019 in total).²

A third rejection cut removes those objects that contain 2 or more peaks within the absorption trough (numbering 761). These objects are eliminated to reduce contamination by objects which display absorption from multiple out-flowing regions which by chance happen to lie at velocities corresponding to the ghost-zone. This leaves just 258 objects which contain a single-peak (or alternatively double-trough) within the C IV absorption region.

Figure 3.1 (upper panel) shows our multi-trough composite spectrum (solid line) created from taking the geometric mean of all objects rejected at this stage after normalising the flux between $\lambda\lambda 1700\text{--}1750\text{\AA}$ to unity. In order to highlight the absorption regions, we also plot a non-BALQSO composite spectrum

²Approximately 28% (1019 out of 3552) of our BALQSOs show evidence for multiple troughs. This compares favourably with previous studies by North et al. 2006 who found that 58 out of 224 (26%) of BALQSOs from SDSS EDR showed evidence of multiple-troughs, and Korista et al. (1993) who found 16 out of 72 objects (22%) showed multiple-troughs.

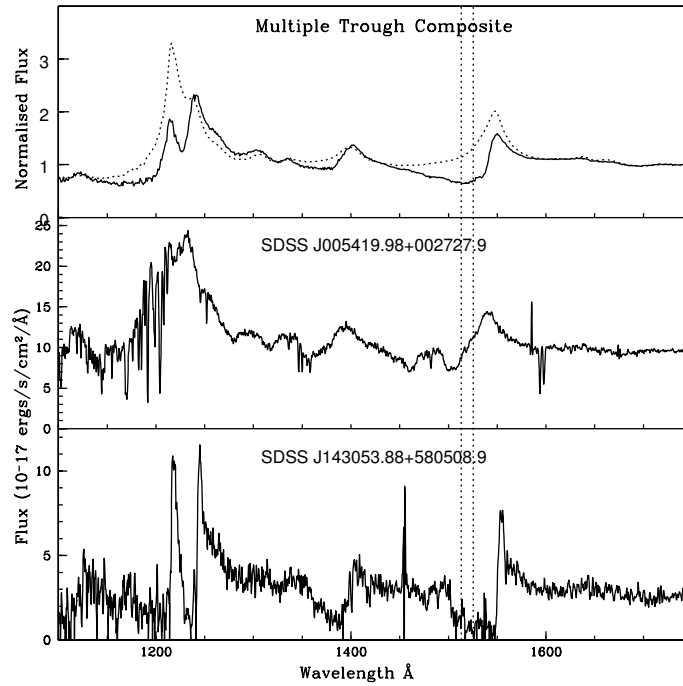


FIGURE 3.1: Top-Panel: Geometric mean composite spectrum of objects (1019) rejected due to having multiple trough features (solid line) fit with a reddened DR5 QSO composite (dashed line). Middle and lower panels: example spectra of individual objects rejected at this stage. The dashed vertical lines indicates the location of the ghost-zone.

(dashed line). The non-BALQSO composite is the geometric mean of all of the quasar spectra in the SDSS DR5 quasar catalogue in the redshift range $1.7 < z < 4.2$ excluding those objects which are also in the BALQSO catalogue of Scaringi et al. 2009, and reddened to fit to the continuum windows in the multi-trough composite spectrum using the SMC extinction law of Pei 1992. For completeness, the middle and lower panels show two example spectra rejected at this stage. We note that our multi-trough composite spectrum shows no evidence for coherent structure within the C IV trough. This suggests that the positions of the various absorption systems in the individual spectra are in general uncorrelated, that is they do not contain a large number of ghost candidates that happen to show additional peaks within the absorption. This is consistent with the hypothesis that these multiple-trough spectra are the result of multiple unconnected absorbing systems.

For the 258 objects which show a single peak in their C IV absorption we make a further cut to remove those objects (189) which show peaks outside of the ghost-zone as defined by North et al. 2006. The

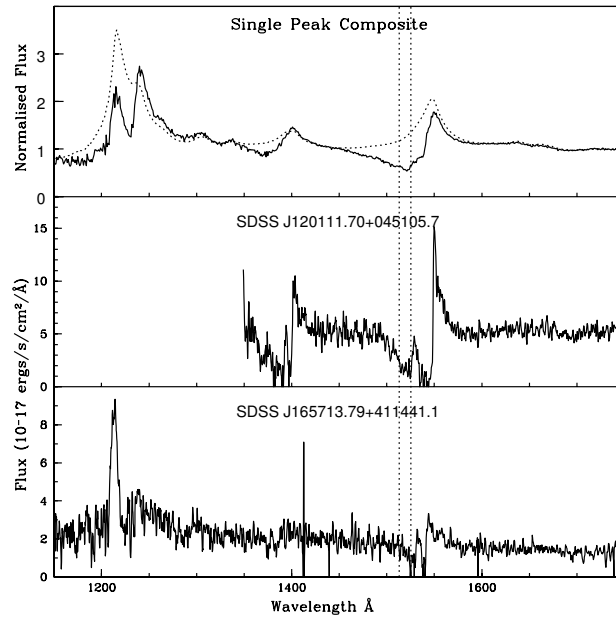


FIGURE 3.2: Top-Panel: Geometric mean composite spectrum of objects (189) rejected due to having double-trough, ghost-like features, that appear outside of the ghost zone (solid line) fit with a reddened DR5 composite (dashed line). Middle and lower panels: example spectra of individual objects rejected at this stage. The dashed vertical lines indicate the location of the ghost-zone.

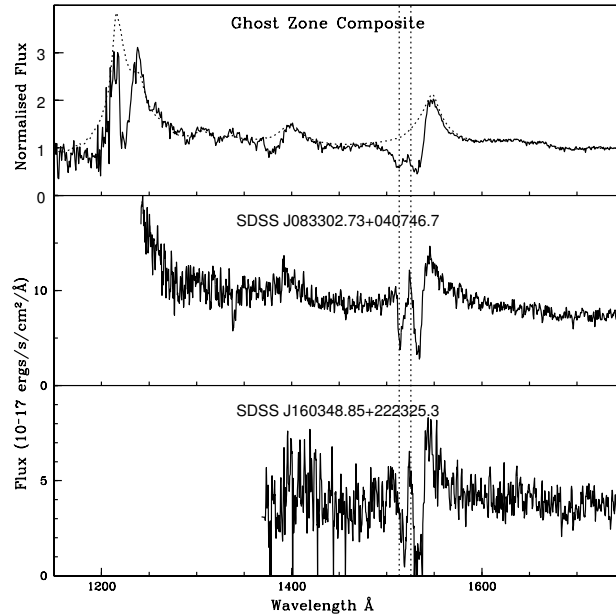


FIGURE 3.3: Top-Panel: Geometric mean composite spectrum of objects (26) rejected due to having insufficient absorption either side of the ghost feature. Middle and lower panels: example spectra of individual objects rejected at this stage. The dashed vertical lines indicate the location of the ghost-zone.

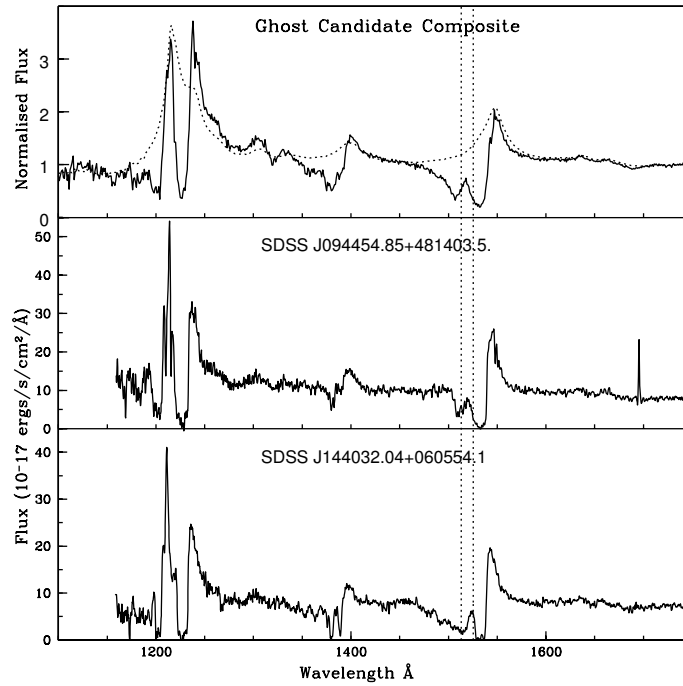


FIGURE 3.4: Top-Panel: Geometric mean composite spectrum of our ghost-candidate sample of 43 objects. Middle and lower panels: example spectra of individual objects making up this sample. The dashed vertical lines indicate the location of the ghost-zone.

ghost zone edges are 5900 km s^{-1} blue-ward of the peaks of the doublet of the emission line in question (in this work C IV) this zone is then expanded to take into account redshift errors by multiplying these boundaries by $1 \pm \Delta z / (1 + z_{med})$, where z_{med} is the median redshift of our sample ($z_{med} = 2.14$), and Δz is the average redshift error ($\Delta z = 0.01$). This results in a ghost zone extending between $\lambda 1513.2 \text{ \AA}$ and $\lambda 1525.4 \text{ \AA}$ for C IV. Our single-peak composite comprising 189 objects whose peak lies outside of the ghost-zone is shown in Figure 3.2 (upper panel, solid line). The middle and lower panels show example spectra of objects rejected at this stage. Each object shows a clear peak located just outside of the limits of the ghost zone.

Interestingly, this composite spectrum shows some evidence of a feature at the low velocity edge of the ghost zone. One possible explanation for this feature is that these objects are genuine ghost-candidates with poorly assigned redshifts. However, on closer inspection of the objects rejected at this stage we find no evidence for features outside of the ghost zone due to random redshift errors. Alternative explanations

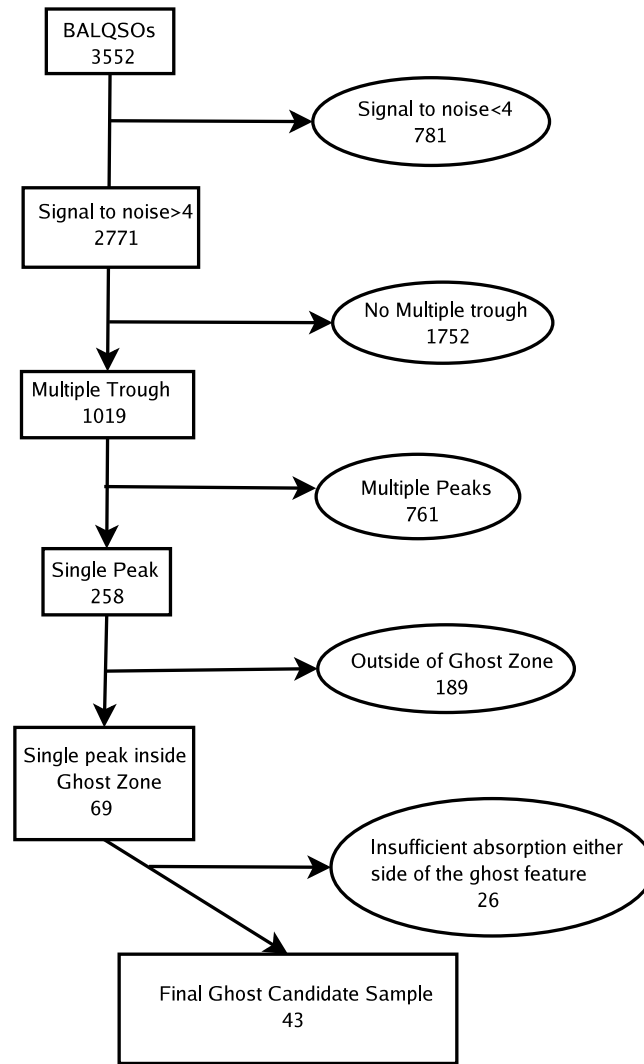


FIGURE 3.5: A flow diagram showing the number of objects rejected at each stage of the ghost selection algorithm..

for the origin of this feature include, (i) intrinsically weaker absorption at lower velocities, or (ii) an abrupt change in the intensity of the (overlying) emission at these velocities.

We make one further cut to remove those objects which do not show significant broad absorption either side of the ghost feature extending from 3000 to 9000 km s^{-1} blue-ward of the emission-line. This cut is chosen to eliminate objects with deep narrow absorption features whose alignment mimics the presence of a ghost feature. Figure 3.3 (upper panel, solid line) displays the composite spectrum of all objects rejected at this stage, while in the middle and lower panels, we give examples of individual objects rejected by this cut. Though the composite spectrum shows a clear feature within the ghost zone, it is not smooth,

instead displaying sharp narrow features, whose separation is larger than the doublet separation of C IV. This reflects both the narrowness of the absorption features (since intrinsically broad humps would be smoothed out in the averaging process yielding low contrast features) which make up this composite, and in addition small differences in their velocities relative to the rest-frame of the source. These differences may result from these features being unrelated to the ghost formation mechanism and appearing in the ghost zone by chance though we cannot preclude the fact that some of the objects rejected at this stage are indeed true ghost-candidates.

Our final sample of 43 ghost-candidate objects comprises the largest sample of objects exhibiting the ghost of Ly- α and the first to allow a detailed statistical analysis of the properties of these objects. Figure 3.4 shows the geometric mean composite ghost-candidate spectrum (solid line), together with a non-BALQSO composite spectrum (dashed line), and two example ghost-candidate spectra (middle and lower panels). Our final ghost-candidate composite spectrum displays a clear smooth double-trough structure located firmly within the ghost zone of a relatively broad absorption trough. Visual comparison of this composite with that formed from objects rejected at the previous stage (i.e. those with insufficient absorption either side of the ghost-zone), indicates that our final sample displays on average narrower Ly- α and C IV emission-lines, stronger Ly- α emission and deeper N V absorption (fulfilling 3 of Arav's criteria for forming observable ghost features), as well as broader Si IV absorption, and suggests that we are indeed isolating those objects most likely to form observable ghost features. Figure 3.5 is a flow-chart summarising the various cuts made in the creation of our ghost-candidate sample.

3.3 Selecting a Comparison Sample

Of the 43 strong ghost-candidates, 21 are at large enough redshift $z > 2.15$ to place Ly- α above the atmospheric cut-off and thus allow us to test for each object all of the criteria deemed necessary for ghost-formation. These are listed in the upper half of Table 3.1. For the remainder, their redshifts are too low to allow a direct measurement of the strength and width of the Ly- α emission-line. For these objects we estimate the strength and width of the Ly- α emission-line using the C IV emission-line as a surrogate, and

substantiated by known correlations between the two lines (see e.g. Wilkes 1984, Ulrich 1989). These objects are listed in the lower half of Table 3.1. For completeness, we have also compiled a sample of BALQSOs showing no evidence for a ghost feature or multiple trough. This allows us to compare the relative frequency with which the ghost-formation criteria are met amongst BALQSOs both with and without ghost features. In order to create such a sample we have performed a number of cuts on the Scaringi et al. 2009 BALQSO sample. As for our ghost-candidate sample we first select for $S/N > 4$, and then select those objects with $z > 2.15$ to allow inspection of the N V and Ly- α emission-lines necessary to test for the presence of strong narrow Ly- α emission and strong N V absorption. The remaining spectra are then visually inspected and any object showing multiple absorption troughs or any other hint of a ghost feature are removed from the sample. We also remove those objects which do not show significant absorption between 3000 and 9000 km s⁻¹. This leaves just 26 objects showing significant C IV absorption between 3000 and 9000 km s⁻¹ with no evidence for a ghost feature or multiple trough. One of these objects SDSS J101056.68+355833.3 shows evidence for a ghost feature in the Si IV absorption line (see A5) and is therefore also removed from our comparison sample leaving just 25 objects. A summary of the rejection cuts made in the creation of our comparison sample is given in Figure 3.6. The geometric mean composite spectrum of our comparison sample is indicated by the dotted line in Figure 3.7. Aside from substantially weaker N V absorption, the strengths and widths of the emission-lines in the comparison sample composite spectrum match those of the ghost candidate composite spectrum remarkably well. The main difference between these two composite spectra appears to be the absence of the low-velocity absorption trough in the comparison sample spectrum. We do not believe this difference arises from the way in which the two samples were selected.

In section 3.4 we use our ghost-candidate sample to test, where possible, the criteria set out by Arav 1996 required by radiative acceleration models to produce an observable ghost feature. We compare the relative frequency with which our ghost candidate spectra meet the criteria necessary for the formation of observable ghost features with our non-ghost comparison sample.

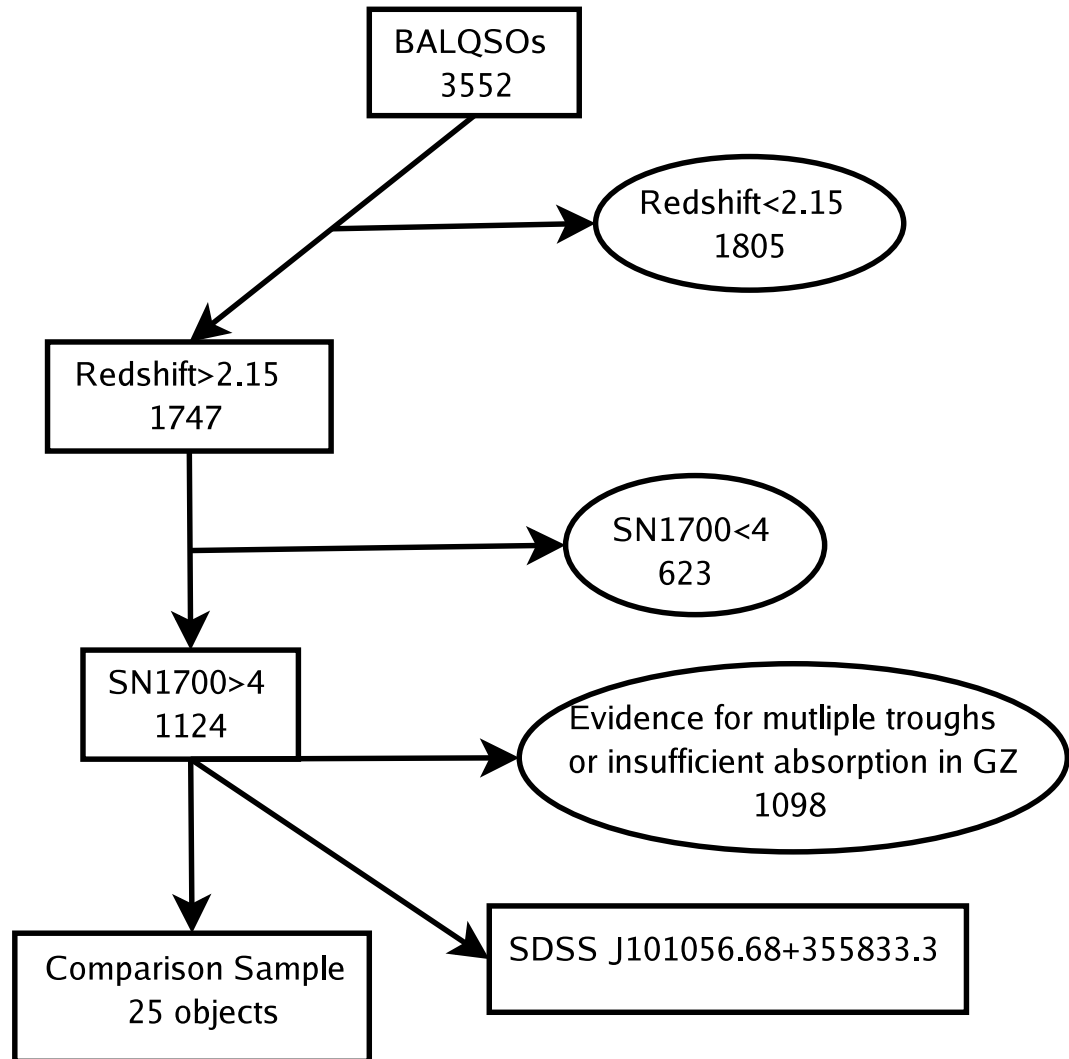


FIGURE 3.6: Flow diagram showing the number of objects rejected at each step in our comparison sample selection algorithm.

3.4 Testing the criteria for the formation of observable ghost features

In this section we present the results of testing the criteria for the formation of observable ghost features. We first concentrate on the sample of 21 ghost-candidate objects for which all of the criteria may be tested and compare these results with those obtained using our non-ghost comparison sample. We then move on to our remaining objects and test where possible whether these objects satisfy the necessary criteria.

3.4.1 Significant C IV broad absorption line

All of the objects in our ghost candidate sample will clearly show significant absorption in the region between 3000 and 9000 km s⁻¹ blue-ward of the C IV emission line as this is required in order to see any potential ghost feature. This criterion is required purely because in order to effect the out-flowing C IV ions in an observable way this outflow must reach significant optical depth and appear as a BAL trough within the spectrum. Our comparison sample has also been chosen to exhibit strong broad absorption, so naturally also fulfils this criterion.

3.4.2 Strong Intrinsic Ly- α emission

In order for the effects of Ly- α radiation on N V to cause a significant increase in the radiation pressure on the outflow as a whole the Ly- α emission line must be intrinsically strong. However, since the ghost of Ly- α is produced by scattering Ly- α photons it can be extremely difficult to measure the strength of the intrinsic Ly- α emission-line. Hence Arav et al. 1995 modified this criterion to allow the C IV and N V emission-lines to be used in situations where the Ly- α emission-line was either significantly absorbed, or had insufficient spectral coverage. This modified criterion requires Ly- α emission to be at least 300% above the continuum and/or both C IV and N V to be at least 100% above the continuum³. They note that

³We note that measuring the strength of a line according to its peak flux can be misleading, since it implies that the underlying line profiles are similar for all objects (and thus the total flux in the line simply scales with the peak flux). For example, a comparison between the C IV emission-line of the composite spectra in Figure 3.7 suggests that both our ghost-candidate and comparison samples display a narrower underlying C IV emission-line. If the widths of the other emission-lines scale with the C IV emission-line width, then we would expect both the Ly- α and N V emission-lines to be similarly narrow.

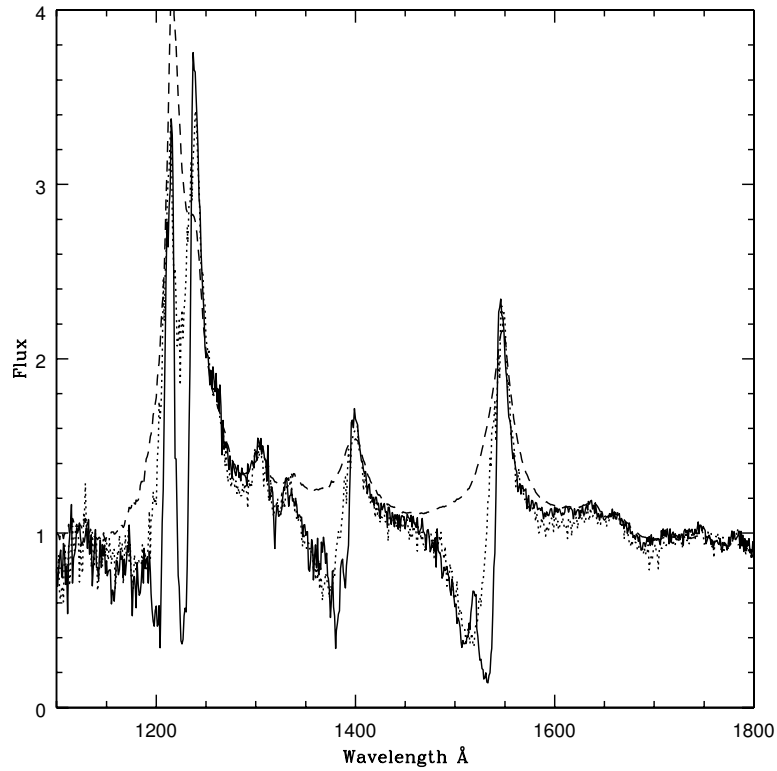


FIGURE 3.7: Comparison between the geometric mean composites formed from (i) 21 ghost-candidates with $z > 2.15$ (solid line), (ii) 25 BALs with featureless broad absorption troughs (dotted line), and (iii) non-BALQSOs from the DR5 QSO catalogue (dashed line).

‘the latter criterion is hardly ideal but observations of non-BAL quasars show that the line strengths roughly scale together’ (Arav et al. 1995). Here we isolate the continuum emission using the SPECFIT package in IRAF. We model the continuum as a reddened power law and fit to the continuum in regions free of contaminating emission- and absorption- lines, where possible. This can be particularly difficult for objects with the highest velocity out-flows as there are few emission/absorption line-free regions. Furthermore, we have not attempted to fit for the continuum short-ward of $\lambda 1280\text{\AA}$ as this region is typically so absorbed and the line-emission so highly blended that no clean continuum regions can be identified. Instead, we fix the continuum strength at short wavelengths to that measured between $\lambda\lambda 1315\text{--}1350\text{\AA}$. This approach is chosen to avoid overestimating the strength of the broad absorption, at the expense of overestimating the strength of the line-emission in a few cases.

In objects whose spectra cover the Ly- α region, 86% (18/21) of the ghost candidate sample meet the

criterion for strong emission-lines compared to 88% (22/25) of the comparison sample. Inspection of the composite spectra for the two samples (Figure 3.7), indicates that the strength of the Ly- α emission-line (relative to the continuum) is broadly similar in the two samples, and both are weaker relative to the non-BALQSO composite, due to the presence of strong N v and Ly- α absorption. For the other lines, the N v emission-line appears stronger on average in our ghost-candidate and comparison samples relative to non-BALQSOs, while there appears little difference in the strength of the C IV emission-line, though we note that in so far as we can measure them, their emission-line widths appear to be narrower on average.

3.4.3 Narrow emission-lines

Models of outflows accelerated by radiative line driving produced by Arav & Begelman 1994 and Arav et al. 1995 suggest that once the line widths exceed 3500 km s^{-1} (FWHM) potential ghost features become undetectable. This is because broader emission-lines will result in a broader, lower contrast feature (since the core of the line, where most of the scattering occurs, is weaker relative to the wings in a broad emission-line c.f a narrow emission-line) which is difficult to detect particularly in low S/N data. Unfortunately, determining the width of the underlying emission-lines in BALQSOs is extremely difficult as the broad absorption in these objects prevents accurate measurements of the shape and strength of the underlying emission-lines and continuum. Given how our ghost-candidate sample was selected we expect all of the ghost-candidates to show significant absorption in the blue wing of Ly- α , N v and C IV, while our comparison sample was chosen to exhibit strong relatively featureless absorption in the blue wing of C IV.

Since we cannot make an accurate measurement of the width of the Ly- α emission-line we instead attempt to estimate its likely width using the C IV emission-line width as a surrogate. For the majority of sources, C IV is severely absorbed, so we estimate its underlying un-absorbed width using model fits to the red wing of the emission-line. We use the same underlying fit for the continuum as was used to measure the emission-line strength (section 3.4.2). We fit the red-wing with a two-component model, a Gaussian core and Lorentzian wings, with the central wavelengths fixed together but allowed to vary slightly from the rest wavelength of C IV. We allow the strength and width of the two components to vary independently and

fit to the red-wing taking care to avoid those regions of the spectrum contaminated by broad He II $\lambda 1640$ and [O III] $\lambda 1663$ emission. The measured width is taken to be the FWHM of the composite fit. If the measured $\text{FWHM} < 3500 \text{ km s}^{-1}$, then the object meets the criterion for the formation of an observable ghost feature.

For our 21 ghost-candidates with $z > 2.15$, only 12 (57%) have $\text{FWHM}(\text{C IV}) < 3500 \text{ km s}^{-1}$. In the remainder, those for which the C IV width can actually be measured (17 objects), 8/17 (47%) also meet this criterion. This fraction is similar to that found for our comparison sample where 12 out of the 20 objects (60%) for which C IV width measurements can be made, also meet this criterion (see Table 3.2 for details). Taking the average of all of the FWHM measured for the ghost candidates gives an average FWHM of $3345 \pm 842 \text{ km s}^{-1}$ which is similar to the upper limit proposed by Arav 1996 and to the average FWHM of C IV found for the comparison sample ($3534 \pm 1160 \text{ km s}^{-1}$). A K-S test on these populations shows no significant difference between the ghost and comparison samples. The difficulty in fitting the C IV line in many of these objects results in large uncertainties in the estimated widths, however it is clear that several of our ghost candidates have emission that is wider than the 3500 km s^{-1} upper limit proposed by Arav 1996. There are a number of possible explanations for this. Firstly, C IV may be a relatively poor surrogate for the width of Ly- α . Alternatively, our sample may suffer from contamination by objects in which the potential ghost feature is produced by a chance alignment of multiple absorption systems or through other mechanisms unrelated to radiative acceleration. If the potential ghost-features are indeed due to line-locking, then it may in-fact be possible to produce an observable ghost feature from emission-lines with widths in excess of 3500 km s^{-1} .

3.4.4 Strong N V broad absorption line

As described in section 3.1, the ghost feature is produced by the increased radiation pressure on out-flowing N V ions by Ly- α photons. Since in this model the N V ions scatter a significant fraction of the incident flux, strong N V absorption is a pre-requisite.

In order to measure the strength of absorption due to N v we use a modified Balnicity index (Weymann et al. 1991). We take the continuum to be equal to the mean flux between $\lambda\lambda 1315\text{--}1330\text{\AA}$, and require that the flux drops to below 90% of this value continuously for $> 1000 \text{ km s}^{-1}$ between 0 and 7000 km s^{-1} blue-ward of the N v emission line. We use the 7000 km s^{-1} limit to avoid contamination by absorption due to Ly- α . Any object with a non-zero value for this measure is considered to show strong N v broad absorption.

Significant N v absorption is measured in all 21 objects from our ghost candidate sample whose redshift allows detection of N v absorption. Only 44% (11/25) of our comparison sample satisfy this criterion. The geometric composites of Figure 3.7, confirm that our ghost-candidate sample displays significantly stronger N v absorption on average than our comparison sample. Moreover, the broadly similar N v emission-line strengths of the ghost-candidate and comparison sample, emphasises the increased importance of N v absorption in the ghost-candidate spectra.

3.4.5 Little far-UV flux

Photo-ionisation models suggest that the far UV spectra of quasars contain a significant number of emission-lines between $\lambda 200$ and $\lambda 1000\text{\AA}$ that will contribute to the radiation pressure on any BAL outflow (Korista et al. 1993). In order for a ghost feature to be observed the radiation pressure of Ly- α on the N v ions in the outflow must be at least comparable in strength to the radiation pressure on all other ions in the outflow. This led Arav to suggest that the far-UV continuum must therefore be necessarily weak in objects showing ghost features. Absorption of far-UV photons both within the host galaxy as well as within our own galaxy preclude direct measurement of the far-UV continuum. However Arav et al. 1995 note that the strength of the He II $\lambda 1640 \text{ \AA}$ emission-line can be used as a surrogate for the far-UV ionising continuum. A strong He II line suggests a similarly strong far-UV flux and vice-versa as this line is produced by photons with energies corresponding to $\lambda 228\text{\AA}$ ($\approx 54 \text{ eV}$).

However, the He II emission-line strength is notoriously difficult to measure even in high quality spectra.

This is because of its close proximity to the [O III] λ 1663 emission-line, as well as its location near the red-wing of C IV, which may extend to relatively high velocities. Thus isolating the broad He II component generally requires multi-component fitting (see e.g. Goad & Koratkar 1998) which without prior information (for example, variability data), is rather subjective.

Since the quality (in terms of S/N) of the individual spectra in both our ghost-candidate and comparison samples is relatively low, we do not attempt to fit to the individual line components. Instead, we use our non-BALQSO composite spectrum as a template for the region of interest, and scale each spectrum to this template, by minimising the residual flux in the region of interest. Our optimisation routine fits for the underlying continuum in both spectra, and adjusts for both redshift errors and the scale factor over the region of interest (nominally $\lambda\lambda$ 1600-1680Å). Since both spectra are first normalised to the flux in the continuum band between $\lambda\lambda$ 1700–1750Å, if for the sake of simplicity we assume that the He II and [O III] emission line strengths scale together, then the derived scaling factor between the ghost-candidate and non-BAL QSO spectra is a measure of the ratio of their He II EWs. Figure 3.8 shows an example of a fit. In the top panel we show the non-BALQSO composite (solid line) and a ghost-candidate spectrum (dotted line). In the middle panel we show the spectra together with their continuum fits spanning the C IV–He II region, while in the lower panel we show a close-up of the non-BALQSO composite and the scaled ghost-candidate spectrum after removal of the underlying continuum. The residual flux under the He II–[O III] lines is indicated by the dot-dashed line. We caution that this fitting process is sensitive to (i) small redshift errors between the spectra, (ii) an appropriate choice of continuum bands (in general the choice of the continuum bands depend on the width of the C IV absorption trough, and most importantly (iii) the S/N of the spectra. Consequently the error on the scale factor is generally quite large. We have visually inspected the results of the fitting process for all of our ghost-candidate and comparison spectra to verify that the fitting procedure has converged correctly, adjusting the continuum bands, and region over which the spectra are scaled when necessary. In Table 3.1 we list the He II scale factors, that is, the multiplication factor necessary to produce the same equivalent width in the ghost-candidate spectrum. A number less than 1 indicates that the ghost-candidate spectrum has larger equivalent width in the line in the region of He II than the non-BALQSO spectrum. Conversely, numbers greater than 1 indicate that

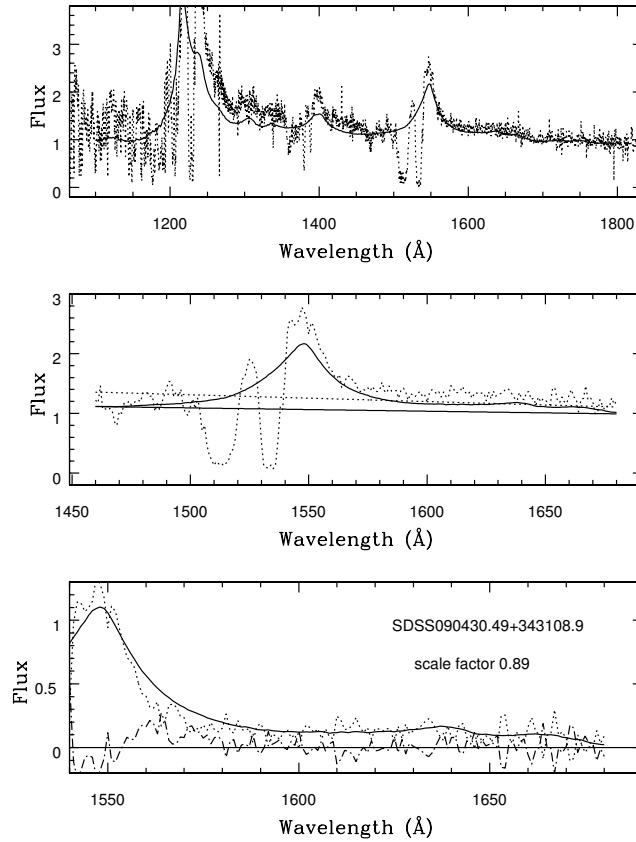


FIGURE 3.8: An illustration of our method for estimating the He II strength. Upper panel – non-BALQSO composite (solid line) and an example ghost-candidate spectrum (dashed line). Middle panel – model fits to the underlying continua. Lower panel – non-BALQSO composite (solid line) and scaled ghost-candidate spectrum, after subtraction of the underlying continuum. The residual flux is indicated by the dot-dashed line.

the ghost candidate has a proportionately weaker He II line. In order to determine error estimates on the derived scale factors, after determining a best-fit solution, we fix all parameters apart from the scale factor, and then minimise on this parameter only. We then calculate the 90% confidence interval on this one interesting parameter from the best-fit model by varying the scale factor until the χ^2 value has increased by 2.71. Both the best-fit scale factor and its range (based on the 90% confidence interval), are given in Tables 3.1 and 3.2.

For our sample of 21 ghost-candidates for which all criteria can be tested, 5 indicate a significantly weaker He II EW, suggesting a weaker than average UV continuum. Only 5 objects show evidence for a stronger than average He II EW. For the rest, there is no significant difference (within the errors) in their He II

EWs when compared to the non-BALQSO composite. For the 22 ghost-candidates for which only some of the criteria can be tested, 5 show evidence for a weaker than average He II EWs, 6 indicate stronger than average He II EWs, and the rest indicate no significant difference in the He II EW when compared to the non-BALQSO composite. Thus only 11/43 (25%) of our ghost-candidate sample appear to satisfy the criteria for a weak UV continuum. Repeating this test on our non-ghost BALQSO comparison sample 8 objects indicate weaker than average He II EW, 9 objects have stronger than average He II EW, and 6 objects show no discernible difference in their He II EW relative to the non-BALQSO composite. For the remaining 2 objects, the fits did not converge, though visual inspection of one of these shows no evidence for significant He II emission.

3.4.6 The width of the ghost feature

If we ignore the likely complex interaction between the Ly- α photons and NV ions (ie. we assume the optical depth in the flow is effectively constant with velocity), then naively one might expect that the ghost-feature should be at least as broad as the Ly- α emission-line responsible for its formation. We note that in fact scattering is likely dominated by the line core where the optical depth is larger. By requiring that any observed ghost feature is at least as broad as Ly- α , we can further refine our ghost-candidate sample to leave only the best ghost-candidates. While the width of any ghost-feature is relatively easy to measure (unless the S/N is low), we are once again limited by the accuracy to which we can measure the width of Ly- α , as this emission is absorbed in the process by which the ghost is formed. Here we again make use of the width of the C IV emission-line (see section 3.4.3) as a surrogate for the width of Ly- α . We isolate the ghost feature by removing the underlying absorption trough by fitting a simple function (cubic spline). We then fit a single Gaussian to the ghost feature to provide an estimate of its width. The measured widths are listed in Table 3.1. We find no correlation between the width of the ghost feature and the width of the C IV emission-line (Figure 3.9). Instead, we find that in the vast majority of cases the ghost feature is narrower than the C IV emission-line (the solid line in Figure 3.9 is $\text{FWHM}(\text{C IV}) = \text{FWHM}(\text{ghost})$).

If we require that the FWHM of the ghost feature matches that of the C IV emission-line to within

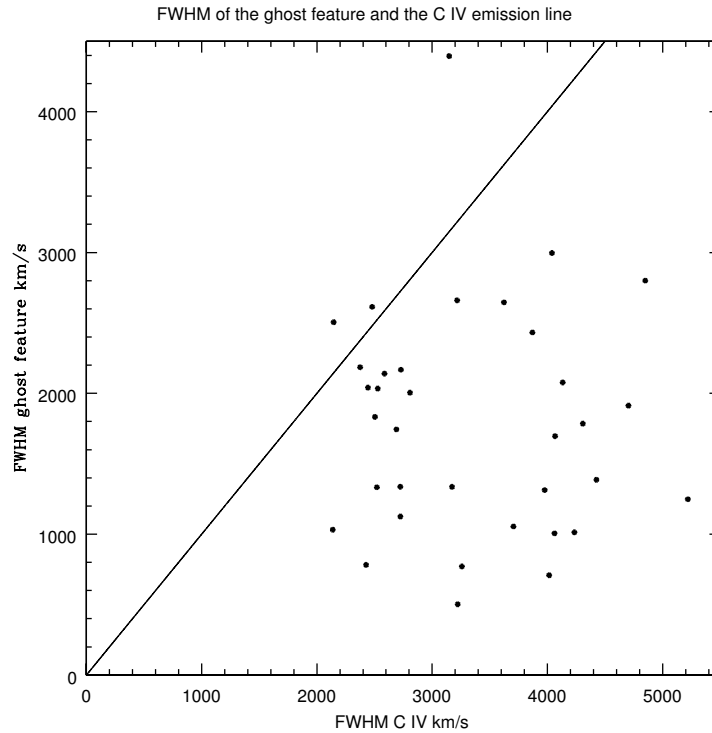


FIGURE 3.9: FWHM (km s^{-1}) of the C IV emission-line and the ghost feature. The solid line shows $\text{FWHM}(\text{C IV}) = \text{FWHM}(\text{ghost})$.

1500 km s^{-1} then 11/20 (for one object we are unable to make emission-line width measurements) of our ghost-candidates for which all ghost-formation criteria can be tested also match this criterion. For our remaining ghost-candidates 8/17 (5 objects have no emission-line width information) also match this criterion. Of the 11 candidates with similar ghost and C IV widths for which all the criteria are testable all 11 show N v absorption, 10 show strong emission lines, 9 have narrow C IV emission but only 2 show evidence for weaker than average He II emission. Of these two one has C IV FWHM of 4040 km s^{-1} while the other fails the criteria for strong emission lines.

3.5 Summary of the results of testing Arav's criteria

For the 43 objects in our ghost candidate sample, 21 are at large enough redshift to allow us to test *all* of the criteria necessary for the formation of an observable ghost feature. Of these 21/21 satisfy the condition for strong N v absorption. 18/21 also satisfy the condition for strong intrinsic Ly- α emission. However,

less than half of the objects (12/21) satisfy the condition for narrow emission-lines, and even fewer (5/21) show weaker than average He II EW. While 11/21 objects satisfy the first 3 criteria, no single object meets all of the requirements for the formation of an observable ghost feature. For the remaining 22 objects, only 3 objects pass 2 of the first 3 criteria, and of these all show stronger than average He II. Of the 5 objects which indicate weaker than average He II strengths, only one can be tested for any of the other criteria, in this case, the width of the emission-line, which it fails.

None of the objects in our ghost-candidate sample are present in the samples produced by Arav 1996 or Korista et al. 1993 due to differences in the redshift ranges over which they were constructed. North et al. (2006) identified 7 strong ghost-candidate spectra in DR3 of the SDSS. 6 of those objects are also in our sample of 43 ghost-candidates. The other, SDSS J142050.34-002553.1. has an assigned redshift of 2.085 in DR5 compared to the 2.103 used by North et al. 2006 and is therefore rejected by our ghost zone cut. Only one of North et al.'s ghost zone final cut is of sufficient redshift to test all of the criteria for the formation of an observable ghost feature SDSS J110623.52-004326.0. This object fails the narrow emission-line requirement. For the other 5 objects, 3 fail the test for narrow emission-lines, and 4 fail the test for weaker than average He II EW.

For our non-ghost comparison sample 12/25 meet the criterion for strong N v absorption. 20/25 meet the requirement of strong Ly α , while 12/22 meet the narrow emission-line width constraint. 9/25 objects show evidence for weaker than average He II strengths. However, only 3 objects meet 3 out of 4 criteria, and none of these meet the weaker than average He II strength. Thus, *none* of the objects in our comparison sample meet all of the criteria necessary for the formation of an observable ghost feature.

A comparison between our ghost-candidate and non-ghost samples suggests that the main difference between them lies in the strength of the absorption, with our ghost candidate sample displaying more objects with strong N v absorption. Comparison of the geometric mean composite spectra of these two samples, and their ratio (Figure 3.12 dashed (ghost-candidate) and dotted (non-ghost comparison spectra) lines), indicates that the ghost-candidate composite shows significantly stronger absorption at lower velocities in

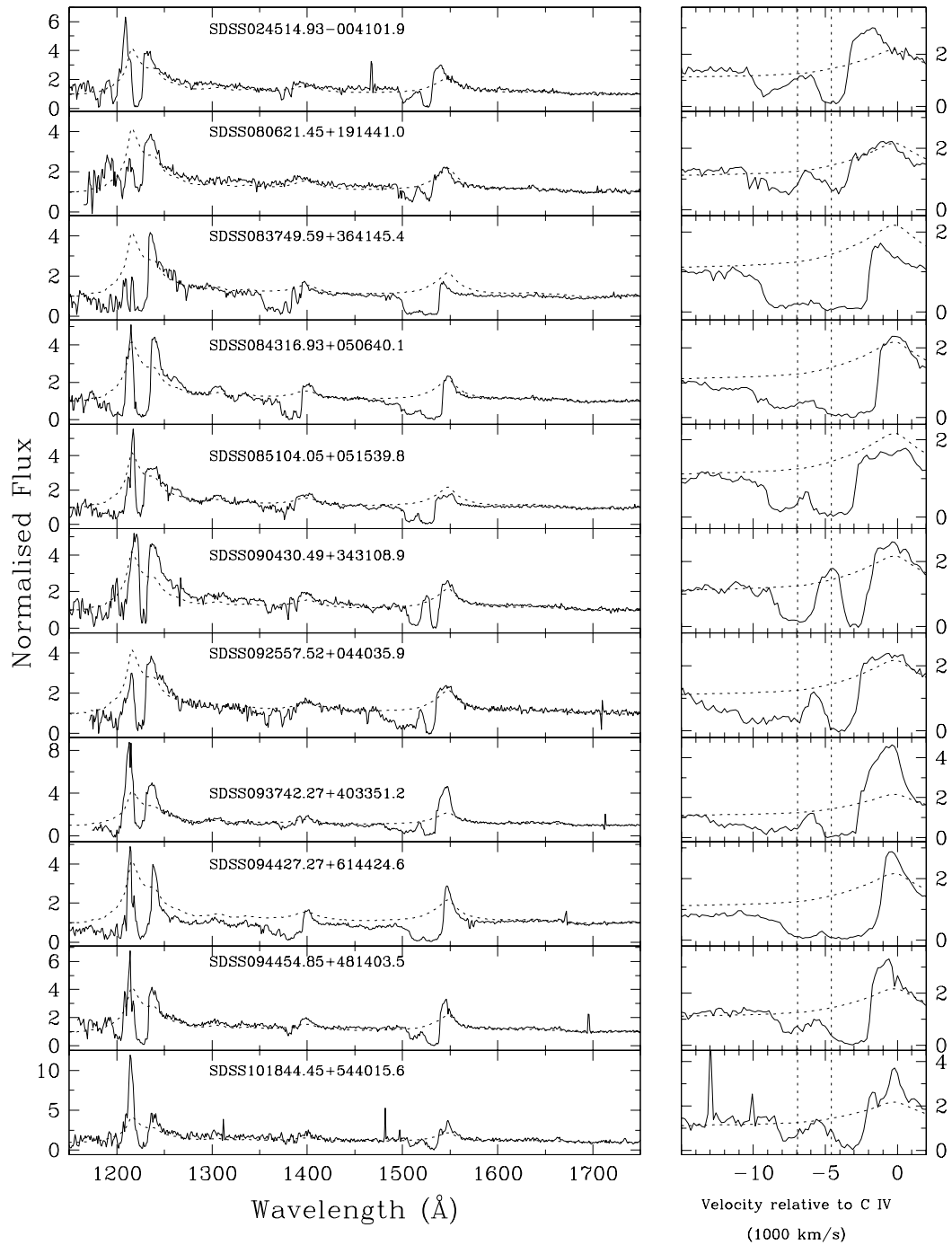


FIGURE 3.10: Spectra of 11 ghost candidates from the best-candidate sample for which all of Arav's criteria can be tested.

all of the strong lines Ly- α , N v, Si IV and C IV.

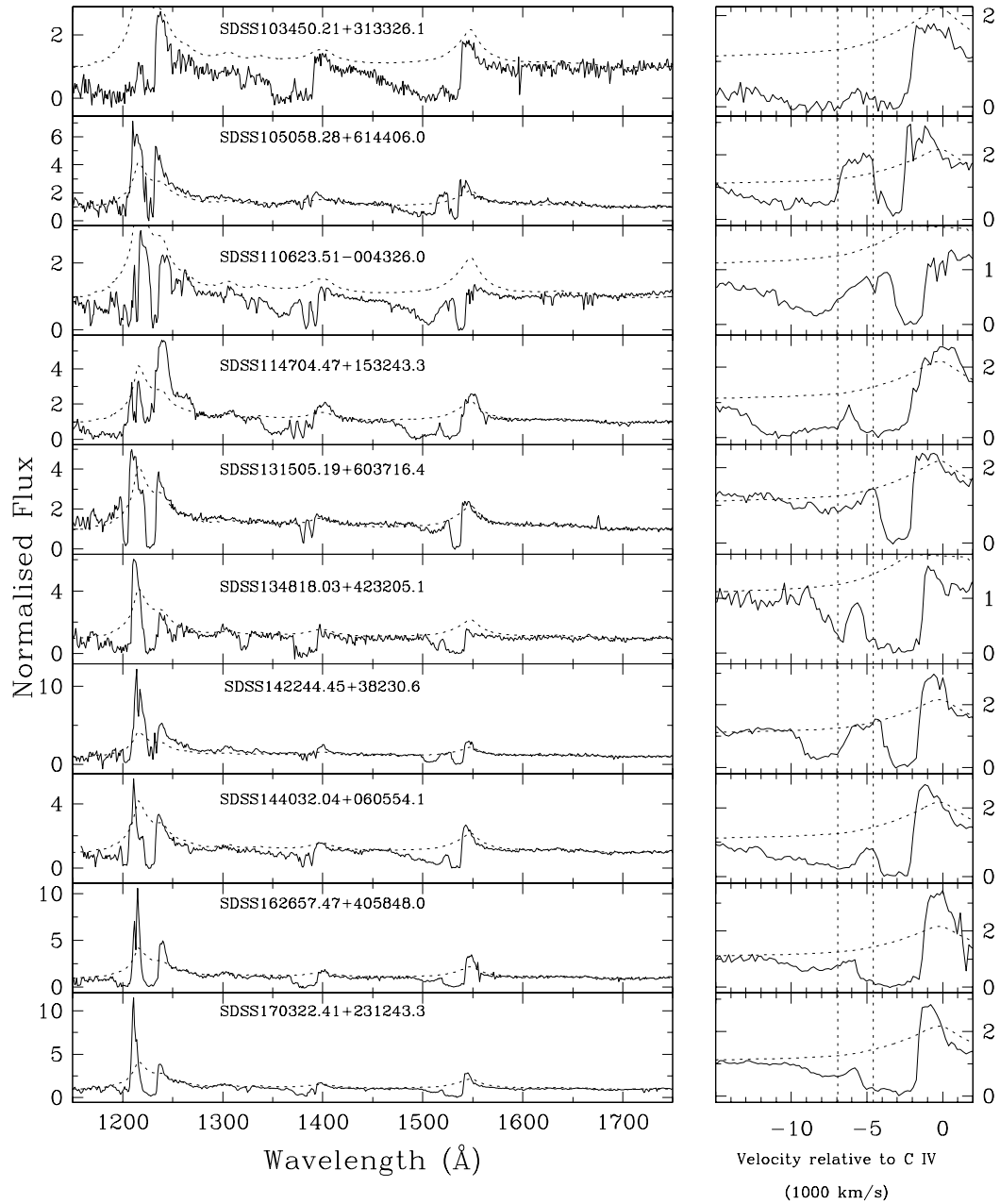


FIGURE 3.11: Spectra of 10 ghost candidates from the best-candidate sample for which all of Arav's criteria can be tested.

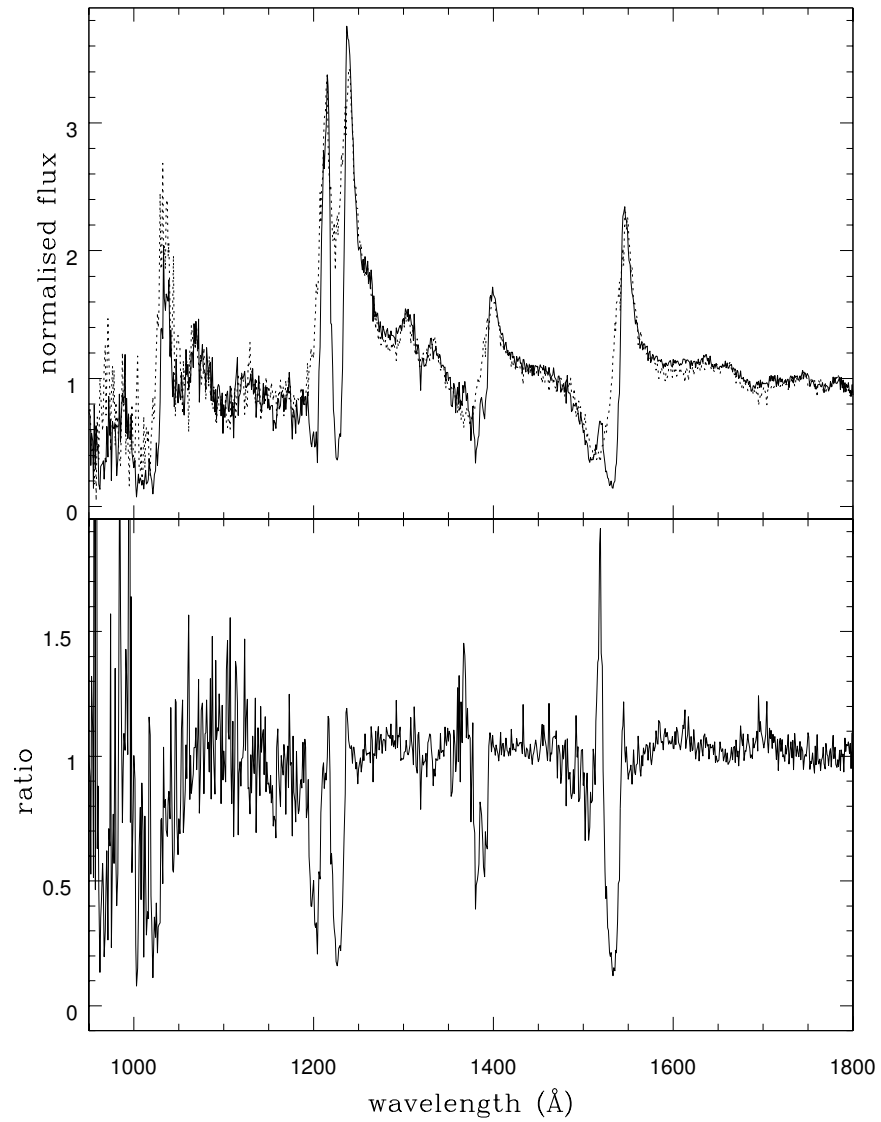


FIGURE 3.12: Upper-panel - composite ghost-candidate (solid line) and comparison (dashed line) spectra. Lower panel - ratio of ghost-candidate to comparison spectra.

Object Name	z	Strong N v BAL	Strong Ly α emission	Narrow lines FWHM (km s ⁻¹)	He II EW scale factor	FWHM Ghost (km s ⁻¹)
024514.93-004101.9	2.802	✓	✓	X(3624)	X1.06 (0.89–1.31)	2646
080621.45+191441.0	2.272	✓	X	X(4307)	✓1.58 (1.23–2.17)	1785
083749.59+364145.4	3.416	✓	X	✓(2807)	✓2.67 (2.05–3.73)	2005
084316.93+050640.1	2.409	✓	✓	✓(2690)	X0.96 (0.85–1.11)	1744
085104.05+051539.8	3.213	✓	✓	X(4324)	✓1.56 (1.31–1.93)	1013
090430.49+343108.9	3.408	✓	✓	X(4067)	X0.89 (0.78–1.00)	1696
092557.52+044035.9	2.266	✓	✓	X(5219)	✓1.41 (1.09–2.07)	1248
093742.27+403351.2	2.258	✓	✓	✓(2725)	X1.00 (0.81–1.23)	1125
094427.27+614424.6	2.337	✓	✓	✓(2426)	X0.76 (0.88–0.87)	782
094454.85+481403.5	2.291	✓	✓	✓(2504)	X0.65 (0.55–0.72)	1833
101844.45+544015.6	3.253	✓	✓	✓(2729)	X0.43 (0.37–0.53)	2168
103450.21+313326.1	2.496	✓	X	X(3943)	X1.41 (0.99–2.48)	
105058.28+614406.0	2.797	✓	✓	✓(2375)	X0.60 (0.53–0.69)	2185
110623.51-004326.0 [†]	2.443	✓	✓	X(4040)	✓3.35 (>1.82)	2996
114704.47+153243.3	3.081	✓	✓	✓(3258)	X0.89 (0.79–1.00)	771
131505.19+603716.4	2.330	✓	✓	X(3976)	X0.97 (0.83–1.18)	1313
134818.03+423205.1	3.066	✓	✓	?	X0.89 (0.73–1.14)	944
142244.45+382330.6	3.728	✓	✓	✓(2146)	X1.16 (0.93–1.51)	2505
144032.04+060554.1	2.297	✓	✓	✓(2723)	X0.89 (0.79–1.00)	1337
162657.47+405848.0	3.051	✓	✓	✓(2520)	X0.49 (0.44–0.55)	1333
170322.41+231243.3	2.634	✓	✓	✓(2138)	X0.93 (0.79–1.05)	1032
005109.45+001636.3	2.036	?	?	X(4850)	X1.30 (0.94–2.00)	2800
023252.80-001351.1 [†]	2.033	?	?	X(4016)	X0.94 (0.82–1.09)	709
033048.50-002819.6 [†]	1.779	?	?	?	✓ > 2.00	1977
081158.10+343624.1	2.106	?	✓	✓(3147)	X1.13 (0.86–1.63)	4395
082006.60+522158.7	2.015	?	?	✓(3217)	?? ^a	2660
091109.46+410155.2	2.128	?	✓	X(4062)	X0.56 (0.49–0.64)	1006
091313.09+411014.2	1.737	?	?	?	✓3.61 (2.62–5.72)	2607
092221.25+084312.8	1.969	?	?	?	✓ > 1.43 ^b	1398
102908.06+365155.2	1.750	?	?	X(3870)	X0.31 (0.28–0.34)	2432
110736.67+000329.4	1.741	?	?	✓(2443)	X1.18 (1.06–1.31)	2041
111255.70+040600.5	1.989	?	?	X(3706)	X0.96 (0.85–1.08)	1055
113831.42+351725.3	2.118	?	✓	✓(2422)	X0.78 (0.69–0.89)	1336
122107.07+074437.0	1.900	?	?	✓(3222)	X0.91 (0.77–1.08)	503
132304.58-003856.5 [†]	1.827	?	?	X(4133)	X1.09 (0.95–1.28)	2077
133428.06-012349.0	1.876	?	?	?	✓(??) ^c	1616
134458.82+483457.5	2.052	?	?	?	X0.89 (0.73–1.12)	1046
141843.95+373750.8	1.782	?	?	X(3596)	X0.38 (0.33–0.44)	
155505.10+442151.3	1.798	?	?	X(4425)	✓1.90 (1.51–2.59)	1386
160335.43+225612.9	2.079	?	✓	✓(2479)	X0.68 (0.60–0.78)	2614
163231.60+294929.7	1.905	?	?	✓(2587)	X0.61 (0.54–0.66)	2140
170056.85+602639.7 [†]	2.123	?	✓	X(4708)	X1.15 (0.99–1.35)	1913
172001.31+621245.7 [†]	1.760	?	?	✓(2528)	X1.73 (1.24–2.95)	2034

Table 3.1: Our Ghost sample and the results of testing Arav’s criteria along with the FWHM of the ghost feature. The objects above the line have $z > 2.15$ and show Ly- α emission in their SDSS spectra.

Object Name	Redshift	Strong N v BAL	Strong Ly α emission	Narrow lines FWHM (km s ⁻¹)	He II EW scale factor
013724.43-082419.9	2.5663	X	✓	✓(3174)	X 0.39 (0.35-0.44)
014648.52-001051.8	2.3853	✓	✓	✓(2186)	X 0.83 (0.77-1.38)
021219.54+141739.1	2.1902	✓	X	X(6457)	X 0.94 (0.82-1.18)
024413.76-000447.5	2.7925	✓	✓	X(3804)	✓ 2.72 (>2.46)
031331.22-070422.8	2.7548	✓	X	?	✓ 3.35 (2.43-5.56)
081906.14+394813.8	3.2071	X	✓	X(4142)	X 0.43 (0.39-0.47)
084348.68+445226.9	2.5821	X	✓	X(4024)	X 1.06 (0.89-1.30)
084554.24+423003.5	2.5568	X	✓	✓(2378)	✓ 3.92 (>1.69)
090115.18+371822.8	2.6173	X	✓	✓(2322)	X 0.30 (0.27-0.33)
093804.52+120011.4	2.2273	X	X	?	✓ 2.03 (1.59-2.79)
095220.88+371622.9	3.0928	✓	✓	✓(3331)	X 0.80 (0.66-1.00)
101324.20+064900.3	2.7675	✓	X	?	✓ > 4.07
101420.52+325931.9	2.3935	X	✓	✓(3256)	X 0.41 (0.37-0.45)
104245.48+365642.2	2.8545	✓	✓	✓(2235)	X 0.44 (0.40-0.50)
110928.51+092403.8	2.1539	X	✓	✓(3452)	X 0.49 (0.43-0.55)
111437.25+503445.9	2.2075	X	✓	X	✓ > 3.63
115901.75+065619.0	2.1906	✓	✓	X	X 1.02 (0.79-1.43)
135559.03-002413.7	2.3438	X	✓	✓(3180)	✓ 1.30 (1.11-1.53)
135912.20+450338.1	2.2794	X	✓	X(3802)	X 0.95 (0.68-1.58)
141225.35+041951.9	2.3882	✓	✓	X(4748)	✓ 0.72 (0.60-0.89)
143559.60+034153.7	2.4646	✓	X	X(4003)	X 1.05 (0.85-1.32)
164148.19+223225.2	2.5061	X	✓	✓(2347)	X 1.12 (1.00-1.46)
165816.78+231653.7	2.5753	X	✓	X(6305)	✓ 1.88 (1.26-3.66)
214113.05-003545.8	2.2329	X	✓	✓(3099)	X 0.49 (0.43-0.54)
223841.88+142154.9	2.2898	✓	✓	✓(2488)	X 0.47 (0.43-0.52)

Table 3.2: As for Table 1, indicating our comparison sample of 25 objects selected to have broad absorption and no ghost-features and the results of testing Arav's criteria for ghost formation.

† Objects identified by North et al 2006 as their best ghost-candidates, their Ghost Candidate Final Cut (GCFC).

^a Poor continuum fit.

^b He II absorbed.

^c He II too weak to be measured.

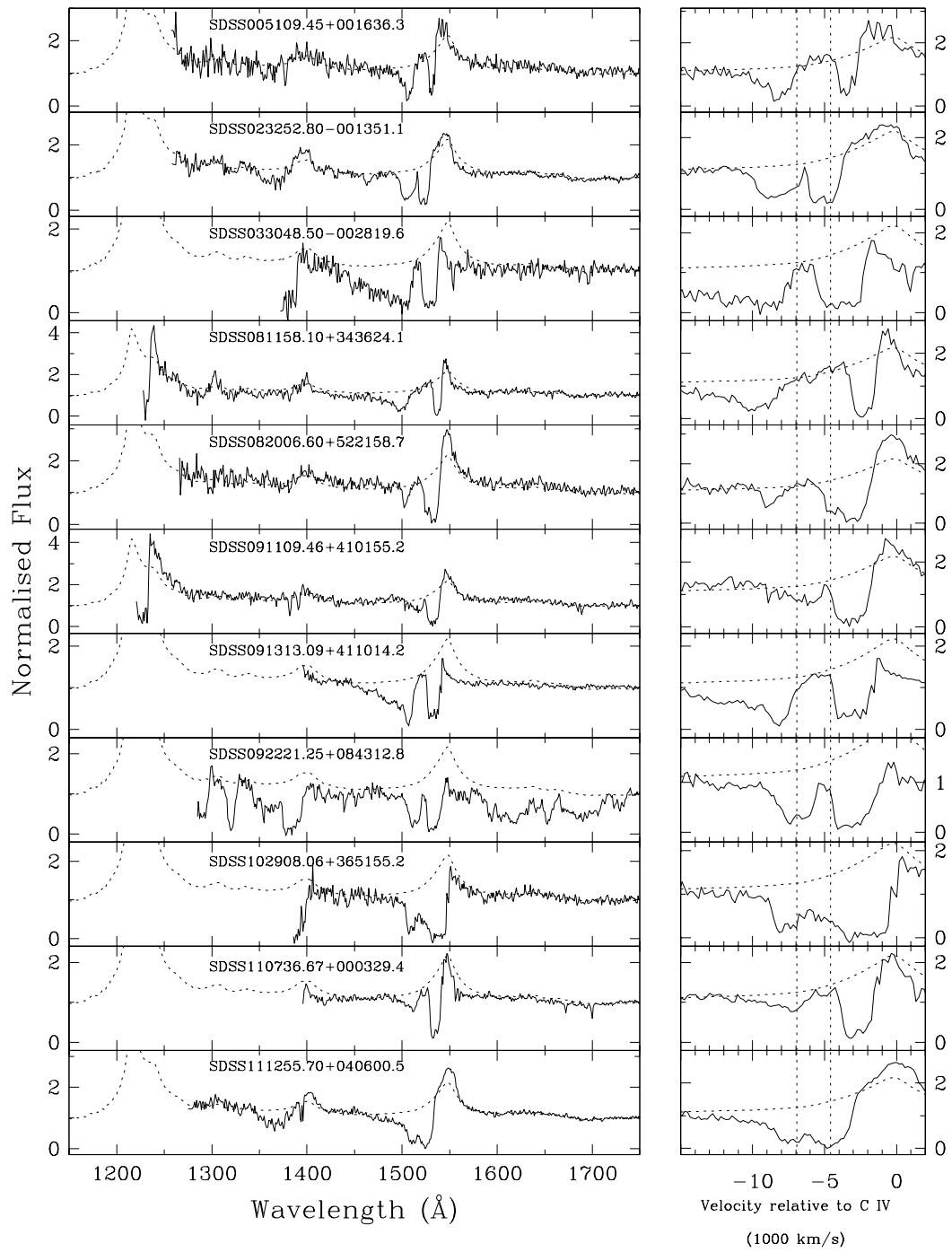


FIGURE 3.13: 11 Ghost candidates for which only some of Arav's criteria can be tested.

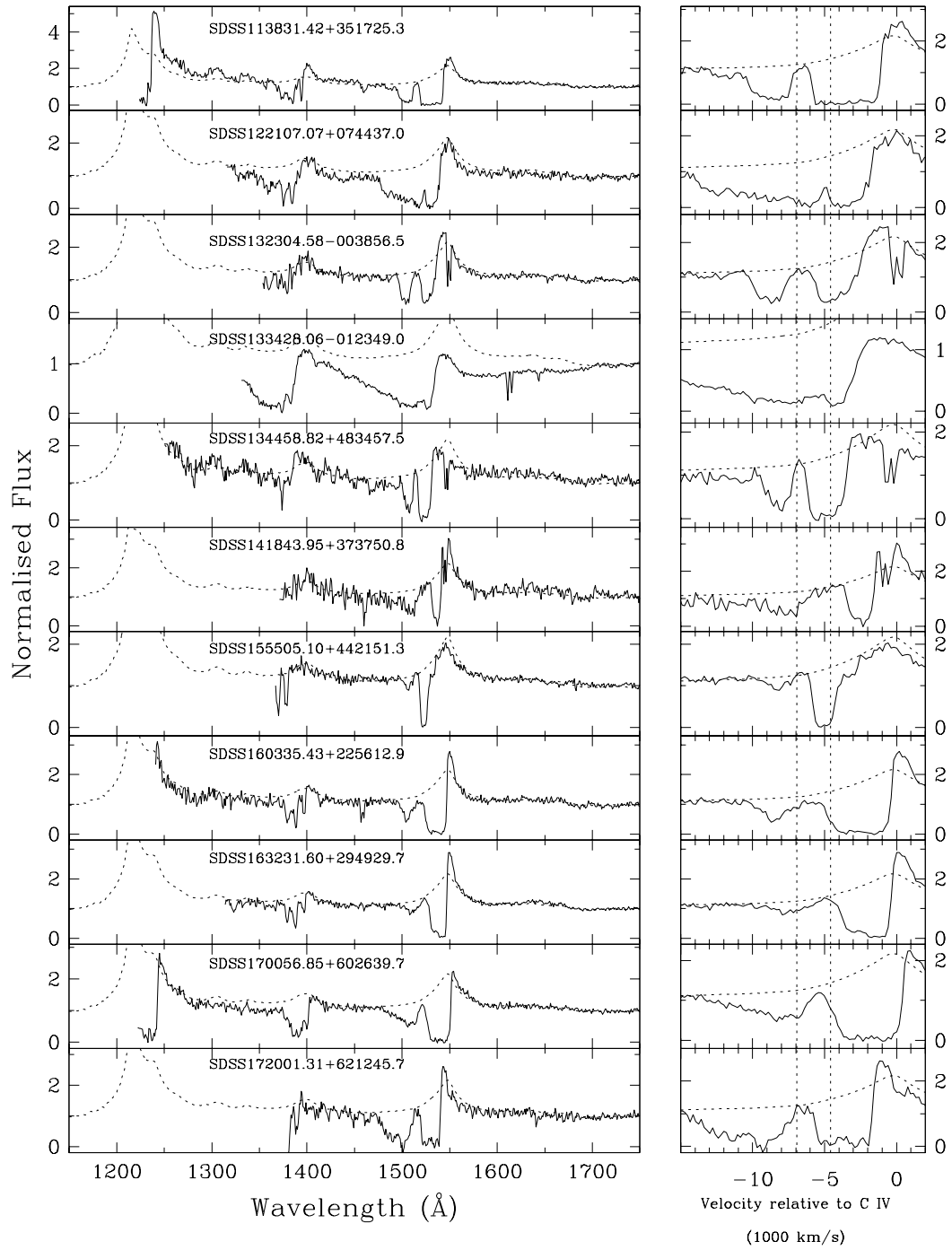


FIGURE 3.14: Another 11 Ghost candidates for which only some of Arav's criteria can be tested.

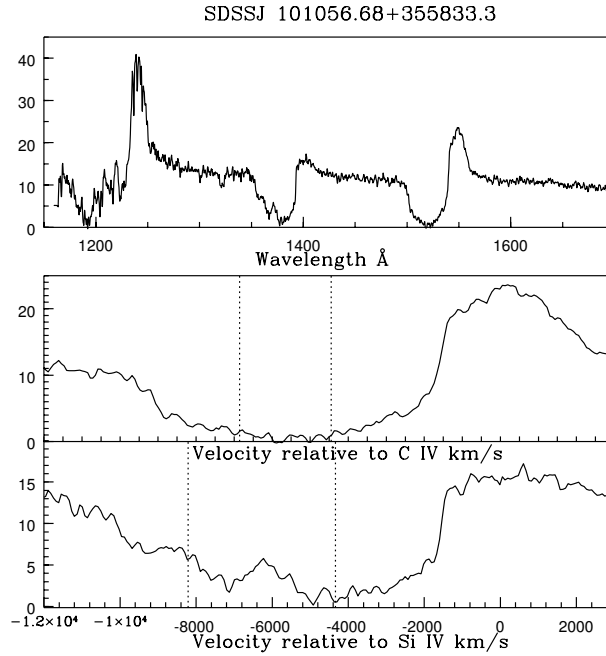


FIGURE 3.15: SDSS J101056.68+355833.3: A possible Si IV ghost showing no evidence of a C IV feature along with close ups in velocity space of the C IV (middle) and Si IV (top) ghost regions. Vertical lines represent the ghost zones.

3.6 SDSS J101056.68+355833.3: Si IV ghost?

This is an object selected for our comparison sample as it shows no hint of a ghost feature within the deep broad C IV absorption. The spectrum is shown in Figure 3.15 along with the flux in velocity space relative to C IV and Si IV showing clearly the potential ghost feature in the Si IV absorption. SDSS J101056.68+355833.3 meets the criteria for strong emission due to C IV and N V emission exceeding 100% of the continuum flux at their peak, shows clear N V absorption, has C IV FWHM measured as 3483 km s^{-1} and an EW of He II measured to be $3.58 \pm 0.82 \text{ \AA}$. These measurements place this object very close to the boundary on several criteria and it would not be surprising to see a ghost feature in this object. While no ghost feature can be seen in the C IV trough, there is a clear feature within the Si IV trough ($\sim 6200 \text{ km s}^{-1}$) within the ghost zone. Due to the greater separation of the Si IV doublet (1933 km s^{-1}) in comparison to the C IV doublet (498 km s^{-1}) a ghost feature in the Si IV would be expected to be wider and weaker. This larger doublet separation is the reason for the wider ghost zone in the Si IV BAL trough. The absence of a C IV feature could be due to an extremely high optical depth in the flow such that the flow

remains optically thick even with the decrease in optical depth caused by the acceleration due to N V ions. However the absorption troughs of C IV and Si IV look very similar with the exception of the potential ghost feature suggesting the optical depths are similar. There is a slight hint of an additional feature within the Si IV at $\sim 8200 \text{ km s}^{-1}$ which is in the appropriate region to be due to the lower wavelength doublet feature from Si IV.

3.7 On the reality of the ghost phenomenon

The results of testing Arav's criteria on our ghost candidate sample are inconclusive. This raises the question of the reality of the ghost phenomenon. As previous samples suggest only weak evidence for an excess of peaks in the ghost region (Korista et al. 1993) this section looks at a number of ways to test for such an excess. In section 3.7.1 we examine the frequency with which peaks occur in regions outside of the ghost-zone by performing the same analysis used to find ghost-candidates using fake ghost-zones. Section 3.7.2 looks for evidence of a ghost feature in residual intensity composite spectra of BALQSOs which have not been selected to exhibit ghost features. The presence of a preferred velocity for peaks within absorption troughs is examined in section 3.7.3. Section 3.7.4 looks at evidence for line-locking features which are not tied to the systematic velocity by lining up the spectra with the start of the lowest velocity absorption component. A K-S test is used to search for evidence of a difference in the distribution of residual intensity in bins either side of the ghost-zone with that within the ghost zone and a Monte Carlo simulation used in section 3.7.6 to perform this search in a different way.

3.7.1 Fake Ghost zones

In order to test whether peaks are more common within the ghost-zone than elsewhere, we repeat the ghost selection method using two "fake" ghost-zones (red-ward and blue-ward of the original ghost-zone), in a similar fashion to North et al. (2006). These zones are created in precisely the same way as the ghost-zone except that the red zone is centred at 4000 km s^{-1} while the blue zone is centred at 8000 km s^{-1} blue-ward

of the C IV emission-line. Of the 258 single peaked objects, 82 have peaks within the “fake” red zone and 50 have peaks within the fake “blue-zone”. Since the original ghost-zone contained 69 objects with single peaks, the evidence for an excess of objects with peaks at a preferred velocity is weak. That is, single peaks within the ghost zone are no more likely than single peaks at other velocities.

We have also examined the link, if any, between the peaks within the C IV absorption trough and N V absorption. In order to select N V BALs we use a modified Balnicity index (Weymann 1991). We take the continuum to be equal to the mean flux between $\lambda\lambda 1315\text{--}1330\text{\AA}$, and require that the flux drops to below 90% of this value continuously for $> 1000 \text{ km s}^{-1}$ between 0 and 7000 km s^{-1} blue-ward of the N V emission line. In order to perform this test we require objects with redshifts in excess of 2.15. From a sample of 1747 objects with $z > 2.15$, we find 1258 N V BALs and 489 N V non-BALs. 27% (340) of the N V BALs show multiple troughs in their C IV absorption compared to only 15.5% (76) of the N V non-BALs. Similarly, 7.6% (95) of the N V BALs and only 3.1% (15) of the N V non-BALs show a single peak in the C IV absorption trough. Among the N V non-BALs we find : i) two objects with single peaks within the ghost-zone, ii) two objects with a single peak in the fake blue zone, and iii) no objects with a single peak in the fake red zone. For the N V BALs, we find : i) 26 objects with single peaks within the ghost-zone, ii) 14 with single peaks within the fake blue zone, and iii) 33 with single peaks within the fake red zone. While these results indicate a strong link between the presence of N V absorption and the mechanism responsible for producing features within the C IV absorption trough, line-locking between Ly- α and NV does not appear to be the dominant mechanism.

In summary, N V BALs are more likely to have multiple troughs within the C IV absorption than N V non-BALs (factor of 2). Further, N V BALs are also more likely to display single-peaks within their C IV absorption than N V non-BALs. Approximately 25% of the single peaked objects are located within the ghost-zone. However, similar numbers are found in both the blue and red fake ghost zones. Thus while strong N V absorption appears to be a strong requirement for the appearance of features within the C IV absorption trough of BALQSOs, there is no preferred velocity for the location of these features.

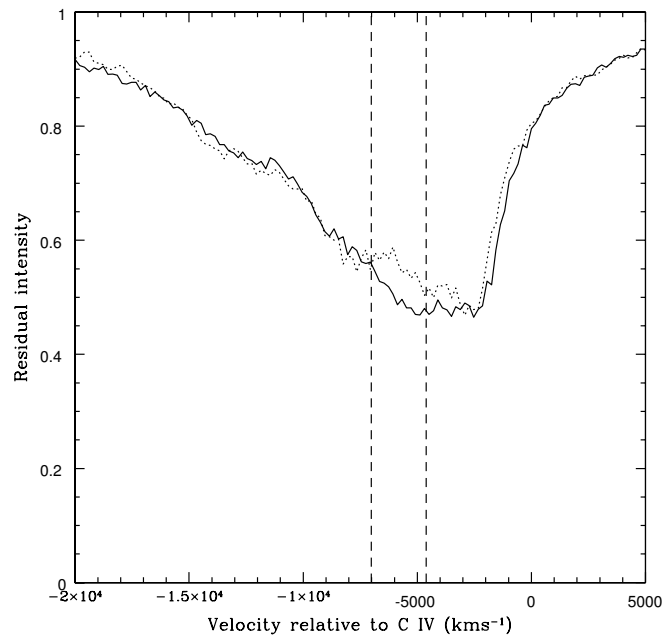


FIGURE 3.16: Geometric mean composite residual intensity spectra of two randomly selected BALQSO samples (without replacement).

3.7.2 Random sampling

We have computed geometric mean residual intensity spectra (the ratio of the geometric mean BALQSO composite divided by a geometric mean non-BALQSO composite spectrum) for two random samples (without replacement) taken from the BALQSO catalogue of Scaringi et al. (2009) (Figure 3.16, sample 1 (solid line), sample 2 (dashed line)). These samples (consisting of 1776 objects each) were generated by sorting the BALQSO catalogue into RA order, and then selecting even-numbered objects for the first sample, and odd-numbered objects for the second sample. The mean residual intensity spectra for both samples are virtually indistinguishable, aside from a small difference ($\sim 15\%$) in the residual intensity in the velocity range $3900\text{--}7800\text{ km s}^{-1}$ blue-ward of line centre, which intriguingly, is precisely where the purported ghost feature should be found. We have checked to see whether there exists an excess of ghost-candidate spectra in either sample, and find that the ghost candidates are spread evenly amongst the samples, with 21 in sample A and 22 in sample B. While there are small apparent differences in the mean residual intensity spectrum in the region of the ghost-feature, neither sample shows convincing evidence of a double-trough feature.

3.7.3 A preferred velocity for peaks?

Here we attempt to address whether there exists any substantive evidence for absorption components at preferred velocities. If ghost features are relatively common, we would expect an excess abundance of peaks within the absorption trough at velocities 5900 km s^{-1} blue-ward of line centre. To address this question we have performed two additional tests. In these tests we work with fluxes instead of residual intensities to avoid complications introduced by uncertainties in fitting the C IV emission-line blue-ward of line centre. In the first, we take the LVQ BALQSO sample of Scaringi et al. 2009, and compare the fluxes in 3 adjacent velocity bins (A, B and C) each with widths of 1000 km s^{-1} , where B is the reference bin and A and C represent the adjacent bins. Sliding these bins from a velocity of $0\text{--}30,000 \text{ km s}^{-1}$ blue-ward of C IV rest, we record the number of times the mean flux in the central bin (bin B) exceeds the mean flux in adjacent bins A and C by more than 3σ . To show the effects of selecting different bin-widths over which the fluxes are measured, we repeat this exercise for bin widths of 500 and 1500 km s^{-1} . The results of this procedure are shown in Figure 3.17 (upper left panel). The distribution of peaks shows a prominent peak at zero velocity, which we associate with the location of the C IV emission-line peak. Ignoring this feature, the peak distribution is a generally smooth function of velocity with no indication of an excess number of peaks at 5900 km s^{-1} blue-ward of line centre. The same analysis performed on our ghost candidate sample, displays a similar peak at zero velocity, and in addition further peaks at around 6000 km s^{-1} and $11,000 \text{ km s}^{-1}$. While the numbers of peaks at higher velocities is only marginally less than that at 5900 km s^{-1} these secondary peaks tend to be smaller and in many cases line up with the edge of the absorption trough.

We have also performed a variation on this method in which instead of measuring the intensities within each bin, we measure the mean gradient of the intensities within each of the bins. A peak is recorded if and only if the gradient in bin A is positive, the gradient in bin A is greater than the gradient in bin B, the gradient in bin B is greater than gradient of C, and the gradient in bin C is negative. Figure 3.17 lower panels shows the result of this test. Again, the peak at zero velocity we associate with the peak of the C IV emission-line. Thereafter the distribution of the locations of the peaks follows a smooth broad function

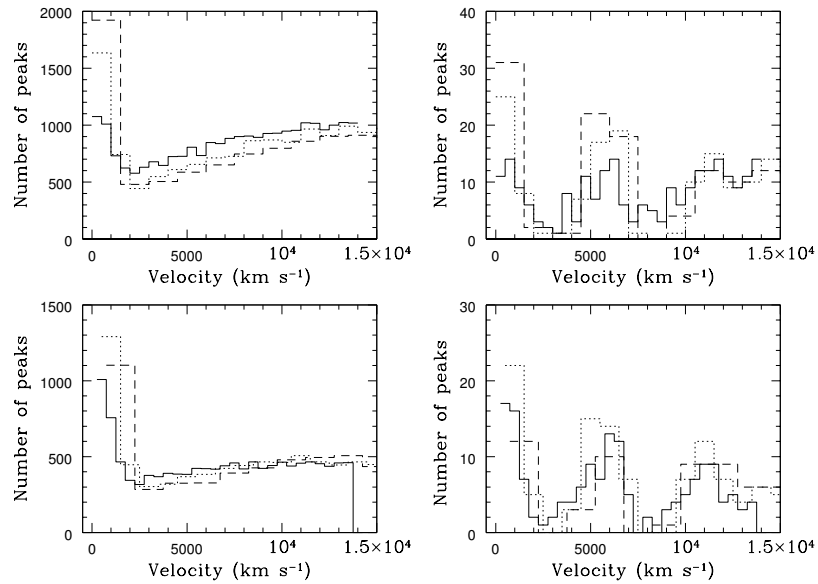


FIGURE 3.17: Distribution functions showing the incidence of peaks as a function of velocity blue-ward of C IV rest wavelength (see text for details). Upper left panel - LVQ BALQSOs, peak distribution functions (solid line 500 km s⁻¹ bins, dotted line 1000 km s⁻¹ bins, dashed lines 1500 km s⁻¹ bins). Upper right panel - as for upper left for the ghost-candidate sample. Lower panels - Distribution of peaks measured using the gradient of the spectra (left- all BALQSOs, right- ghost-candidates).

with a maximum at approximately 15,000 km/s. As with the previous test, varying the bin widths between 500-1500 km s⁻¹ does not significantly alter the results.

These additional tests suggest that for the general BALQSO population, there is no substantive evidence that there exist preferred velocities for the location of peaks within the broad absorption troughs of BALQSOs. Thus if ghosts are real they are certainly rare, as was first suggested by Arav. We note that the incidence of single peaks (or double troughs) in our sample 258/3552 (7%) is significantly smaller than that found by Korista et al. 1993 (22%), likely a result of the small number statistics of this earlier study.

3.7.4 Appearance of double-troughs at other velocities

In the second test we verify whether there exist associated troughs (via line-locking) at velocities other than systemic. We do this by aligning each spectrum according to the location of the red-edge of the first BAL trough and thereby search for evidence of a bi-modal distribution of sub-troughs. Here, the red-edge

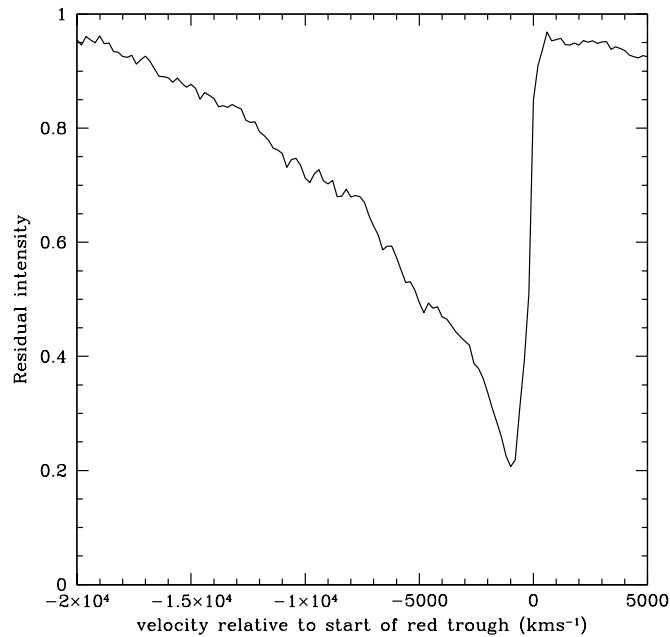


FIGURE 3.18: Residual intensity composite spectrum compiled after aligning all spectra to the position of the first (lowest velocity) absorption trough. We see no indication of a second trough at the known separation of Ly- α -N v.

is defined as in Korista et al. (1993) to be where the residual intensity falls below 0.75 and remains below this level for more than 1000 km s^{-1} . The resultant geometric mean residual intensity spectrum is shown in Figure 3.18. As one might expect, the residual intensity is somewhat steeper at lower velocities, a result of aligning the first troughs in velocity space. However, the remainder of the spectrum is a smooth function of velocity, with no indication of additional sub-troughs. Thus, as with Korista et al. (1993) we find no evidence for line-locking features at velocities other than systemic.

Unlike Korista et al. (1993) the distribution of velocities of the first trough peaks at velocities between $1500\text{--}2000 \text{ km s}^{-1}$ blue-ward of line-centre, thereafter the number of objects contributing to each velocity bin shows a smooth linear decline. Thus while there appears a preference for the onset of BALs toward lower velocities, there is no indication of other preferred blue-ward velocities. This again suggests that the incidence of the double-trough signature among the BALQSO population as a whole is generally low. We note that the distribution of redshifted troughs are similarly peaked toward lower velocities and may indicate a preferred launch radius for the out-flowing gas.

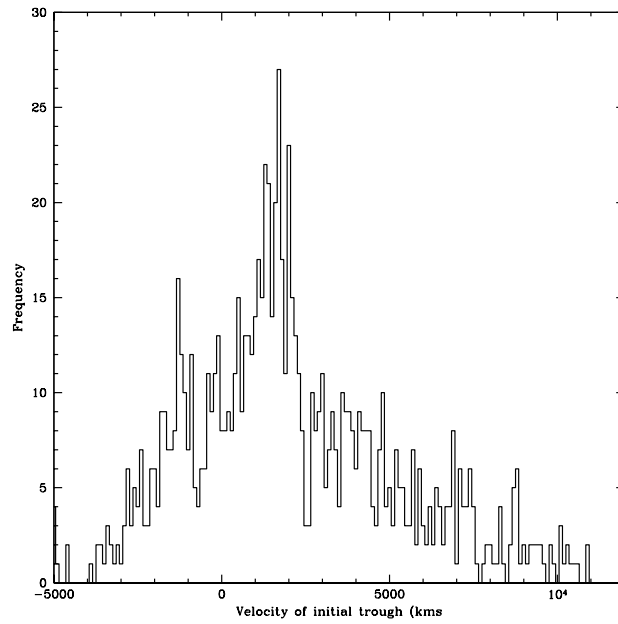


FIGURE 3.19: The frequency distribution of velocities of the first absorption trough (km s^{-1}).

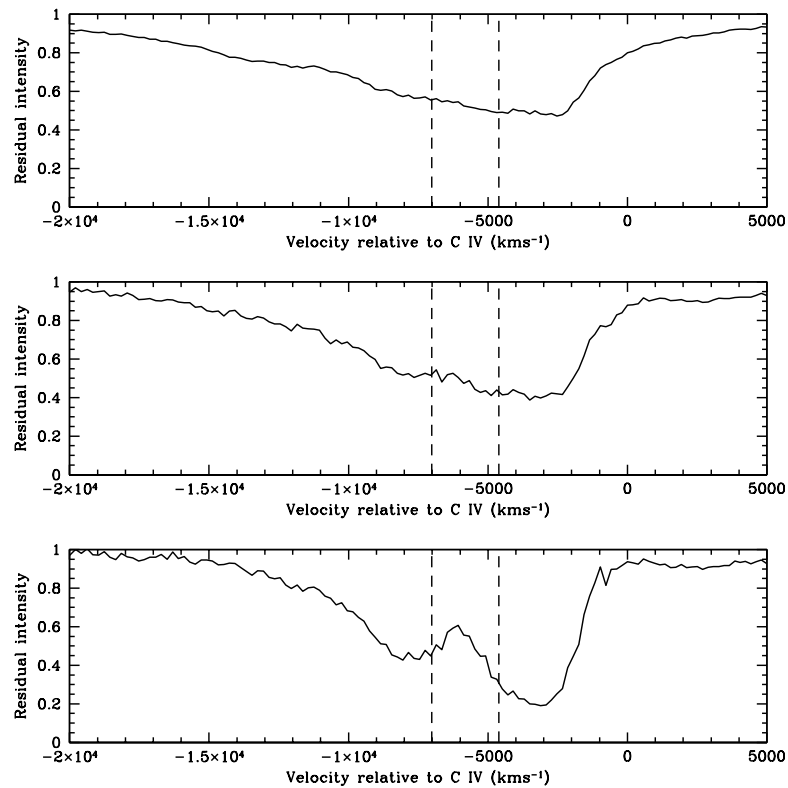


FIGURE 3.20: Residual intensity spectra of (i) the multi-trough sample, (ii) the single peak sample, and (iii) ghost-candidate sample. See text for details

BALQSO Sample	Sample Size	K-S probabilities $\times 100\%$	
		Sub-trough 1	Sub-trough 2
LVQ BALs	3552	10^{-2}	5.9
MTS	1019	5×10^{-3}	23.8
MTS A	510	1.2	34.9
MTS B	509	2.1	4.1
Single Peak Sample	258	3.7	41.4
Ghost Zone Sample	69	0.2	0.1

Table 3.3: K-S tests on the multi-trough phenomenon

3.7.5 K-S test

In our third test, we compute the mean residual intensities in 3 separate velocity bins, one centred on the expected location of any ghost-feature, the other taken from bins either side of this feature, ie. velocity bins at $4000\text{--}5000 \text{ km s}^{-1}$, $5500\text{--}6500 \text{ km s}^{-1}$ (the reference bin), and $10000\text{--}11000 \text{ km s}^{-1}$ respectively. We then use the Kolmogorov-Smirnov (KS) test to check whether the distribution of residual intensities within each of these velocity bins belongs to the same population as the reference bin. The residual intensity spectra we use for this test are (i) the total sample of BALQSOs from Scaringi et al. (2009), the randomly selected samples 1 and 2 described above, our Multi-trough sample from rejection cut 2, our single peak sample from rejection cut 3 and our candidate ghost sample. The results of this test are presented in Table 3.7.5.

Table 3.7.5 gives the probability that the K-S statistic of the sub-trough with the reference trough (i.e. the ghost zone) would be exceeded by chance if they were drawn from the same population. That is, lower K-S probabilities indicate more significant differences between the chosen velocity bin and the reference bin. Our analysis shows that only for our ghost sample do *both* sub-troughs 1 and 2 indicate significant differences from the reference bin (K-S probabilities less than 0.1%). This is as expected, since members of this sample were selected precisely because they showed significant ghost-like features. The single peak sample shows no evidence that the residual intensity of the ghost zone is drawn from a different population to that of sub-trough 2. This suggests that the single peak sample does not have a systematic peak and that the position of peaks within the absorption is random and unrelated to Ly- α -N v line locking.

BALQSO Sample	$\langle D \rangle$	Monte Carlo Probability x 100%
LVQ BALs	-0.01197	98.88
MTS	-0.03918	99.8
Single Peak Sample	0.007355	35.8
Ghost Zone Sample	0.16932	0.0

Table 3.4: Monte Carlo simulations of the double trough phenomenon

3.7.6 A Monte Carlo test for ghosts

Korista et al. (1993) described one further test for an excess of double-trough features bracketing the Ly- α -N v line-locking region, which we repeat here for completeness. In this Monte Carlo simulation, we test how frequently the depth of the double-trough structure is exceeded by a random arrangement of residual intensity differences among each of the 3 velocity bins (see Korista et al. 1993 for details). For each spectrum, we can form 6 residual intensity differences from 3 velocity bins. For each spectrum in our BALQSO catalogue we randomly pick 2 from the 6 possible residual intensity differences and calculate their mean value, i.e. an average residual intensity difference. We then define $\langle D \rangle_{random}$ to represent the mean of these average intensity differences across our BALQSO sample. $\langle D \rangle_{random}$ is then compared to $\langle D \rangle$, formed by averaging the mean residual intensity differences between sub-troughs 1 and 2 with the reference bin, again averaged across our whole sample. $\langle D \rangle$ can take on any value between ± 1 . Values of $\langle D \rangle$ near +1 indicate a strong double-trough structure. Conversely, a value of $\langle D \rangle$ near -1 indicates a strong trough at the position of the reference bin. Values near zero are indicative of a smooth trough passing through the velocity bins.

To test how frequently a double-trough structure having a contrast at least as large as that observed in the sample mean could arise by chance, we repeat this process 10,000 times for each sample, and determine the number of times $\langle D \rangle_{random}$ exceeds $\langle D \rangle$, normalised to 10,000. The results of these simulations are shown in Table 3.7.6.

Since we only find strong evidence for the double-trough structure within our ghost zone sample (chosen for precisely that reason), we conclude that there is indeed no strong evidence for an excess of objects with sub-troughs bracketing the ghost-zone among the BALQSO population at large. Indeed, the high probabilities found for both the LVQ sample and for the multi-trough sample, strongly suggest that multi-trough features are randomly distributed in velocity. We therefore conclude that many of the objects previously identified as strong ghost-candidates in previous studies may simply be multi-trough interlopers masquerading as ghosts due to the chance alignment of multiple un-associated absorption systems.

3.8 Summary

The evidence presented in this chapter suggests that features within the ghost zone are no more common than features at other velocities. It also suggests that those objects with features in the ghost zone do not meet the criteria set out by Arav et al. 1995 significantly more often than objects without features, with the exception of the greater number of N v BALs within the ghost-candidate sample. However N v absorption also appears to be more common amongst objects with features at other velocities suggesting that the presence of features in the C IV BALs may be related in some way to N v absorption but that the mechanism behind this relationship is not based on the radiative line driving interaction between the N v absorbers and the Ly- α emission. In conclusion there is no substantive evidence that the features seen at around 5900 km s^{-1} are created by the effects of radiative line driving or that these features are anything more than the chance alignment of multiple absorbing systems.

Chapter 4

High S/N moderate resolution spectroscopic observations of ghost-candidate spectra with GMOS and WHT

The majority of the ghost candidates in DR5 of the SDSS are relatively low signal to noise ($S/N < 10$ per pixel in more than half of the ghost candidates). This does not dramatically effect the measurement of the strength and width of the strongest emission lines (e.g. Ly- α , C IV). However constraining the strength of the far-UV continuum, via the He II emission line strength, is virtually impossible in low S/N data as the line is weak in most quasars ($EW \sim 0.5 \text{ \AA}$ see Vanden Berk et al. 2001) and expected to be weaker still in the ghost candidates (Arav 1996).

In order to improve the accuracy of the measurement of the He II strength, in addition to allowing confirmation of the other tests of Arav's criteria, we obtained moderate resolution, broad-band, long-slit spectra of 11 ghost candidate objects, of which 8 are present in the ghost candidate final cut as presented in Chapter 3. 8 of the 11 targets were observed using the William Herschel Telescope during the nights of the 26th and 27th May 2008. The remaining 3 spectra were obtained as queue scheduled observations taken using the Gemini North telescope during the 2008A semester in March.

The reduction of these data is described in detail in this chapter. The resultant spectra are presented here. Any changes seen in these spectra compared with the SDSS spectra are discussed and Arav's criteria tested using the higher S/N WHT data.

4.1 The William Herschel Telescope and Intermediate Dispersion Spectrograph and Imaging System

The William Herschel Telescope (WHT) is a 4.2m optical telescope and forms part of the Isaac Newton group of telescopes situated at the Observatorio de la Roque de los Muchachos on La Palma. The observations described here were taken using both the red and blue arms of the Intermediate Dispersion Spectrograph and Imaging System (ISIS) mounted at the Cassegrain focus.

4.1.1 ISIS

ISIS is a double armed spectrograph which splits the source light into red and blue beams using a dichroic. A dichroic material is one which has different optical properties for different wavelengths of light. Using specifically designed dichroic materials incoming light can be split into two beams of differing wavelengths. This allows simultaneous broad-band spectra to be taken in the red and blue ends of the visible spectrum. The detectors can then be separately optimised, resulting in higher sensitivity at both red and blue wavelengths and allowing broader spectral coverage. The blue arm uses an EEV12 CCD detector which is a thinned anti-reflection (AR) coated 4096x2048 pixel array with 13.5 micron pixels. The red arm utilises the RED+ CCD detector which is also AR coated and comprises 4096x2048 pixels, each 15 microns across.

4.2 WHT Observations and Data reduction

4.2.1 WHT Sample Selection

At the time of writing the telescope proposal for these observations the ghost candidate catalogue was in an early form based on somewhat arbitrary selection criteria. This early catalogue was used to select objects for follow up observations. Objects were selected for follow up for a variety of reasons. SDSS J113831.42+351725.3 and SDSS J170056.85+602639.7 were included as the greater spectral coverage in the blue of the WHT, compared to the SDSS telescope, allows these observations to cover the Ly- α and N v region and test for the presence of N v absorption. SDSS J101844.45+544015.6, SDSS J114704.47+153243.3, SDSS J134458.82+483457.5 and SDSS J162657.47+405848.0 are included as they were considered amongst the best candidates at the time of writing the proposal and higher signal to noise spectra would allow more accurate testing of the He II emission line strength, as well as the strength and width of other emission lines (Ly- α , N v, C IV). As the observing schedule was not favourable to the RA's of our chosen targets SDSS J164152.30+305851.7 and SDSS J212412.60+095923.3 are included, despite not being in the ghost candidate final cut at the time of the proposal. A full list of targets, along with the details of the observations taken, is given in Table 4.1.

4.2.2 Instrumental Set Up

The observations use the 5700 dichroic as, although the response in the crossover region is more complicated than the 5300 dichroic, the former provides the least disruption to the regions of interest in our target spectra, namely the C IV emission and absorption line region, the N v emission and absorption line region and the Ly- α and He II emission line regions. The dichroic response shown in Figure 4.1 is taken from http://www.ing.iac.es/Astronomy/instruments/isis/isis_dich.html. The response of the blue side crosses that of the red side at around 5575Å and the response towards this point is quite complicated, especially on the red side. This may cause some problems with the calibration in this region so any features close to this point should be treated carefully.

Target	Redshift	Filter(s)	Exposure Time (s)	Airmass	Paralactic Angle		Observed Angle
					Start	End	
SDSS101844.45+544015.6	3.25	R158B and R158R	1500	1.23	126.71	118.94	108.0
SDSS101844.45+544015.6	3.25	R158B and R158R	1500	1.28	118.80	111.83	108.0
SDSS101844.45+544015.6	3.25	R158B and R158R	1500	1.26	95.51	95.51	90.0
SDSS113831.42+351725.3	2.11	R158B and R158R	1200	1.10	99.58	95.53	90.0
SDSS113831.42+351725.3	2.11	R158B and R158R	1200	1.14	95.47	92.10	90.0
SDSS113831.42+351725.3	2.11	R158B and R158R	1200	1.19	92.05	89.10	90.0
SDSS114704.47+153243.3	3.08	R158B and R158R	1200	1.25	61.68	63.28	60.0
SDSS114704.47+153243.3	3.08	R158B and R158R	1200	1.33	63.31	64.38	60.0
SDSS134458.82+483457.5	2.05	R158B and R158R	1500	1.18	119.45	111.93	105.0
SDSS134458.82+483457.5	2.05	R158B and R158R	1500	1.24	111.86	105.37	105.0
SDSS134458.82+483457.5	2.05	R158B and R158R	1500	1.31	105.30	99.56	105.0
SDSS162657.47+405848.0	3.05	R158B and R158R	1400	1.02	188.94	165.21	122.0
SDSS162657.47+405848.0	3.05	R158B and R158R	1400	1.03	164.85	144.52	122.0
SDSS162657.47+405848.0	3.05	R158B and R158R	1400	1.04	144.23	129.29	122.0
SDSS162657.47+405848.0	3.05	R158B and R158R	1400	1.06	129.09	118.37	122.0
SDSS164152.30+305851.7	2.00	R158B and R158R	1500	1.03	99.90	93.85	90.0
SDSS164152.30+305851.7	2.00	R158B and R158R	1500	1.05	93.79	90.03	90.0
SDSS164152.30+305851.7	2.00	R158B and R158R	1500	1.09	89.98	87.08	90.0
SDSS170056.85+602639.7	2.12	R158B and R158R	1400	1.22	148.86	140.49	135.0
SDSS170056.85+602639.7	2.12	R158B and R158R	1400	1.25	140.36	132.55	135.0
SDSS170056.85+602639.7	2.12	R158B and R158R	1400	1.29	132.42	125.16	135.0
SDSS212412.60+095923.3	1.9137	R158B and R158R	1200	1.22	305.61	309.06	305.0
SDSS212412.60+095923.3	1.9137	R158B and R158R	1200	1.16	309.12	313.71	305.0
SDSS212412.60+095923.3	1.9137	R158B and R158R	1200	1.12	313.79	319.91	305.0

Table 4.1: WHT observation targets, filters and exposure times.

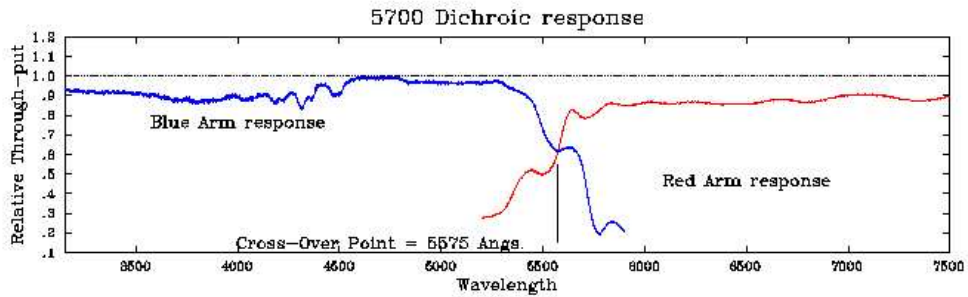


FIGURE 4.1: Dichroic response for the 5700 dichroic presented for the blue and red arms of the detector. Found at http://www.ing.iac.es/Astronomy/instruments/isis/isis_dich.html.

The lowest resolution gratings were chosen to maximise throughput as high resolution is not required to resolve the ghost features, which are typically around 2000kms^{-1} wide. These gratings are the R158B (158 lines mm^{-1}) with a dispersion of around 1.6 \AA/pixel , depending on the observing conditions, using the EEV12 CCD detector in the blue arm. This set up provides spectra in the wavelength range $3500\text{ \AA} < \lambda < 5700\text{ \AA}$. The R158R (158 lines mm^{-1}) provides a dispersion of approximately 1.8 \AA/pixel using the RED+ CCD detector in the red arm. This observing set up provides spectra in the range $5500\text{ \AA} < \lambda < 9000\text{ \AA}$. The resolution of these spectra corresponds to around 200 kms^{-1} , easily enough to resolve ghost features as well as allowing reasonably accurate line-width measurements. The RED+ detector is relatively unaffected by fringing in the regions of interest. Figure 4.2 shows that the fringing modulation of the RED+ detector using the R158R grating is of the order 1% below 9000 \AA .

The target observations were obtained using a long-slit of width 1.5 arc-seconds, wide enough to capture the vast majority of source light in typical observing conditions for the site. In order to minimise slit losses for the standard star observations the slit width for these observations was increased to 5 arc-seconds.

4.2.3 WHT Observations

The data described in this section were obtained over the nights of the 26th and 27th May 2008 on the WHT. Zero second bias exposures were taken at the beginning of each night along with flat-fields obtained using short exposures allowing a lamp to illuminate the dome. Twilight sky flat-field observations were

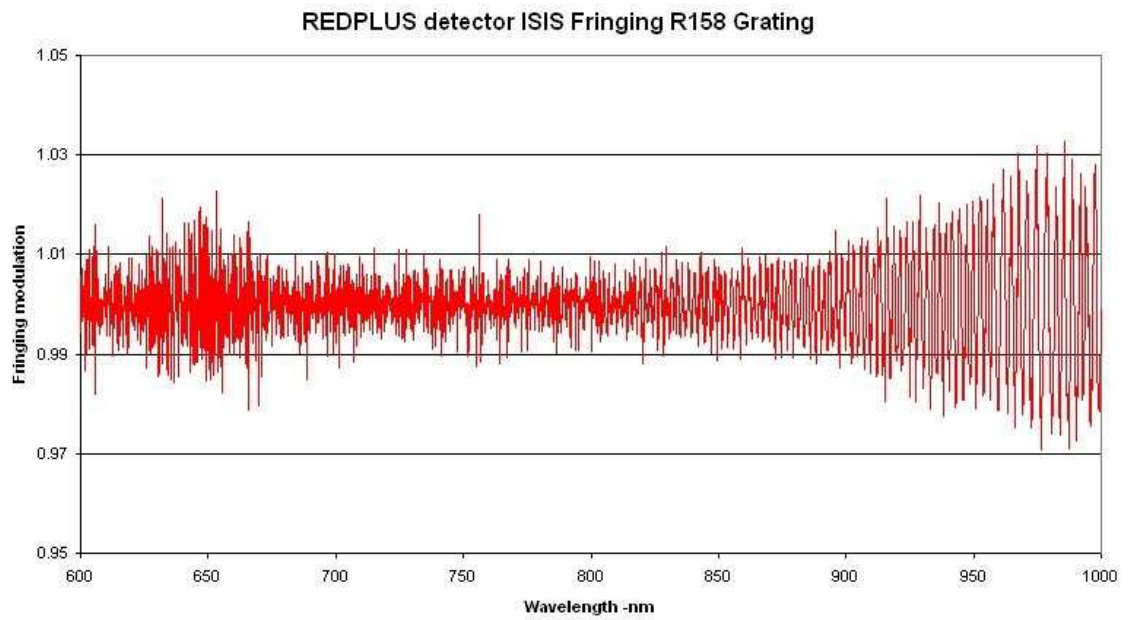


FIGURE 4.2: Fringing modulation for the RED+ detector using the R158 grating that was used for these observations. Taken from http://www.ing.iac.es/Engineering/detectors/g3_ultra_red+.html.

also obtained at the beginning of each night. The twilight flats are much more difficult to take as the sky brightness varies rapidly at twilight. Twilight flats have some advantages over dome flats as the light enters the telescope in the same way as for the science observations. This allows an illumination correction to be performed. These flat-field observations will be used to correct for any variation in the sensitivity of the CCD introduced by differing illumination or pixel response, they were all taken in both the red and blue arm using the instrumental set up used for the target observations.

After pointing the telescope and before taking the observations of each target and calibration object, arc lamp spectra were taken in order to accurately calibrate the wavelength scale. Each target is observed on multiple occasions to minimise problems caused by cosmic ray impacts. Standard stars were observed before the target observations at approximately the same airmass as our targets in order to minimise the effects of atmospheric extinction when performing flux calibrations. The standard star observations were taken using a 5 arc second slit in order to avoid losing flux.

As the amount of refraction of light in the atmosphere is wavelength dependent spectra can be effected by slit-losses (Filippenko 1982). Blue-light suffers more refraction than red light and will therefore be offset from the true object position by a larger amount, resulting in blue light being lost from the spectrum. This problem can be minimised by using a wider slit, by observing only at low airmass or by observing close to the parallactic angle, the angle at which the slit is normal to the horizon resulting in atmospheric refraction being along the axis of the slit. Increasing the slit width results in an increase in the background light leading to a lower signal to noise ratio and is therefore undesirable. Observing close to zenith is clearly preferable, as it also reduces problems caused by atmospheric extinction, but is not possible for many of our targets as they did not appear at high elevations. The majority of targets were observed within 10 degrees of the parallactic angle. Only SDSS J162657.47+405848.0 is observed at a large angle to the parallactic and this object is close to zenith during the observations so slit-losses should be minimal as the incoming light is almost normal to the atmosphere resulting in only a minimal amount of refraction. The observed angle and the parallactic angle at the start and end of the observation are given in Table 4.1.

4.2.4 Data Reduction

In order to produce accurate wavelength and flux calibrated spectra from these data a number of data reduction steps are required. These steps were carried out using a variety of **IRAF** (<http://iraf.noao.edu/>) packages.

Debiasing and flat-fielding

Debiasing and flat-fielding were performed using the *ccdred* package (Valdes 1988) in **IRAF**. The zero exposure time images were combined, using the *zerocombine* routine to take the mean of each pixel, and the resulting bias image subtracted from the rest of the images, an example of a bias image is shown in Figure. 4.3. The red-arm has a typical bias level of 3923 ADU and standard deviation of 1.9 in the combined image, the blue-arm has mean 2436 ADU and standard deviation 5.3.

Bias subtracted dome flat-field images were then combined using the *flatcombine* routine. This combined flat-field image was fit with a simple function to remove the variation due to the spectrum of the lamp used to illuminate the dome. This was performed using the *response* routine which produces an image representing the response of the detector to a uniform field. All of the bias subtracted images are divided by this flat-field response image to correct for variations in the response of the detector with position. An example of a flat-field image is given in Figure 4.4 and an example of a response fit is shown in Figure 4.5. The variations in flat-field image can be seen in the response fit, pixel number in the image is increasing to the right. The response fit shows the rapid drop off in sensitivity caused by the dichroic response on the right, and the lack of reflection from the telescope at short wavelengths on the left.

Once the images have been debiased and dome flat-field corrected, sections in the cross-dispersion dimension (i.e. spatial cuts) are examined to ensure that the illumination is close to uniform across the CCD. Figure 4.6 shows that the dome flat-fields have done a good job and the twilight flats are not required to correct for the illumination of the CCD by the telescope.

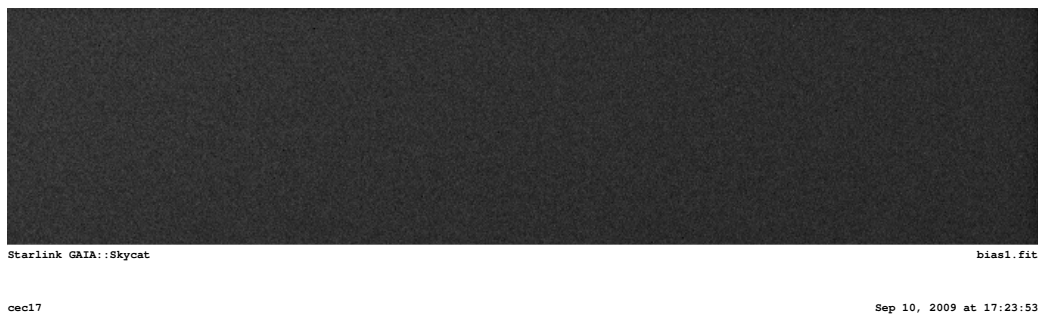


FIGURE 4.3: An example of a bias image taken using WHT.



FIGURE 4.4: An example of a dome flat image taken using WHT.

```
NOAO/IRAF V2.14EXPORT cec17@speed.star.le.ac.uk Thu 17:50:37 10-Sep-2009
func=spline3, order=6, low_rej=550, high_rej=0, niterate=1, grow=0
total=2100, sample=601, rejected=0, deleted=0, RMS= 798.9
Fit the normalization spectrum for FLAT
lampflat blue
```

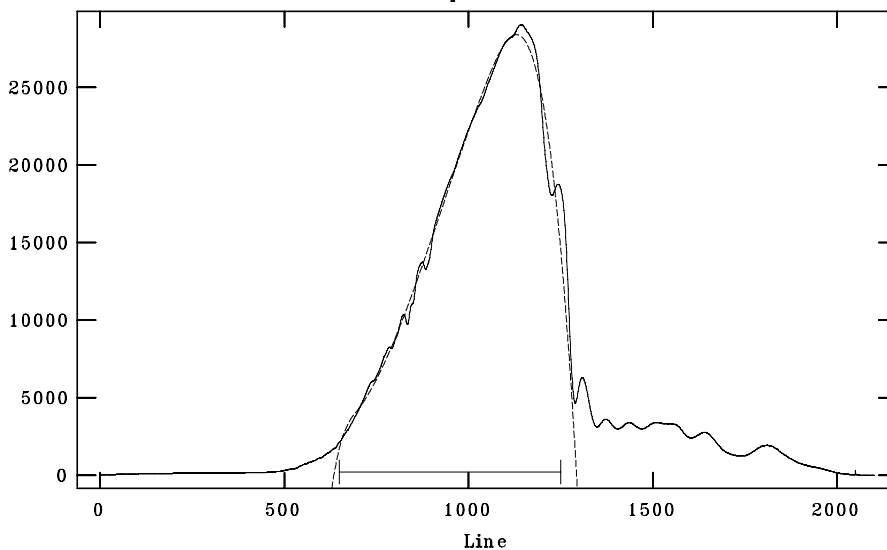


FIGURE 4.5: An example of a response fit to a flat-field image. The bar on the bottom shows the region used for the fit, which is a 6th order cubic spline.

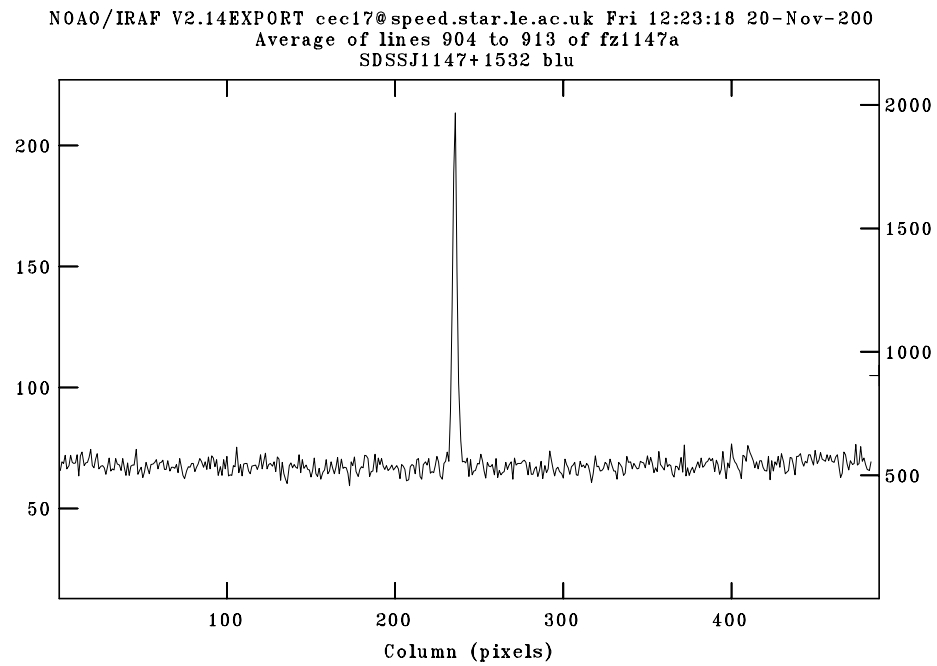


FIGURE 4.6: A cross-section of a flat-field corrected image, showing that the flux is close to uniform across the image.

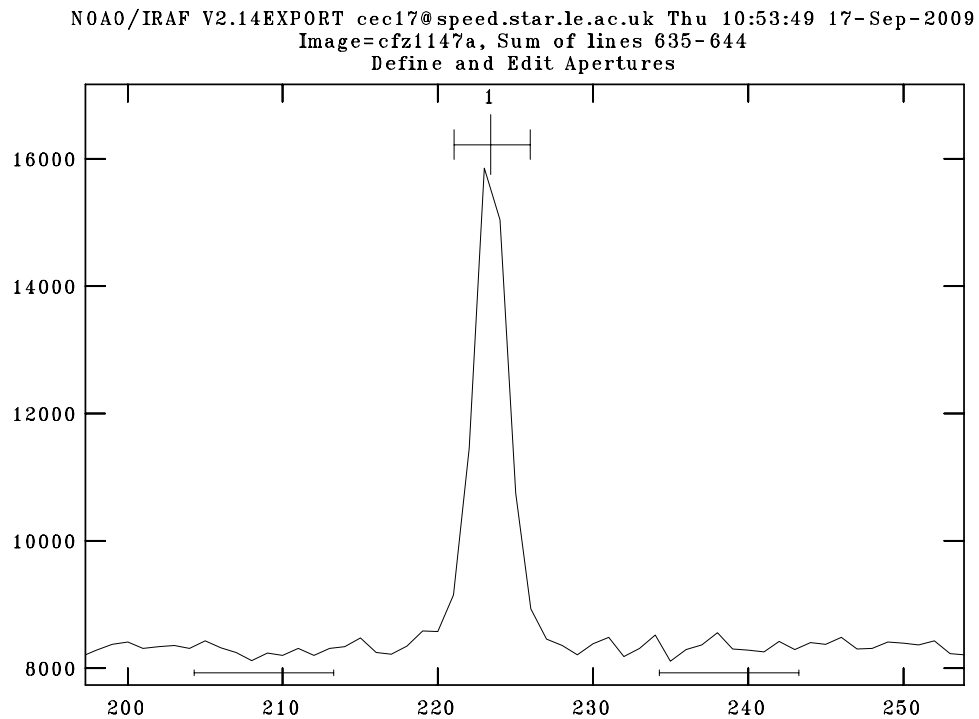


FIGURE 4.7: An example of the aperture used to extract a WHT spectra. The aperture is labelled one and bounded by the bar. The lines at the bottom on either side show the background regions.

4.2.5 Extracting 1-d spectra

One dimensional object spectra were extracted from the 2-d bias and flat-field corrected images using the *apall* tool which outputs a spectrum, background spectrum and background subtracted spectrum in addition to an error spectrum. This tool was used interactively to fit an appropriate aperture width and background region such that the flux of the target is contained within the aperture, an example of an aperture and background region is shown in Figure 4.7.

The apertures were chosen to ensure that the majority of flux from the target is contained within the aperture without introducing unnecessary noise by including regions of only background flux, the exact placement of the apertures is somewhat arbitrary but the differences in the final spectra introduced by small changes to the aperture boundaries are minimal.

The background regions are chosen to be obviously outside of the profile of the spectrum, as well as not including any regions of obvious excess flux caused by additional objects or cosmic rays. A linear fit between these background regions is used to estimate the background flux within the aperture.

The aperture is then traced along the object spectrum to take into account any movement of the spectra across the detector, this fit is usually almost linear and I have typically used a 2nd order cubic spline fit. An example trace is shown in Figure 4.8 this shows that while the spectra is not quite parallel to the detector the drift is very small (≈ 6 pixels across 1250 in this case). The aperture remains of the same size throughout the trace only the centre of the aperture is varied.

Wavelength Calibration

Arc lamp spectra were taken throughout the night before and after observations of each target and standard comparison star. The lamps used were Cu-Ar and Cu-Ne arc lamps and exposure times were 2.0 seconds in the red-arm and 20.0 seconds in the blue-arm. These exposure times were used as they provide good signal to noise without the brightest lines being saturated. An example arc observation is shown in Figure 4.9. Arc

NOAO/IRAF V2.14EXPORT cec17@speed.star.le.ac.uk Thu 10:56:07 17-Sep-2009
 func=spline3, order=2, low_rej=3, high_rej=3, niterate=0, grow=0
 total=128, sample=128, rejected=0, deleted=5, RMS=0.06871
 Aperture 1 of cfz1147a

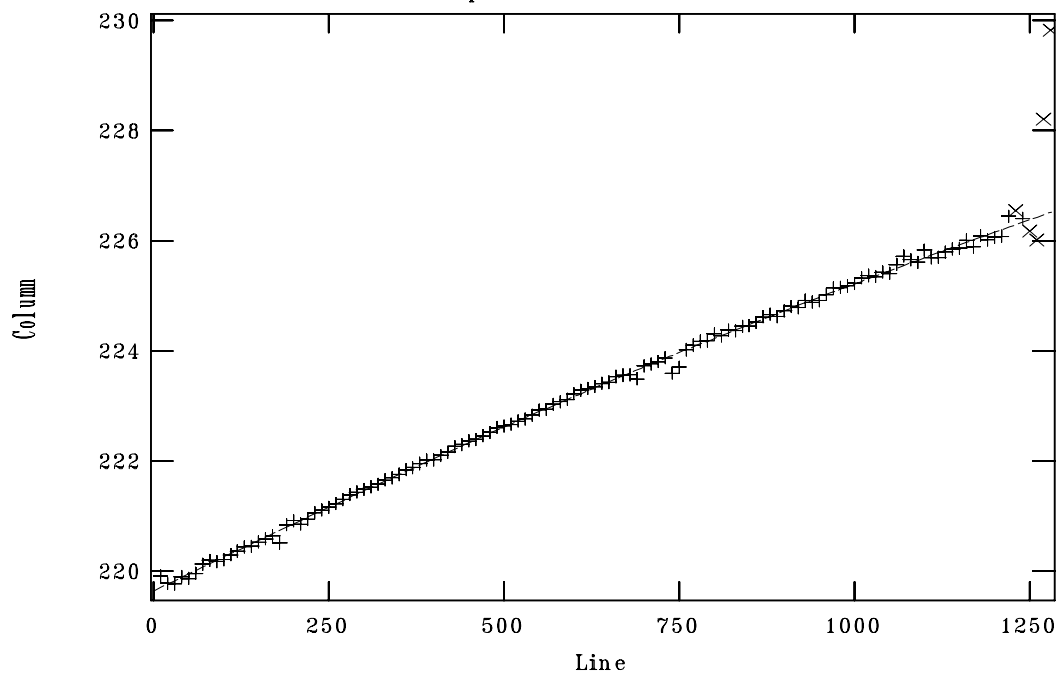


FIGURE 4.8: Example of a trace along the aperture of a WHT spectra. the diagonal crosses are points which have been excluded from the fit, which was a 2nd order cubic spline.

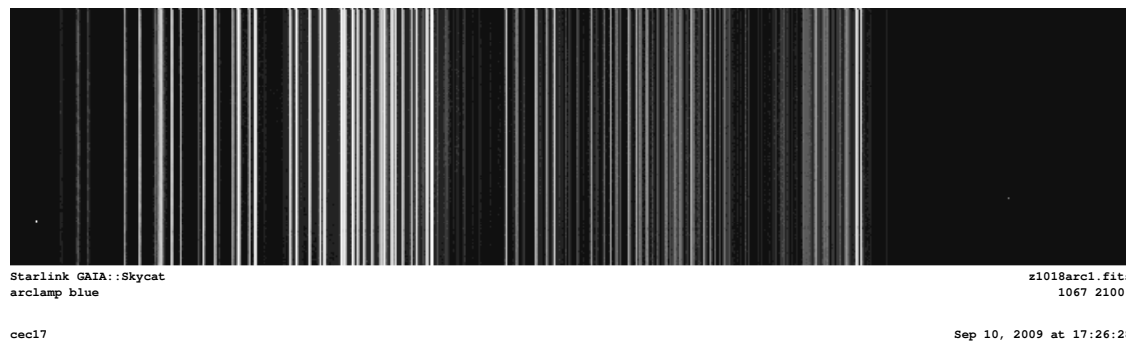


FIGURE 4.9: An arc lamp image taken using the CuAr and CuNe arc lamps.

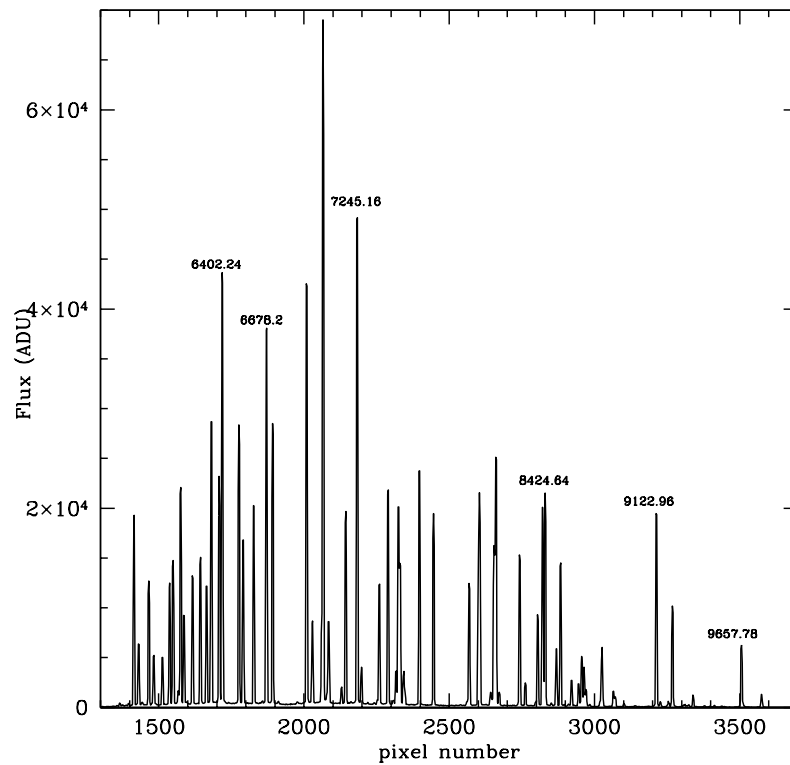


FIGURE 4.10: An extracted arc lamp spectra.

spectra are extracted using *apall* with the same aperture and trace that was used for the target observation they will be used to calibrate. An example of an extracted arc spectrum is shown in Figure 4.10.

After extracting the arc lamp spectra, lines of known wavelength within these spectra were manually identified and marked using the *identify* routine. Some of the prominent lines in Figure 4.10 have been labelled with their wavelength in Å. Many more lines are identified and used by the *identify* routine to produce a map of wavelength as a function of pixel number by fitting a simple function to the identified points. This dispersion solution is used with the *dispcor* package to produce wavelength calibrated spectra.

Flux Calibration and Extinction Correction

The spectrophotometric standard stars were reduced in the same manner as the target spectra. An example of a reduced wavelength calibrated standard spectrum is given in Figure 4.11. The **IRAF** tool *standard* was

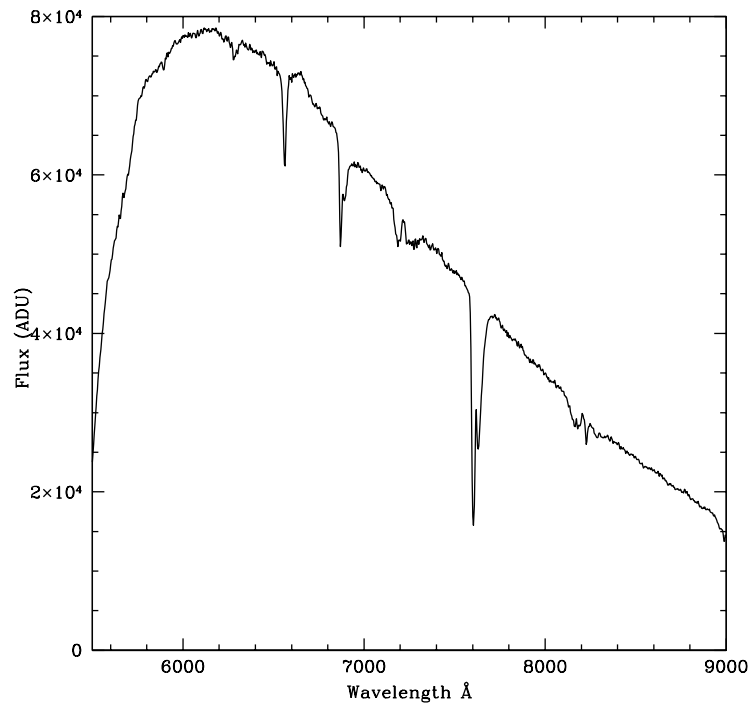


FIGURE 4.11: A wavelength calibrated standard star spectrum used to produce a sensitivity function.

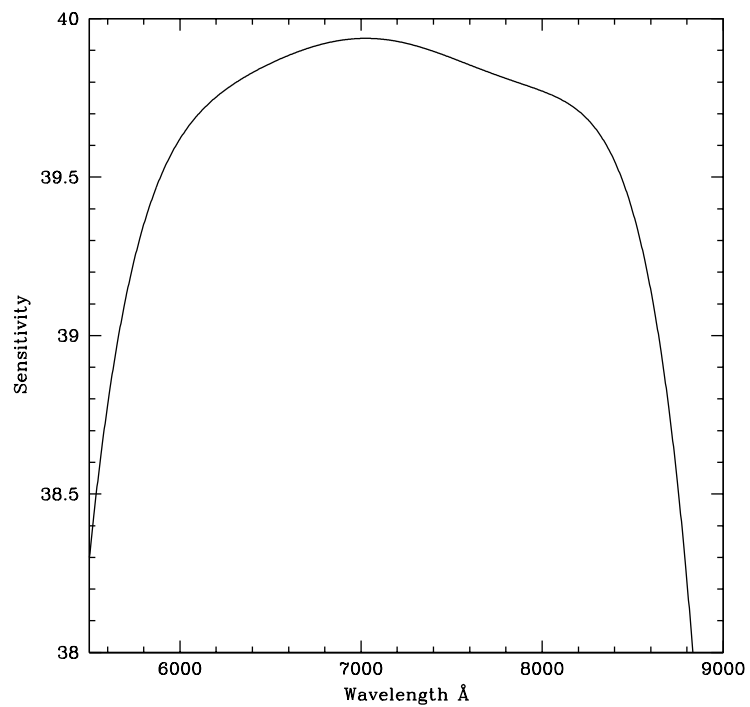


FIGURE 4.12: An example WHT sensitivity function (sensitivity is in units of $2.5\text{Log}_{10}[\text{counts} / (\text{ergs}/\text{cm}^2)]$).

used taking as input the standard star spectrum and the tabulated fluxes in various wavelength ranges as well as the exposure time and airmass and producing a sensitivity value for each of the tabulated wavelengths. These sensitivity values were then used in the *sensfunc* routine and fit with a low order (typically order=5) cubic spline function to produce a continuous sensitivity function (like the one shown in Figure 4.12) allowing the target spectra to be flux calibrated. Outlying points produced by absorption features were removed prior to the fitting of the sensitivity function in order to avoid small scale rapid variation in the sensitivity function.

The *calibrate* tool was used to flux calibrate and extinction correct the target spectra using the sensitivity function created from the standard star spectrum taken before the target at a similar airmass. The extinction correction uses the La Palma extinction data to remove the effect of absorption within the atmosphere. Each observation is calibrated separately and they are then combined, removing cosmic rays using the sigma clipping algorithm in the *scombine* tool.

The dichroic response will also have some impact on the spectra. However, as this response is coupled with the detector response and instrument throughput and partially corrected for during the flux calibration no attempt to correct for the dichroic response has been made. For this reason there may be significant discrepancies in the flux calibration between the red end of the blue arm spectra and the blue end of the red arm spectra.

The method used to combine spectra from the red and blue arms of the instrument depends on the quality of the spectra in the crossover region. For example SDSS J113831.42+351725.3 and SDSS J134458.82+483457.5 are simply joined together at 5600 Å as the spectra match closely in the crossover region. Red and blue spectra of SDSS J114704.47+153243.3 are combined by taking the mean, weighted by the errors, of the two spectra between 5500 and 5600 Å. All of the other objects have their spectra combined using an error weighted mean between 5550 and 5600 Å.

4.2.6 SDSS Flux Calibration

The SDSS spectra shown in previous chapters have all been the versions released in data release 5 (DR5 Adelman-McCarthy et al. 2007). Later releases DR6 (Adelman-McCarthy et al. 2008) and DR7 (Abazajian et al. 2009) have contained re-calibrated versions of these spectra with some changes in the flux and wavelength calibration. Of particular note is the change in the flux calibration presented in DR6. In this release the spectrophotometric fluxes were matched to the point-spread function of the plate at the time of the observations, whereas in previous releases they had been matched to the fiber magnitudes. This change results in a significant increase in the published fluxes (30 to 40% in the majority of objects presented here).

I would note that the DR7 spectra (which use the DR6 method of flux calibration, with some minor modification in some cases) are on average around 40% brighter than the WHT follow up spectra whilst the DR5 spectra match the WHT fluxes to within a few percent in the majority of cases. Whilst it is possible that these objects have dimmed between the time of the SDSS observations and the follow up WHT observations it seems more likely that the re-calibration present in Adelman-McCarthy et al. 2008 has produced less accurate fluxes than those presented in DR5, or that there is some systematic error in the flux calibration of the WHT data. The observing conditions for the WHT observations were not ideal and the absolute fluxes are likely to only be accurate to around 10%. Both DR5 and DR7 versions of the SDSS spectra are presented in this Chapter.

4.2.7 Object Spectra

Due to the differences between the DR5 and DR7 versions of the SDSS spectra of these objects the WHT spectra are shown in this section along with both of these versions of the SDSS spectra. In addition to these plots, plots of the C IV and Si IV absorption are given in velocity space to allow easy comparison between the absorption in these lines. These absorption plots are shown along with a scaled version of the DR7 SDSS spectra to allow comparison of the shape of any features within the absorption in the

two observations. I also present continuum normalised plots of the SDSS DR5 and WHT spectra in the rest-frame wavelengths to highlight any changes in the shape or equivalent width of absorption and emission lines. The crossover region for the 5700 dichroic occurs at 5575 \AA and is marked with a dashed line in plots which cover this region. Fluxes at wavelengths within $\pm 50 \text{ \AA}$ of this point are subject to significant uncertainties. The WHT spectra of SDSS J101844.45+544015.6, SDSS J114704.47+153243.3, SDSS J134458.82+483457.5 and SDSS J164152.30+305851.7 are shown after a small correction to the wavelength calibration performed by cross-correlating the spectra with the SDSS DR5 spectra of the same objects.

SDSS J101844.45+544015.6

This object was observed on both the 26th and 27th of May 2008 as it set early in the night and was not visible for long enough to produce a significantly improved signal to noise spectrum with observations from a single night. Two observations were taken on the 26th of May, one at an airmass of 1.23 and the other at an airmass of 1.28, and one the following night at an airmass of 1.26. The observed standard star was SP1036+433 and was observed at an airmass of 1.07 on the first night and 1.10 on the second.

Both SDSS DR5 and DR7 spectra are shown in Figure 4.13 with the top panel showing the DR7 spectrum and the lower panel the DR5 version. The WHT spectrum is plotted as the solid line in both panels. This object has a redshift of 3.25 according to the SDSS and the major emission lines are labelled on the DR5 plot in the lower panel. Figure 4.13 clearly shows the increased signal to noise ratio within the WHT spectrum. The S/N in the WHT spectrum measured between 1700 and 1750 \AA in the rest-frame of the source is 9.8 per pixel. The SDSS DR7 spectrum has higher resolution than the WHT spectrum so in order to compare the S/N the SDSS DR7 spectrum is binned to the same resolution as the WHT spectrum, the S/N is then measured to be 4.8 per WHT pixel. The higher quality of the WHT spectrum and the possible change in the flux of the object are the only significant differences between the WHT and SDSS spectra. This can be seen more clearly in Figure 4.14 which shows the WHT and SDSS DR5 spectra in the source rest-frame and normalised to continuum fits. The degree to which this object has dimmed is

difficult to establish due to the significant variation in flux calibration presented by the SDSS, however as more than 6 years (≈ 1.4 years in the rest frame) have passed between the SDSS observation on the 17th of April 2002 and the WHT observation it would not be unreasonable to see significant flux changes (O'Brien et al. 1988).

The rest-frame equivalent widths of the prominent emission lines are measured by fitting a reddened power law to the continuum and summing any excess flux in the region of the emission line. The C IV EW is measured between 1530 and 1575 Å in the source rest-frame and the Si IV EW is measured in the rest-frame between 1380 and 1420 Å. This method is used to measure the C IV and Si IV EWs throughout this chapter. The DR5 and DR7 SDSS spectra give C IV EWs of 66.7 ± 0.8 Å and 66.3 ± 0.8 Å respectively. The quoted errors on this measurement are the statistical errors only. The true error will be larger, with the largest contribution arising from inaccurate continuum placement. The C IV emission in the WHT spectrum has rest-frame EW of 74.5 ± 0.3 Å suggesting that the strength of the emission line has increased and/or the continuum flux has fallen. The Si IV emission line tells a similar story with rest-frame EWs of 39.8 ± 1.0 Å and 38.6 ± 1.1 Å measured from the SDSS observations compared with 45.0 ± 0.5 Å from the WHT data.

The C IV emission line FWHM for the WHT observation is 3730 ± 70 km s⁻¹ which is similar to the 3820 ± 250 km s⁻¹ measured from the DR7 SDSS spectrum and comparable to the 3500 km s⁻¹ upper limit proposed by Arav 1996. This measurement is taken by removing the continuum fit to calculate the EWs and then fitting a Gaussian to the unabsorbed parts of the emission line and minimising χ^2 . This method is used to calculate FWHM of the C IV lines throughout this Chapter. The errors on the FWHM measurement are the the statistical errors found by fixing the strength and centre of the Gaussian component and varying the width until the χ^2 value increases by 2.73. The true error on the FWHM will include significant contribution from errors in the continuum placement, as well as the choice of regions to exclude as being absorbed, and is therefore difficult to quantify. The absorption troughs of both C IV and Si IV are shown in Figure 4.15. The SDSS spectrum shown in Figure 4.15 is the DR7 version as the improved reduction produces cleaner spectra. There is some evidence for a small increase in absorption due to C IV between

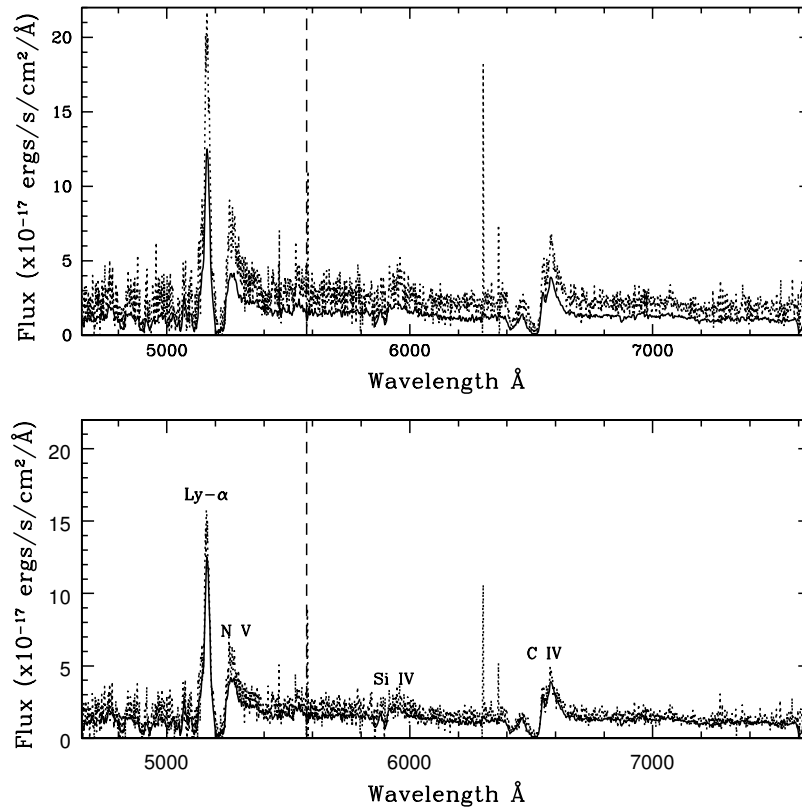


FIGURE 4.13: WHT spectrum of SDSS J101844.45+544015.6 (solid) along with the DR7 (top panel-dotted) and DR5 (bottom panel-dotted) versions of the SDSS spectrum of the same object the vertical dashed line represents the crossover between the red and blue arms of ISIS at 5575 Å.

9000 and 10000 kms^{-1} . However the structure of the absorption remains almost identical elsewhere in the C IV trough and throughout the Si IV trough.

The WHT spectrum still shows strong N V absorption as well as strong emission lines. The He II emission line is fit with a scaled version of the He II emission from the DR5 composite in the same way as in Chapter 3. The emission is stronger in this object than the composite by a factor of $2.11^{+0.3}_{-0.23}$ which is consistent with the 1.96 ± 0.49 found from the DR5 SDSS spectrum.

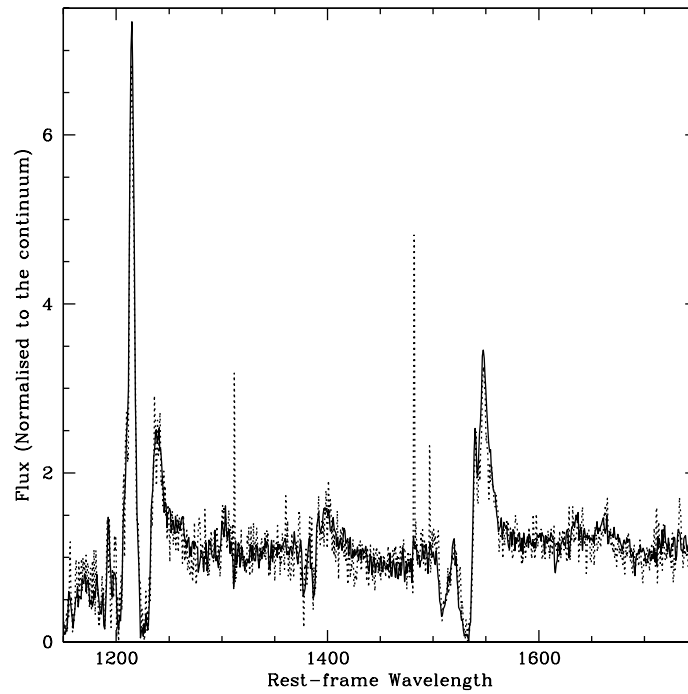


FIGURE 4.14: Continuum normalised spectra of SDSS J101844.45+544015.6 from the SDSS DR5 (dotted) and WHT (solid) observations

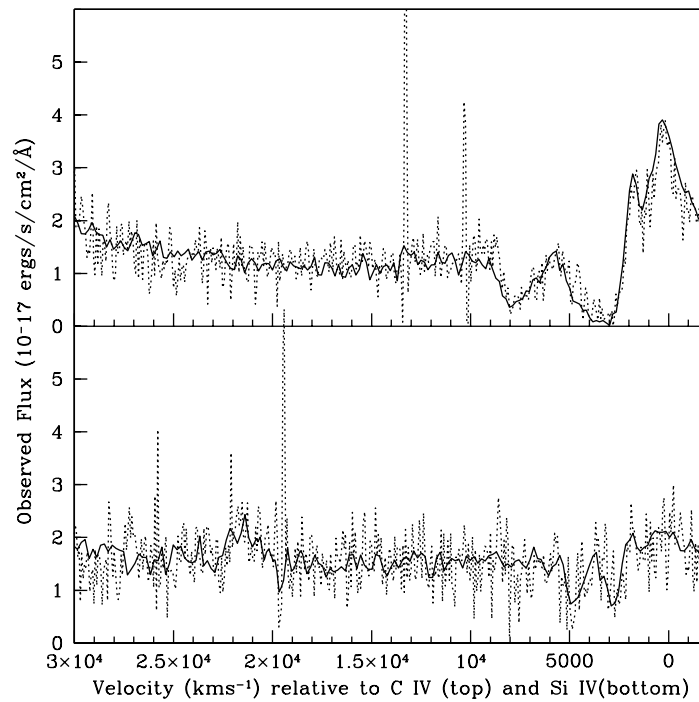


FIGURE 4.15: C IV (top) and Si IV (bottom) absorption troughs in velocity space of SDSS J101844.45+544015.6 from the SDSS DR7 (dotted and scaled) and WHT (solid) observations

SDSS J113831.42+351725.3

Figure 4.16 shows significant changes to the spectrum of this object between the SDSS observation taken on the 3rd May 2005 and the WHT spectrum which was obtained on the 27th May 2008 3.07 years later (0.98 years in the source rest frame). Both DR5 and DR7 versions of the SDSS spectra are shown in Figure 4.16 with the major emission lines labelled on the DR5 plot in the bottom panel. This object is at redshift 2.11 so all of the information relevant to the testing of Arav's criteria is contained within the blue arm of the ISIS observations. The standard star used to flux calibrate this spectrum was observed at an airmass of 1.07 slightly lower than the target, which was observed between 1.10 and 1.19.

The WHT spectrum clearly shows higher S/N than both the SDSS spectra, when measured between 1700 and 1750 Å in the rest-frame (35.0 per pixel compared to 16.4 per WHT pixel measured from the SDSS DR7 spectrum binned to match the WHT resolution as for the previous object). The WHT observation also shows clear broad absorption due to N v that was not covered by the SDSS observations. However the most important difference from the point of view of this study occurs in the C IV BAL trough. The absorption blueward of the potential ghost feature identified in the SDSS spectrum has almost completely disappeared. This suggests that this absorption is not related to the trough redward of the feature which remains at a similar depth, although this may be due to the lower velocity trough remaining on the saturated part of the curve of growth. The C IV and Si IV absorption troughs are shown in velocity space in Figure 4.18. The SDSS spectrum in this figure is the DR7 version and has been scaled to match the WHT flux between 1700 and 1750 Å in the rest-frame of the source. Based upon the WHT spectrum one would conclude that this object is not a good ghost candidate and it would certainly not be selected as such on the basis of this spectrum.

Both the C IV and Si IV emission lines show reduced equivalent widths in the WHT spectrum, this is clearly seen in the continuum normalised spectra from the WHT and SDSS DR5 spectra shown in Figure 4.17 . The equivalent width of C IV is measured to be 41.0 ± 0.2 Å in the WHT spectrum around 20% less than the 51.1 ± 0.4 Å and 46.1 ± 0.3 Å in the DR5 and DR7 SDSS spectra respectively. The equivalent width

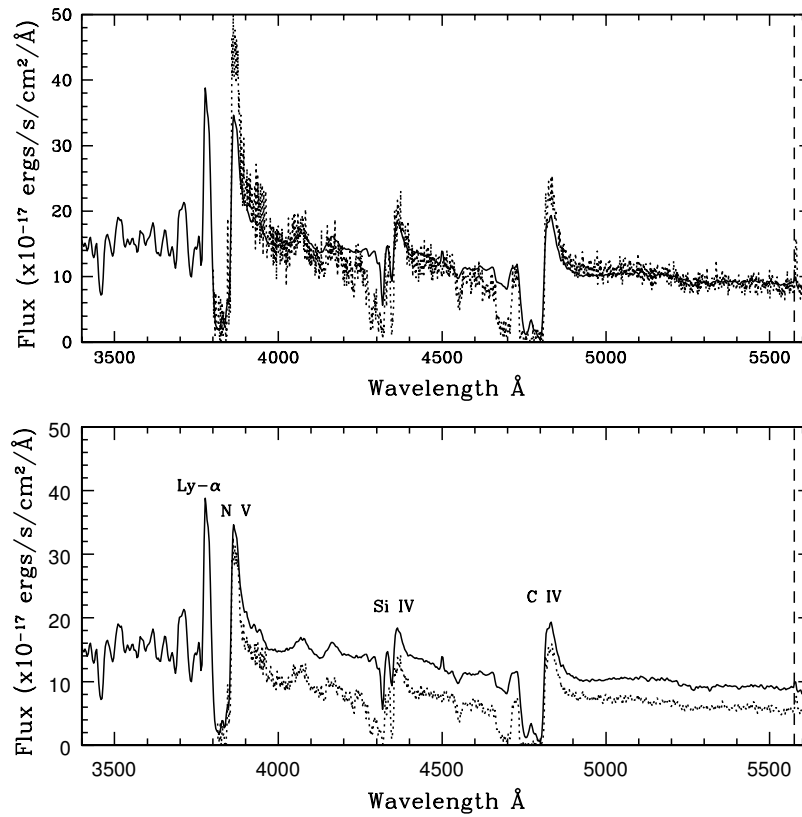


FIGURE 4.16: WHT spectrum of SDSS J113831.42+351725.3 (solid) along with the DR7 (top panel-dotted) and DR5 (bottom panel-dotted) versions of the SDSS spectrum of the same object. The vertical dashed line represents the crossover between the red and blue arms of ISIS at 5575 Å.

of Si IV is 31.9 ± 0.2 Å in the WHT spectrum falling between the 24.0 ± 0.4 and 27.4 ± 0.3 found in the SDSS DR5 and DR7 spectra. Whilst this object is no longer considered to be a good ghost candidate it is worth noting that the decrease in the strength of the C IV emission line, relative to the continuum, results in this object failing Arav's criteria for strong emission lines. The FWHM of the C IV emission line is measured to be 3530 ± 130 km s⁻¹ which straddles the limit suggested by Arav 1996. The SDSS spectra have FWHM measured as 3830 ± 150 km s⁻¹ from DR5 and 3330 ± 150 km s⁻¹ from DR7. The He II emission line region is of similar strength to that found in the DR5 composite, the emission in the WHT spectrum requires a scaling factor of 0.96 ± 0.1 (the DR5 SDSS spectrum needs a scaling factor of 0.98 ± 0.20). A more detailed analysis of the changes seen in this object is presented in Chapter 5.

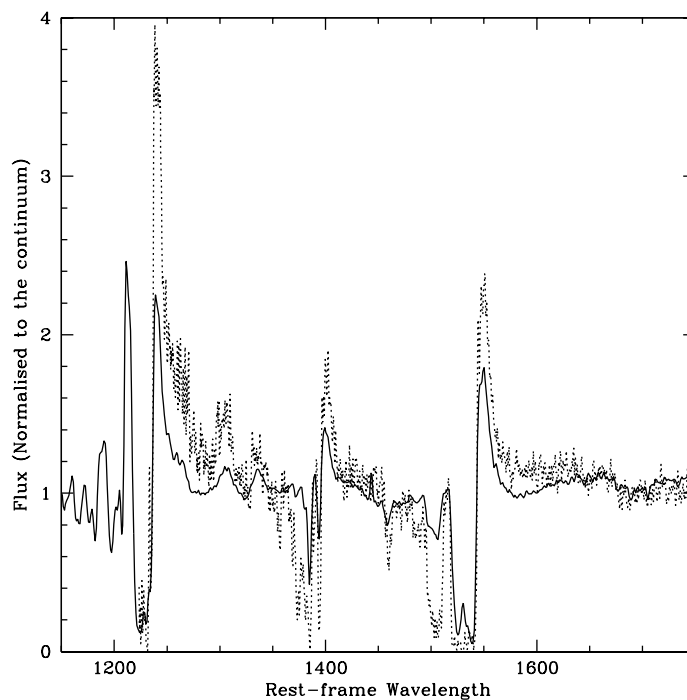


FIGURE 4.17: Continuum normalised spectra of SDSS J113831.42+351725.3 from the SDSS DR5 (dotted) and WHT (solid) observations

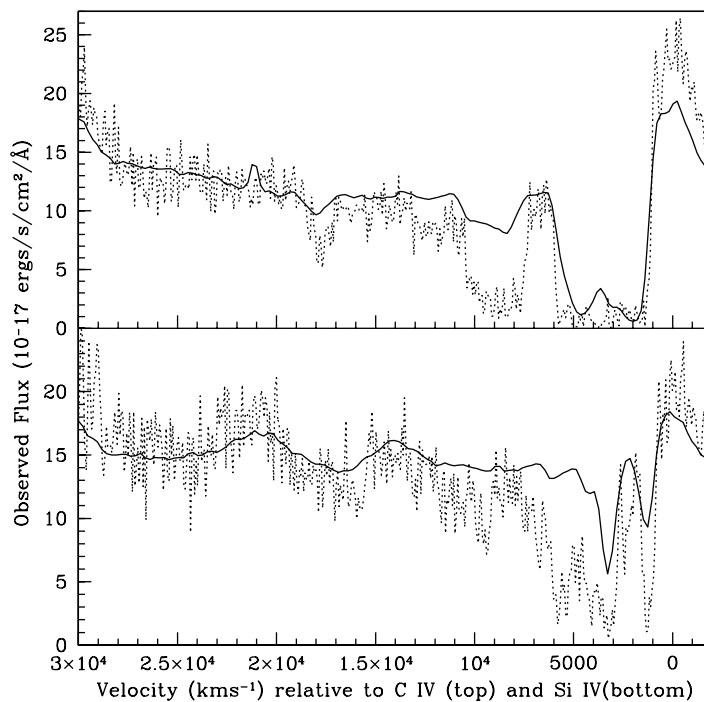


FIGURE 4.18: C IV (top) and Si IV (bottom) absorption in velocity space for the WHT (solid) and SDSS DR7 (dotted and scaled) spectra of SDSS J113831.42+351725.3

SDSS J114704.47+153243.3

The SDSS observation of this object was taken on the 19th of December 2004 around 3 and a half years prior to the WHT follow up observations obtained on the 26th May 2008. At the redshift of this source, 3.08, this corresponds to 0.86 years in the source rest-frame. The WHT spectrum is produced from two observations obtained at an airmass of 1.25 and 1.33, the standard star spectrum used for these observations was taken at an airmass of 1.15.

Figure 4.19 shows the WHT follow up observation of SDSS J114704.47+153243.3 along with the DR5 SDSS spectra in the bottom panel and the DR7 version in the top panel. The dashed line shows the dichroic crossover and prominent emission lines are labelled in the bottom panel. Figure 4.20 shows continuum normalised WHT and SDSS DR5 spectra in the source rest-frame. It is clear from this figure that there is little change in the shape of C IV absorption or emission components. The apparent change in the Si IV emission could be due to the dichroic response as this emission is relatively close to the crossover region. The S/N in the WHT spectrum measured between 1700 and 1750 Å in the rest-frame is 15.9 per pixel compared to the 11.4 measured from the same region of the SDSS DR7 spectrum after binning to the same resolution as the WHT spectrum.

The EW of emission in C IV is measured as 60.8 ± 0.3 Å and 62.3 ± 0.4 Å in the SDSS DR5 and DR7 spectra and is around 10% lower at 54.9 ± 0.1 Å in the WHT follow up, again the errors quoted are statistical and the true error on these values will be largely due to the placement of the continuum. The Si IV emission has an EW of 45.5 ± 0.4 Å and 46.8 ± 0.5 Å in the SDSS spectra and 42.5 ± 0.2 Å in the WHT spectra.

Fig. 4.21 shows the C IV and Si IV absorption regions in velocity space for the WHT follow up spectrum along with the SDSS DR7 observation which has been scaled to match the flux of the follow up spectra in the rest frame region between 1700 and 1750 Å. This allows easier comparison of the shape of the absorption features. The figure shows no great difference in the shape of the C IV emission or absorption. As the Si IV absorption is both fairly complex and likely to be affected by the dichroic response it is

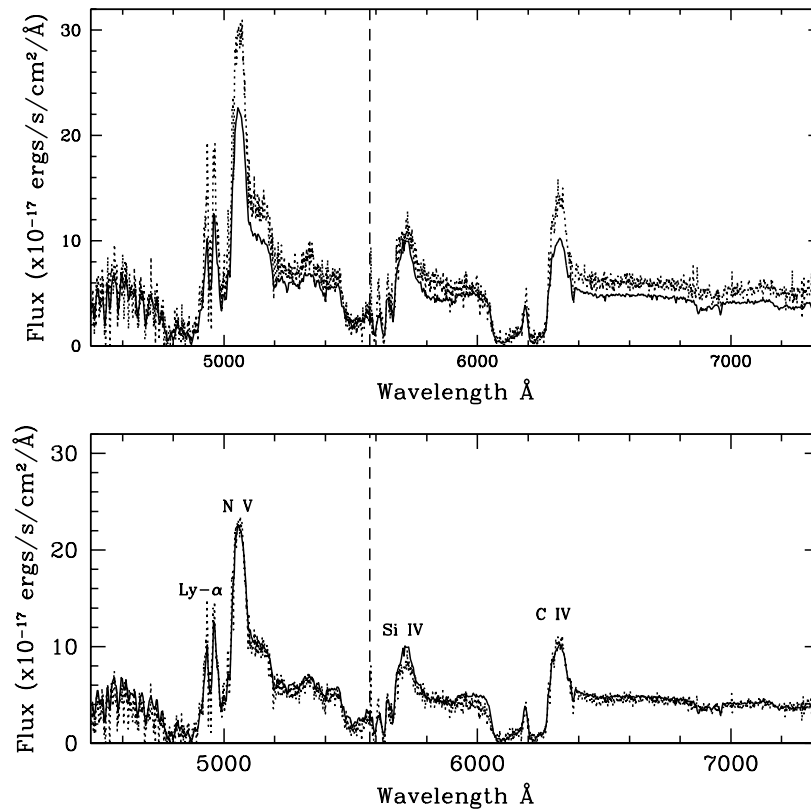


FIGURE 4.19: WHT spectrum of SDSS J114704.47+153243.3 (solid) along with the DR7 (top panel-dotted) and DR5 (bottom panel-dotted) versions of the SDSS spectrum of the same object. The vertical dashed line represents the crossover between the red and blue arms of ISIS at 5575 Å.

difficult to draw any firm conclusions regarding this absorption, however it seems unlikely that any change is particularly large.

The FWHM of the C IV emission line is measured from the WHT spectrum to be $3730 \pm 40 \text{ km s}^{-1}$ compared to the $3210 \pm 90 \text{ km s}^{-1}$ measured from the DR5 SDSS spectrum and the $3410 \pm 150 \text{ km s}^{-1}$ from the SDSS DR7 spectrum. The WHT measurement exceeds the 3500 km s^{-1} limit set by Arav 1996 however the 'true' error on this value may be much larger than the 40 km s^{-1} statistical error. The WHT spectrum also shows strong N V absorption and has N v and C IV emission lines which meet the criteria for strong emission. The He II region is well fit by the DR5 composite which has its emission scaled by a factor of $0.92^{+0.11}_{-0.09}$ consistent with the object having He II emission of average strength. This is also true of the $0.96^{+0.19}_{-0.16}$ measured from the DR5 SDSS spectrum.

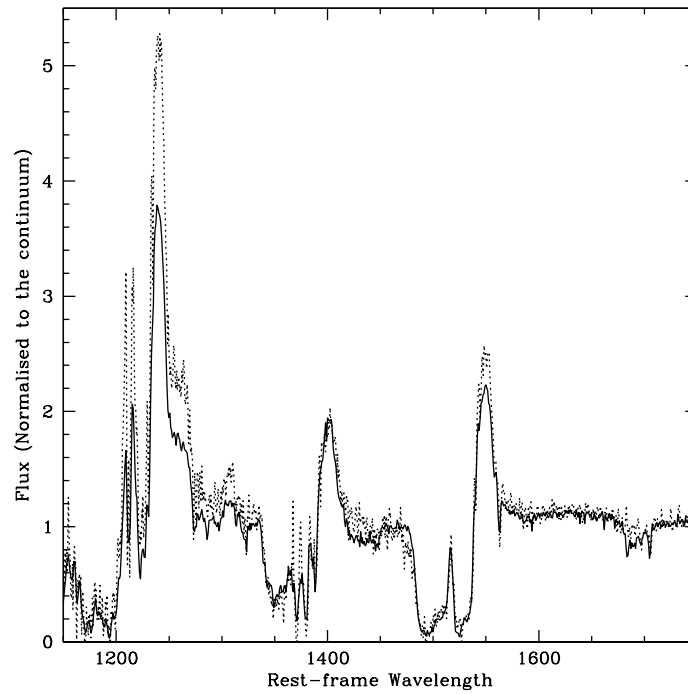


FIGURE 4.20: Continuum normalised spectra of SDSS J114704.47+153243.3 from the SDSS DR5 (dotted) and WHT (solid) observations

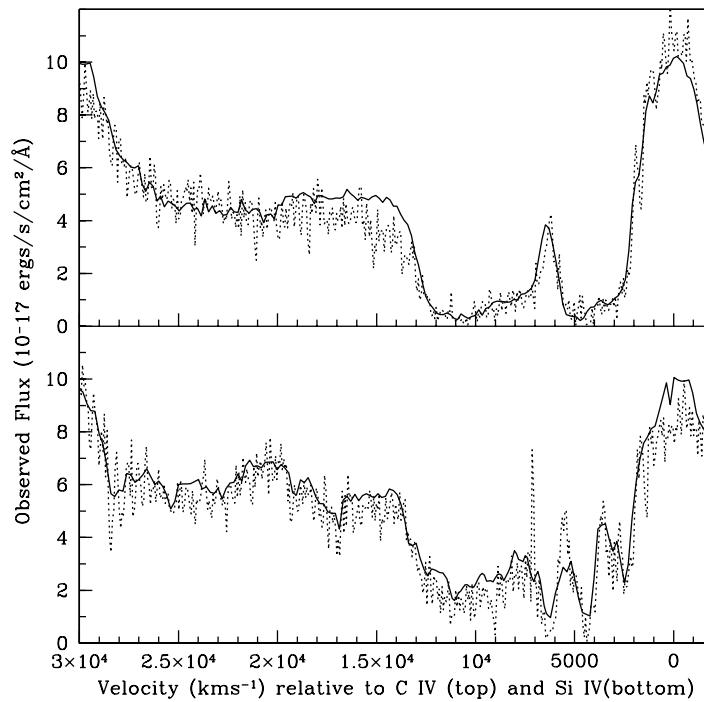


FIGURE 4.21: C IV (top) and Si IV (bottom) absorption troughs in velocity space of SDSS J114704.47+153243.3 from the SDSS DR7 (dotted and scaled) and WHT (solid) observations.

SDSS J134458.82+483457.5

Figure 4.22 shows both the DR7 and DR5 versions the SDSS spectrum of SDSS J134458.82+483457.5, taken on the 7th of April 2003, along with the follow up WHT spectrum taken on the 27th of May 2008. The redshift of this object is given by the SDSS as 2.05 so the 5.13 years between the observations corresponds to 1.68 years in the source rest-frame. The standard SP1321+363, which is used in the flux calibration of the WHT spectrum, was observed at an airmass of 1.12, slightly lower than the airmass of the target observations that range from 1.18 to 1.31, as this object was setting rapidly at the time of the observations. The differences around the N V emission line are unlikely to be real changes as the sensitivity of the WHT observations at this point is low.

The SDSS spectrum is extremely noisy making it difficult to judge which features in the absorption trough are real and which are simply the result of noise. The WHT spectrum has a S/N of 22.1 per pixel between 1700 and 1750 Å. After binning the SDSS DR7 spectrum to match the resolution of the WHT spectrum the S/N measured in the same region is 10.6 per WHT pixel. In order to more easily compare the emission and absorption in the WHT and SDSS DR5 spectra they are plotted normalised to the continuum in Figure 4.23. There appears to be little change in the C IV emission line. The Si IV emission line in the WHT spectrum extends further to the blue although this is almost certainly due to changes in the absorption. The blue end of these spectra show large differences but this region is highly uncertain in both spectra.

The equivalent width of the C IV emission line is measured to be 52.0 ± 0.5 Å and 58.2 ± 0.6 Å in the DR5 and DR7 SDSS spectra respectively and 53.9 ± 3.1 Å in the WHT spectrum. The Si IV emission line has an EW measured as 46.1 ± 0.6 Å and 45.0 ± 0.6 Å for the SDSS spectra and 43.6 ± 2.6 Å in the WHT spectrum. There seems to be some evidence for increased high velocity absorption due to Si IV and C IV in the WHT spectrum. The C IV and Si IV absorption troughs are shown in Figure 4.24, they are shown in velocity space to allow easier comparison between the features in the C IV and Si IV absorption. Figure 4.24 includes the DR7 SDSS spectrum due to the improved calibration of this data release. The additional structure in the C IV BAL, appearing at around 12000, 15000 and 20000 kms^{-1} would have

resulted in this object being rejected at the Single Peak stage of our candidate selection on the basis of the WHT spectrum alone. The Si IV absorption seems to have moved to higher velocity, from ≈ 4000 and 6000 km s^{-1} to ≈ 6000 and 8000 km s^{-1} . As well as becoming stronger, there is also some evidence for additional absorption at around 22000 km s^{-1} .

The WHT spectrum of this object fails a number of Arav's criteria. The C IV and N V emission lines are very weak and the C IV emission line has a FWHM measured to be $4900 \pm 250 \text{ km s}^{-1}$ well in excess of the 3500 km s^{-1} limit suggested by Arav 1996. There is insufficient spectral coverage to allow testing of either the strength of Ly- α emission or the strength of N V absorption. The He II emission region requires the DR5 composite emission in this region to be scaled by a factor of 1.34 ± 0.90 , which precludes determination of the strength of the far-UV continuum. The WHT spectrum shows additional features within the absorption, it also fails two of Arav's tests while the others are inconclusive or untestable in this spectrum. This suggests that the ghost candidate feature is not produced by the mechanism proposed by Arav.

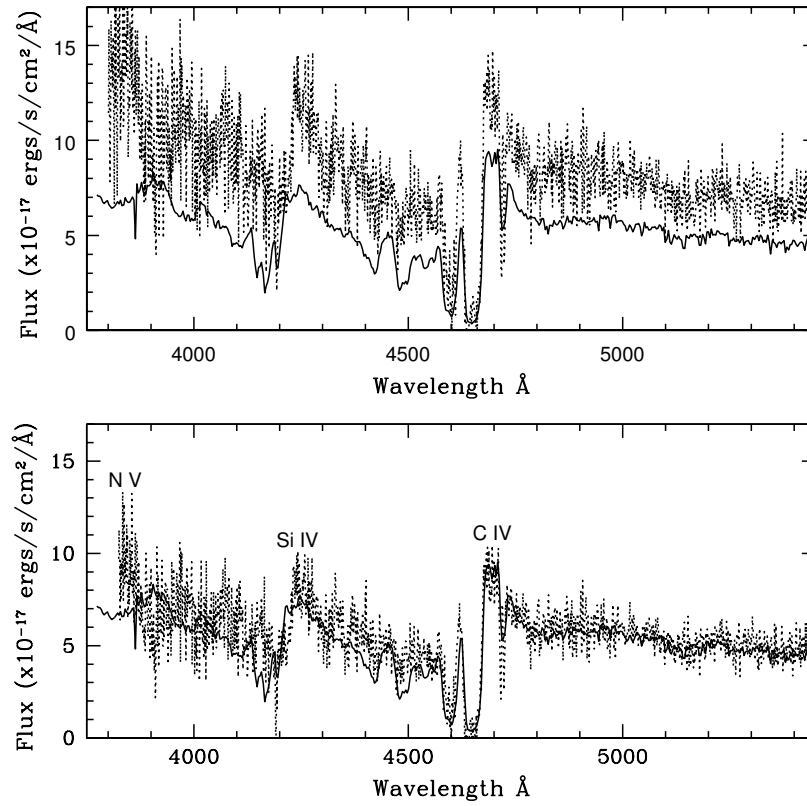


FIGURE 4.22: WHT spectrum of SDSS J134458.82+483457.5 (solid) along with DR7 (top panel-dotted) and DR5 (bottom panel-dotted) versions of the SDSS spectrum of the same object.

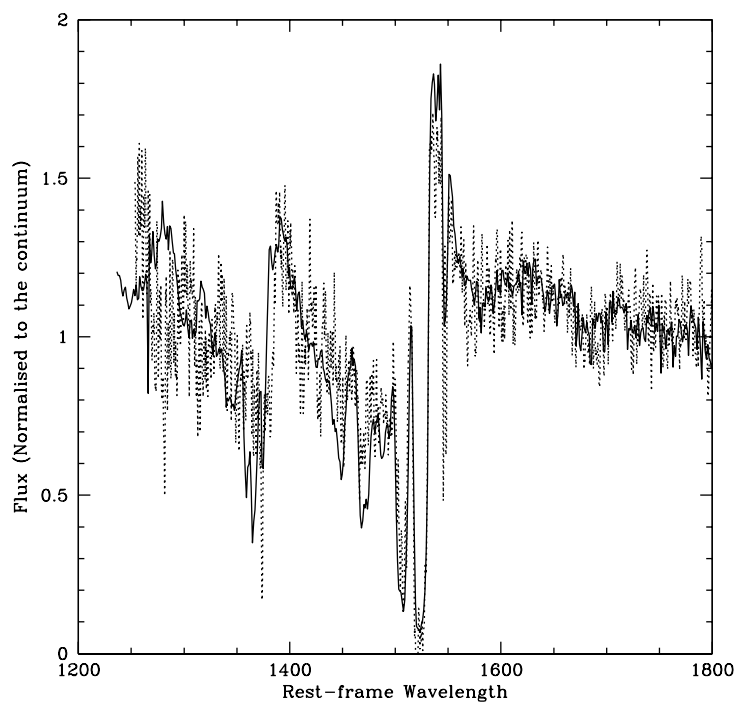


FIGURE 4.23: Continuum normalised spectra of SDSS J134458.82+483457.5 from the SDSS DR5 (dotted) and WHT (solid) observations

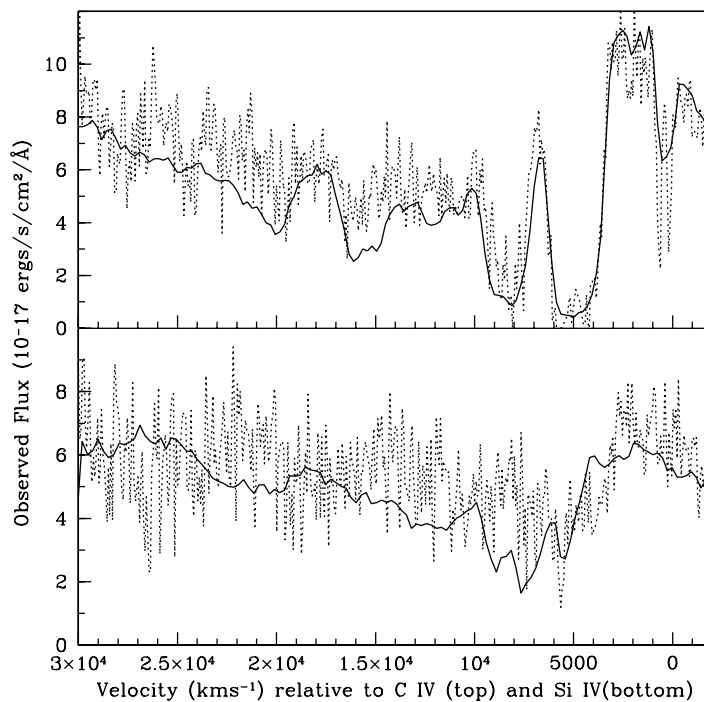


FIGURE 4.24: C IV (top) and Si IV (bottom) absorption in velocity space for the WHT (solid) and SDSS DR7 (dotted and scaled) spectra of SDSS J134458.82+483457.5.

SDSS J162657.47+405848.0

This object was observed during a period of very good (sub arc-second) seeing, close to zenith. To minimise background flux the slit used was narrowed to 1.3 arc-seconds. The standard, SP1626+36 was observed using a 3 arc-second slit at an airmass of between 1.01 and 1.02, the airmass of the target observations increased from 1.02 to 1.06 during the 4 observations. The WHT spectrum shown in Figure 4.25 along with SDSS spectra taken over 6 years earlier on the 15th of April 2002 from DR7 (top) and DR5 (bottom). The source is at redshift 3.05 so the gap between observations is 1.51 years in the source rest-frame. The WHT spectrum has a S/N measured between 1700 and 1750 Å in the source rest-frame to be 11.8 per pixel compared to 10.5 per WHT pixel measured from the DR7 SDSS spectrum after binning to match the WHT resolution.

Figure 4.26 shows the WHT and SDSS DR5 spectra in the rest-frame, normalised to the continuum. This allows easy comparison of the shape of emission and absorption features and their equivalent widths. The rest-frame equivalent width of the C IV emission line is measured to be 63.1 ± 0.1 Å and 61.9 ± 0.4 Å in the DR5 and DR7 SDSS spectra respectively and 59.2 ± 0.1 Å in the WHT spectrum. The Si IV emission line has an EW measured in the rest-frame as 32.8 ± 0.1 Å and 31.2 ± 0.4 Å for the SDSS spectra and 31.4 ± 0.2 Å in the WHT spectrum. The slight decrease in the EW of C IV emission is not clear in Figure 4.27, which shows the absorption line regions for the C IV and Si IV lines in velocity space. The SDSS DR7 spectra shown in Figure 4.27 has been normalised to the WHT spectra in the region between 1700 and 1750 Å in the rest frame, the greater flux in the WHT observation in this figure is likely to be due to differences in the normalisation region as the shape of the absorption and emission in C IV is very similar. Any changes in the Si IV emission line should be treated tentatively as this region may be affected by the dichroic response, the crossover region occurs within the Si IV absorption trough and is marked in Figure 4.25 by the vertical dashed line.

The WHT spectrum of this object clearly meets the criteria for strong emission lines set out by Arav 1996 as do both DR5 and DR7 versions of the SDSS spectrum. The FWHM of the C IV emission line is

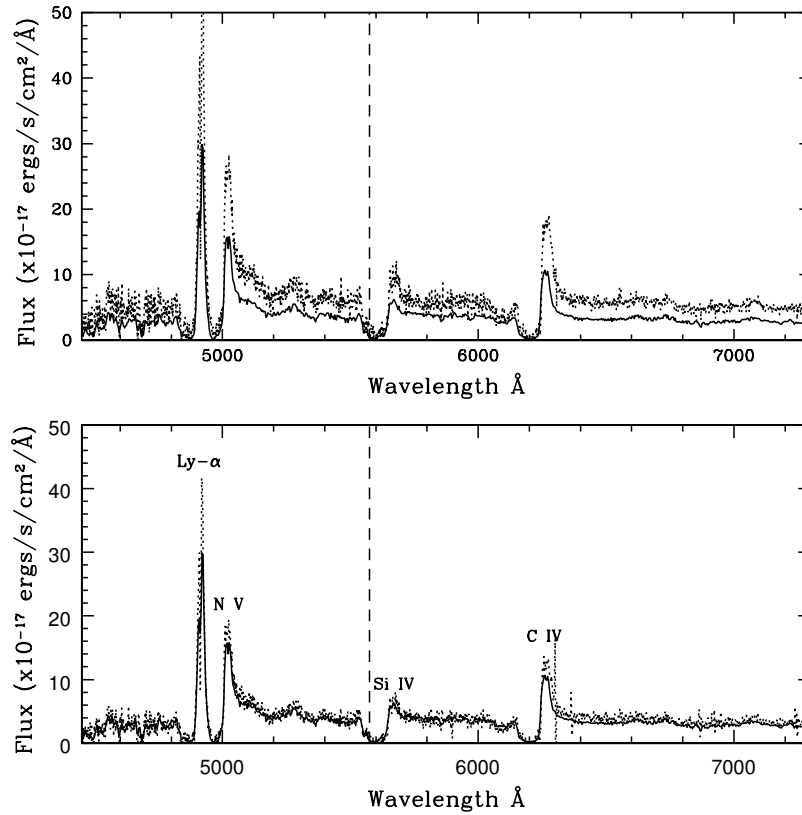


FIGURE 4.25: WHT spectrum of SDSS J162657.47+405848.0 (solid) along with the DR7 (top panel-dotted) and DR5 (bottom panel-dotted) versions of the SDSS spectrum of the same object. The vertical dashed line represents the crossover between the red and blue arms of ISIS at 5575 Å.

measured to be $2345 \pm 25 \text{ km s}^{-1}$, somewhat narrower than the $2750 \pm 75 \text{ km s}^{-1}$ measured from the SDSS DR7 spectrum and the $3110 \pm 20 \text{ km s}^{-1}$ measured from the SDSS DR5 spectrum. All of these values fall below the 3500 km s^{-1} upper limit proposed by Arav 1996. The He II emission line region in the WHT spectrum is well fit by a DR5 composite which has this region scaled by a factor $1.58^{+0.19}_{-0.16}$ compared to 1.26 ± 0.19 in the DR5 SDSS spectrum, suggesting that this object has slightly stronger than average He II emission and that the far-UV resonance lines are likely to contribute significantly to the radiative acceleration of the broad absorption lines.

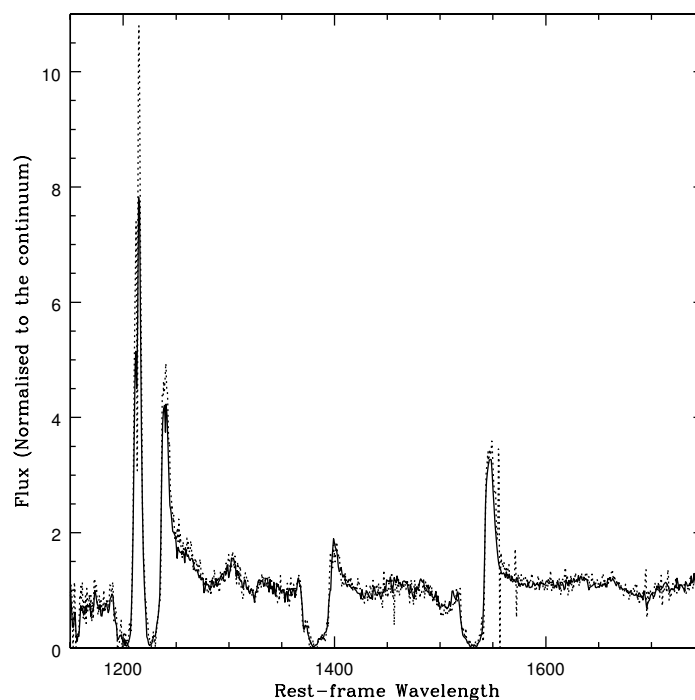


FIGURE 4.26: Continuum normalised spectra of SDSS J162657.47+405848.0 from the SDSS DR5 (dotted) and WHT (solid) observations

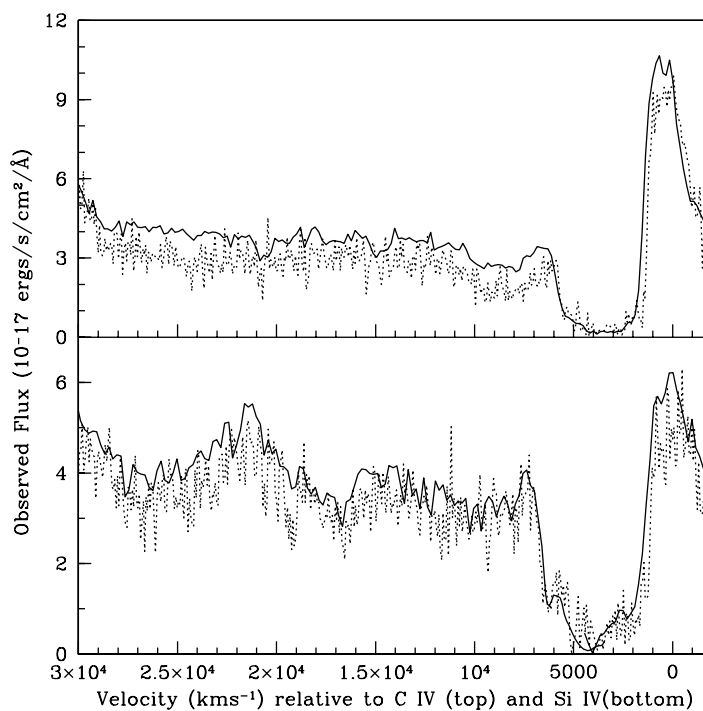


FIGURE 4.27: C IV (top) and Si IV (bottom) absorption troughs in velocity space of SDSS J162657.47+405848.0 from the SDSS DR7 (dotted and scaled) and WHT (solid) observations.

SDSS J170056.85+602639.7

Figure 4.28 shows the WHT spectrum of this object along with the SDSS DR7 spectrum in the top panel and the DR5 spectrum in the lower panel. The SDSS observation was taken on the 1st of June 2000 almost 8 years (2.56 years in the source rest-frame, at redshift 2.12) before the WHT spectrum. The standard star used to flux calibrate the WHT data for this spectrum was observed before the target observations at an airmass of 1.19 and after them at an airmass of 1.31 and the average of the two resulting sensitivity functions used. The airmass of the target observations range from 1.22 to 1.29.

Figure 4.29 shows the continuum normalised WHT and SDSS DR5 spectra in the source rest-frame. This allows easy comparison of the shape and EW of emission and absorption features and clearly shows the higher S/N in the WHT spectrum. The WHT spectrum has $S/N \sim 36.3$ between 1700 and 1750 Å in the source rest frame compared to 17.8 in the same region of the DR7 SDSS spectrum, after binning this spectrum to match the resolution of the WHT spectrum. The equivalent width of the C IV emission line is measured to be 39.3 ± 0.3 Å and 39.1 ± 0.3 Å in the DR5 and DR7 SDSS spectra respectively and 35.1 ± 0.1 Å in the WHT spectrum. The Si IV emission line has an EW measured as 22.1 ± 0.3 Å and 20.5 ± 0.3 Å for the SDSS spectra and 24.8 ± 0.1 Å in the WHT spectrum. The C IV line does appear to be somewhat weaker in the WHT spectrum as does the N V emission line.

The WHT spectrum has increased spectral coverage in the blue end showing clear N V broad absorption along with a narrow remnant of the Ly- α emission line. Other than the additional coverage and greater S/N in the WHT spectrum there is little difference in the shape of the spectra. This is also true for the absorption troughs of C IV and Si IV which are shown in velocity space in Figure 4.30. The SDSS spectra in this figure is the DR7 version and has been scaled to match the flux of the WHT spectrum between 1700 and 1750 Å in the source rest-frame.

The FWHM of the C IV emission line in the WHT spectrum is found to be 6390 ± 70 km s⁻¹, similar to the 6680 ± 270 km s⁻¹ and 6685 ± 250 km s⁻¹ from the SDSS DR7 and DR5 spectra respectively. These

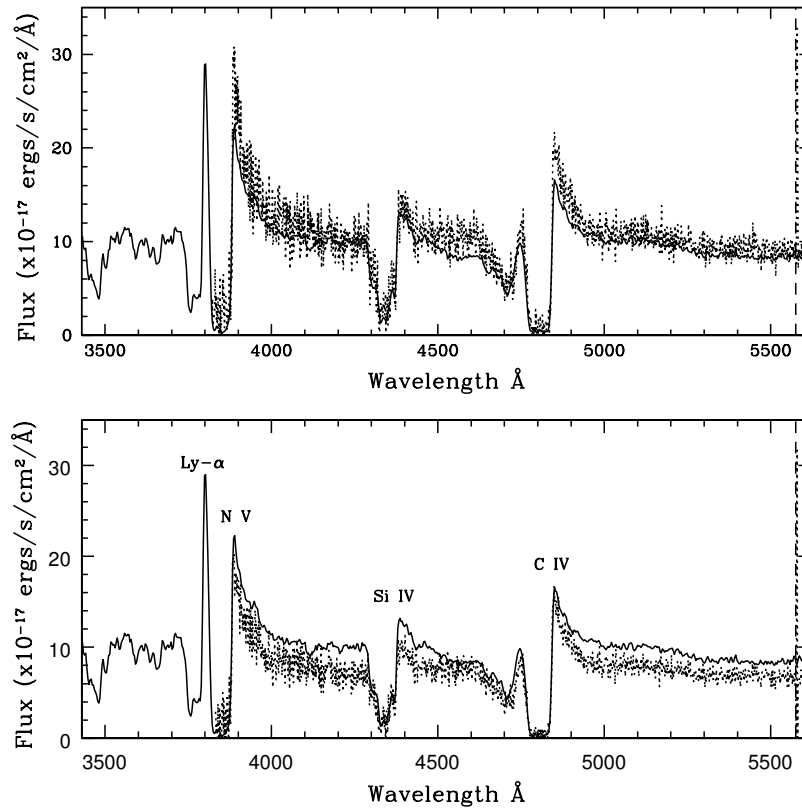


FIGURE 4.28: WHT spectrum of SDSS J170056.85+602639.7 (solid) along with the DR7 (top panel-dotted) and DR5 (bottom panel-dotted) versions of the SDSS spectrum of the same object. The vertical dashed line represents the crossover between the red and blue arms of ISIS at 5575 Å.

values are all well above the 3500 km s^{-1} upper limit proposed by Arav 1996 and whilst the measurements are effected by difficulties in pinpointing the line centre due to absorption there is little doubt that C IV emission in this object is broad. The WHT spectrum of this object fails Arav's test for strong emission lines as the C IV emission line peak flux is less than the continuum flux. The He II emission line region is fit by using a modified composite spectrum scaled in the same way as described in Chapter 3. The scaling factor required for this to be a good fit to the WHT spectrum is $1.16^{+0.15}_{-0.11}$ suggesting the He II emission in this object is fairly close to average strength. The only one of Arav's criteria that is met by the WHT spectrum is the requirement for strong broad N V absorption suggesting the feature in the C IV absorption of this object is produced by a mechanism other than that proposed by Arav.

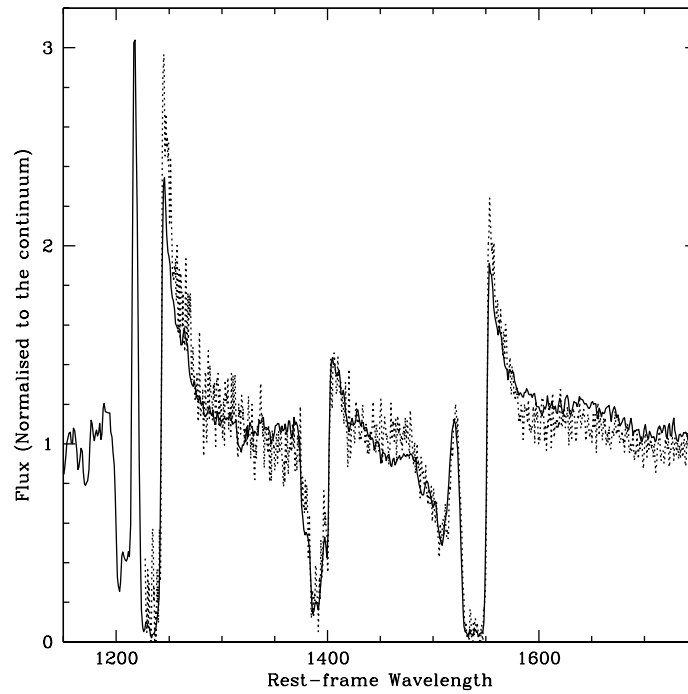


FIGURE 4.29: Continuum normalised spectra of SDSS J170056.85+602639.7 from the SDSS DR5 (dotted) and WHT (solid) observations

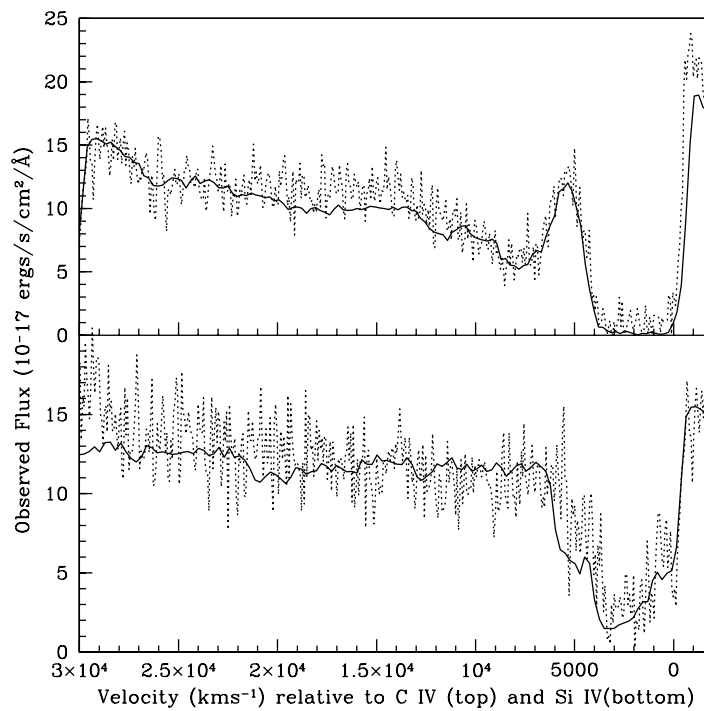


FIGURE 4.30: C IV (top) and Si IV (bottom) absorption troughs in velocity space of SDSS J170056.85+602639.7 from the SDSS DR7 (dotted and scaled) and WHT (solid) observations.

SDSS J164152.30+305851.7

This object was rejected at the single peak stage of our ghost candidate selection as the potential ghost feature is extremely weak and of low S/N in the SDSS spectrum. The WHT spectrum taken on the 27th May 2008 is shown in Figure 4.31 along with the DR7 (top) and DR5 (bottom) versions of the SDSS spectrum obtained on 22nd May 2003, 1.67 years earlier in the source rest-frame at redshift 2.00.

The WHT spectrum has a S/N per pixel of 62.2 measured between 1700 and 1750 Å in the source rest-frame compared to 10.6 from the same region of the DR7 SDSS spectrum, measured after binning the SDSS spectrum to match the resolution of the WHT spectrum. Due to the extremely deep and broad absorption in this object it is extremely difficult to identify the continuum, particularly short-ward of C IV. Uncertainties in the measured continuum strength will result in large errors on equivalent width measurements, which are difficult to quantify and not accounted for. Figure 4.32 shows the WHT and SDSS DR5 spectra in the source rest-frame normalised to the continuum. This allows easier comparison of the shape and EW of absorption and emission features. The C IV EW is measured as 32.4 ± 0.3 Å and 28.9 ± 0.2 Å in the SDSS DR7 and DR5 spectra and 32.7 ± 0.2 Å in the WHT spectrum. The Si IV EW is measured as 16.8 ± 0.2 Å and 25.5 ± 0.3 Å in the SDSS compared with 23.3 ± 0.1 Å in the WHT spectrum.

The C IV and Si IV absorption is shown in Figure 4.33 and shows a complex structure which combined with the relatively low signal to noise ratio in the SDSS observation makes it difficult to pinpoint any change within this absorption. The WHT spectrum shows three clear peaks within the C IV absorption, the highest velocity of which may be due to a cosmic ray or similar noise spike. However, the separation of the other peaks (~ 1500 km s⁻¹) is too large for them to be caused by the C IV doublet and strongly suggests that this is not a ghost feature. The additional coverage in the blue of the WHT spectrum clearly shows N V absorption with two separate absorbing components.

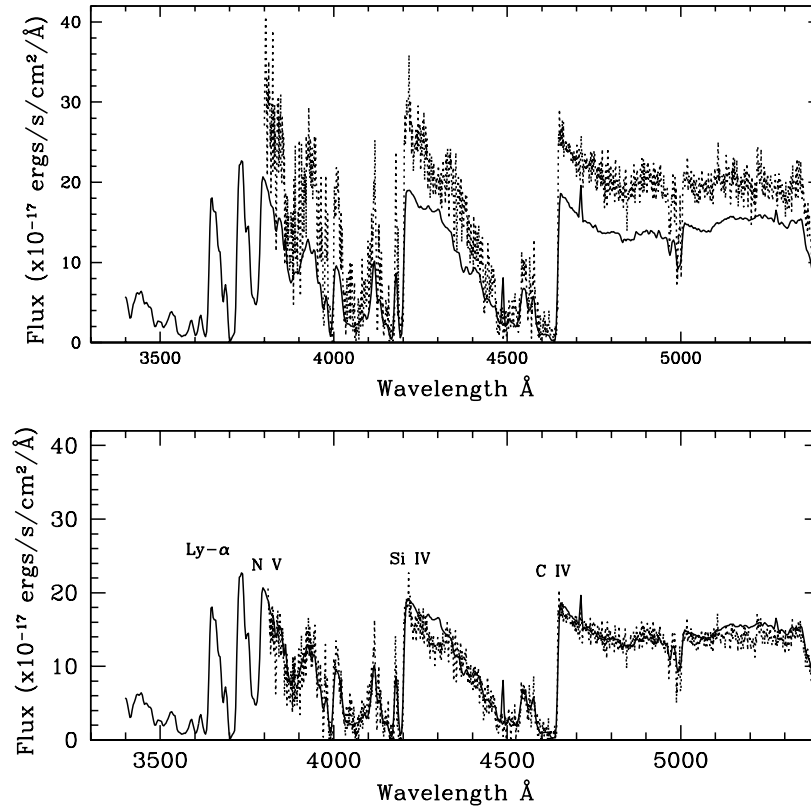


FIGURE 4.31: WHT spectrum of SDSS J164152.30+305851.7 (solid) along with the DR7 (top panel-dotted) and DR5 (bottom panel-dotted) versions of the SDSS spectrum of the same object.

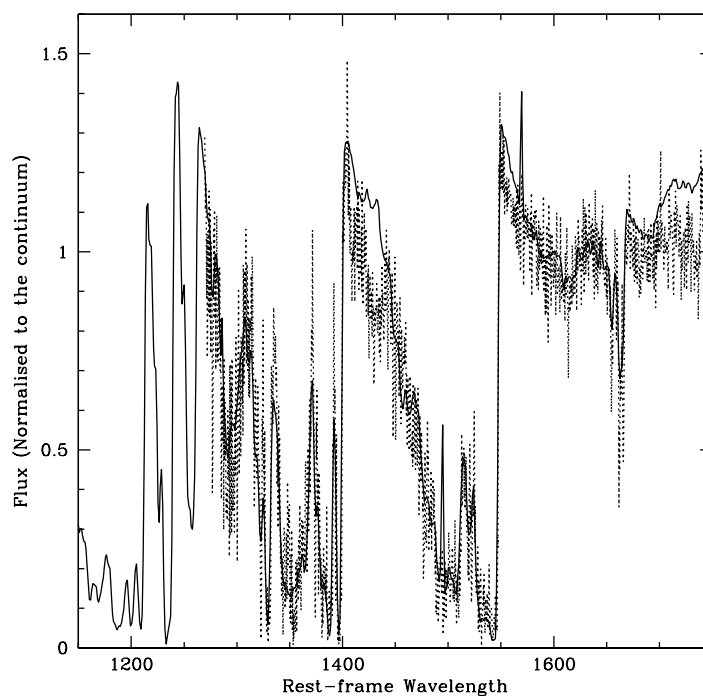


FIGURE 4.32: Continuum normalised spectra of SDSS J164152.30+305851.7 from the SDSS DR5 (dotted) and WHT (solid) observations

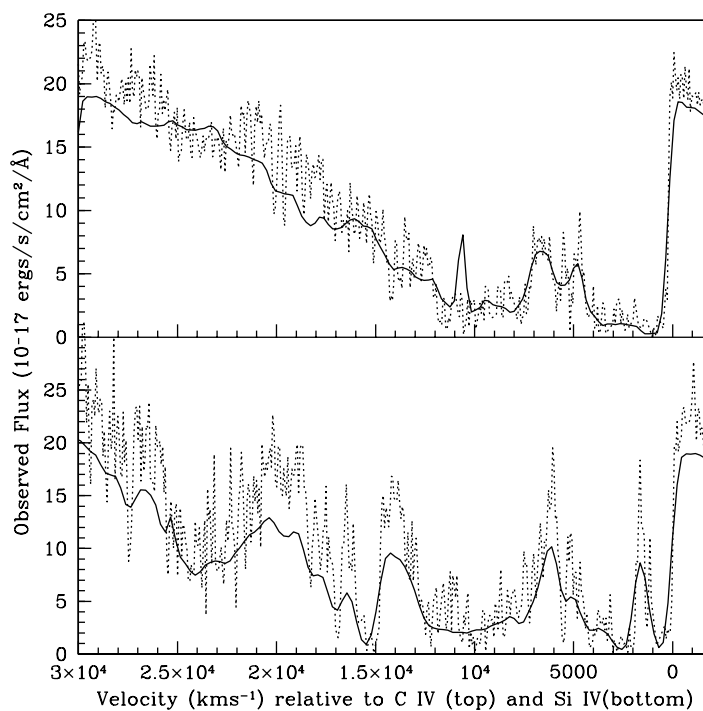


FIGURE 4.33: C IV (top) and Si IV (bottom) absorption troughs in velocity space of SDSS J164152.30+305851.7 from the SDSS DR7 (dotted and scaled) and WHT (solid) observations.

SDSS J212412.60+095923.3

This object was rejected at the single peak stage of the ghost candidate selection due to the identification of two peaks within the ghost zone. However, the WHT spectra shown as the solid line in Figure 4.34 shows a single feature that is much broader than those present in the SDSS spectra. Both the DR7 (top) and DR5 (bottom) versions of the SDSS spectra, which was observed on 11th July 2002, are shown in Figure 4.34. The 5.87 years between observations corresponds to 2.02 years in the source rest frame at a redshift of 1.91.

The WHT spectrum has a S/N per pixel of 14.6 measured between 1700 and 1750 Å in the source rest-frame compared to 9.6 from the same region of the DR7 SDSS spectrum after binning this spectrum to match the WHT resolution. Figure 4.35 shows the WHT and SDSS DR5 spectra in the source rest-frame normalised to the continuum. This allows easier comparison of the shape and EW of absorption and emission features. There is no evidence for a change in the EW of the C IV or Si IV emission lines with the former being measured as 59.3 ± 0.5 Å and 60.9 ± 0.1 Å in the DR7 and DR5 SDSS spectra respectively and 62.0 ± 1.3 Å in the WHT spectrum. The Si IV emission line EW is measured as 39.4 ± 0.7 Å and 46.4 ± 0.1 Å in the SDSS spectra and 47.6 ± 1.2 Å in the WHT spectrum.

The greater coverage of the blue end of the visible spectrum in the WHT reveals strong N V and Ly- α emission lines separated by a strong N V broad absorption line. The absorption due to C IV and Si IV is shown in velocity space in Figure 4.36. The two separate features seen in the SDSS DR7 spectrum at approximately 4000 and 5000 kms^{-1} appear to have been replaced by a single wider and stronger feature by the time the WHT observation was taken. The merging of these two features may be a result of the improved S/N in the WHT spectrum. In any case the single feature makes a much more convincing case to be a ghost feature than those seen in the SDSS spectra. However there is not very much absorption either side of this feature, which would result in it being rejected at the final stage of the ghost selection process on the basis of the WHT spectrum alone.

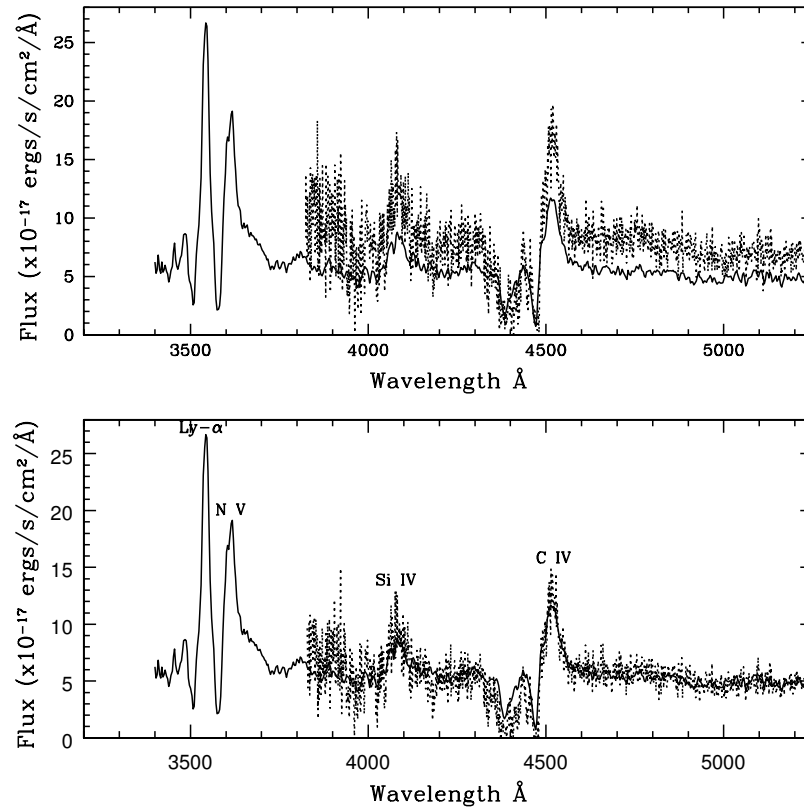


FIGURE 4.34: WHT spectrum of SDSS J212412.60+095923.3 (solid) along with the DR7 (top panel-dotted) and DR5 (bottom panel-dotted) versions of the SDSS spectrum of the same object.

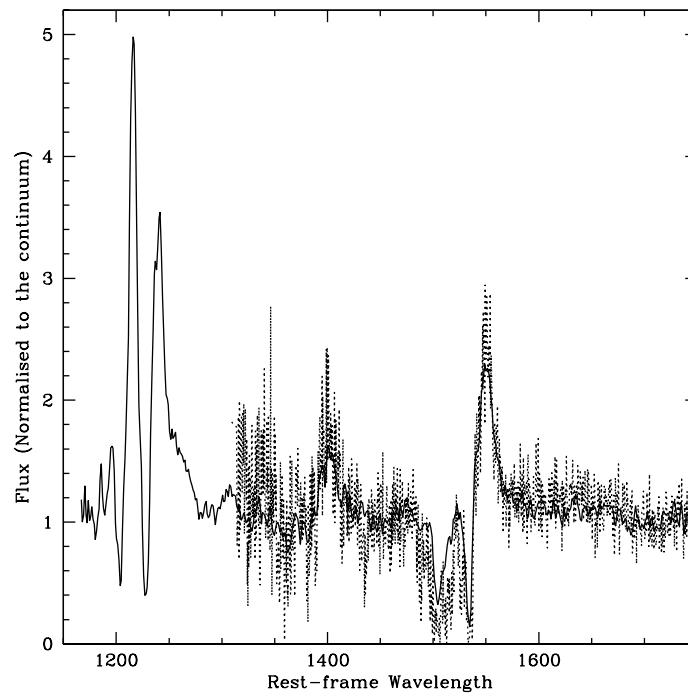


FIGURE 4.35: Continuum normalised spectra of SDSS J212412.60+095923.3 from the SDSS DR5 (dotted) and WHT (solid) observations

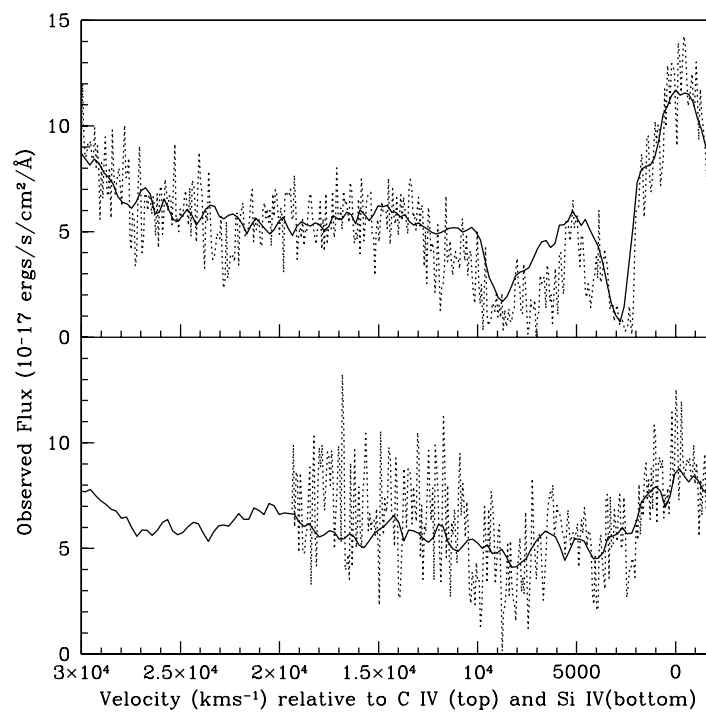


FIGURE 4.36: C IV (top) and Si IV (bottom) absorption troughs in velocity space of SDSS J212412.60+095923.3 from the SDSS DR7 (dotted and scaled) and WHT (solid) observations.

4.3 Gemini Observations and Data Reduction

4.3.1 The Gemini Observatory

The Gemini observatory consists of two 8.1m telescopes, Gemini South situated on the summit of Cerro Pachon in Chile and Gemini North on Mauna Kea, Hawaii. The observations presented here were taken with the Gemini North telescope in queue mode by Gemini staff using the Gemini Multi-Object Spectrograph (GMOS) mounted at the Cassegrain focus. The GMOSs enable long-slit spectroscopy on both the Gemini-North and Gemini-South telescopes and were built as a collaboration of the Astronomy Technology Centre at the ROE, the University of Durham in the UK, and the Herzberg Institute of Astrophysics in Canada.

4.3.2 Sample Selection

As the Gemini telescopes have a significantly larger area than the WHT our targets for these observations are generally fainter and higher redshift objects. This is also influenced by the GMOS detector on Gemini North which is not very sensitive in the blue-end of the visible spectrum. Therefore in order to view the Lyman- α and N V emission we require higher redshift objects than would be the case with the WHT. The candidates were selected due to their high redshift as well as having relatively low signal to noise ratios in their SDSS spectra, allowing Gemini observations to be a significant improvement.

Only those objects for which reasonable spectra could be taken during poor observing conditions were included, leaving the three objects presented within this section. Of these objects, SDSS J115007.65+542737.1 has since been removed from our final candidate list, a consequence of insufficient absorption blue-ward of the ghost feature.

4.3.3 Instrumental Set Up

Queue scheduled observations were taken in the long-slit spectroscopy set up using a 1.5 arc sec slit. The GG455 filter was used for observations of all the targets in the blue end of the spectra along with the B600 (600 lines mm^{-1}) dispersing grating with a blaze wavelength of 461nm. Redder observations were taken of SDSS J115007.65+542737.1 and SDSS J142244.45+382330.6 using the OG515 filter and R400 (400 lines mm^{-1}) grating which has a blaze wavelength of 764nm. The GMOS North detector consists of 3 CCDs each 2048x4068 13.5 micron pixels separated by 0.5mm. Dark current in these CCDs is negligible for our observations. Due to the presence of gaps within the detectors each target was observed using two different central wavelengths shifted by approximately 10 \AA for each observational set up, in order to ensure no gaps are present in the final spectrum.

4.3.4 Observed data

The list of target observations is given in Table 4.2 along with the filter and disperser set-up, central wavelength, airmass and exposure time. These observations were taken over a number of nights during March 2008 as part of the 2008A semester. In addition to the target observations Gemini also provide calibration frames. These include a bias frame taken on the 24th Feb 2008, lamp flats observed either directly before or directly after the target observations, using identical instrumental set-up, as well as observations of the standard star HZ44 using both instrumental set-ups. The standard was observed on the 27th March at an airmass of 1.689 using the R400 grating and on the 28th March at an airmass of 1.641 using the B600 grating. It is not ideal to have standard observations observed on different nights to the target observations or at such high airmass and this may limit the accuracy of the flux calibration process.

4.3.5 Data Reduction

Gemini provide an **IRAF** package for the reduction of long-slit GMOS data (<http://www.gemini.edu/sciops/data-and-results/processing-software>). I have used version 1.10 of this package for some of the data reduction

Table 4.2: GMOS observations

Target	Filter	Disperser	Exposure Time (s)	Central Wavelength(\AA)	Airmass
SDSS085104.05+051539.8	GG455	B600	600	5700	1.035
SDSS085104.05+051539.8	GG455	B600	600	5700	1.034
SDSS085104.05+051539.8	GG455	B600	600	5700	1.034
SDSS085104.05+051539.8	GG455	B600	600	5800	1.038
SDSS085104.05+051539.8	GG455	B600	600	5800	1.044
SDSS085104.05+051539.8	GG455	B600	600	5800	1.052
SDSS115007.65+542737.1	GG455	B600	600	5700	1.242
SDSS115007.65+542737.1	GG455	B600	600	5700	1.253
SDSS115007.65+542737.1	GG455	B600	600	5700	1.267
SDSS115007.65+542737.1	GG455	B600	600	5800	1.286
SDSS115007.65+542737.1	GG455	B600	600	5800	1.305
SDSS115007.65+542737.1	GG455	B600	600	5800	1.326
SDSS115007.65+542737.1	OG515	R400	600	7300	1.214
SDSS115007.65+542737.1	OG515	R400	600	7300	1.214
SDSS115007.65+542737.1	OG515	R400	600	7300	1.215
SDSS115007.65+542737.1	OG515	R400	600	7400	1.219
SDSS115007.65+542737.1	OG515	R400	600	7400	1.224
SDSS115007.65+542737.1	OG515	R400	600	7400	1.231
SDSS142244.45+382330.6	GG455	B600	600	5700	1.055
SDSS142244.45+382330.6	GG455	B600	600	5700	1.057
SDSS142244.45+382330.6	GG455	B600	600	5700	1.061
SDSS142244.45+382330.6	OG515	R400	600	7300	1.055
SDSS142244.45+382330.6	OG515	R400	600	7300	1.055
SDSS142244.45+382330.6	OG515	R400	600	7300	1.056
SDSS142244.45+382330.6	OG515	R400	600	7400	1.060
SDSS142244.45+382330.6	OG515	R400	600	7400	1.065
SDSS142244.45+382330.6	OG515	R400	600	7400	1.072

but due to problems with the wavelength calibration part some data reduction steps use different **IRAF** packages. All observations and calibration data were processed using the *gprepare* task which checks the header files to ensure they have all of the relevant keywords necessary for the rest of the data reduction. *gprepare* also adds a mask definition file, which marks the position of the slit on the detector preparing the files for further reduction routines within the gemini package.

Chip Gaps

The reason that Gemini data require a specific data reduction package is that the data contains gaps which are present due to the detector being split into 3 CCDs, simply combining them will result in discontinuities in bias and flat frames and could lead to calibration problems. The *gmosaic* routine stitches the 3 CCDs together into a single image appropriately accounting for the chip gaps to ensure that the process does not introduce discontinuities in the spectra.

Debiasing and flat-fielding

The *gbias* routine takes the bias frame after it has been through *gprepare* and *gmosaic* and uses it to produce a single continuous bias image. The unprocessed bias images provided with the Gemini data are shown in Figures 4.37 to 4.39. The mean bias value in the three sections is quite different, it is 752.5 ± 2.1 ADU for the first, 611.3 ± 0.6 ADU for the second and 373.8 ± 0.7 ADU for the third section. The *gbias* routine combines the three images into a single bias frame for use with *gsreduce* to bias correct all of the science frames.

gsflat takes a flat-field image, like that shown in Figure 4.40 and uses it to produce a flat-field response such as that shown in Figure 4.41 appropriately accounting for the spectrum of the lamp used to produce the flat-field. The *gsreduce* routine is called using the appropriate bias and flat-field response images to produce debiased and flat-field corrected 2-d spectra in a single image with no gaps. The package does this by removing the bias level from the images after they have been processed by *gprepare*, and then

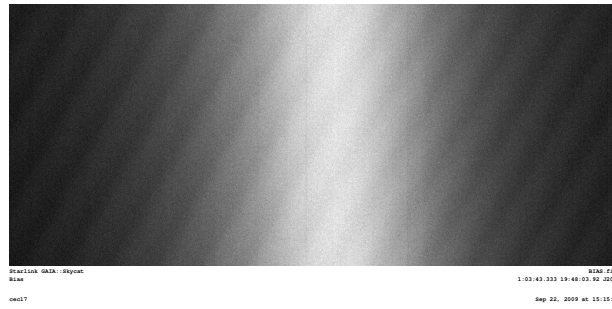


FIGURE 4.37: The first section of the Gemini bias image.

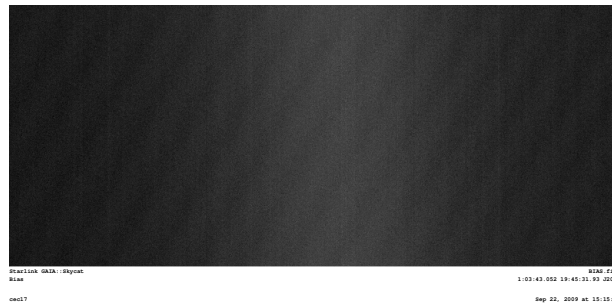


FIGURE 4.38: The second section of the Gemini bias image.

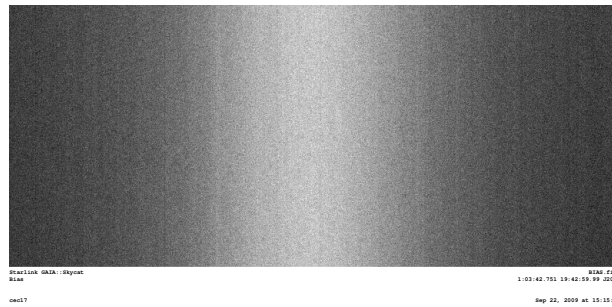


FIGURE 4.39: The third section of the Gemini bias image.

dividing the remaining image by the flat-field response.

Further data reduction steps using the *gemini IRAF* package encountered problems, however 1-d spectra can be extracted from these 2-d spectra in the same manner as for the WHT observations, as the 2d images at this stage have been appropriately processed to remove the effects of CCD noise and variable illumination.

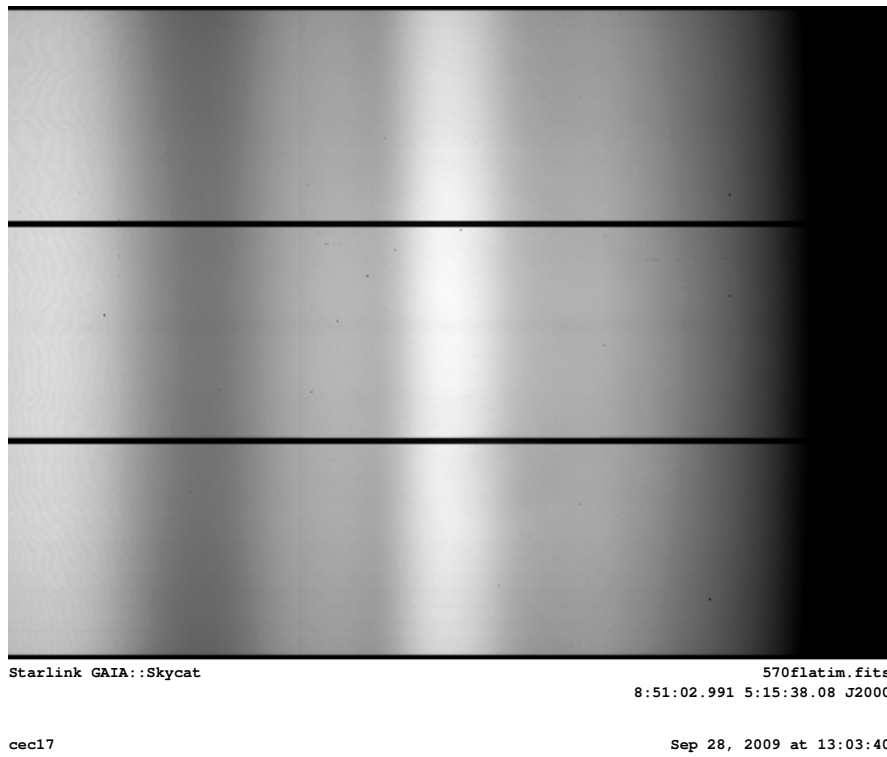


FIGURE 4.40: A Gemini flat-field image.

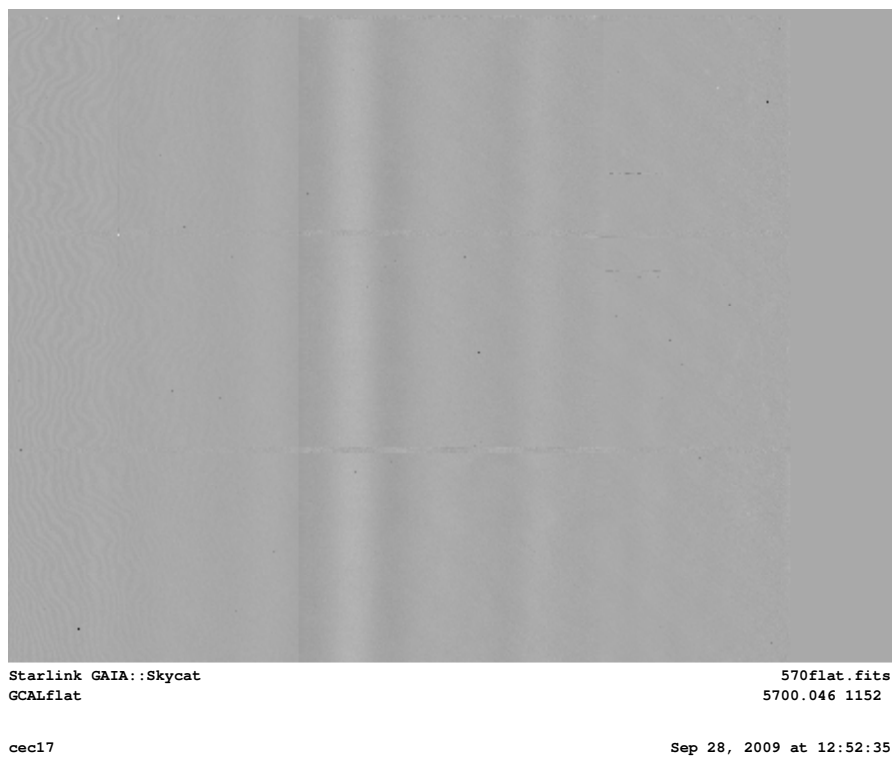


FIGURE 4.41: A Gemini flat-field response image produced by *gsflat*.

4.3.6 Extracting 1-d spectra

The *apall* task was used to extract spectra from the bias and flat-field corrected observations as well as the arc lamp and standard star spectra. An aperture and background region are fit to the 2-d image and then traced along the chip in exactly the same way as for the WHT observations. The spectra are extracted from these apertures along with variance spectra for the target observations, and the background region subtracted from the observed spectra of the targets and standards, as determined from a linear fit between background regions either side of the object spectrum. The arc spectra do not require absolute fluxes and as the spectra covers the entire chip, no background subtraction is used when extracting arc spectra.

Wavelength Calibration

The *identify* task is used on the extracted CuAr arc spectra in order to tag the emission lines with their wavelengths. An example arc spectrum with some major emission lines marked is shown in Figure 4.42. This allows the routine to fit a simple function, typically almost linear and in all these cases fit with a 2nd order cubic spline, representing the wavelength as a function of position. This function is then used with the *dispcor* routine to wavelength calibrate the target and standard spectra.

Flux Calibration and Extinction Correction

The standard observation provided with the Gemini data was taken at an airmass of above 1.6 which is substantially higher than the airmass of the targets and may lead to inaccuracies in the flux calibration. Sensitivity functions are produced using the *standard* and *sensfunc* routines. The *standard* routine takes the wavelength calibrated standard spectra and uses tabulated fluxes for the star to produce a series of sensitivity points. These points are passed on to the *sensfunc* routine which fits a simple function to them producing a continuous sensitivity function. The derived sensitivity function for the R400 disperser and OG515 filter is shown in Figure 4.43. The sensitivity function for the B600 disperser and GG455 filter is shown in Figure 4.44.

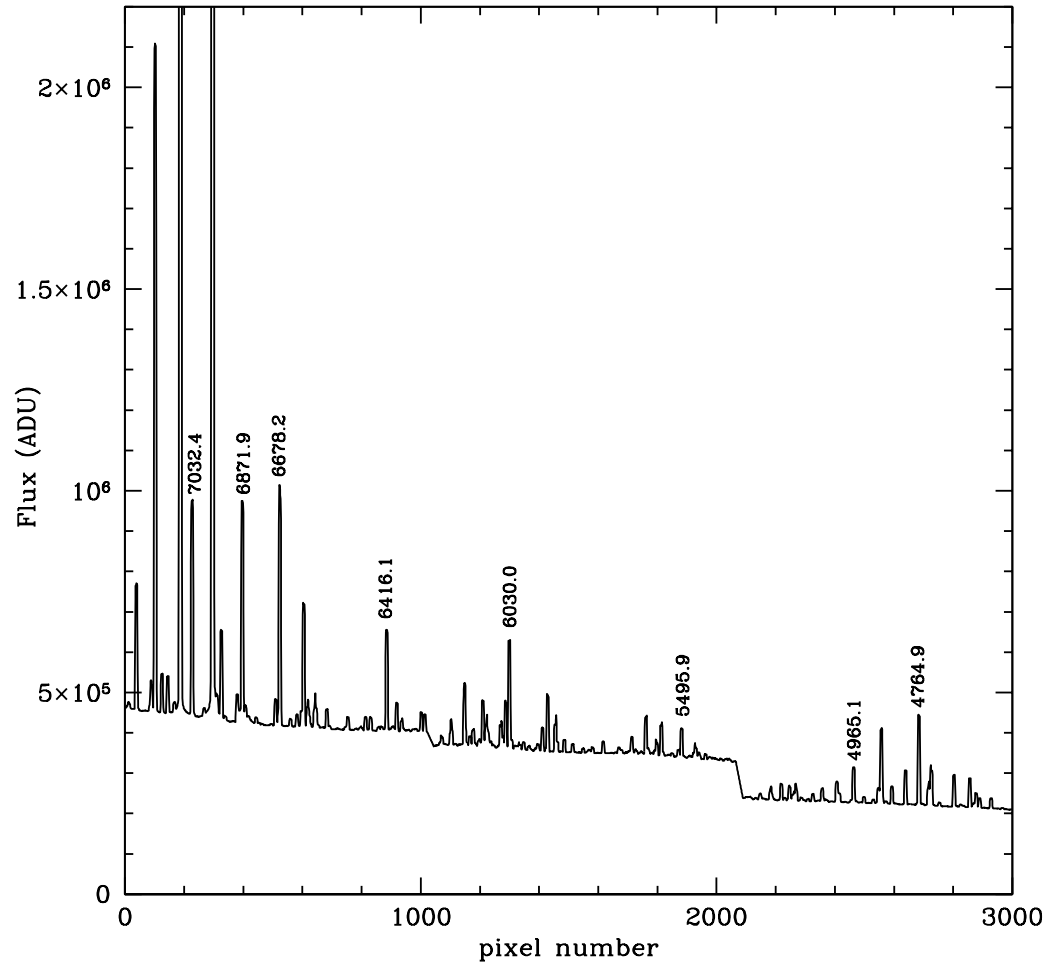


FIGURE 4.42: An Arc Lamp spectrum produced using the B600 grating and GG455 filter

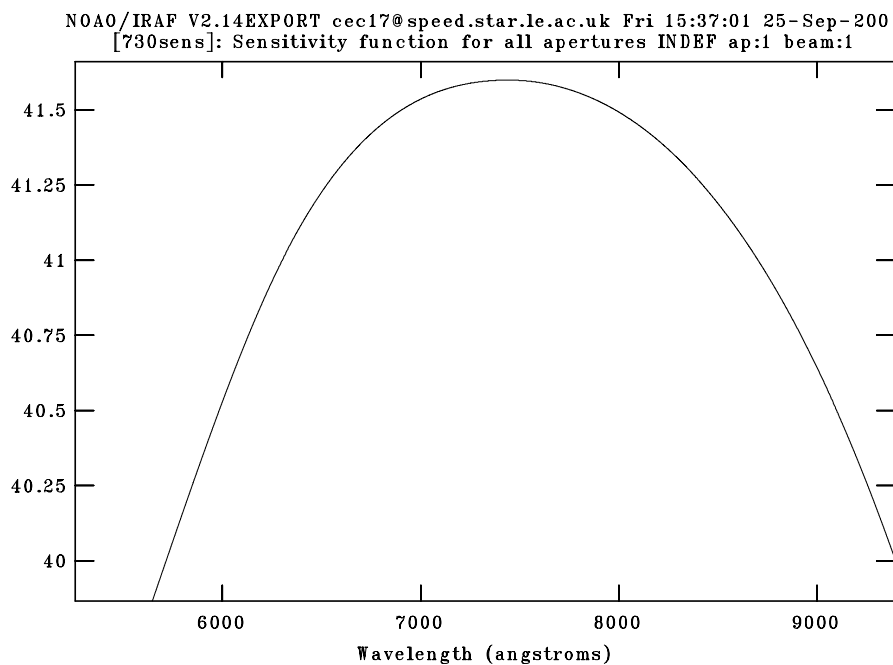


FIGURE 4.43: GMOS sensitivity function using the R400 grating and OG515 filter (in units of $2.5\text{Log}_{10}[\text{counts/s}/\text{\AA}/\text{ergs/cm}^2/\text{s}/\text{\AA}]$).

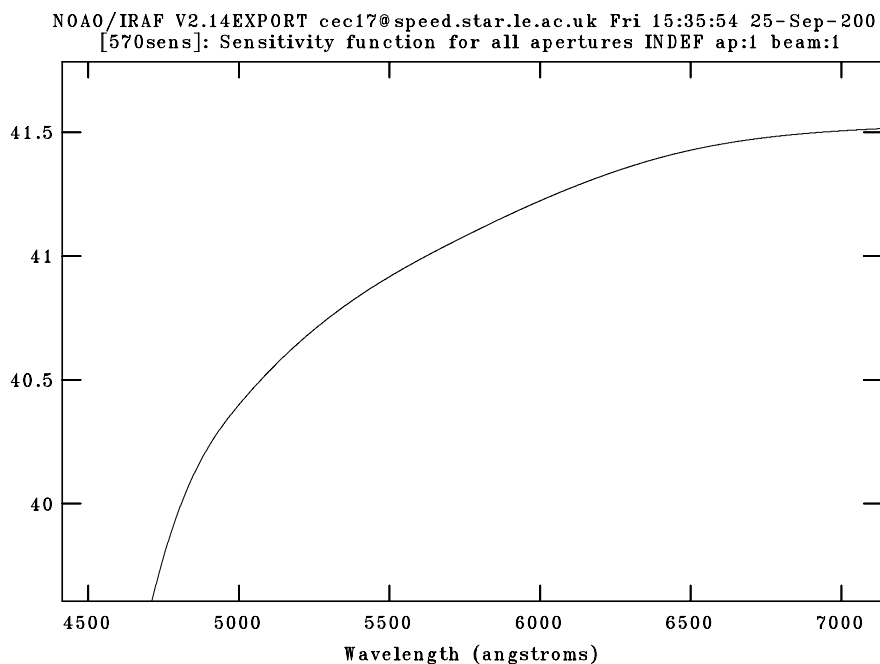


FIGURE 4.44: GMOS sensitivity function using the B600 grating and GG455 filter (in units of $2.5\text{Log}_{10}[\text{counts/s}/\text{\AA}/\text{ergs/cm}^2/\text{s}/\text{\AA}]$).

4.3.7 Object Spectra

Gemini spectra are indicated as solid lines in the following section with the SDSS DR5 (lower panel) and DR7 (upper panel) spectra indicated by dotted lines. All spectra are shown in the observed frame and the major emission lines are labelled (lower panel). The C IV and Si IV absorption regions are also shown in velocity space, and continuum normalised Gemini and SDSS spectra are shown in the source rest-frame. Arav's criteria are tested and the results presented along with measurements of the C IV and Si IV EW.

SDSS J085104.05+051539.8

Figure 4.45 shows the Gemini spectra observed at an airmass of approximately 1.04 on the 24th of March 2008 along with both the DR5 (bottom) and DR7 (top) versions of the SDSS spectrum observed on the 31st of January 2003. The source has a redshift of 3.21 so the 5.15 years between observations corresponds to 1.22 years in the source rest-frame.

The S/N of the SDSS DR7 spectrum is 15.5 per pixel measured between 1580 and 1620 Å in the source rest-frame (as the Gemini spectra does not cover 1700 to 1750 Å). As the Gemini spectrum is slightly higher resolution it is binned into the same resolution as the SDSS spectrum to compare the S/N which is then measured to be 50.9 per SDSS pixel. Other than this increased S/N there are very few significant differences between the shapes of the SDSS and Gemini spectra. This is shown more effectively by Figure 4.46 which gives the Gemini and SDSS DR5 spectra in the source rest-frame normalised by dividing through by a reddened power law fit to the continuum. The EW of the C IV emission line is measured to be 52.6 ± 0.3 Å in the Gemini spectrum compared to 56.5 ± 0.3 Å and 53.8 ± 0.3 Å in the SDSS DR5 and DR7 spectra respectively. The Si IV emission line has EW of 43.7 ± 0.3 Å in the Gemini spectrum and 45.2 ± 0.4 Å and 42.2 ± 0.4 Å in the SDSS spectra.

Figure 4.47 shows the absorption troughs of the C IV and Si IV lines in velocity space, the SDSS spectra in this plot is the DR7 version and has been scaled to match the flux of the Gemini spectrum between 1580

and 1620 \AA in the rest-frame. This plot shows some evidence for stronger Si IV absorption between 3000 and 10000 km s^{-1} which is not reflected in the C IV absorption at these velocities. The C IV absorption is however stronger between 14000 and 18000 km s^{-1} as well as between 22000 and 24000 km s^{-1} . These additional troughs would have resulted in this object being rejected at the single peak stage of the ghost selection process, however the ghost feature in this object and the absorption directly surrounding it remain essentially unchanged.

The red side of the C IV emission line in the Gemini spectrum is fit with a Gaussian profile. This fit gives a FWHM of $3770 \pm 180 \text{ km s}^{-1}$, slightly lower than the $4340 \pm 180 \text{ km s}^{-1}$ and $4030 \pm 190 \text{ km s}^{-1}$ from the SDSS DR5 and DR7 spectra, but still larger than the 3500 km s^{-1} upper limit proposed by Arav. The Ly- α emission in the Gemini spectrum is strong enough for this object to pass the test for strong emission lines despite relatively weak C IV emission. The He II emission line region is well fit to the same region of a composite spectrum when the composite is multiplied by a factor 0.49 ± 0.21 . This weak He II emission suggests that the far-UV continuum may be similarly weak resulting in the resonance lines in this region contributing little to the radiative acceleration of the broad absorption lines as is required by Arav's models.

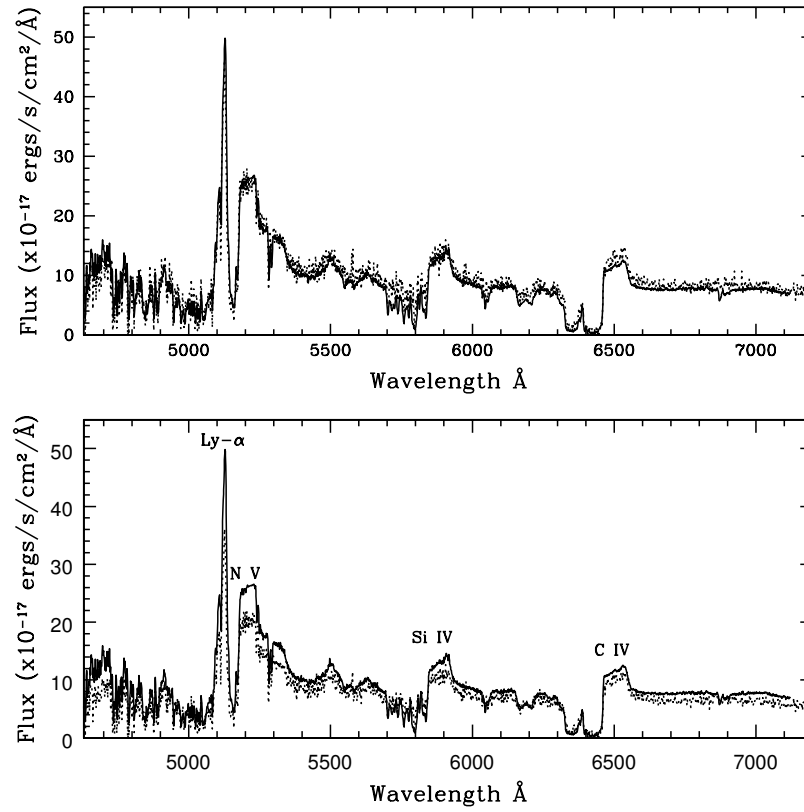


FIGURE 4.45: Gemini spectrum of SDSS J085104.05+051539.8 (both panels solid) along with SDSS spectrum of the same object (both dashed DR5-bottom panel. DR7-top panel).

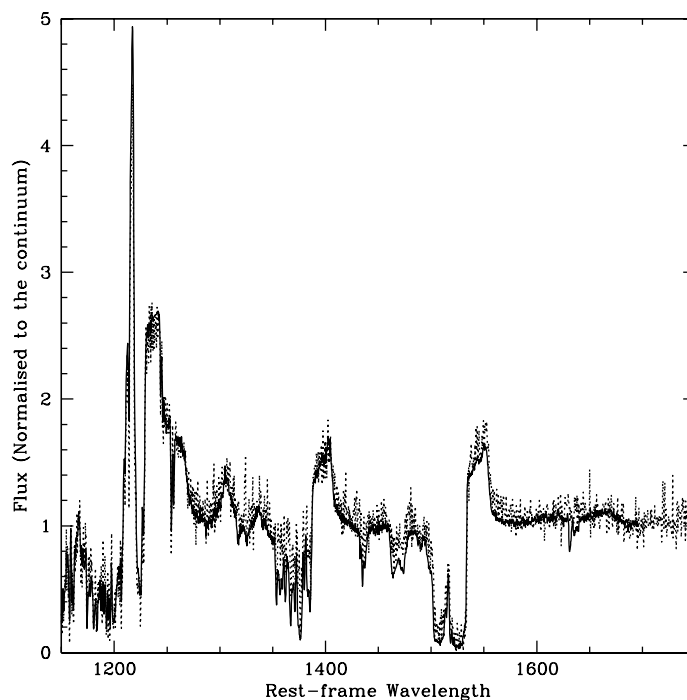


FIGURE 4.46: Continuum normalised Gemini (solid) and SDSS DR5 (dotted) spectra of SDSS J085104.05+051539.8

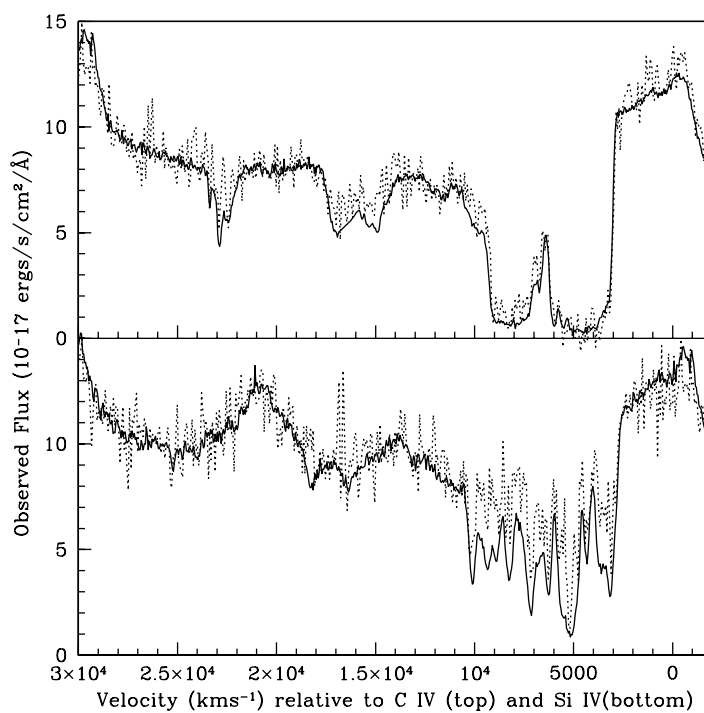


FIGURE 4.47: C IV (top) and Si IV (bottom) absorption in velocity space for the Gemini (solid) and SDSS DR7 (dotted and scaled) spectra of SDSS J085104.05+051539.8.

SDSS J115007.65+542737.1

The Gemini spectrum of this object was observed at an airmass of 1.22 on the 16th of March 2008 and is shown in Figure 4.48 along with the DR5 (bottom) and DR7 (top) versions of the SDSS spectrum observed on the 30th of April 2003. The 4.88 years between observations corresponds to 1.08 years in the source rest-frame at redshift 3.52.

The S/N of the Gemini observation is measured between 1705 and 1750 Å in the source rest-frame, since this spectrum is absorbed below 1705 Å. The measured S/N is 15.0 per pixel compared to 6.3 per pixel in the same region of the SDSS DR5 spectrum. The Gemini spectrum is brighter than both the SDSS reductions but shows little difference in the spectral shape (the absorption at ~ 7600 Å is due to problems with the removal of the Oxygen A-band sky line and is also present in the Gemini spectrum of SDSS J142244.45+352330.6 (Figure 4.51)). In order to compare the shape of the spectra the Gemini and SDSS DR5 spectra are shown in Figure 4.49 in the source rest-frame and normalised to a reddened power law fit to the continuum. The EW of the C IV emission line is measured to be 66.5 ± 0.4 Å in the Gemini spectrum compared to 71.5 ± 0.4 Å and 69.6 ± 0.4 Å in the SDSS DR5 and DR7 spectra respectively. The Si IV emission line has EW of 40.5 ± 0.2 Å in the Gemini spectrum and 47.1 ± 0.4 Å and 45.0 ± 0.4 Å in the SDSS spectra.

Figure 4.50 shows the C IV and Si IV absorption troughs in velocity space. The SDSS spectrum in this figure is a scaled version of the DR7 reduction matched to the Gemini flux between 1705 and 1750 Å in the source rest-frame. There is little change in either the C IV or Si IV absorption. The Gemini spectrum confirms that the multiple features seen in the Si IV absorption are real and are not due to noise within the SDSS spectrum.

The red side of the C IV emission line is fit with a Gaussian in the same manner as for previous objects. These fits provide C IV FWHM measurements of 5390 ± 180 km s⁻¹ in the Gemini spectrum, slightly lower than the 5510 ± 190 km s⁻¹ from the SDSS DR7 spectra but still significantly broader than the proposed

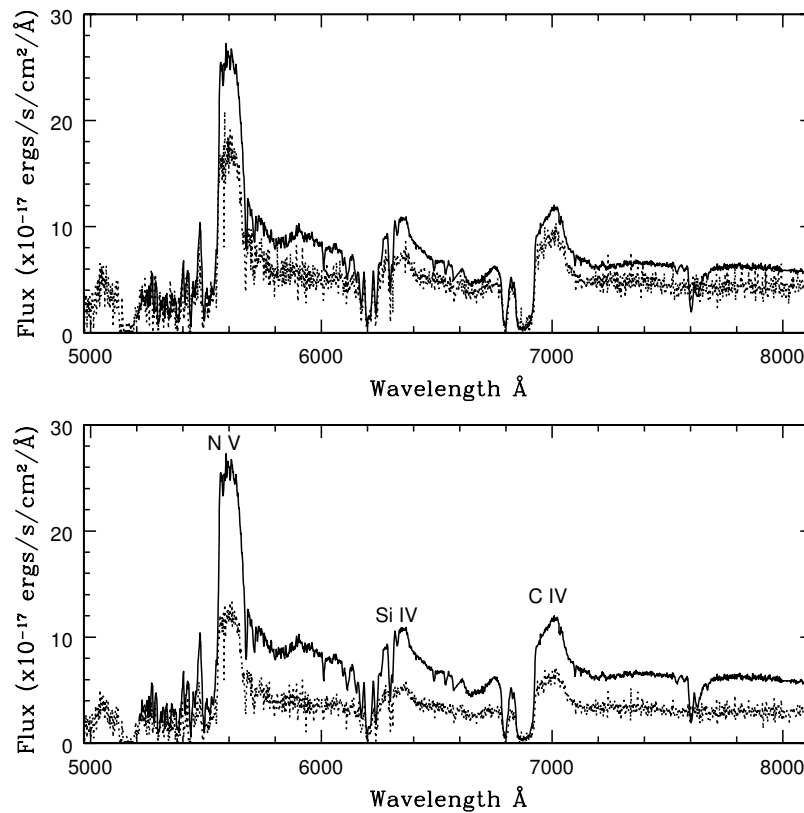


FIGURE 4.48: Gemini spectrum of SDSS J115007.65+542737.1 (both panels solid) along with SDSS spectrum of the same object (both dashed DR5-bottom panel. DR7-top panel).

3500 km s^{-1} limit.

The C IV emission line peak in the Gemini spectrum is $98 \pm 12\%$ of the continuum flux, so it is not clear whether or not it meets Arav's criteria for strong emission lines. This criteria is met by the SDSS DR5 spectrum. The He II emission strength is measured in the same way as for the Gemini spectrum of SDSS J085104.05+051539.8 and found to be 0.47 ± 0.20 times the strength in the composite spectrum, suggesting the far-UV continuum in this object is relatively weak.

The failure of this spectrum to meet two of Arav's criteria combined with the relatively narrow band of absorption blueward of the potential ghost feature strongly suggest that this feature was not created by radiative acceleration and that it is more likely to be a chance alignment of two separate absorbing outflows.

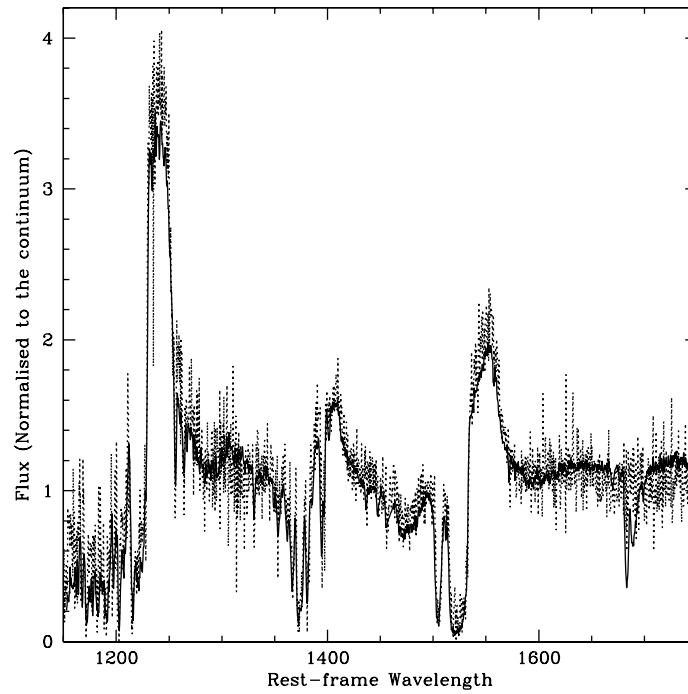


FIGURE 4.49: Continuum normalised Gemini (solid) and SDSS DR5 (dotted) spectra of SDSS J115007.65+542737.1

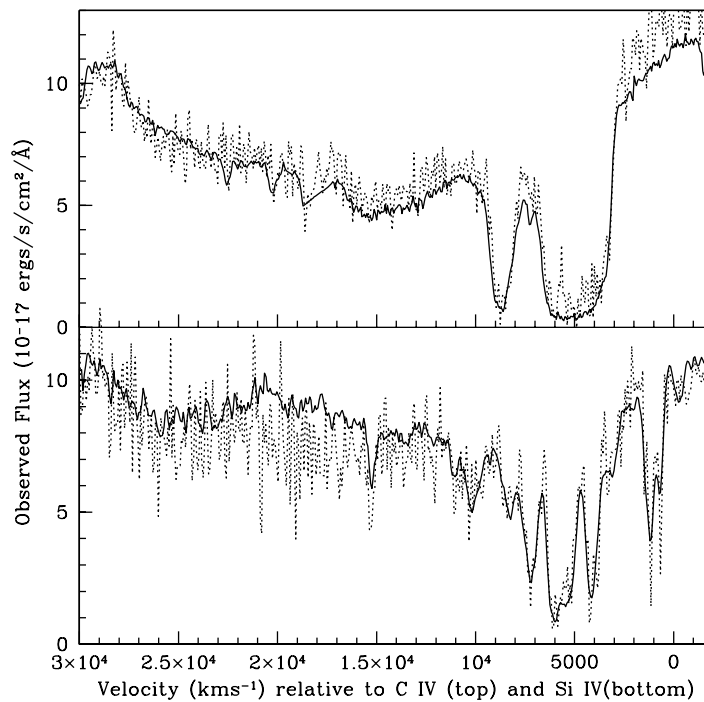


FIGURE 4.50: C IV (top) and Si IV (bottom) absorption in velocity space for the Gemini (solid) and SDSS DR7 (dotted and scaled) spectra of SDSS J115007.65+542737.1.

SDSS J142244.45+382330.6

Figure 4.51 shows both the DR5 (bottom) and DR7 (top) versions of the SDSS spectrum of this object observed on the 20th of March 2004 along with the follow up Gemini spectrum. The Gemini observations were taken on the 26th of March 2008 at an airmass of 1.06. The 4 years and 6 days between observations corresponds to 0.85 years in the source rest-frame at redshift 3.73.

The Gemini spectra has a S/N ratio of 26.8 per SDSS pixel measured between 1700 and 1750 Å in the source rest-frame after binning into the same resolution as the SDSS DR7 spectrum which has S/N of 5.7 per pixel. As mentioned with regard to the previous object the absorption at ~ 7600 Å is due to problems with sky line subtraction and is not intrinsic to the object. The Gemini spectrum is very similar to the SDSS spectra other than a change in the N v emission line which appears to be around 30% brighter at its peak when compared to the continuum. This increased N v strength is clearly visible in Figure 4.52 which shows the Gemini and SDSS DR5 spectra normalised to a continuum fit in the source rest-frame.

Figure 4.53 shows the C IV and Si IV absorption troughs in velocity space for the Gemini spectrum and a version of the DR7 SDSS spectrum scaled to match the Gemini flux between 1700 and 1750 Å in the source rest-frame. The lowest velocity Si IV absorption trough seems to have disappeared. There is little change to the rest of the Si IV absorption this change is likely to be due to the absorber moving out of the line of sight. The rest-frame EW of the C IV emission line is 58.3 ± 0.4 Å in the Gemini spectrum compared to 55.9 ± 0.4 Å in SDSS DR5 and 55.0 ± 0.5 Å in SDSS DR7. Si IV rest-frame EWs are 38.0 ± 0.3 Å and 37.5 ± 0.3 Å in the DR5 and DR7 SDSS spectra and 27.2 ± 0.3 Å in the Gemini spectrum.

The FWHM of C IV in the Gemini spectrum is measured by fitting a Gaussian to the red side of the emission and found to be 3280 ± 120 km s⁻¹ which is larger than the 2950 ± 130 km s⁻¹ found from the DR7 spectrum but still below the 3500 km s⁻¹ limit proposed by Arav. The emission lines meet the criteria for strong emission in both the Gemini and SDSS spectra and N v absorption is clearly present. The He II emission line is fit in the same manner as for the other objects and found to be 0.75 ± 0.24 times the strength

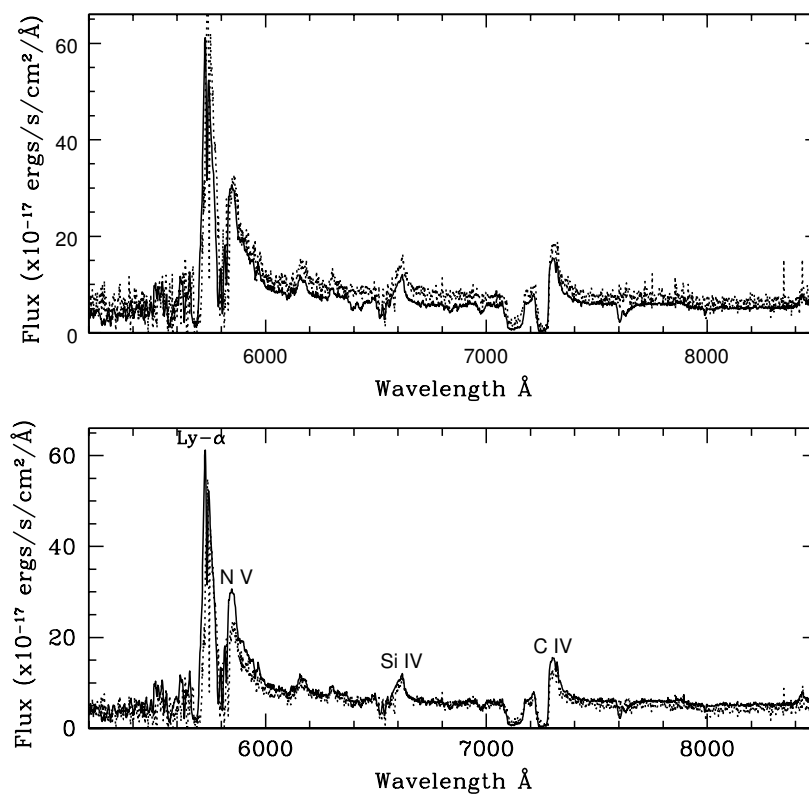


FIGURE 4.51: Gemini spectrum of SDSS J142244.45+352330.6 (both panels solid) along with SDSS spectrum of the same object (both dashed DR5-bottom panel. DR7-top panel).

of the emission in the composite. This is very marginal evidence for weaker He II but does suggest that the far-UV continuum is unlikely to be unusually strong. The Gemini spectrum meets all of the criteria making this object one of the more convincing ghost candidates.

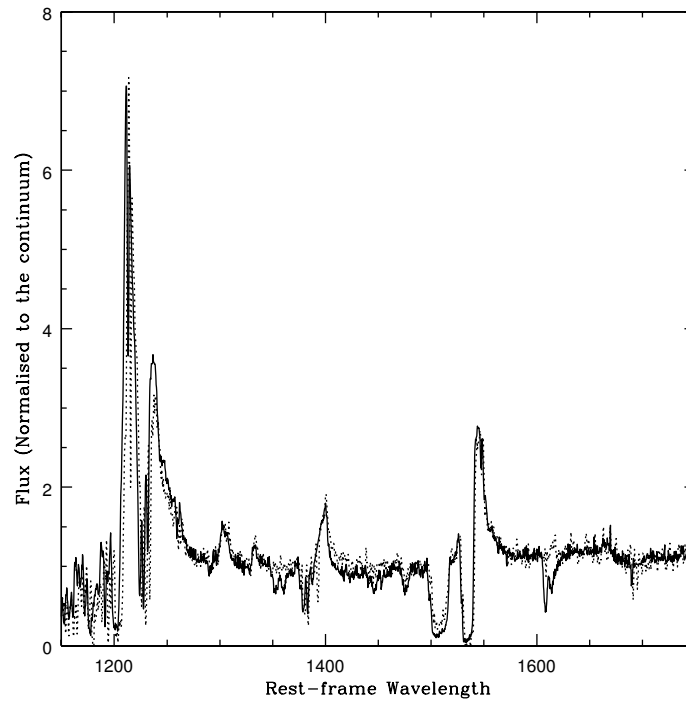


FIGURE 4.52: Continuum normalised Gemini (solid) and SDSS DR5 (dotted) spectra of SDSS J142244.45+352330.6

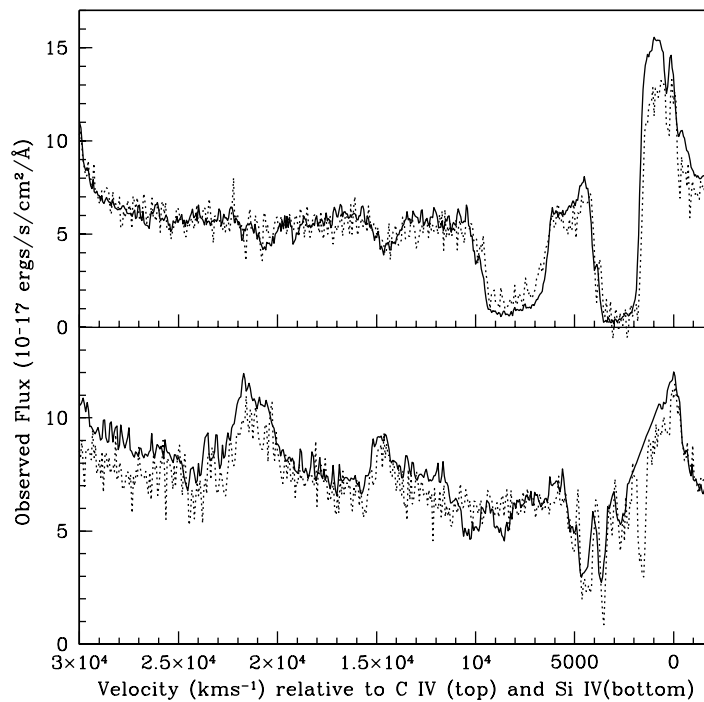


FIGURE 4.53: C IV (top) and Si IV (bottom) absorption in velocity space for the Gemini (solid) and SDSS DR7 (dotted and scaled) spectra of SDSS J142244.45+352330.6.

4.4 Ghosts and Arav's Criteria

After inspecting both SDSS and the follow up spectra of the objects presented in this Chapter I would conclude, based purely on the C IV absorption trough that 6 of these objects remain good ghost candidates. These 6 objects are SDSS 1018+5440, SDSS 1147+1532, SDSS 1626+4058 and SDSS 1700+6026 observed with the WHT and SDSS 0851+0515 and SDSS 1422+3823 observed using Gemini North. SDSS J2124+0959 shows two separate peaks within the absorption in its SDSS spectra, however the WHT follow up observation shows only a single peak. The improved S/N ratio in the WHT spectrum of SDSS J1344+4834 reveals complex multi-component absorption suggesting that the candidate ghost feature is likely to be due to a chance alignment of absorbing components. SDSSJ 1138+3517 is clearly not a good ghost candidate as the WHT spectrum shows no ghost feature. SDSS 1641+3058 and SDSS 1150+5427 were not considered to be worth a place in the GCFC and the follow up spectra do not improve their case for inclusion.

Arav's criteria have been tested for all of the objects presented in this chapter and the results are summarised in Table 4.3. In this section I will discuss the results of these tests for the 6 ghost candidates mentioned above.

SDSS 1700+6026 fails to meet the criteria for strong emission lines based on the WHT spectrum with both N V and C IV peak fluxes falling below the required level. In addition the C IV emission in this object has a FWHM far above the 3500 km s^{-1} limit proposed by Arav. I would therefore suggest that the feature in this object is unlikely to be produced by the method proposed by Arav 1996.

SDSS 1018+5440 has C IV FWHM measured to be $3730 \pm 70 \text{ km s}^{-1}$ from the WHT observation, however errors from the continuum placement and the significant impact of absorption on the shape of the emission line mean that the underlying C IV emission in this object may be narrower than this value. The He II emission in this object is approximately twice as strong as in the DR5 quasar composite. This suggests that the far-UV continuum in this object is likely to be stronger than average casting doubt on the ghost

nature of the feature within the C IV absorption.

SDSS 1147+1532 meets the criteria for strong emission and has He II emission of approximately average strength. The FWHM of the C IV emission line in the WHT observation is $3730 \pm 70 \text{ km s}^{-1}$ although for the same reasons given for SDSS 1018+5440 this does not necessarily mean the true width of the underlying emission fails Arav's criteria.

SDSS 0851+0515 shows strong Ly- α emission and has relatively weak He II suggesting the far-UV continuum will contribute less than average to radiative acceleration of outflowing C IV ions. However the FWHM of the C IV emission line is $3770 \pm 180 \text{ km s}^{-1}$ as measured from the Gemini observation. The C IV emission line in this object is poorly fit by a Gaussian which will make this measurement less accurate, combined with the reasons given previously the emission lines may be narrow enough for the feature in the C IV absorption trough to be produced via radiative acceleration.

SDSS 1626+4058 has strong narrow emission lines. The He II emission in this object is marginally stronger than average suggesting a slightly stronger far-UV continuum. However this criteria is not clearly defined and the error on the He II measurement is large so I would not rule out the possibility that the feature in this object is the ghost of Ly- α .

SDSS 1422+3823 has strong narrow emission lines and the SDSS spectra shows He II emission of average or slightly below average strength. The He II emission in the Gemini spectrum is masked by absorption due to a sky line. This object is the most promising ghost candidate for which follow up observations have been obtained.

4.5 Summary

Follow up spectra of 11 ghost candidates, 8 of which are in the GCFC from Chapter 3 have been presented. 8 of these objects were observed using the WHT and 3 using Gemini North. Arav's criteria have, where

possible, been tested on these spectra and the results of these tests are summarised in Table 4.3. 6 of these objects still show strong evidence for a ghost feature. Of these 6 all show N V absorption and all except SDSS1700+6026 meet the criteria for strong emission. 4 of these 6 objects have C IV FWHM measured between 3200 and 3800 kms^{-1} , SDSS1626+4058 is the only object that shows C IV emission clearly narrower than 3500 kms^{-1} and SDSS1700+6026 shows C IV emission clearly broader than this. The He II emission line strength is not accurately defined in these objects but it appears to be of average strength in most of them.

The majority of the observed objects show no notable differences between the shape of the SDSS and follow up spectra. However the absorption blue-ward of the potential ghost feature in SDSS1138+3517 has weakened considerably in the WHT observation whilst the emission red-ward of the ghost zone remains at a similar level to the SDSS observation (see Figure 4.18). The C IV absorption has also changed in SDSS 2124+0959, the SDSS observation shows two peaks within this absorption whilst in the WHT follow up observation the peaks have joined and a single much broader feature is seen (Figure 4.36). Chapter 5 looks in more detail at the changes which have occurred in SDSS J113831.42+351725.3 and the information that this can give us regarding the location and physical conditions of the absorbing material.

Object Name	Telescope	N v BAL	C IV FWHM (kms ⁻¹)	Line Strengths			He II Scale to the composite
				Ly- α	N v	C IV	
SDSSJ1018+5440	WHT	✓	3730±70	630±10	150±10	245±5	2.11 ^{+0.3} _{-0.23}
	SDSS	✓	3820±250	580±40	170±30	225±25	1.96±0.49
SDSSJ1138+3517	WHT	✓	3530±130	145±5	120±5	80±5	0.96±0.10
	SDSS	✓	3830±150		280±30	140±15	0.98±0.20
SDSSJ1147+1532	WHT	✓	3730±40	105±5	270±5	125±5	0.92 ^{+0.11} _{-0.09}
	SDSS	✓	3210±90	225±20	430±20	160±10	0.96 ^{+0.19} _{-0.16}
SDSSJ1344+4834	WHT	untested	4900±250	untested	45±45	105±20	1.34±0.90
	SDSS	untested	untested	untested	45±40	85±60	1.30±0.30
SDSSJ1626+4058	WHT	✓	2345±25	680±5	323±3	225±5	1.58 ^{+0.19} _{-0.16}
	SDSS	✓	(3110±20)	900±35	390±20	260±15	1.26±0.19
SDSSJ1700+6026	WHT	✓	6390±70	146±2	60±5	86±2	1.16 ^{+0.15} _{-0.11}
	SDSS	untested	6685±250	untested	195±20	125±10	0.88±0.16
SDSSJ1641+3058	WHT	untested	5400±350	12±3	40±5	40±5	
	SDSS	untested	5700±900	untested	untested	40±10	
SDSSJ2124+0959	WHT	untested	3630±350	400±20	250±20	130±20	
	SDSS	untested	2950±130	untested	untested	170±20	
SDSSJ0851+0515	Gemini	✓	3770±180	390±25	145±15	65±10	0.49±0.21
	SDSS	✓	4340±180	350±15	170±15	80±10	0.62±0.15
SDSSJ1150+5427	Gemini	✓	5390±180	120±30	245±35	100±10	0.47±0.20
	SDSS	✓	5070	259	368	118	
SDSSJ1422+3823	Gemini	✓	3280±120	690±40	265±30	200±15	
	SDSS	✓	2146	615±25	200±20	170±15	0.75±0.24

Table 4.3: Tests of Arav's Criteria for the Gemini and WHT observations (SDSS DR5 values are given in brackets and all linestrengths are given in % of the continuum at peak flux)

Chapter 5

SDSS J113831.42+351725.3

Observations of SDSS J113831.42+351725.3 taken several years apart show clear changes in the structure of the broad absorption within this object (see figure 5.1). In order to easily compare the emission and absorption lines in the spectra they are fit with a power law continuum to which they are scaled (see Figure 5.1). This allows easy visual identification of the changes to the EW of the absorption and emission-line features. Similar variabilities in broad absorption line strengths have been reported in the literature (Barlow 1993, Hamann et al. 2008). In order to distinguish between changes in the covering fraction, caused by absorbing clouds moving in and out of the line of sight, and changes in the ionisation of the absorbing material requires accurate estimates of the underlying continuum and emission lines. These estimates will allow constraints to be placed on the ionic column density of a variety of species. In general the complexity of the absorption will prevent accurate determination of the level of saturation which would lead to gas covering fraction estimates. This means that the majority of the constraints on column densities will be lower limits. These lower limits can be used together with photo-ionisation calculations to provide valuable information about the metallicity, hydrogen column density, ionisation state and location of the absorbing gas within this object as well as any changes in the ionisation state of the gas between observations.

Once these parameters (Z_G , N_H , n_H , U , r) have been determined it will be possible to estimate the mass outflow rate, \dot{M}_{out} , which can be compared to the accretion rate, calculated from an estimate of

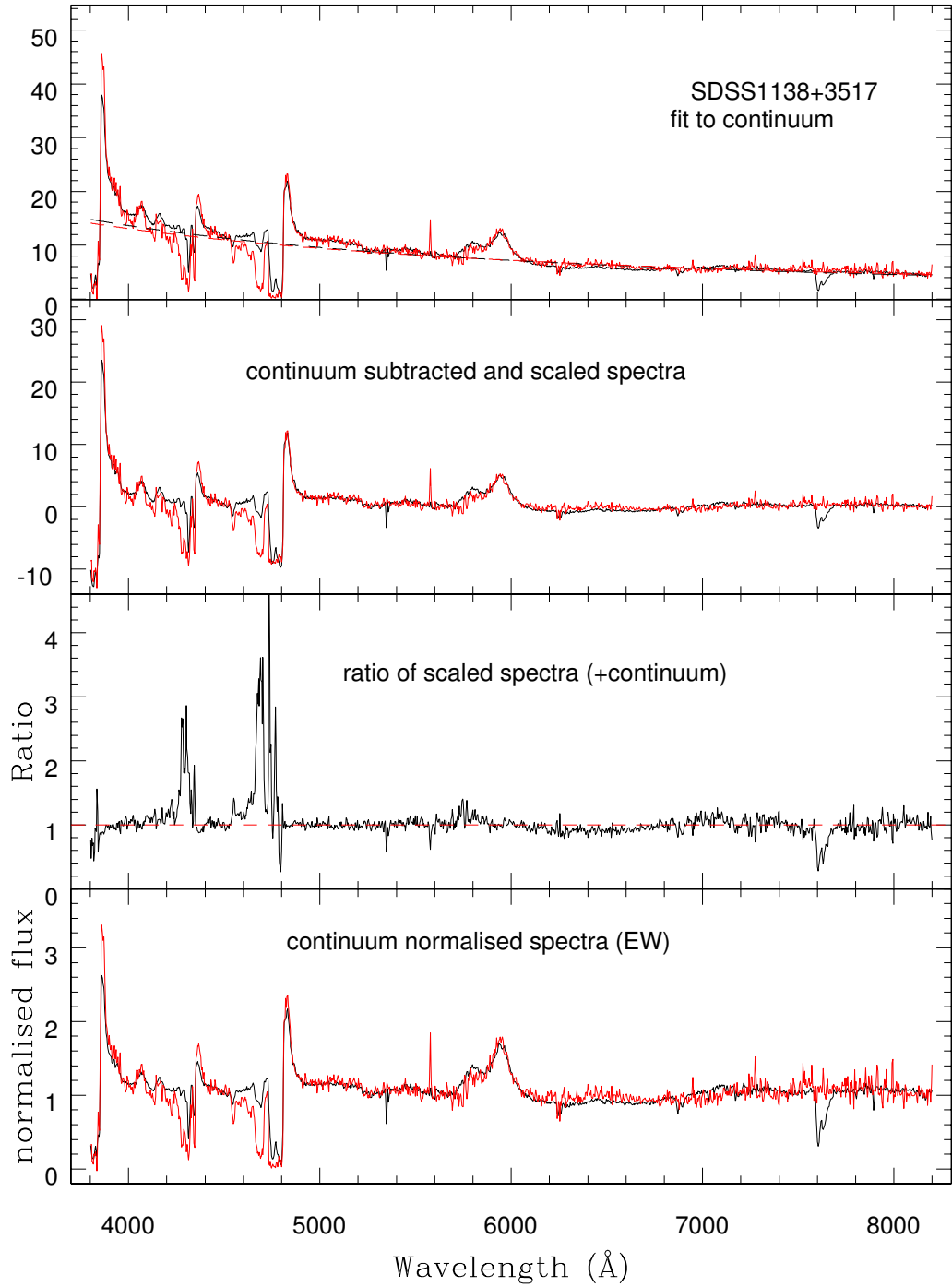


FIGURE 5.1: Continuum scaling the SDSS and WHT observations of SDSS J1138+3517. The top panel shows the continuum fits (dashed) to the data (solid), the upper middle panel shows the spectra scaled with the continuum subtracted. The lower middle panel shows the ratio of the WHT spectrum to the SDSS spectrum after they have been scaled and continuum normalised. The lower panel shows the continuum normalised spectra allowing changes to the EW to be easily seen. The SDSS data (and fit) are shown in red and the WHT data in black.

the black hole mass, and the Eddington accretion rate. Outflows may be important in quenching star formation in their host galaxy (Scannapieco et al. 2005, Springel et al. 2005) as well as on a larger scale by providing heating to gas within galaxy clusters preventing cooling flows (Di Matteo et al. 2005, Brüggén & Kaiser 2002, Ruszkowski & Begelman 2002). Combining \dot{M}_{out} with the observed outflow velocity will allow the kinetic luminosity to be calculated. The magnitude of this parameter can be used to determine the potential impact of the outflow on the environment around the AGN.

5.1 Observations

SDSS J113831.42+351725.3 was observed on the 3rd of May 2005, 3 years and 24 days before the WHT follow up observations taken on May 27th 2008. This gap corresponds to 0.98 years in the rest frame of the source ($z=2.12$). The SDSS observation has a signal-to-noise ratio per pixel of $\simeq 10.5$ measured between 1700 and 1750 Å in the rest-frame of the source. The resolution of the SDSS data is approximately 140 km s^{-1} per 2 pixel resolution element. The WHT observation has a signal-to-noise ratio of 35.0 per pixel also measured between 1700 and 1750 Å in the source rest-frame and a resolution of approximately 450 km s^{-1} . Further details of the WHT observations and their reduction can be found in Chapter 4, section 4.2.

5.2 Constraining ionic column densities

Column densities for the absorbing ions are estimated using a variety of different methods. Firstly by using curve of growth analysis as described in section 5.2.2. Secondly by fitting doublet components with Gaussian velocity distributions. The column density of each component can then be obtained from equation 5.2.3 using the width and peak optical depth of the component fit. This method is described in detail in section 5.2.3. Thirdly the column density can be estimated by direct integration of the apparent optical depth profile as described by Savage & Sembach (1991) and in section 5.2.4 of this thesis. All of these methods produce *lower limits* on the optical depth as they assume complete coverage of the

continuum source. Decreasing the covering fraction will require higher optical depths for the covering gas and larger column densities. Larger optical depths and column densities will also be required if some of the observed flux within the absorption trough results from scattering off gas which is not covered by the outflowing material. These methods, which rely on the apparent optical depth have been shown to be a poor approximation for a number of BAL outflow troughs, which show highly saturated absorption and/or partial coverage (Telfer et al. 1998, Churchill et al. 1999, Ganguly et al. 1999). In order to take into account variation in the properties of the absorber as a function of line of sight velocity two different models were used. Section 5.2.5 describes a partial covering model. This model assumes an homogeneous absorbing material but in this case this material only covers part of the source, the rest of the source is covered by gas with $\tau=0$. The covering fraction estimated using this technique can then be used to modify the equivalent width of absorption and apply the curve of growth method to the modified EWs. A more complex alternative to partial covering is to assume that the optical depth follows a power law distribution (e.g. an inhomogeneous absorber model). The details of this model are discussed in section 5.2.6 and by de Kool et al. 2002a and Arav et al. 2005. However before any measurement of the absorption can take place an accurate underlying emission-line template is required as in the majority of sources the absorption also covers the broad emission-line region.

5.2.1 Fitting the underlying continuum and line emission

In order to model the underlying emission (and hence determine the pseudo-continuum) 12 different quasar composites have been used to fit the regions in the SDSS and WHT spectra which are least effected by emission or absorption. All 12 composites have been produced by taking the geometric mean of a quasar sub-sample after first putting the spectra into their rest-frame and normalising to unity between 1700 and 1750 Å. The 12 quasar sub-samples are compiled from DR5 of the SDSS and comprise quasars with redshifts between 1.7 and 4.2. Four of these composites are made up of the lower, lower-middle, upper-middle and upper quartile of C IV emission equivalent width as measured by the SDSS. Four are formed from the four quartiles of C IV FWHM and four from the four quartiles of C IV peak flux relative to the continuum (see Figure 5.2 for all of these composite spectra). These composites are modified by allowing

the slope, scale and amount of reddening due to dust (assumed to follow the SMC extinction curve of Pei 1992) to vary in the same manner as in section 2.1 of Chapter 2. Once the continuum has been fit the emission line regions of the composites are scaled by multiplying the flux above the continuum by a common factor and minimising χ^2 over the part or parts of the emission line that appear to be unabsorbed. The regions used for both the linear fit and the calculation of χ^2 for the fit to the various lines are given in Table 5.1. The scaled composite which best fits the emission line region (this is the lowest line width composite for both the C IV and Si IV lines in the SDSS spectra) is used to provide an initial intensity, I_0 , prior to the absorption. I_0 is used in the determination of residual intensity, R (equation 5.2.1)

$$R = \frac{I}{I_0} \quad (5.2.1)$$

where I_0 is the intensity entering the absorber and I is the intensity exiting the absorber and optical depth, τ (equation 5.2.2).

$$\tau = \ln\left(\frac{I_0}{I}\right) \quad (5.2.2)$$

For the WHT spectrum none of the composites provide a particularly good fit to the emission line region and instead a simple Gaussian emission line is used to provide estimates of I_0 . The fits used are shown in Figures 5.3 to 5.6 along with the χ^2 values from the contributing regions and the resulting residual intensity plot.

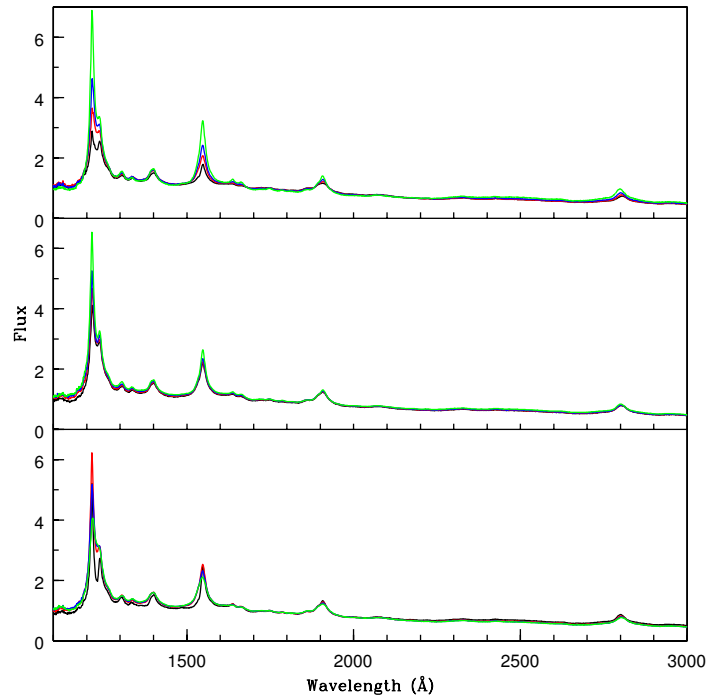


FIGURE 5.2: Top, composites composed of the four quartiles of C IV EW (the lowest EW is in black, then red then blue and the largest EW in green). Middle, Composites composed of the four quartiles of C IV peak flux relative to the continuum (largest in green then blue, red and smallest in black). Lower panel, Composites composed of the four quartiles of C IV FWHM (largest in green then blue, red and smallest in black).

Emission Line	Emission Region		SDSS Fit Region
	Start	Finish	
C IV $\lambda\lambda 1549\text{\AA}$	1460 \AA	1600 \AA	1546.4-1579.5 \AA
Si IV $\lambda\lambda 1400\text{\AA}$	1360 \AA	1440 \AA	1396.1-1419.5 \AA
Mg II $\lambda\lambda 2800\text{\AA}$	2700 \AA	2900 \AA	2785.0-2820.5 \AA
N V $\lambda\lambda 1240\text{\AA}$	1230 \AA	1300 \AA	1241.0-1280.0 \AA

Table 5.1: Wavelength boundaries used to scale the composite emission lines

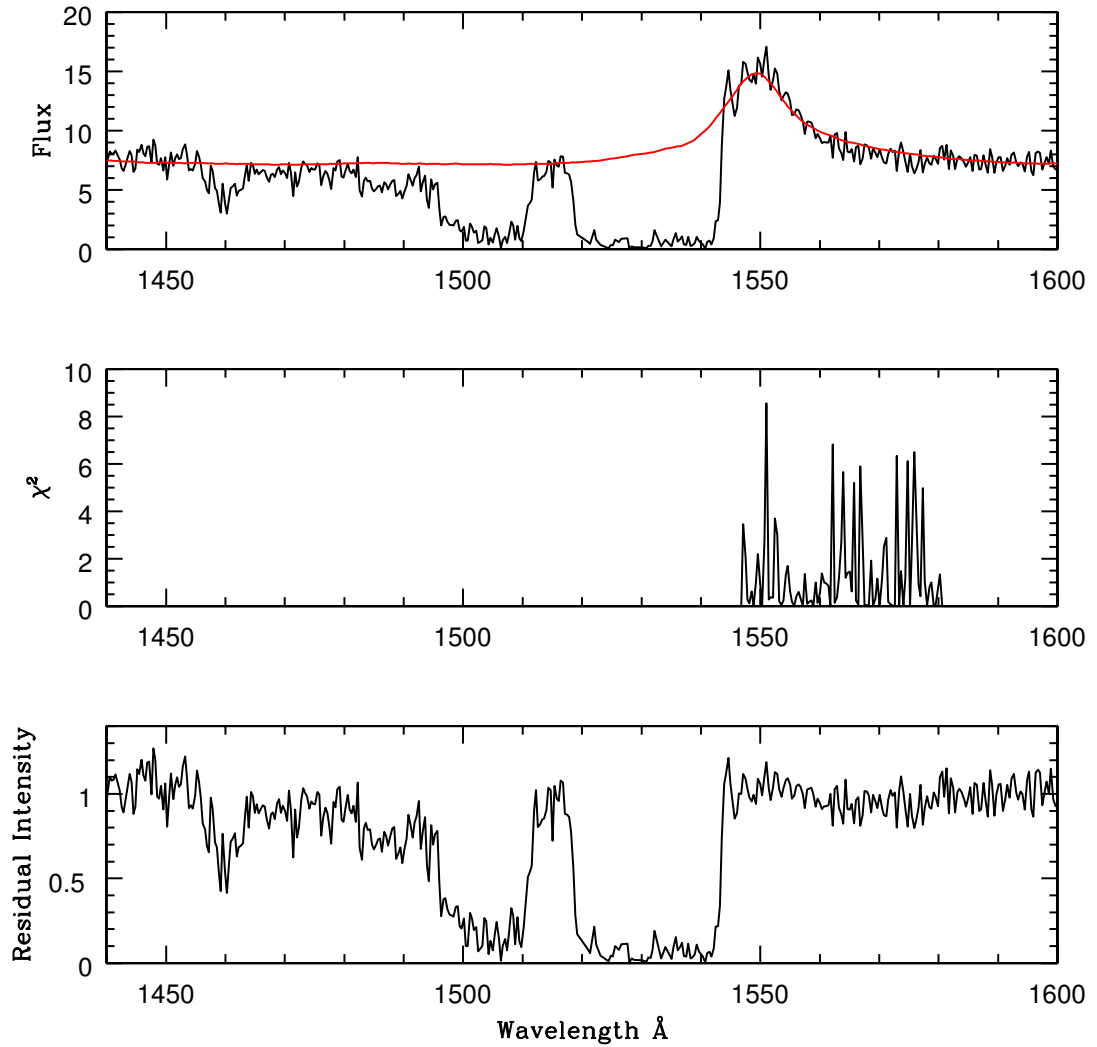


FIGURE 5.3: Continuum and emission line fits to the C IV emission and absorption region of the SDSS spectrum of SDSS1138+3517. The top panel shows the fit (red line) to the data (black line). The middle panel shows the χ^2 values for the region used to fit the emission line. The lower panel shows the resulting residual intensity spectrum.

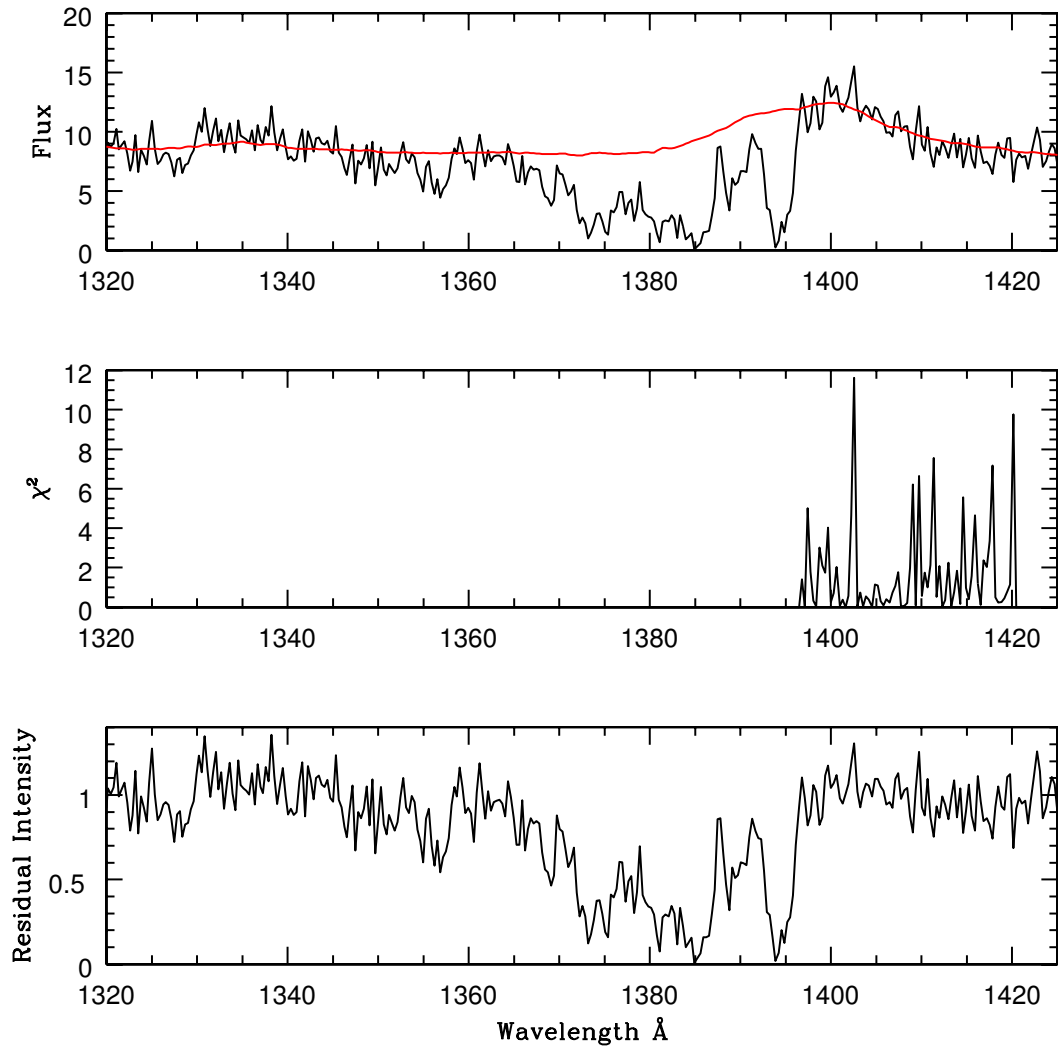


FIGURE 5.4: Continuum and emission line fits to the Si IV emission and absorption region of the SDSS spectrum of SDSS1138+3517. Panels as for fig. 5.3.

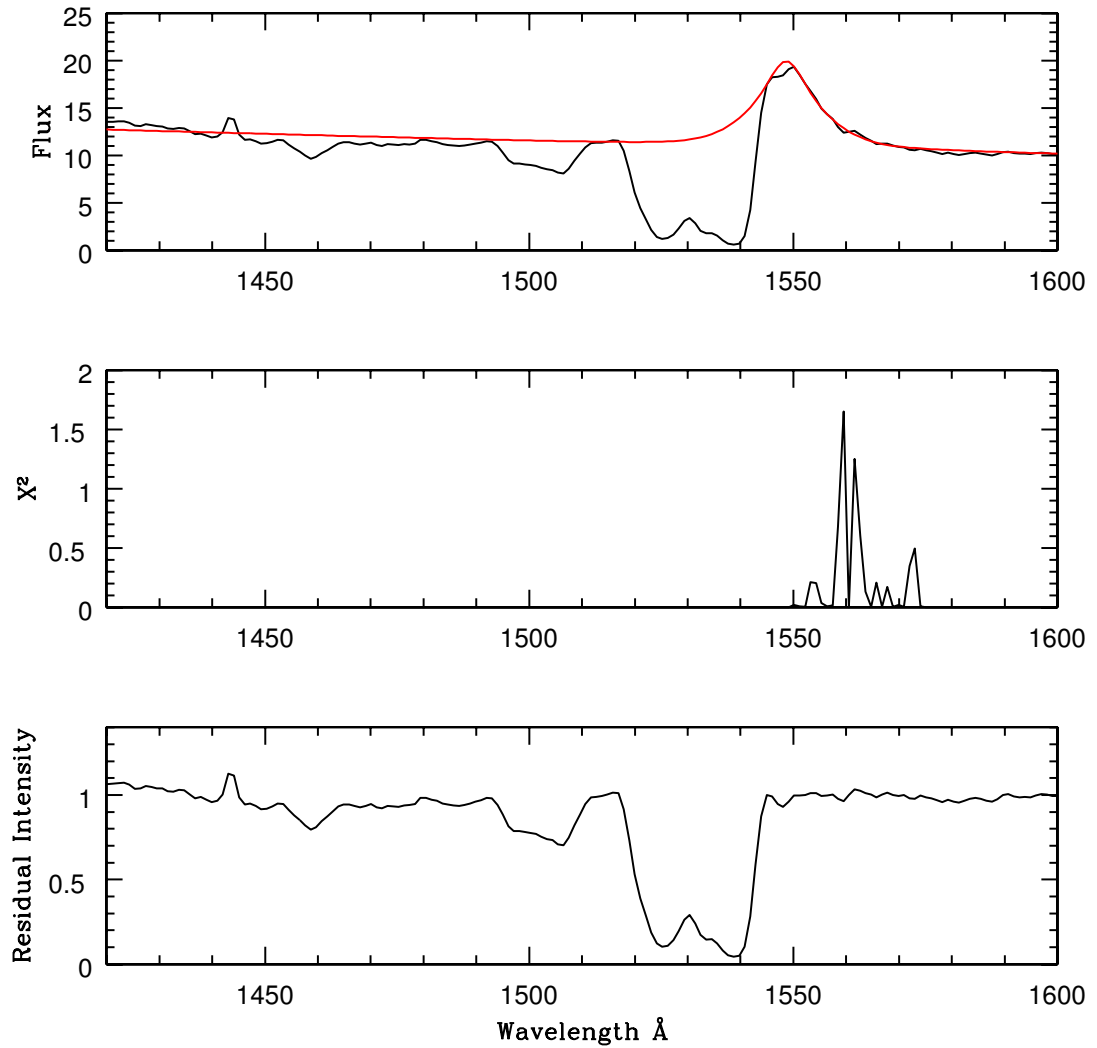


FIGURE 5.5: Continuum and emission line fits to the C IV emission and absorption region of the WHT spectrum of SDSS1138+3517. Panels as for fig. 5.3.

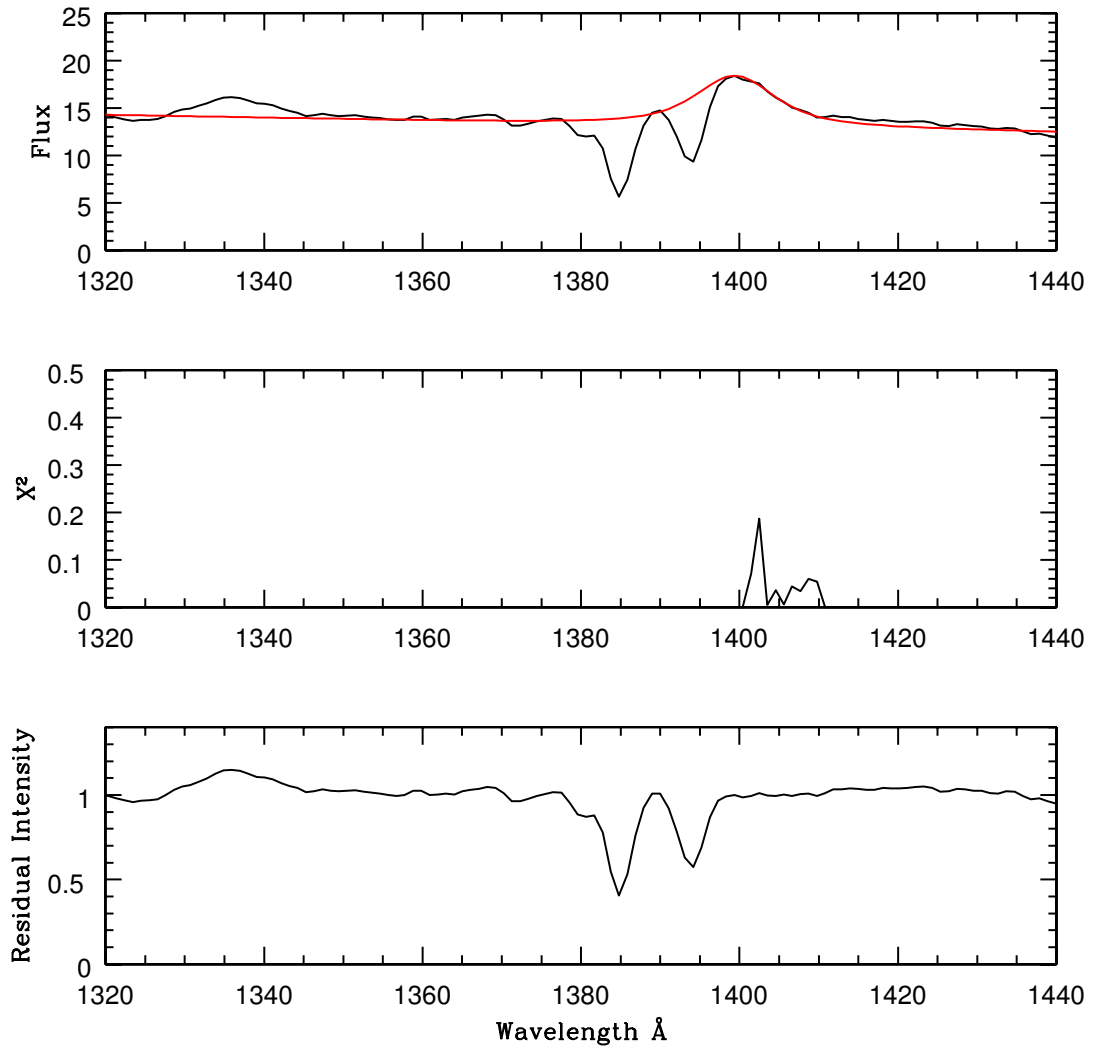


FIGURE 5.6: Continuum and emission line fits to the Si IV emission and absorption region of the WHT spectrum of SDSS1138+3517. Panels as for fig. 5.3.

5.2.2 The Curve of Growth

The curve of growth (Spitzer 1978) is the name given to the relationship between the equivalent width of absorption, the ionised column density of the absorber and the peak optical depth. Historically equivalent widths have been widely used because they are independent of the instrument used to measure them. However, as the flux absorbed by a volume of gas depends upon the amount of flux entering that volume, the equivalent width of absorption does not grow linearly with increasing optical depth. By assuming that the gas has a Maxwellian line of sight velocity distribution and that the absorption cross-section per ion follows a Lorentzian distribution, it can be shown that the wavelength dependence of the absorption cross section follows a Voigt profile. This profile is dominated by the Gaussian component close to line centre, known as the 'Doppler core'. As the Lorentzian component drops more slowly than the Gaussian component it will dominate far from the core creating extended 'damping wings'. A line is said to be unsaturated if the residual intensity at line centre is non-negligible. At low optical depths ($\tau_0 \ll 1$) the equivalent width is proportional to the optical depth at line centre. This is called the linear part of the curve of growth as the equivalent width grows linearly with peak optical depth for a given value of b , where b represents the Doppler parameter and is a measure of the velocity width of the absorption. As the optical depth increases the residual intensity at line centre drops to essentially zero. In this region of the curve of growth the equivalent width of absorption grows as $\log(\tau_0)^{1/2}$. This is a very slow function of τ_0 . This region is known as the saturated part of the curve of growth. At very large optical depth the absorption in the Doppler core is completely saturated and the increase in equivalent width with peak optical depth results from the damping wings. This results in the equivalent width growing with $\tau_0^{1/2}$, and consequently this region is known as the damping or square-root part of the curve of growth.

Doublet emission lines are normally used to determine the position on the curve of growth as they provide two different measures of the strength of absorption where the ratio of the oscillator strengths is theoretically known and the density of the ions must be the same (as the lines are from the same ion). We therefore require equivalent width measurements for each of the doublet components. The optical depth, and therefore the equivalent width, depends on the line oscillator strength, f , as well as the ionised column, N ,

and Doppler parameter, b , and by using this dependence it is possible to determine where on the curve of growth the absorber lies. This can be determined by comparing the equivalent width derived from the curve of growth for given values of N and b to the measured values. By minimising χ^2 one can then find the best fitting values of N and b . Unfortunately for SDSS J1138+3517 the C IV absorbing components are considerably broader than the doublet separation, and therefore the individual doublets cannot be easily resolved. However Si IV absorption in the WHT spectrum shows a clearly resolved doublet. The stronger component has an EW of $2.18 \pm 0.2 \text{ \AA}$ and the weaker component has an EW of $1.49 \pm 0.1 \text{ \AA}$. The curve of growth analysis described above yields a b value of $215_{-40}^{+60} \text{ kms}^{-1}$ and an ionised column density of $4.02_{-0.55}^{+0.70} \times 10^{14} \text{ cm}^{-2}$. The best fitting curve of growth for Si IV in this observation is shown in Figure 5.7 along with the measured equivalent widths and their calculated column densities. The errors on the b and N values are calculated by fixing all of the other parameters to their best fit values and varying the remaining parameter until χ^2 has increased by 2.71 resulting in a 90% confidence interval on one interesting parameter. The same analysis has not been attempted on the SDSS Si IV absorption as the absorption is more complex with multiple overlapping components making it very difficult to isolate individual components from which EWs can be measured. It is clear from Figure 5.7 that the Si IV absorption is on the linear part of the curve of growth. However only a modest increase in the column density would result in the line moving onto the saturated region. As the SDSS observation shows significantly more Si IV absorption it is quite likely that this absorption is saturated.

5.2.3 Multi-component fitting

If the absorbing material follows the assumptions made in the curve of growth analysis, the ionic column density, N , is related to the Doppler parameter, b , and optical depth at line centre, τ_0 , by equation 5.2.3

$$N = \frac{m_e c}{\pi e^2} \frac{b}{f \lambda_0} \tau_0 \quad (5.2.3)$$

where m_e is the electron mass, c the speed of light, e the charge of an electron, f the oscillator strength of the transition, and λ_0 the rest wavelength of the transition. This equation allows the column density to be estimated by fitting Gaussian optical depth profiles to the absorbing components provided that the optical

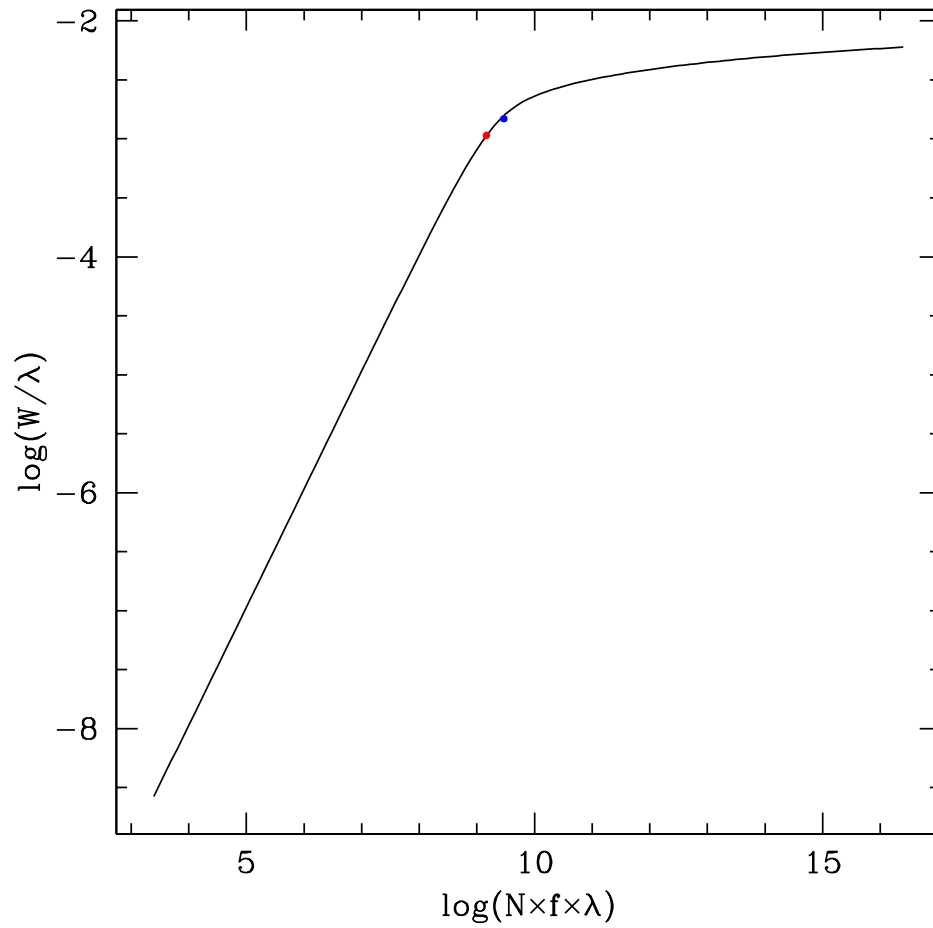


FIGURE 5.7: The curve of growth for Si IV absorption in SDSS1138+3517. The x-axis is the log of the Column density multiplied by the wavelength (λ) in cm and the oscillator strength, f . The y-axis is the equivalent width of absorption divided by the wavelength. The circles mark the position of the two doublet components of Si IV on the curve. The errors on these positions are not included on this plot as they are less than 0.1 on each axis.

depth is small enough that the Gaussian component dominates over the damping wings. The column density will be underestimated by equation 5.2.3 if the source is only partially covered by the absorber as the optical depth will be underestimated.

The absorption is fit using multiple Gaussian components allowing the ratio of the doublet line-strengths to vary between 1 and 2. These limits are chosen because the ratio of oscillator strengths for the Si IV and C IV doublets will result in the stronger component having an optical depth that is twice as large as the weaker component. However if partial covering is present the derived optical depths will be significantly smaller than the true optical depth and the measured peak optical depths will move closer together. We vary the optical depth, line-strength ratio, outflow velocity and velocity width of each component in order to minimise χ^2 . In the majority of observed lines fitting the absorption requires multiple components. The separation of the C IV doublet is only 493 km s^{-1} which is comparable to the width of the components and the resolution of the data making it difficult to treat the doublets individually. The greater separation of the Si IV doublet allows more information on the doublet ratio and therefore the saturation of the absorption to be obtained. However in the SDSS spectra the absorption due to both C IV and Si IV is complex and deep suggesting saturation is important even if coverage of the continuum source is complete. The complexity of the absorption in the SDSS spectra requires several overlapping components. The absorption components and the resulting fits are shown in Figures 5.8 to 5.11. Equation 5.2.3 is used to calculate the column density for each of the doublets for all components. The total column density of the ion is calculated by summing the larger of the two doublet column densities for each component. As the optical depth and therefore the column density may be larger due to partial covering this column density is a lower limit only. Table 5.2 indicates the components used to fit the absorption along with the column density calculated from equation 5.2.3. The reported errors are the 90% confidence limits on one interesting parameter. The errors on the column density are based only on the errors on the derived peak optical depth. The details of the Si IV and C IV absorption fits are discussed below.

Spectrum	Line	Outflow velocity (kms^{-1})	Width (kms^{-1})	τ_0	Column Density ($\times 10^{15} \text{cm}^{-2}$)
SDSS	C IV ₁₅₄₉	8240±50	380±30	1.25 ^{+0.15} _{-0.4}	0.53 ^{+0.08} _{-0.18}
SDSS	C IV ₁₅₅₁			1.25±0.15	1.07±0.15
SDSS	C IV ₁₅₄₉	9575±70	640±50	0.90±0.15	0.65±0.12
SDSS	C IV ₁₅₅₁			0.90 ^{+0.1} _{-0.15}	1.29 ^{+0.18} _{-0.24}
SDSS	C IV _{TOTAL}				2.36 ^{+0.2} _{-0.3}
SDSS	Si IV ₁₃₉₃	1820±15	200±15	2.30 ^{+0.55} _{-0.2}	0.104 ^{+0.026} _{-0.012}
SDSS	Si IV ₁₄₀₂			2.3±0.2	0.207±0.024
SDSS	Si IV ₁₃₉₃	2890±40	200±30	0.8 ^{+0.35} _{-0.15}	0.036 ^{+0.009} _{-0.017}
SDSS	Si IV ₁₄₀₂			0.50±0.15	0.045±0.015
SDSS	Si IV ₁₃₉₃	4280±50	445 ⁺²⁰ ₋₄₀	1.35±0.15	0.135 ^{+0.019} _{-0.016}
SDSS	Si IV ₁₄₀₂			1.2±0.2	0.241 ^{+0.042} _{-0.046}
SDSS	Si IV ₁₃₉₃	5410±40	140±40	0.55±0.15	0.017±0.007
SDSS	Si IV ₁₄₀₂			0.5±0.15	0.032±0.013
SDSS	Si IV _{TOTAL}				0.525±0.055
WHT	C IV ₁₅₄₉	2080±20	325±10	2.10±0.10	0.77±0.44
WHT	C IV ₁₅₅₁			2.10±0.10	1.53±0.87
WHT	C IV ₁₅₄₉	2990±30	300±20	1.40±0.10	0.47±0.05
WHT	C IV ₁₅₅₁			0.70±0.10	0.47±0.07
WHT	C IV ₁₅₄₉	4580±20	610±15	1.60±0.10	1.10±0.07
WHT	C IV ₁₅₅₁			0.85±0.10	1.17±0.14
WHT	C IV ₁₅₄₉	8510±60	400±50	0.19±0.02	0.086±0.014
WHT	C IV ₁₅₅₁			0.19±0.02	0.171±0.028
WHT	C IV ₁₅₄₉	9830±90	640±80	0.18±0.03	0.130±0.027
WHT	C IV ₁₅₅₁			0.10±0.02	0.144±0.034
WHT	C IV _{TOTAL}				3.49±0.89
WHT	Si IV ₁₃₉₃	1920±20	300±15	0.85±0.05	0.0574±0.0044
WHT	Si IV ₁₄₀₂			0.55±0.05	0.0743±0.0077
WHT	Si IV _{TOTAL}				0.0743±0.0077

Table 5.2: Details of the components used to fit the absorption in the SDSS and WHT spectra of SDSS J1138+3517

Si IV

The SDSS Si IV fit is shown in Figure 5.8. The fit is complex and comprises a minimum of 4 doublet components with outflow velocities ranging from $1820 \pm 15 \text{ km s}^{-1}$ up to $5410 \pm 40 \text{ km s}^{-1}$. There are additional Si IV absorption components at higher velocities, but they are much weaker than the lower velocity features and will not alter the column density measurements by a significant amount. These 4 doublet absorption components vary in column density from $3.2 \pm 1.3 \times 10^{13} \text{ cm}^{-2}$ to $2.4 \pm 0.4 \times 10^{14} \text{ cm}^{-2}$ and are labelled 1 to 4 near the peak optical depth of each doublet component in order to show which components are linked. The lowest velocity component shows evidence of saturation with the peak optical depth of the two components measured to be above 2. The low residual intensities are strong evidence that this part of the absorber covers more than 90% of the continuum source. The total column density of Si IV measured from these components is $5.25 \pm 0.55 \times 10^{14} \text{ cm}^{-2}$. Figure 5.8 shows evidence that component 3 is in fact two components (see the higher velocity doublet of this component), however adding more components to the fit does not greatly reduce the resulting χ^2 value or add much insight into what is happening beyond confirming the fact that this outflow is complex.

The WHT Si IV fit shown in Figure 5.9 is a single component fit only, though there is evidence for a further absorption component (labelled 2 in Figure 5.9) at higher velocity. The reason why this component has not been fit is because the lower velocity doublet component is significantly stronger than the higher velocity one, contrary to what would be expected of absorption due to outflowing Si IV. The higher velocity component of the doublet which has been fit is significantly stronger than the lower velocity one suggesting the absorption is not strongly saturated. The column density required to fit the weaker doublet component is $7.43 \pm 0.77 \times 10^{13} \text{ cm}^{-2}$ almost ten times lower than the column density calculated from the SDSS fit and also considerably less than the $4.02_{-0.55}^{+0.70} \times 10^{14} \text{ cm}^{-2}$ suggested by the curve of growth analysis in section 5.2.2.

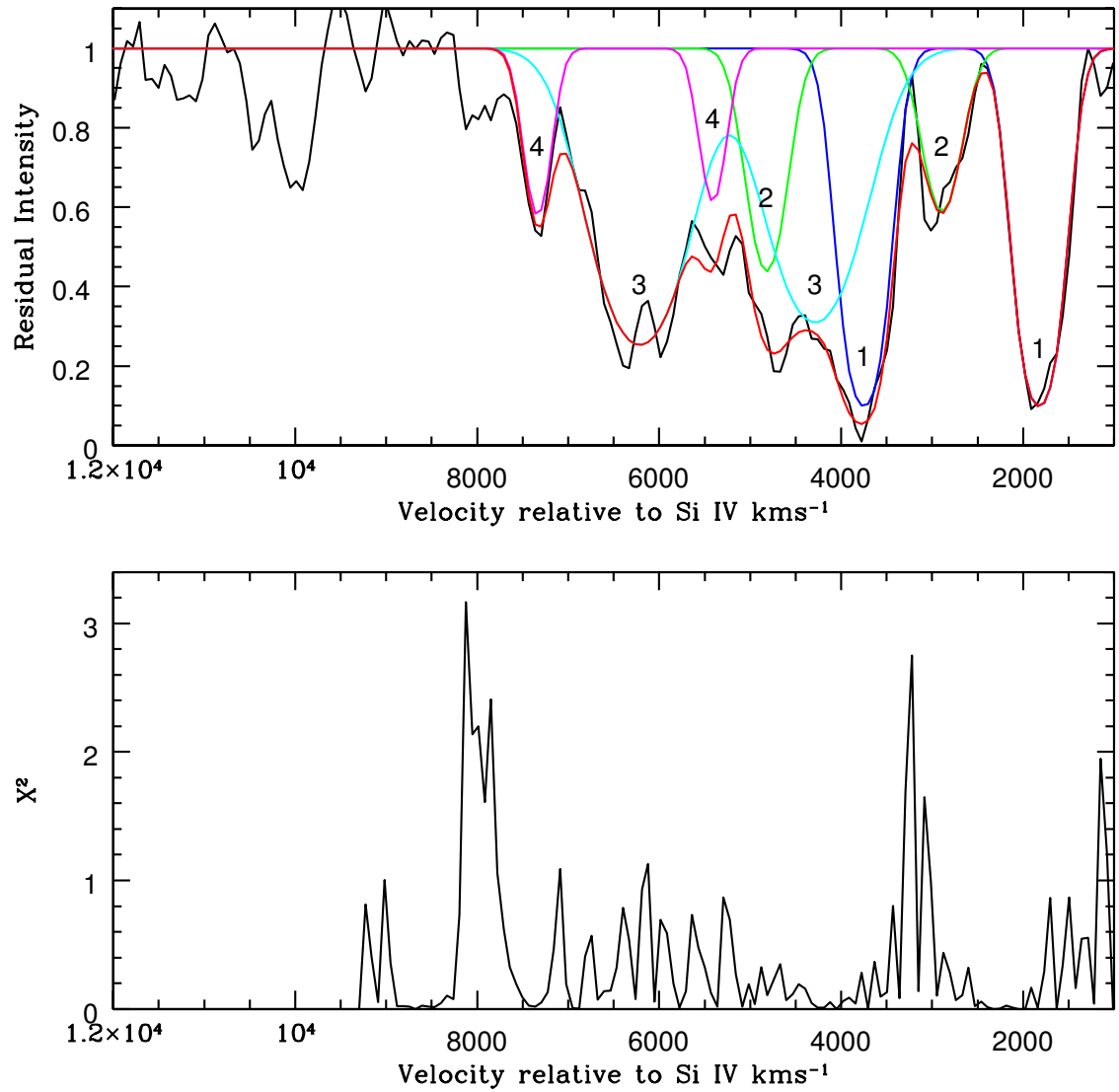


FIGURE 5.8: Gaussian fits to the Si IV absorption in the SDSS spectrum of SDSS J1138+3517. Top panel shows the residual intensity along with the fit. The four doublet components are labelled 1 to 4 in order of increasing outflow velocity close to the peak optical depth of each doublet. The lower panel shows the χ^2 values for the fit regions.

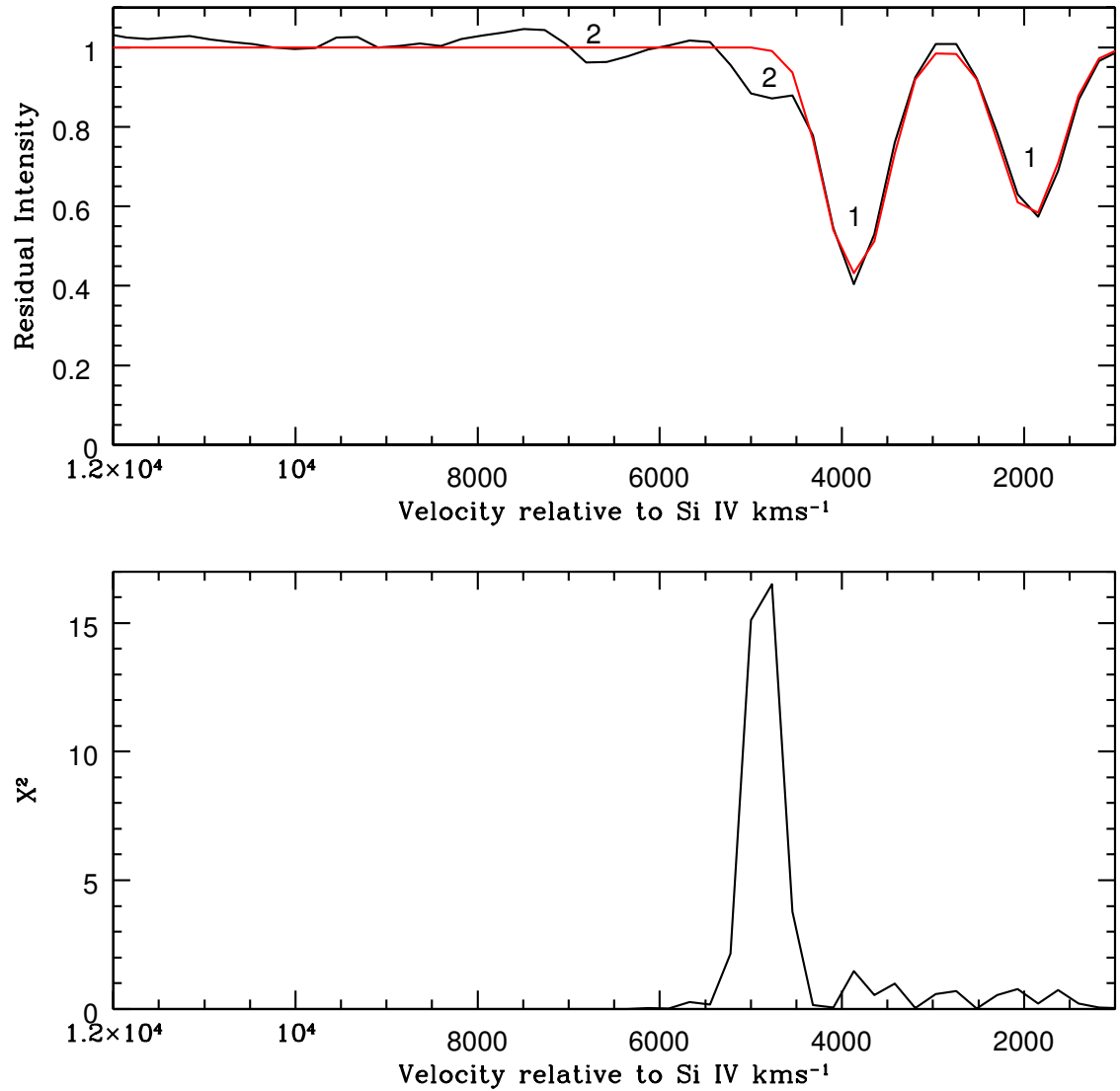


FIGURE 5.9: Gaussian fits to the Si IV absorption in the WHT spectrum. Top panel shows the residual intensity along with the fit. The fit component is labelled 1 another possible absorption doublet has been labelled 2. Lower panel shows the χ^2 values for the fit regions.

C IV

The SDSS C IV fit is shown in Figure 5.10. As the absorption between 2000 and 6000 kms^{-1} is completely saturated the optical depth in this region is unconstrained and the column density can be arbitrarily high. This requires complete coverage of the continuum source. The two component fit to the higher velocity absorption suggests a column density of $2.36_{-0.3}^{+0.2} \times 10^{15} \text{cm}^{-2}$ is responsible for this absorption.

The WHT C IV fit is shown in Figure 5.11 and includes a three component fit to the lower velocity absorption with a total column density of $3.17 \pm 0.88 \times 10^{15} \text{cm}^{-2}$ for this region. The absorption in this region requires coverage of greater than 95% of the continuum source. The higher velocity absorption is fit with a two component model with a column density of $3.15 \pm 0.44 \times 10^{14} \text{cm}^{-2}$. This is almost an order of magnitude lower than that obtained in the SDSS fit. Assuming the column density of the lower velocity component scales with that of the higher velocity component this suggests that the column density of the low velocity component in the SDSS observation is greater than $2 \times 10^{16} \text{cm}^{-2}$. The total column density for the WHT C IV absorption fit is $3.49 \pm 0.89 \times 10^{15} \text{cm}^{-2}$.

5.2.4 Estimating the Column Density using analysis of apparent optical depth profiles

Savage & Sembach (1991) describe a method of estimating column densities by using the apparent optical depth, obtained using the observed spectrum which is a convolution of the true spectrum and the instrumental spread function. The apparent optical depth can be converted to an estimate of the column density per unit velocity, $N(v)$, using equation 5.2.4.

$$N(v) = \frac{m_e c}{\pi e^2} \frac{1}{f \lambda} \tau(v) = \frac{3.768 \times 10^{14}}{f \lambda} \tau(v) \quad (5.2.4)$$

where λ is in \AA and $N(v)$ is in $\text{atoms cm}^{-2} (\text{kms}^{-1})^{-1}$. The total column density, N , can then be obtained

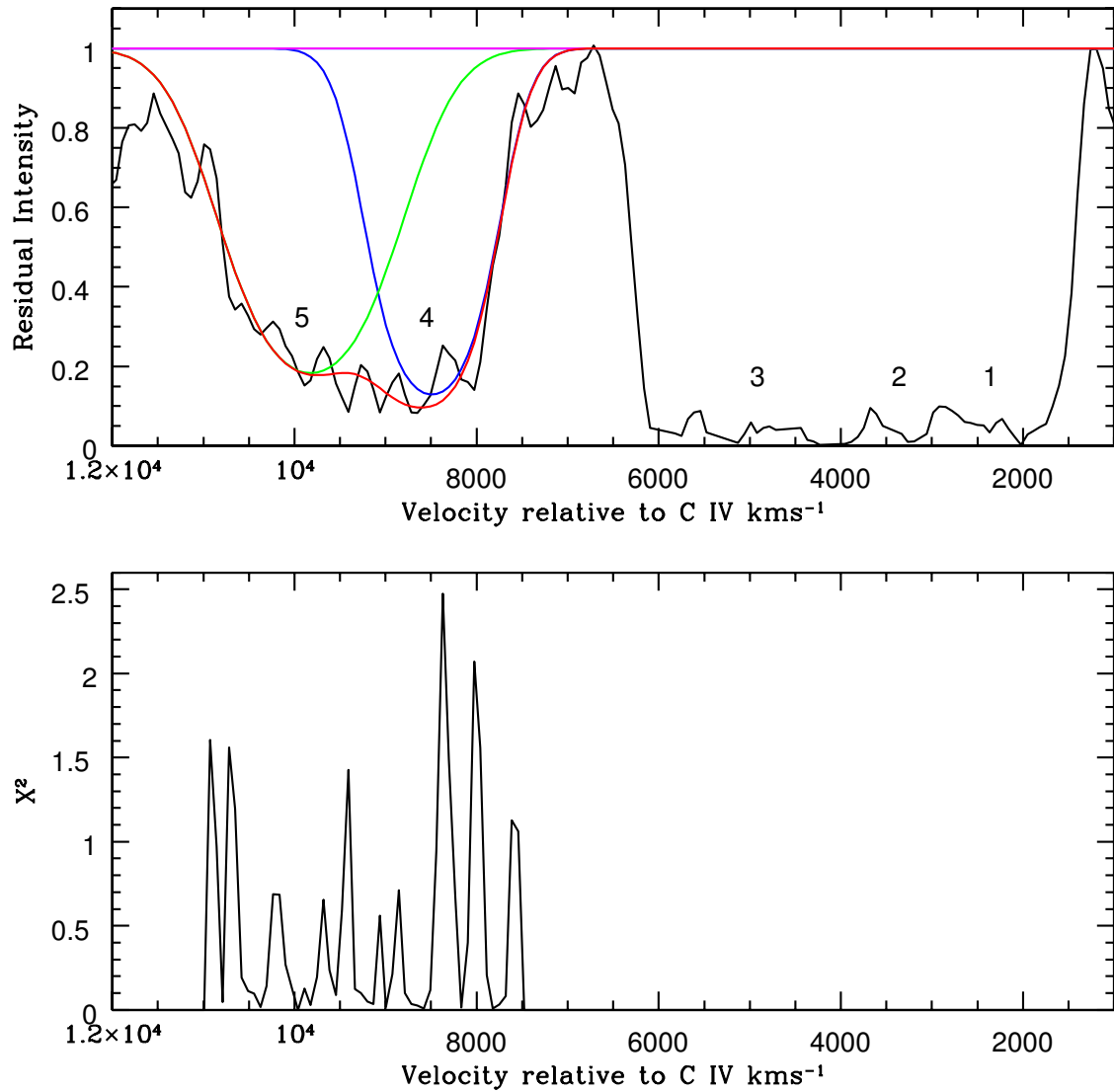


FIGURE 5.10: Gaussian fits to the C IV absorption in the SDSS spectrum. Top panel shows the residual intensity along with the fit. The fit components are labelled 4 and 5, the labels 1,2 and 3 mark the positions of the three components fit to the lower velocity component of the WHT spectrum and have not been fit for the SDSS data as the residual intensity is so low. The lower panel shows the χ^2 values for the fit regions.

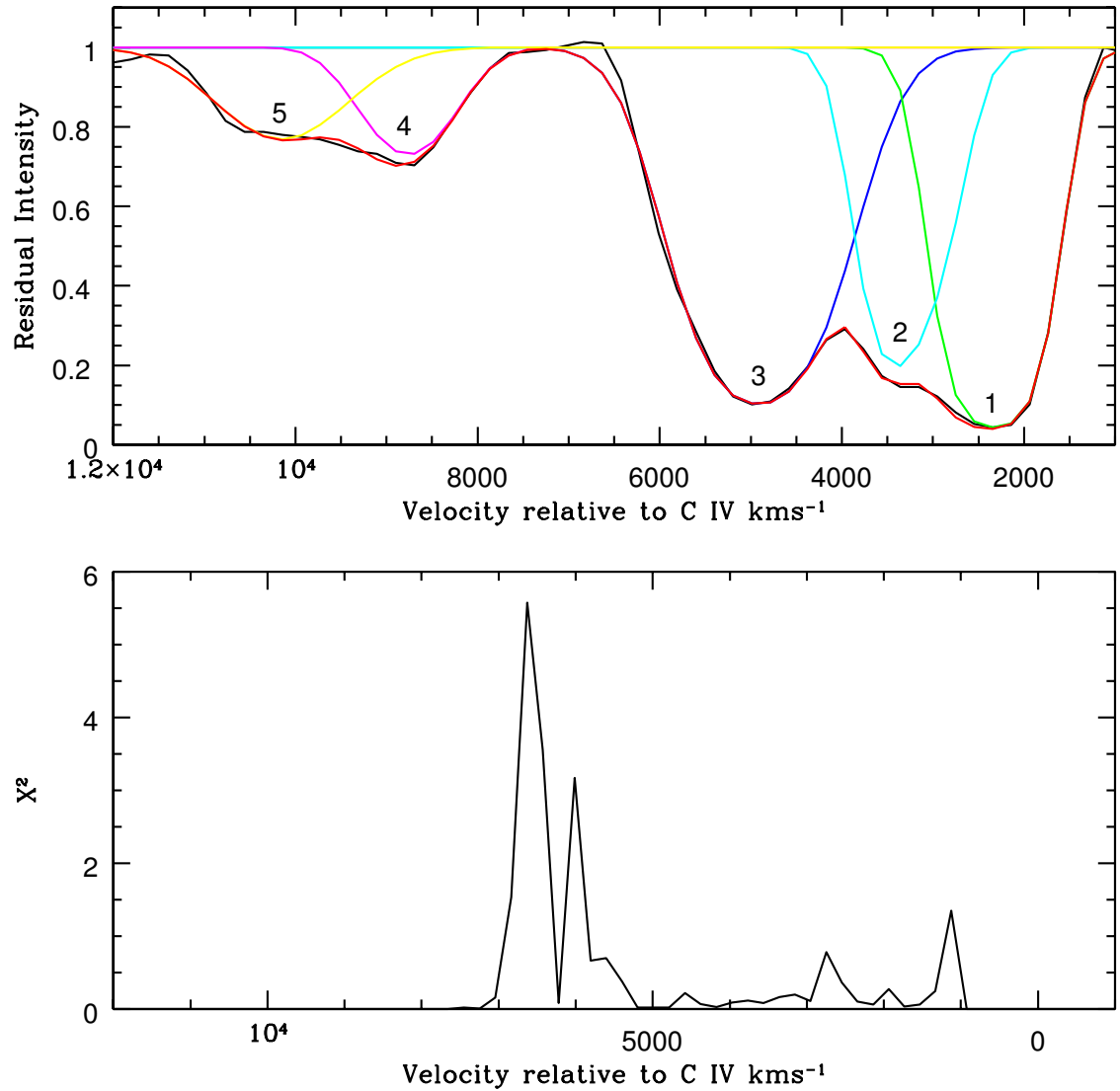


FIGURE 5.11: Gaussian fits to the C IV absorption in the WHT spectrum. The five separate components are marked on the top panel which shows the components and total fit to the residual intensity. The lower panel shows the χ^2 values for the fit regions.

by integrating over the absorbed region as in equation 5.2.5. The advantage of this method is that it is independent of, and requires no assumptions about, the functional form of the velocity distribution.

$$N = \frac{m_e c}{\pi e^2 f \lambda} \int_{-\infty}^{\infty} \tau(v) dv \quad (5.2.5)$$

As the absorption present in SDSS J1138+3517 is broad and contains multiple components the problem is complicated by the overlap between the two doublet features as in general the absorption at a given wavelength is a combination of absorption from the two doublets at different velocities. This makes it difficult to access the additional information on saturation that could be obtained from the ratio of the strength of absorption from each doublet. Integrating over all of the absorption using the values of f and λ appropriate for the weaker of the two lines will result in an appropriate column density for those regions absorbed by the weaker doublet plus an additional column density due to the absorption from the stronger component. If saturation does not effect the absorption then the column density estimated for the stronger component in this way will be approximately double the true column density. Overlapping components will increase the optical depth. However, as they do so in a linear fashion (i.e. the total optical depth from overlapping components of optical depth τ_1 and τ_2 is equal to $\tau_1 + \tau_2$) the contribution of each component to the column density (equation 5.2.5) will be the same as if the components did not overlap. The estimate based on using only the weaker doublet will therefore be no more than three times the true column density and 1/3 of this estimate will be a lower limit on the true column density. Any saturation effects or partial coverage will result in an underestimation of the column density by this method. Table 5.3 shows the velocities used and the corresponding column densities calculated using the weaker doublet along with the lower limit on the column density. Only the Si IV absorption in the WHT spectrum shows a clearly resolved doublet. The column density per unit velocity calculated for each component is shown in Figure 5.12. The larger column density measurements are from the weaker component which shows there is some saturation in this absorption.

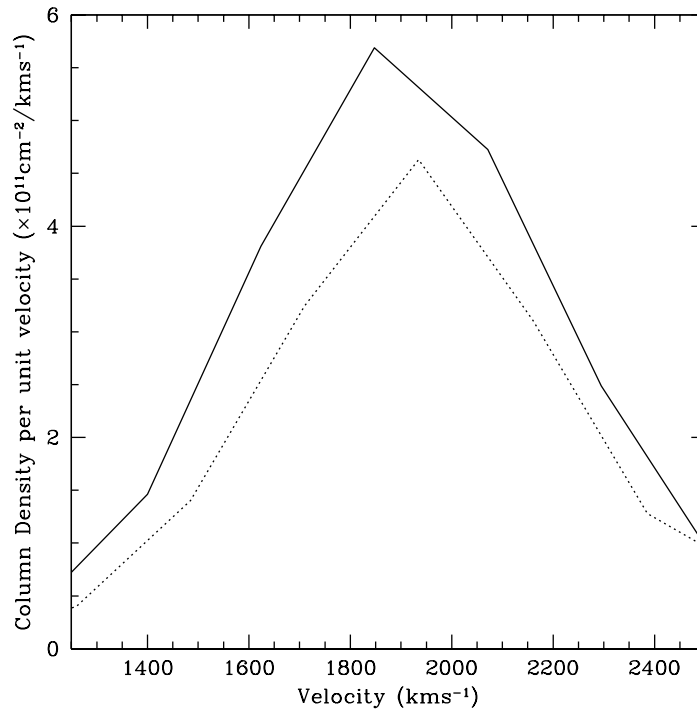


FIGURE 5.12: $N(v)$ calculated for Si IV absorption in the WHT spectrum using equation 5.2.4. The solid line is the weaker component and the dashed line is the stronger component

Observation	Emission Line ID	Velocity range (kms^{-1})	Calculated Column Density ($\times 10^{14} \text{cm}^{-2}$)	Lower Limit On Column Density ($\times 10^{14} \text{cm}^{-2}$)
SDSS	Si IV $\lambda\lambda 1400 \text{ \AA}$	0-10000	67.2 ± 6.7	22.4 ± 2.2
SDSS	C IV $\lambda\lambda 1549 \text{ \AA}$	0-12000	547 ± 55	182 ± 18
SDSS	Mg II $\lambda\lambda 2800 \text{ \AA}$	0-12000	3.87 ± 0.4	1.29 ± 0.1
WHT	Si IV $\lambda\lambda 1400 \text{ \AA}$	0-8000	12.0 ± 1.2	4.00 ± 0.4
WHT	C IV $\lambda\lambda 1549 \text{ \AA}$	0-12000	239.0 ± 24	79.5 ± 8.0
WHT	N V $\lambda\lambda 1240 \text{ \AA}$	0-6000	371.0 ± 37	124 ± 12

Table 5.3: Column densities calculated using the apparent optical depth method. The errors are based on a 10% uncertainty in the positioning of the continuum.

5.2.5 Partial Coverage

The previous methods all implicitly assume that the source is completely covered by a single homogeneous absorber, however this has been shown to be untrue for a number of broad absorption line quasars (Telfer et al. 1998; Churchill et al. 1999; Arav et al. 1999a; Arav et al. 1999b). The simplest modification to complete coverage by a homogeneous absorber is to assume a homogeneous absorber with optical depth τ covering part of the source with the rest of the source passing through material with $\tau=0$. Assuming the expected two to one ratio of optical depths between the blue and red components of an absorption line it can be shown that the covering fraction at a given velocity, $C(v)$ is given by equation 5.2.6, where $I_R(v)$ is the residual intensity of the red component at a given velocity and $I_B(v)$ the residual intensity of the blue component at the same velocity. This equation will give a value for the covering fraction as long as the residual intensities are in the allowed range $I_R(v) \geq I_B(v) \geq I_R(v)^2$. The optical depth of the red component, $\tau(v)$, is then given by equation 5.2.7. In order to perform this analysis the absorption components must be fully resolved. Thus this analysis is restricted to the WHT Si IV absorption only.

$$C(v) = \frac{I_R(v)^2 - 2I_R(v) + 1}{I_B(v) - 2I_R(v) + 1} \quad (5.2.6)$$

$$\tau(v) = -\ln \left[\frac{I_R(v) - I_B(v)}{1 - I_R(v)} \right] \quad (5.2.7)$$

Before calculating covering fractions and optical depths the data from the blue component is interpolated into the same velocity space as the red data. The optical depth and covering fraction are calculated between 1200 and 2600 kms^{-1} , chosen because outside of this velocity range the residual intensities do not fall in the range $I_R(v) \geq I_B(v) \geq I_R(v)^2$ and equations 5.2.6 and 5.2.7 are no longer appropriate. The resulting covering fraction, $C(v)$, is shown along with the residual intensities, I_R and I_B , in Figure 5.13. These data show the common result that the covering fraction follows the shape of the blue absorption suggesting that the shape of the trough is determined predominantly by variations in the gas covering fraction with velocity,

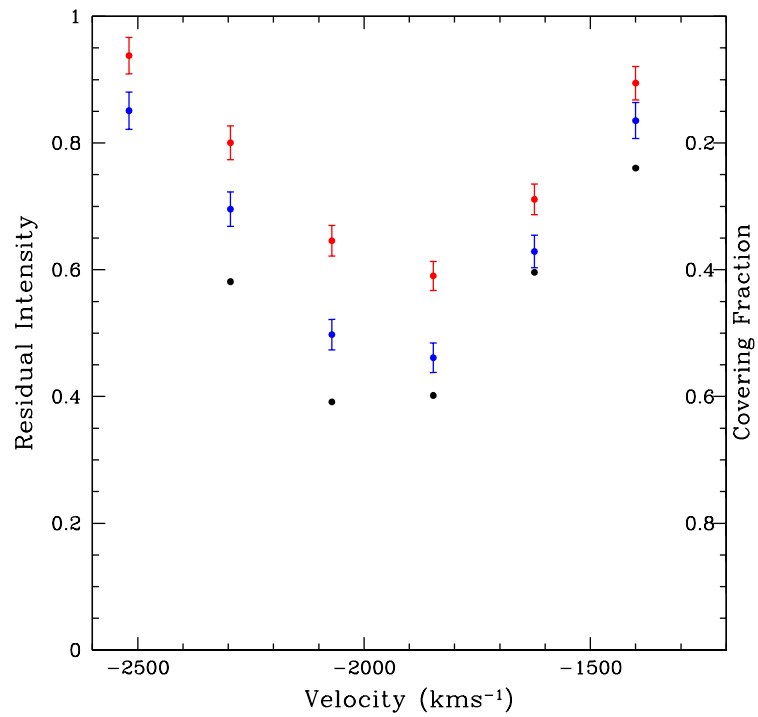


FIGURE 5.13: The red and blue points are the measured residual intensities of the red and blue absorption components of the Si IV absorption from the WHT observation of SDSS J1138+3517. The black points show the covering fraction calculated from equation 5.2.6 (shown increasing downwards so that the uncovered fraction is below the points).

rather than velocity dependent variations in the optical depth (Arav et al. 1999b; de Kool et al. 2001). The average ionised column density of Si IV based on the optical depth and covering fractions is calculated from equation 5.2.4 multiplied by the covering fraction. This gives $N_{Si\ IV} = 6.7 \pm 0.2 \times 10^{14} \text{cm}^{-2}$.

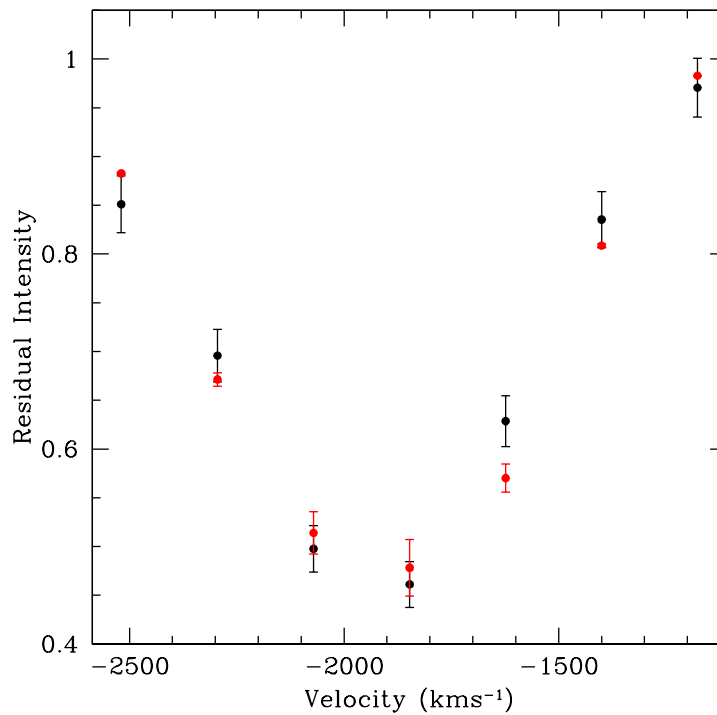


FIGURE 5.14: The black points are the residual intensity of the blue absorption component of the Si IV absorption seen in the WHT spectrum of SDSS J1138+3517. The red points are the fit produced by using a partial coverage model and fitting the data to the red absorption component. The error bars on the fit are based on the errors on the covering fraction and not the errors on the residual intensity of the red absorption component.

If instead of allowing the covering fraction and optical depth to vary with velocity the covering fraction is assumed to remain constant with velocity, the residual intensity of the blue component can be predicted from the residual intensity of the red component. The expected value of the blue component can then be compared to the actual residual intensity in order to find the value of the covering fraction that minimises χ^2 . The column density can then be calculated using equation 5.2.4 and modified by multiplying by the covering fraction. Fitting this absorption gives a covering fraction of $0.56^{+0.07}_{-0.05}$ resulting in an ionised column density of Si IV measured between 1000 and 2600 kms^{-1} of $6.6^{+0.7}_{-0.5} \times 10^{14} \text{cm}^{-2}$. The resulting fit to the data is shown in Figure 5.14. Using the value of the covering fraction to modify the EW measurements and repeat the curve of growth analysis performed in section 5.2.2 gives an ionised column density of $7.1 \pm 0.7 \times 10^{14} \text{cm}^{-2}$ consistent with the results obtained above.

5.2.6 An inhomogeneous absorber model

An alternative way to model the absorbing material is to assume that the optical depth profile across the source varies as some function of position. This method was employed by de Kool et al. 2002a and de Kool et al. 2002b as well as Arav et al. 2005 who showed that the results obtained by using Gaussian and power law optical depth functions are very similar.

I have therefore followed their procedure and used a model where the optical depth across the source varies as $\tau = \tau_{max}x^a$ where τ_{max} is the peak optical depth, x is a measurement of the position along the source (where $0 \leq x \leq 1$), and a is the power law slope which is always positive. In order to constrain a a similar method to that used for the partial covering method is employed. The value of a is fixed and the optical depth calculated for values of τ_{max} in 1000 bins across the source, the residual intensity for each bin and the total residual intensity calculated. The value of τ_{max} which produces the residual intensity for each point in the red absorption trough is then found and used to predict the residual intensity of the corresponding point in the blue absorption trough by assuming the ratio of optical depths takes the theoretical two to one value. This then allows χ^2 to be calculated and minimised as a function of only a . Since this analysis also requires resolved doublets it is performed on the WHT Si IV absorption only. The absorption is best fit by $a=3.1^{+1.0}_{-0.7}$, resulting in an ionised column density of $5.57^{+1.1}_{-0.6} \times 10^{14} \text{cm}^{-2}$. This fit is shown in Figure 5.15.

Figures 5.16 and 5.17 show how the values of the mean optical depth, $\bar{\tau}$, calculated based on the power law model vary from the values of τ that would be calculated based on a partial covering model. It also shows how the residual intensities in the blue component differ from what one might expect from complete coverage by a homogeneous absorber. These differences are shown for a variety of values of the power law slope and are much larger for steeper slopes.

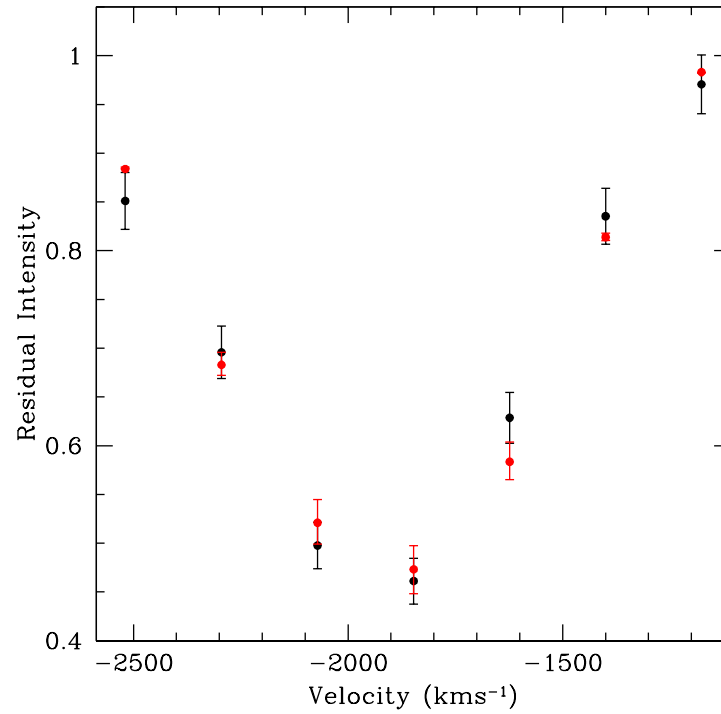


FIGURE 5.15: The black points are the residual intensity of the blue absorption component of the Si IV absorption seen in the WHT spectrum of SDSS J1138+3517. The red points are the fit produced by using a inhomogeneous coverage model where the optical depth varies as a power law across the source. The error bars on the fit are based on the errors on the power law slope and not the errors on the residual intensity of the red absorption component.

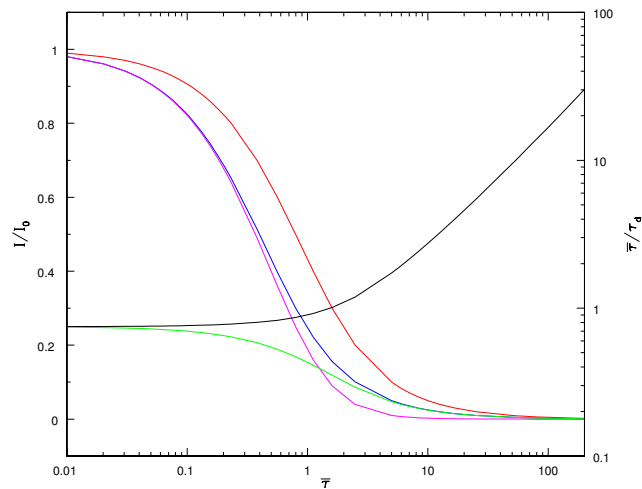


FIGURE 5.16: The values of the residual intensity observed in the red (I_R shown in red) and blue (I_B shown in blue) components of the absorber based on an optical depth model following the equation given. The magenta line shows the square of the residual intensity in the red (I_R^2) which is what one would be expected for the residual intensity in the blue if the absorption was from complete coverage by a homogeneous absorber. The green line shows $1 - C$, where C is the covering fraction that would be calculated from a partial coverage model assuming a homogeneous absorber. Finally the black line shows the ratio of the mean optical depth in the power law model to the optical depth calculated from a partial coverage model with the same values of I_R and I_B .

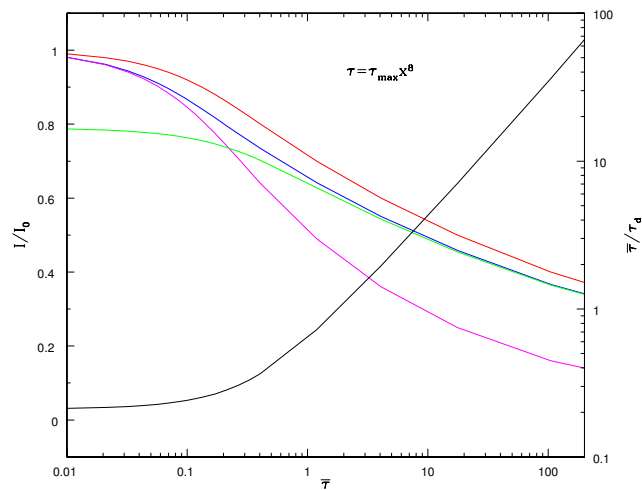


FIGURE 5.17: The values of the residual intensity observed in the red (I_R shown in red) and blue (I_B shown in blue) components of the absorber based on an optical depth model following the equation given. The magenta line shows the square of the residual intensity in the red (I_R^2) which is what one would be expected for the residual intensity in the blue if the absorption was from complete coverage by a homogeneous absorber. The green line shows $1 - C$, where C is the covering fraction that would be calculated from a partial coverage model assuming a homogeneous absorber. Finally the black line shows the ratio of the mean optical depth in the power law model to the optical depth calculated from a partial coverage model with the same values of I_R and I_B .

5.2.7 Column Density Estimates

Column densities have been estimated for a number of different absorbers in both SDSS and WHT observations of SDSS J1138+3517 using a variety of different methods. The estimates obtained are summarised in Table 5.2.7. Component fitting gives column densities significantly lower than those obtained by direct integration. As described in section 5.2.4, since the direct integration method gives a firm lower limit, this value is taken to be the lower limit when it exceeds the values obtained via other methods. Three of these methods require resolved doublet components and are only testable for the WHT Si IV data. The curve of growth analysis is one such method and the column density calculated agrees closely with the value obtained by direct integration. The two methods which do not assume complete coverage of the source give Si IV ionised column densities around 50% larger than the lower limits calculated from the other methods and importantly provide firm upper limits allowing more stringent constraints on the physical conditions within the gas.

The C IV absorption requires an ionised column density of greater than $1.82 \times 10^{16} \text{cm}^{-2}$ in the SDSS observation and greater than $7.95 \times 10^{15} \text{cm}^{-2}$ in the WHT observation, both of these limits are based on direct integration. The Si IV absorption in the SDSS observation requires an ionised column density in excess of $2.24 \times 10^{15} \text{cm}^{-2}$ and this is again based on direct integration. The WHT Si IV absorption shows resolved doublet features which allow a more detailed analysis. Using the partial coverage method the ionised column density required to produce this absorption is $6.61_{-0.5}^{+0.7} \times 10^{14} \text{cm}^{-2}$. By using a power law optical depth profile the absorption can be reproduced by an ionised column density of $5.57_{-0.6}^{+1.1} \times 10^{14} \text{cm}^{-2}$. If we assume that the real distribution of gas falls between the partial coverage and power law models then the absorption is produced by an ionised column density between $5.0 \times 10^{14} \text{cm}^{-2}$ and $7.3 \times 10^{14} \text{cm}^{-2}$. The Mg II absorption in the SDSS observation requires an ionised column density in excess of $1.29 \times 10^{14} \text{cm}^{-2}$ and the N V absorption in the WHT observation requires an ionised column density exceeding $1.24 \times 10^{16} \text{cm}^{-2}$.

Observation	Emission Line	Column Density Estimates ($\times 10^{14} \text{cm}^{-2}$)					Partial Coverage Curve of Growth
		Curve of Growth	Fitting Components	Direct Integration	Partial Covering	Power law	
SDSS	Si IV $\lambda\lambda 1400\text{\AA}$		5.25 ± 0.55	22.4 ± 2.2			
SDSS	C IV $\lambda\lambda 1549\text{\AA}$		23.6^{+2}_{-3} *	182 ± 18			
SDSS	Mg II $\lambda\lambda 2800\text{\AA}$			1.29 ± 1.3			
WHT	Si IV $\lambda\lambda 1400\text{\AA}$	$4.02^{+0.70}_{-0.55}$	0.743 ± 0.077	4.00 ± 0.4	$6.61^{+0.7}_{-0.5}$	$5.57^{+1.1}_{-0.6}$	7.1 ± 0.7
WHT	C IV $\lambda\lambda 1549\text{\AA}$		34.9 ± 8.9	79.5 ± 8.0			
WHT	N V $\lambda\lambda 1240\text{\AA}$			124 ± 12			

Table 5.4: A summary of column density estimates produced by the five different methods described. The Curve of Growth column gives the estimated column density using the curve of growth analysis in section 5.2.2. The Fitting Components column gives the column density estimated by fitting Gaussian absorption profiles to the absorption as described in section 5.2.3. The Direct Integration column gives the lower limit on the column density calculated by directly integrating the apparent optical depth as described in section 5.2.4. The partial coverage column gives the optical depth calculated by partial coverage as described in section 5.2.5. The power law column gives the column density measured assuming a power law distribution of optical depth as described in section 5.2.6. The final column gives the column density measured by the curve of growth method using EWs modified to take into account partial coverage. * This column density is measured from only the higher velocity components. The true column density will be much larger as the lower velocity absorption is saturated.

5.3 Changes between the SDSS and WHT observations

It is clear from the ionised column densities that changes have occurred between the SDSS and WHT observations. From Figure 5.1 it is clear that the C IV and Si IV absorption has weakened significantly between the SDSS and WHT observations as is found in section 5.2. The EWs of the C IV, Si IV and N V emission lines have also decreased slightly. Such changes are likely to be due to either a change in the covering fraction of the outflow or a change in the ionisation state of the gas. In order to examine the physical conditions within the gas and attempt to explain the changes seen between the observations section 5.4 looks at photo-ionisation models of the absorbing gas.

5.4 Photo-Ionisation Models

The limits on the ionised column densities derived from the various absorption lines can be used to obtain information on the physical state and location of the absorbing gas. In order to do this we compute a grid of photo-ionisation calculations of the gas surrounding the AGN using an appropriate model of the ionising continuum for this source. These models are computed using version 08.00 of Cloudy (Ferland et al. 1998). Cloudy is a 1 dimensional code designed to calculate the physical conditions within a non-equilibrium gas exposed to an external radiation source (Ferland et al. 1998). Cloudy calculates the temperature and ionisation state of the gas in a large number of zones, starting with the illuminated face of the cloud. Once these have been calculated for each zone the intensity and shape of the radiation impacting the next zone can be computed. This allows the temperature and ionisation state of the next zone to be calculated. This process is continued until either the edge of the cloud is reached or the temperature has dropped below 4000K as at this point the gas will be essentially neutral and not contribute significantly to the ionised column density of anything other than neutral atoms. A large number of physical processes contribute to the heating, cooling and ionisation of the gas, and these processes are modelled by calculations within Cloudy. Hazy, the codes documentation which is available from <http://www.nublado.org/> contains the details of these calculations, which are not discussed here as they are not the subject of this thesis.

Cloudy calculates emission line strengths, ionisation fractions and ionised columns for various species for a given hydrogen column density, N_H , gas density, n_H , ionisation parameter, U , and the shape of the ionising continuum. U , the ionisation parameter, is a measure of the ratio of the density of photons of wavelength $<912 \text{ \AA}$ to hydrogen densities at the illuminated face of the cloud and depends on the shape of the ionising spectrum, the gas density and the distance of the gas from the ionising continuum source (equation 5.4.1). By using an appropriate quasar spectrum as our ionising source and requiring that the calculated column densities for absorbing ions meet the limits imposed by the calculations in section 5.2 we can constrain the values of hydrogen column density, gas density and U . The allowed values of U and n_H can then be used to place constraints on the distance between the AGN and the absorbing gas using equation 5.4.1.

$$U = \frac{Q(H)}{4\pi r^2 c n_H} \quad (5.4.1)$$

$Q(H)$ is the total number of hydrogen ionising photons emitted by the ionising continuum per second, r is the distance from the ionising continuum source, c the speed of light and n_H and U the hydrogen density and ionisation parameter respectively. $Q(H)$ can be calculated from the quasar spectrum allowing the distance to be found from U and n_H .

In order to calculate the ionisation state of the gas Cloudy requires as input a spectrum of the ionising continuum. The spectrum used here is a standard AGN spectrum described by Mathews & Ferland 1987 parameterised by a 'big blue bump' temperature, T_{BB} of 10^6 K , an optical to ultraviolet power law slope, α_{UV} , a hard X-ray power law with a slope α_X and α_{OX} the spectral index between 2500 \AA and 2 keV . Typical values of α_{UV} and α_X for quasars are 0.0 and -1.0 respectively and these values are used throughout. For α_{OX} we estimate the slope from the optical flux using equation 5.4.2 which is equation 12 from Wilkes et al. 1994. L_O is the specific intensity at 2500 \AA in the rest-frame in units of $\text{erg s}^{-1} \text{ Hz}^{-1}$ which for this object is approximately 1×10^{34} leading to $\alpha_{ox} = 1.92 \pm 0.09$.

$$\alpha_{OX} = (0.11 \pm 0.02)(\log(L_O) - 30.5) + (1.53 \pm 0.02) \quad (5.4.2)$$

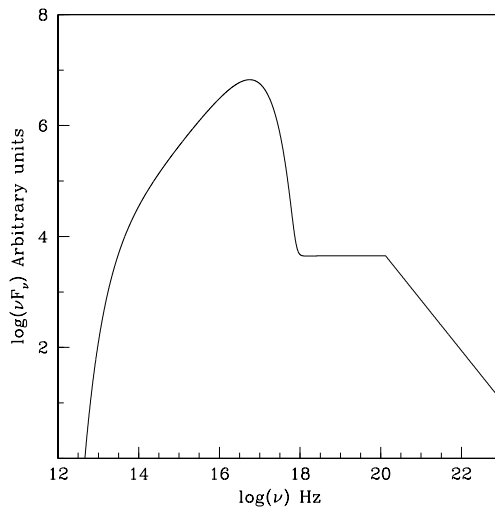


FIGURE 5.18: The spectral energy distribution of the ionising spectrum used by Cloudy to compute the models. The νF_ν axis is in arbitrary units as the absolute flux Cloudy uses is based on the input value of the ionisation parameter.

The spectrum used for these calculations has $\alpha_{OX}=1.9$ and is shown in Figure 5.18. Models were also calculated using $\alpha_{OX}=1.6$, but the difference in the ionisation fractions and ionised column densities was found to be small. Cloudy also requires as input the hydrogen gas density and a total hydrogen column density. For simplicity we assume solar abundances as any deviation from this can be calculated using the method of Hamann 1997 (see section 5.3). Finally the intensity of the quasar spectrum at the ionised face of the cloud is fixed by the Ionisation parameter U . Cloudy outputs, amongst other things, the reflected and transmitted continuum, emission-line intensities as well as the column densities and ionisation fractions of each ionisation state for a large number of atoms. These are calculated for a range of values of U , N_H and n_H .

5.4.1 Models

Ionised columns for a large number of ions have been calculated for gas with Hydrogen densities of $10^5, 10^7, 10^9$ and 10^{11} cm^{-3} and total Hydrogen gas column densities of $10^{20}, 10^{21}, 10^{22}, 10^{23}$ and 10^{24} cm^{-2} illuminated by the AGN spectrum described in section 5.4 with \log_{10} of the ionisation parameter between -5 and 1. The resulting N^{4+} , C^{3+} , Si^{3+} and Mg^+ ionised column densities are plotted against ionisation parameter for a selection of these models in Figures 5.19 to 5.28. Also included on these

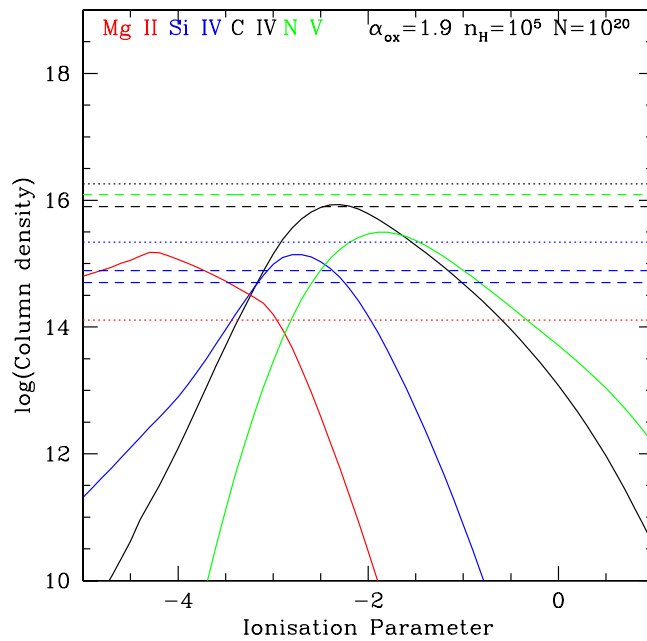


FIGURE 5.19: Ionised Column density as a function of ionisation parameter calculated by Cloudy using a quasar spectrum with $T_{BB}=10^6\text{K}$, $\alpha_{OX}=1.9$, $\alpha_{UV}=0.0$ and $\alpha_X=-1.0$ illuminating gas with a density of 10^5 cm^{-3} and a Hydrogen column density of 10^{20} cm^{-2} . The different colours represent different ionised species, the colour key is in the top left hand corner. The dashed lines represent the lower limits on column density from the WHT spectrum and the dotted lines are the lower limits based on the SDSS spectrum. The WHT Si IV upper and lower limits are both shown by dashed blue lines, the ionised column of Si IV should lie between these lines.

plots are the lower limits for these ions calculated using the absorption in the SDSS and WHT spectra of SDSS J1138+3517. The colour code shown on the plots is used for both the calculated ionised column densities and the limits from the SDSS and WHT data. The SDSS limits are shown as dotted lines and are all lower limits. The WHT limits are shown as dashed lines, the C IV and N V limits are just lower limits but the Si IV absorption has both upper and lower limits.

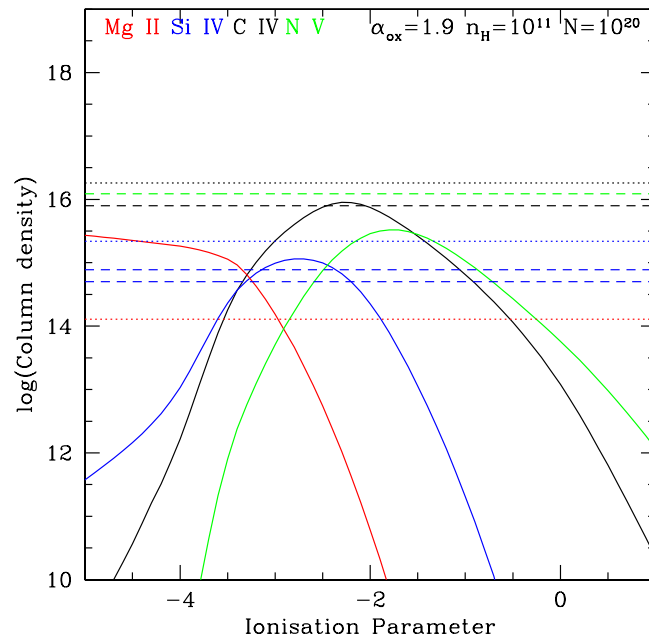


FIGURE 5.20: Ionised Column density as a function of ionisation parameter with $n_H=10^{11} \text{ cm}^{-3}$ and $N_H=10^{20} \text{ cm}^{-2}$. The colour code is in the top left. The dashed lines are WHT lower limits (except for Si IV see caption of fig 5.19) and dotted lines are SDSS lower limits.

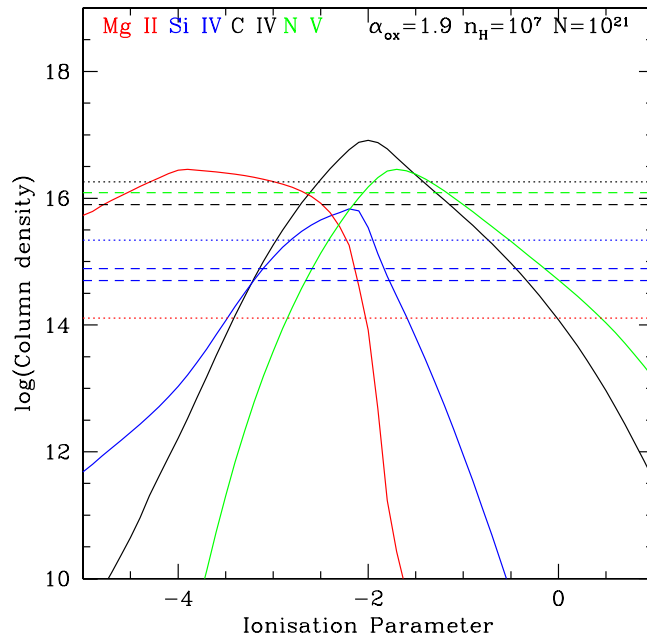


FIGURE 5.21: Ionised Column density as a function of ionisation parameter with $n_H=10^7 \text{ cm}^{-3}$ and $N_H=10^{21} \text{ cm}^{-2}$. The colour code is in the top left. The dashed lines are WHT lower limits (except for Si IV see caption of fig 5.19) and dotted lines are SDSS lower limits.

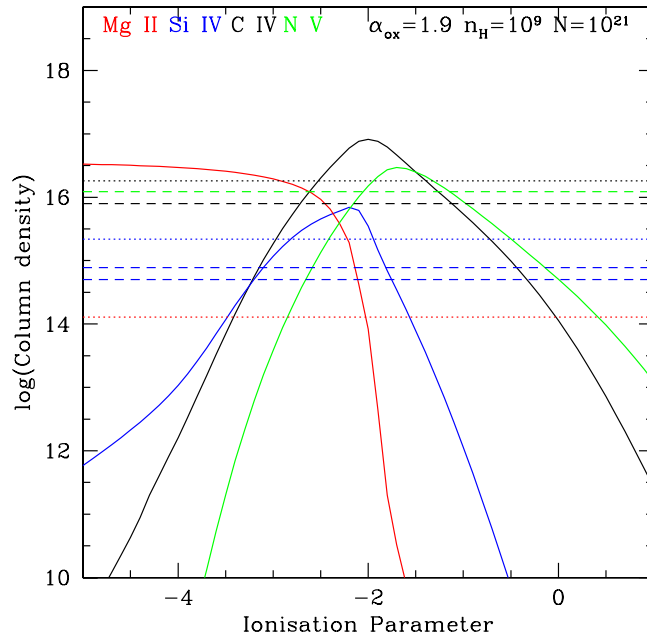


FIGURE 5.22: Ionised Column density as a function of ionisation parameter with $n_H=10^9 \text{ cm}^{-3}$ and $N_H=10^{21} \text{ cm}^{-2}$. The colour code is in the top left. The dashed lines are WHT lower limits (except for Si IV see caption of fig 5.19) and dotted lines are SDSS lower limits.

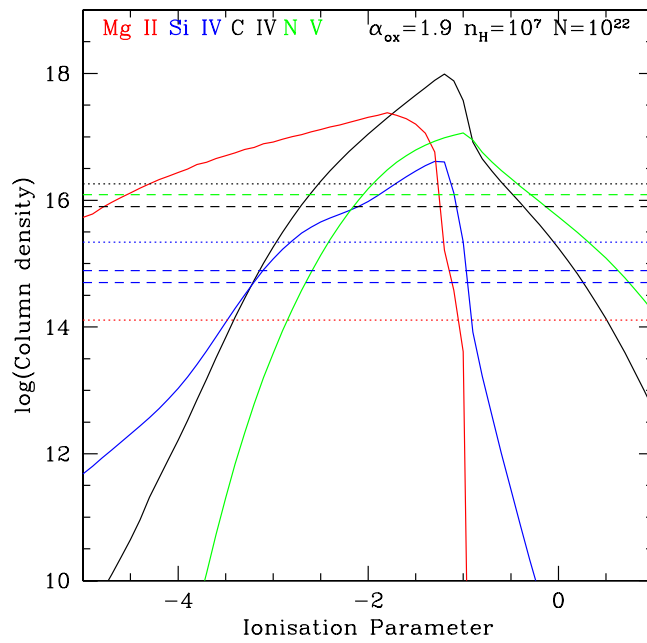


FIGURE 5.23: Ionised Column density as a function of ionisation parameter with $n_{\text{H}} = 10^7 \text{ cm}^{-3}$ and $N_{\text{H}} = 10^{22} \text{ cm}^{-2}$. The colour code is in the top left. The dashed lines are WHT lower limits (except for Si IV see caption of fig 5.19) and dotted lines are SDSS lower limits.

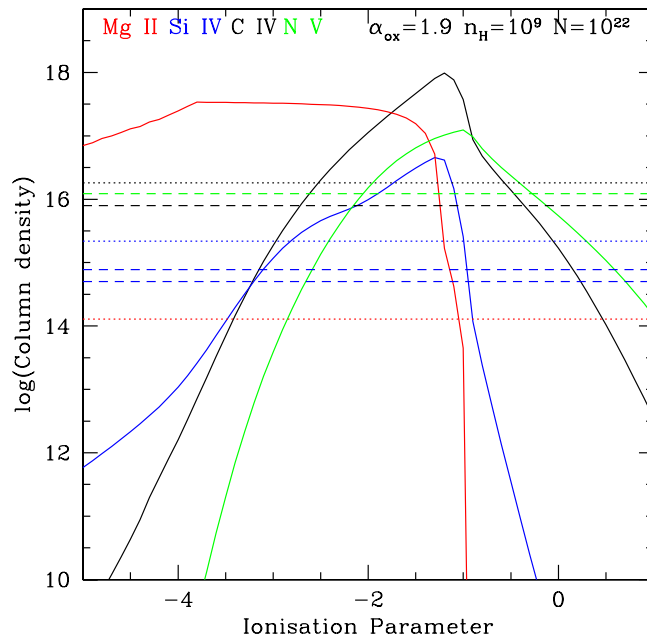


FIGURE 5.24: Ionised Column density as a function of ionisation parameter with $n_{\text{H}} = 10^9 \text{ cm}^{-3}$ and $N_{\text{H}} = 10^{22} \text{ cm}^{-2}$. The colour code is in the top left. The dashed lines are WHT lower limits (except for Si IV see caption of fig 5.19) and dotted lines are SDSS lower limits.

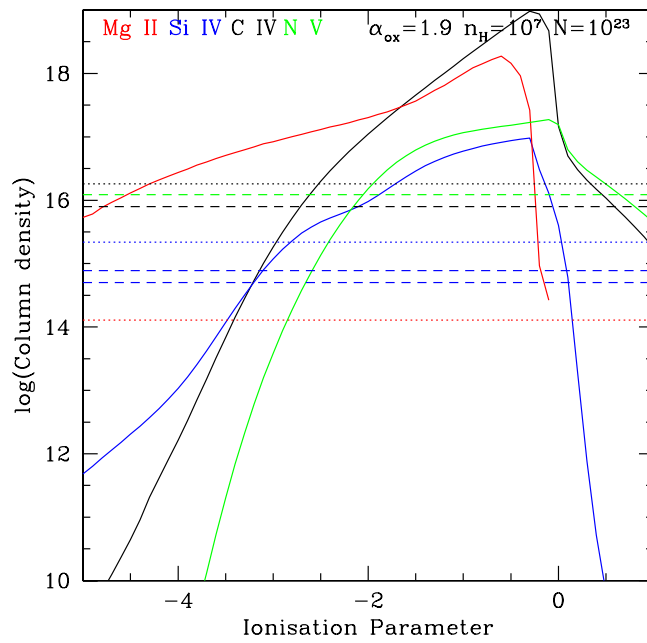


FIGURE 5.25: Ionised Column density as a function of ionisation parameter with $n_H=10^7 \text{ cm}^{-3}$ and $N_H=10^{23} \text{ cm}^{-2}$. The colour code is in the top left. The dashed lines are WHT lower limits (except for Si IV see caption of fig 5.19) and dotted lines are SDSS lower limits.

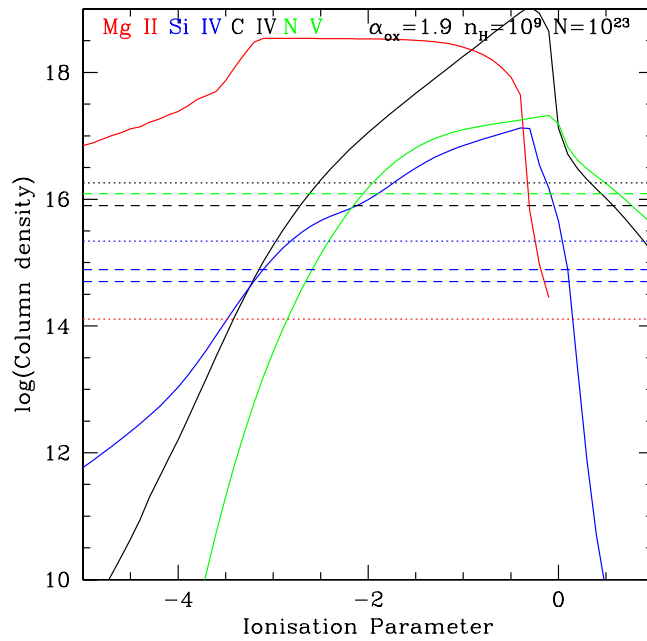


FIGURE 5.26: Ionised Column density as a function of ionisation parameter with $n_H=10^9 \text{ cm}^{-3}$ and $N_H=10^{23} \text{ cm}^{-2}$. The colour code is in the top left. The dashed lines are WHT lower limits (except for Si IV see caption of fig 5.19) and dotted lines are SDSS lower limits.

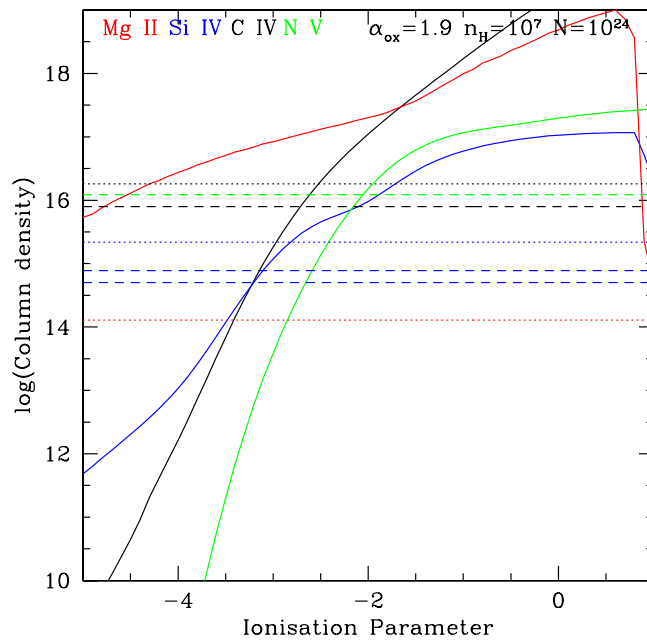


FIGURE 5.27: Ionised Column density as a function of ionisation parameter with $n_H=10^7 \text{ cm}^{-3}$ and $N_H=10^{24} \text{ cm}^{-2}$. The colour code is in the top left. The dashed lines are WHT lower limits (except for Si IV see caption of fig 5.19) and dotted lines are SDSS lower limits.

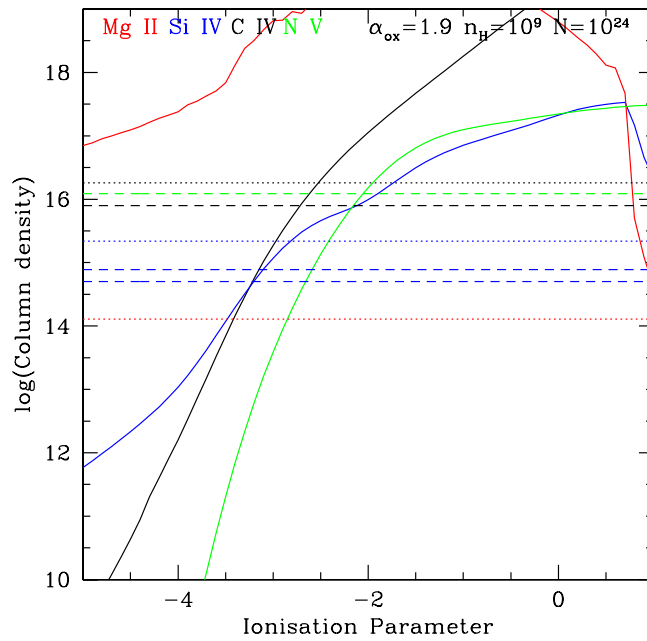


FIGURE 5.28: Ionised Column density as a function of ionisation parameter with $n_H=10^9 \text{ cm}^{-3}$ and $N_H=10^{24} \text{ cm}^{-2}$. The colour code is in the top left. The dashed lines are WHT lower limits (except for Si IV see caption of fig 5.19) and dotted lines are SDSS lower limits.

5.4.2 Constraints on the physical conditions within the absorbing clouds

Using the limits on the ionised column densities from the SDSS and WHT spectra it is possible to place limits on U , N_H and n_H . In order for a model to be plausible it must be able to simultaneously satisfy the limits on ionised columns for the various species at some range of the ionisation parameter. Once limits have been placed on U and n_H it is possible to calculate the total ionising photon flux, $Q(H)$ using the input spectrum fixed to match the measured flux in the observations. $Q(H)$ can then be used along with limits on U and n_H to place limits on the distance, r , between the ionising source and the absorbing material using equation 5.4.1. This section will look at the two observations in turn before discussing possible causes of the changes described in section 5.3. The mass and kinetic luminosity of the outflow are discussed in section 5.5.

SDSS

As only lower limits on the ionised column densities of Si IV, C IV and Mg II are found from the SDSS spectra there are a wide range of parameters that are capable of satisfying these limits. The Si IV and C IV limits require Hydrogen column densities, N_H , in excess of 10^{20}cm^{-2} . With $N_H=10^{20} \text{cm}^{-2}$ the ionised columns of these species do not exceed the lower limits for any value of $\log_{10}(U)$ as can be seen in Figures 5.19 and 5.20. With $N_H=10^{21} \text{cm}^{-2}$ the SDSS limits allow values of $\log_{10}(U)$ ranging from -2.6 to -1.9 (see Figures 5.21 and 5.22). This range is slightly effected by changes in the gas density, n_H , with the lower limit decreasing from -2.4 to -2.6 as gas density increases. The upper limit also decreases with increasing density from -1.9 to -2.0 . The upper limit on $\log_{10}(U)$ is set by the ionised column density of Mg II and increases significantly with N_H . It is -1.0 at $N_H=10^{22} \text{cm}^{-3}$ (see Figures 5.23 and 5.24), 0.0 at $N_H=10^{23} \text{cm}^{-3}$ (see Figures 5.25 and 5.26) and above 1.0 at $N_H=10^{24} \text{cm}^{-3}$ (see Figures 5.27 and 5.28). The lower limit, set by the ionised column density of C IV, does not change drastically as N_H increases. Using equation 5.4.1 and $\log_{10}(U)=-2.6$ gives a distance to the ionising source of $4.7 \pm 0.2 \times 10^{21} n_{H6}^{-1/2} \text{cm} \equiv 1500 \pm 10 n_{H6}^{-1/2} \text{pc}$ where n_{H6} is the hydrogen density in units of 10^6cm^{-3} . As this is based on a lower limit for U the material could be closer to the source, at higher U .

WHT

Using the covering fraction and inhomogeneous absorber model it is possible to place both upper and lower limits on the ionised column density of Si IV at the time of the WHT observation. Having both upper and lower limits places much more stringent constraints on the possible range of U at given N_H and n_H . The Si IV limits used are the lower limit from the power law optical depth model and the upper limit from the partial coverage model. These limits provide stringent constraints on the value of U at given N_H , with two regions in U providing appropriate values. The lower U of these bands remains fairly constant with N_H giving limits $-3.3 < \log_{10}(U) < -3.0$, this is because the position of the low U region is determined by the value of U at which there are enough ionising photons to produce the required ions. The allowed high U region is typically very narrow and increases as N_H increases as the more material present the higher values of U that will allow the appropriate ions to be formed within a cloud. The lower region of U for which the Si IV limits are met is not at high enough ionisation parameter for the C IV or N V lower limits to be met. This is not the case for the higher U region. None of the $N_H=10^{20}\text{cm}^{-2}$ models are able to provide enough absorbing material to be consistent with the lower limit on N V absorption. With $N_H=10^{21}\text{cm}^{-2}$ the value of $\log_{10}(U)$ is constrained to be between -1.8 and -1.6 . This provides a lower limit of $\log_{10}(U)=-1.8$ for the WHT data as higher values of N_H move the region for which the Si IV limits are met to higher U . As both C IV and N V are more highly ionised than Si IV they are produced marginally closer to the ionising continuum and will therefore produce larger ionised column densities at higher values of N_H and U (see Figures 5.23 to 5.28). This means that when the Si IV limits are met by the higher U values the limits on C IV and N V will also be met. Consequently this means that increasing the value of N_H to an arbitrarily high value is not ruled out by these limits, the models simply require larger and larger values of U . We therefore only have a lower limit on the value of $\log_{10}(U)$. Using this limit ($\log_{10}(U) > -1.8$) in equation 5.4.1 along with the value of $Q(H)$ calculated for the input spectrum by Cloudy the distance of the absorbing material from the cloud is calculated to be $1.8 \pm 0.1 \times 10^{21} n_{H6}^{-1/2}$ cm $\equiv 600 \pm 5 n_{H6}^{-1/2}$ pc where n_{H6} is the hydrogen density in units of 10^6 cm^{-3} . Again this limit is based on a lower limit on U , higher values of U will give a smaller distance so this is an upper limit.

Are the observations consistent with a change in ionisation parameter?

The change in the absorption within this object has two obvious possible causes. One is that material has moved out of the line of sight between the observations and the other is a change in the ionisation of the outflow. We can use the ionised column densities of C IV and Si IV to measure the size of any change in ionisation parameter by assuming that the ratio of C to Si remains constant. The ratio of C IV to Si IV in the outflow will then depend on the value of U (and to a lesser degree N_H and n_H). The ratio of C to Si abundances can be calculated using equation 5.4.3 which is equation 2 from Hamann 1997.

$$\left[\frac{C}{Si}\right] = \log \left[\frac{N(C\ IV)}{N(Si\ IV)}\right] + \log \left[\frac{f(Si\ IV)}{f(C\ IV)}\right] + \log \left(\frac{Si}{C}\right)_{\odot} \quad (5.4.3)$$

Assuming that these lower limits on the ionised columns of C IV and Si IV are accurate column density measurements, which is a very weak assumption, and that the metallicity doesn't change this allows the change in the ionisation parameter between observations to be estimated by plotting $\left[\frac{C}{Si}\right]$ as a function of U for given values of N_H , n_H . This has been done for the full range of these values calculated in section 5.4, however as the plots are all extremely similar only two are included here in Figures 5.29 and 5.30. From these figures it is clear the the ionisation parameter is larger at the time of the WHT observation. However, this may be due to the C IV column density being significantly underestimated for the SDSS observation as it appears to be highly saturated.

The lower limit on the Si IV ionised column density from the SDSS observation is larger than the upper limit from the WHT observation, the ionised column density of C IV has also decreased between the SDSS and WHT observations. The values of U for which the limits are met for the WHT observations suggest that the Si IV and C IV absorption would decrease with an increase in U . This is consistent with the finding from the C and Si ratio that U increases between the SDSS and WHT observations. If the value of U has increased between the two observations then one would expect to see an increase in the luminosity of the UV continuum. It is difficult to tell whether this is indeed the case due to problems with the flux calibration between the SDSS DR5 and DR7 data and the WHT observations. These issues have been discussed in Chapter 4. In addition an increase in U would result in a decrease in the ionised column density responsible for the C IV, Si IV and N V emission lines in the BLR, if the ionisation state in this region is similar to that

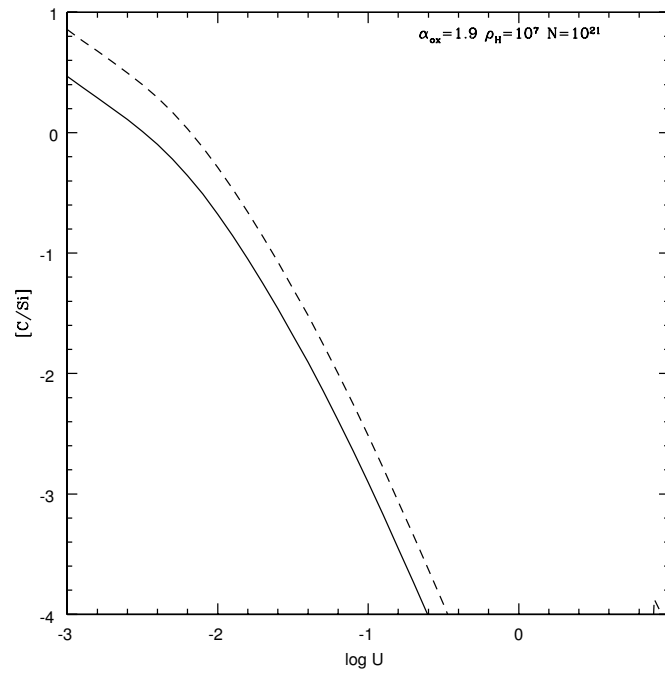


FIGURE 5.29: $\left[\frac{C}{Si}\right]$ as calculated from equation 5.4.3 using ionisation fractions computed with $N_H=10^7$, $n_H=10^{21}$. The dashed line is based on the WHT Column density lower limits and the solid line on the SDSS lower limits.

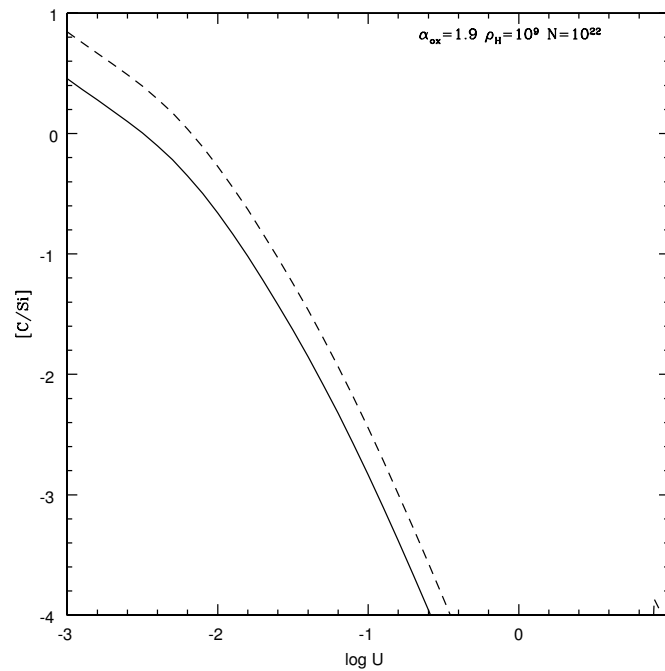


FIGURE 5.30: $\left[\frac{C}{Si}\right]$ as calculated from equation 5.4.3 using ionisation fractions computed with $N_H=10^9$, $n_H=10^{22}$. The dashed line is based on the WHT Column density lower limits and the solid line on the SDSS lower limits.

in the outflow. Such a decrease in emission line EW is evident in Figure 5.1. This suggests that an increase in ionisation parameter caused by a change in the luminosity is consistent with the observations.

5.5 Mass of the outflow

The lower limits on U have given upper limits on the distance from the ionising source, a lower limit on this distance can be implied by the absorption of the broad C IV and Si IV lines. As some of the underlying emission line flux is absorbed the absorbing material must lie outside of the broad line region. The size of the broad emission-line region can be estimated using the luminosity of the source at 1450 Å from scaling relationships derived for nearby AGN (Kaspi et al. 2005). This luminosity is only slightly different between the two observations which both give sizes of approximately $3.6 \pm 0.4 \times 10^{18}$ cm \equiv 1.17 ± 0.1 pc for the broad line region. The upper limits on the distance to the absorbers in both observations are consistent with the absorbing material being outside of the broad line region for all reasonable densities. We can therefore place boundaries on the distance between the absorbing material and the black hole. The mass of the outflowing material, \dot{M}_{out} can be found by using equation 5.5.1 (taken from Crenshaw et al. 2009), where r is the distance from the source, N_H the hydrogen column density, μ the mean atomic mass per proton, m_p the mass of a proton, C the covering fraction as viewed from the source and v_r the radial outflow velocity. This equation can be rewritten as equation 5.5.2 where r_{22} is the radius in units of 10^{22} cm, N_{H21} the column density in units of 10^{21} cm $^{-2}$ and v_3 the velocity in units of 1000 kms $^{-1}$.

$$\dot{M}_{out} = 8\pi r N_H \mu m_p C v_r \quad (5.5.1)$$

$$\dot{M}_{out} = 740 r_{22} N_{H21} \mu C v_3 M_{\odot} yr^{-1} \quad (5.5.2)$$

Depending on the value of the distance and hydrogen column density the estimated mass within the outflow can range from a few solar masses per year up to several hundreds of solar masses per year. In order to get an idea of the scale of the outflow one can estimate the accretion rate onto the black hole required to produce the quasar luminosity, this can also be compared to the Eddington Luminosity. In order to

calculate the mass of the black hole the gas in the broad line region is assumed to be virialised, this then allows equation 5.5.3 to be used. The size of the broad line region was estimated as $3.6 \pm 0.4 \times 10^{18}$ cm from the UV luminosity and the effective velocity, v_{eff} can be estimated from the width of the C IV emission line to be ~ 2400 kms^{-1} .

$$M = f \frac{v_{eff}^2 R}{G} \quad (5.5.3)$$

Where f is the virial coefficient which depends on the BLR geometry and is typically between 1 (McLure & Dunlop 2004) and 5.5 (e.g. Onken et al. 2004). Using $f=5$ gives an estimate of $1.56 \times 10^{10} M_{\odot}$ for the black hole mass. The Eddington accretion rate for a black hole of this mass, assuming 10% of the rest mass is converted to luminosity, is approximately $350 M_{\odot}$ per year. The bolometric luminosity, L_{BOL} , can be estimated from $L_{BOL} \sim 4.36 \lambda L_{\lambda}(1450 \text{ \AA})$ (Warner et al. 2004) as around 7.8×10^{47} ergs s^{-1} . This luminosity requires an accretion rate of $140 M_{\odot}$ per year, again assuming 10% of the rest mass is converted to luminosity, and suggests that the black hole is accreting at a significant fraction of the Eddington rate. The fact that this object is accreting at close to the Eddington rate is to be expected if the outflow is driven radiatively. The Luminosity of the source has to approach Eddington in order to have the required power to drive an outflow, although the force multiplier due to line-driving can be large resulting in outflows in sub-Eddington systems (see e.g. Castor et al. 1975).

If we assume that the outflow is only just outside the broad line region for the WHT observations we can use the ionisation parameter in this location to provide an upper limit on N_H . This can be done by using equation 5.4.1 to provide an upper limit on the value of U , this upper limit is $U < \frac{4 \times 10^5}{n_H^4}$ which gives $\log_{10}(U)=1.6$ for $n_H=10^8 \text{ cm}^{-3}$. Even for this relatively high density this provides little constraint on the value of N_H as at $N_H=10^{24} \text{ cm}^{-2}$ the value of U required to meet the ionised column density limits set by the WHT Si IV observations does not exceed this limit. If we assume that $n_H=10^8 \text{ cm}^{-3}$, $N_H=10^{24} \text{ cm}^{-2}$, the outflow is at the edge of the broad line region, covers 10% of the source, has an velocity of 2400 kms^{-1} and $\mu = 1$ the mass outflow rate is $64 M_{\odot}$ per year. If at the other end of the scale we assume the outflow is produced at the greatest allowed distance (assuming $n_H=10^4 \text{ cm}^{-3}$, 10% coverage and $\mu = 1$) then we find the mass of the outflow is $840 M_{\odot}$ per year. It appears then that the mass of the outflow in this object is between about a third and a few times the accretion rate onto the black hole.

As the outflow in this object is between 1 and a few thousand parsecs from the continuum source the distance it will have moved between the observations is considerably smaller than the distance from the source. The upper limit on the distance of $15 \pm 10 n_{H4}^{-1/2}$ kpc is consistent with values calculated in other objects. Dunn et al. 2010 find a broad absorption line system in an object of similar luminosity to SDSS J1138+3517 ($L_{BOL} = 5.0 \times 10^{47}$ erg s⁻¹) at a distance of between 6 and 17 kpc. Similarly Narayanan et al. 2004 find maximum distances of intrinsic narrow absorption systems at relatively high velocity between 1.8 and 7 kpc for objects with bolometric luminosities between 1.9×10^{47} and 9.6×10^{47} erg s⁻¹ although the actual distance of these absorbers from the continuum source could be considerably lower. The estimated mass outflow rate in SDSS J1138+3517 is between a few and a few hundred solar masses per year. Assuming a hundred solar masses per year at an average velocity of 4000 kms⁻¹ this corresponds to a kinetic luminosity ($L_{KE} = 1/2 \dot{M}_{out} v^2$) of 1.0×10^{45} erg s⁻¹. This is around the kinetic luminosity of the similar object discussed in Dunn et al. 2010 and is also comparable to the kinetic luminosity seen in high velocity X-ray outflows (Pounds & Page 2006). Outflows such as this, if present in all galaxies with rapidly accreting central black holes, may be responsible for setting the observed $M_{BH}-\sigma$ relation (Di Matteo et al. 2005). This energy is also similar to that required by Rafferty et al. 2006 to prevent cooling flows in galaxy clusters providing a possible feedback mechanism for preventing the formation of extremely large galaxies at the centre of clusters.

5.6 Summary

This chapter presents photo-ionisation models of the outflow seen in SDSS J1138+3517. Observations of this outflow obtained at two different epochs suggest an increase in the ionisation parameter between the two observations. This is backed up by similar changes in the emission lines. The material is located between tens and thousands of parsecs from the ionising continuum consistent with the outflow lying outside of the BLR. Little information on the density of the outflow is available as the lines observed show little variation with density. However, assuming densities similar to those measured in other BALQSO outflows then the rate at which mass is outflowing in this absorber is comparable to the accretion rate onto

the black hole required to account for the luminosity of the central source. The kinetic luminosity carried by this outflow represents a very significant amount of energy and if such outflows are common in quasars then they will have a considerable impact on the evolution of the galaxies in which they reside.

Chapter 6

Conclusions and Future Work

6.1 Conclusions

The mechanism responsible for the acceleration of the blue-shifted absorption seen in BALQSOs is of interest for a number of reasons. In addition to their importance in AGN unification schemes (e.g. Elvis 2000) these outflows are energetically important in the evolution of their host galaxies and may also play a role in the evolution of the cluster in which the AGN typically reside. The aim of this thesis was to investigate this mechanism by compiling a sample of objects exhibiting evidence for a radiative line-locking feature known as the ghost of Lyman- α .

6.1.1 BALQSOs

The identification of the broad blue-shifted absorption characteristic of BALQSOs is not a simple task. There are many potential sources of contamination including intrinsic absorption from the host galaxy. It is also unclear whether the mini-BALs seen in some sources are created via the same mechanism as traditional BALQSOs (Gibson et al. 2009b). Chapter 2 examines the strengths and weaknesses of the metrics used to identify samples of BALQSOs. Namely the balnicity index (BI:Weymann et al. 1991) and the absorption index (AI:Hall et al. 2002;Trump et al. 2006). Evidence of a bi-modality in the log(AI) distribution has been presented along with evidence that the AI erroneously selects numerous objects showing

little absorption. The incompleteness of BI selected samples particularly for relatively low velocity outflows is noted as an issue with this metric. A robust hybrid method consisting of the use of LVQ algorithms and visual inspection of outliers has been presented (see Knigge et al. 2008 and Scaringi et al. 2009). This method was used to produce a sample of 3552 BALQSOs from DR5 of the SDSS representing a BAL fraction of 12.5%. This fraction is likely to be an underestimate of the true BAL fraction as the algorithm used by the SDSS to select quasars for spectroscopic follow up has been designed to find normal QSOs (Richards et.al 2002).

6.1.2 The ghost of Lyman- α

From a parent sample of 3552 BALQSOs we have compiled a sample of 43 objects exhibiting evidence of the ghost of Ly- α (Chapter 3) and described the method used to select them. The sample of ghost candidates fails to meet Arav's criteria significantly more often than a comparison sample, with stronger broad N v absorption the only significant difference between the two samples.

This draws into question the reality of the ghost phenomenon and prompted an analysis of the location of peaks in C IV absorption troughs. This analysis suggests that the number of objects one would expect to find within the ghost zone by chance is comparable to the number of candidates that have been found. Indeed further investigation shows no evidence for an increased number of peaks around the ghost zone compared to other velocities. These findings strongly suggest that the ghost of Ly- α is not a real feature and that the relatively weak evidence found by Korista et al. 1993 was due to chance. The vast majority of objects from the ghost candidate sample show strong N v absorption and while this is not true of the comparison sample it does appear that features within the C IV absorption are significantly more common in those objects which show strong broad N v absorption. The possibility that these features were produced by shadowing of the Ly- α emission is discussed and a composite spectrum in which the velocity of the first absorption trough is fixed presented. This composite shows no evidence for a feature produced by the shadowing mechanism discussed by Korista et al. 1993.

The follow up observations discussed in Chapter 4 do not change this picture, indeed one of the better ghost candidates SDSS J113831.42+351725.3 shows much weaker evidence of a ghost feature in the follow up observation. The significant changes to this object, amongst the largest changes seen in the absorption of any BALQSO are discussed in Chapter 5 and the following section.

6.1.3 SDSS 1138+3517

Changes to the C IV and Si IV absorption in this object allow constraints to be placed on the physical conditions in the absorbing material. This in turn allows constraints to be placed on the distance from the ionising continuum. The lower limit on the distance to the source is found to be approximately 100 pc depending on the density of the material but is definitely consistent with the absorption occurring outside of the broad line region in this object, which is approximately 1 pc across. The Mass outflow rate depends on many unknown quantities but is likely to be between a fraction of M_{\odot} and several tens of M_{\odot} . This source is accreting close to the Eddington rate and this mass outflow is comparable to, though probably smaller than, the accretion rate. The resulting kinetic luminosity for this outflow is of order 10^{44} ergs s^{-1} , a significant energy that will have considerable impact on the future evolution of this galaxy. The changes observed are found to be consistent with an increase in the ionisation parameter, this is also consistent with the decrease in the EW of the C IV, Si IV and N V emission lines in this object.

6.1.4 Summary

At the beginning of this thesis I set out to determine the nature of the driving mechanism behind the accelerating outflows responsible for the broad absorption lines seen in approximately 15% of quasars. Upon its completion it is clear that this question remains open. However, the research presented in Chapter 3 and Cottis et al. 2010 strongly suggests that a key signature of radiative line driving (the ghost of Ly- α) if present is indeed very rare, with the majority of ghost candidates being the result of the chance alignment of multiple absorption systems. The ghost of Ly- α had previously been seen as the strongest evidence for radiative acceleration of BALQSO outflows. Changes to the absorption in one of the ghost-candidates

observed with the WHT are discussed in detail in Chapter 5. These changes suggests the evidence for the ghost mechanism provided by this object is weak but they do allow constraints to be placed on the location and ionisation of the outflowing material. Whilst the evidence for radiative acceleration has been weakened by this work the mechanism responsible for the acceleration of the high velocity outflows in BALQSOs remains a matter for debate.

6.2 Future Work

Clear evidence in support of any particular mechanism for the acceleration of BAL outflows remains elusive. In order to make progress in our attempt to answer this question we require as much information on the physical state of the outflowing material as we can extract.

6.2.1 Constraining the physical conditions in BAL outflows

In order to further narrow the possible range of conditions within broad absorption line outflows it would be useful to obtain high S/N, high resolution spectra of a large number of BALQSOs. Such high quality spectra would allow the doublets of C IV to be resolved which would allow much more stringent constraints to be placed on the conditions within the absorbing gas, although in the case of SDSS J1138+3517 this absorption may be saturated, limiting the information that can be found in higher quality data. It would also be beneficial for these observations to cover multiple lines from the same species as this would allow determination of the covering fraction and/or distribution of this gas. Such observations have been undertaken by Bautista et al. 2010 who find Fe II absorption located approximately 1 kpc from the ionising continuum. However increasing the number of objects for which such analysis can be undertaken would provide valuable information on the range of properties in these outflows.

The ionised column densities could then be used to constrain the ionisation parameter, Hydrogen density, Hydrogen column density and distance from the ionising continuum (see e.g. Chapter 5). With observations of multiple objects it would then be possible to investigate the position of the absorption to look for

any relationship between the velocity of absorption and its position or ionisation. This may allow us to determine whether the outflows are launched at high velocity and then decelerated or launched at lower velocity and accelerated. The luminosity of the central source may also be an important factor in determining the launch point of any outflow and its maximum velocity. With enough high quality observations it may be possible to determine how the outflow velocity correlates with source luminosity.

6.2.2 The importance of N v absorption in complex C IV BALs

The result, presented in section 3.7.1, that the presence of features within the C IV absorption trough is related to the strength of the N v absorption is an intriguing one. This may be due to ionisation effects, as N v is more highly ionised than C IV it may be that higher ionisation is in some way linked to the complexity of the absorption. The effect may also be related to the metal abundances within these objects as Hamann 1997 found strong evidence for metallicities considerably above Z_{\odot} in BALQSO outflows. Whatever the cause of this connection it seems worthy of further study. I would propose a detailed look at the correlation between the complexity of absorption in C IV and the strength of absorption in N v. Any such study should look into the location of peaks within the C IV absorption to look in detail at the structure of the N v absorption at the corresponding velocity.

Bibliography

- Abazajian et al. 2009, 'The seventh data release of the sloan digital sky survey', *ApJS* 182, 543.
- Abdo et al. 2010, 'The spectral energy distribution of fermi bright blazars', *ApJ* 716, 30.
- Adelman-McCarthy et al. 2007, 'The fifth data release of the sloan digital sky survey', *ApJS* 172, 634.
- Adelman-McCarthy et al. 2008, 'The sixth data release of the sloan digital sky survey', *ApJS* 175, 297.
- Antonucci, R. R. J. & Miller, J. S. 1985, 'Spectropolarimetry and the nature of ngc 1068', *ApJ* 297, 621.
- Arav, N. 1996, 'The 'ghost of lyman- α ' as evidence for radiative acceleration in quasars', *ApJ* 465, 617.
- Arav, N., Becker, R. H., Laurent-Muehleisen, S. A., Gregg, M. D., White, R. L., Brotherton, M. S. & de Kool, M. 1999b, 'What determines the depth of broad absorption lines? keck hires observations of balqso 1603+3002', *ApJ* 524, 566.
- Arav, N. & Begelman, M. C. 1994, 'Modelling the double-trough structure observed in broad absorption line qosos using radiative acceleration', *ApJ* 434, 479.
- Arav, N., Kaastra, J., Kriss, G. A., Korista, K. T., Gabel, J. & Proga, D. 2005, 'X-ray/ultraviolet campaign on the mrk 279 agn outflow: Constraining inhomogeneous absorber models', *ApJ* 620, 665.
- Arav, N., Korista, K. T., Barlow, T. A. & Begelman, M. C. 1995, 'Radiative acceleration of gas in quasars', *Nature* 376, 576.
- Arav, N., Korista, K. T., de Kool, M., Junkkarinen, V. T. & Begelman, M. C. 1999a, 'Hubble space telescope observations of the broad absorption line quasarpq 0946+301', *ApJ* 516, 27.
- Arav, N. & Li, Z.-Y. 1994, 'The role of radiative acceleration in outflows from broad absorption line qosos. i. comparison with o star winds', *ApJ* 427, 700.
- Arav, N., Li, Z.-Y. & Begelman, M. C. 1994, 'Radiative acceleration in outflows from broad absorption line quasi-stellar objects. ii. wind models', *ApJ* 432, 62.
- Bardeen, J. M. 1974, 'Properties of black holes relevant to their observation', *IAU Symposium* 64, 132.
- Barlow, T. A. 1993, Time variability of broad absorption-line QSO's, PhD thesis, California Univ.
- Bautista, M. A., Dunn, J. P., Arav, N., Korista, K. T., Moe, M. & Benn, C. 2010, 'Distance to multiple kinematic components of quasar outflows: Very large telescope observations of qso 2359-1241 and sdss j0318-0600', *ApJ* 713, 25.
- Becker, R. H., Gregg, M. D., Hook, I. M., McMahon, R. G., White, R. L. & Helfand, D. J. 1997, 'The First Radio-loud Broad Absorption Line QSO and Evidence for a Hidden Population of Quasars', *ApJ* 479, L93.

- Becker, R. H., White, R. L., Gregg, M. D., Brotherton, M. S., Laurent-Muehleisen, S. A. & Arav, N. 2000, 'Properties of radio-selected broad absorption line quasars from the first bright quasar survey', *ApJ* 538, 72.
- Blandford, R. D. & Payne, D. G. 1982, 'Hydromagnetic flows from accretion discs and the production of radio jets', *MNRAS* 199, 883.
- Bottoff, M., Korista, K. T., Shlosman, I. & Blandford, R. D. 1997, 'Dynamics of Broad Emission-Line Region in NGC 5548: Hydromagnetic Wind Model versus Observations', *ApJ* 479, 200.
- Bower, R. G., Benson, A. J., Malbon, R., Helly, J. C., Frenk, C. S., Baugh, C. M., Cole, S. & Lacey, C. G. 2006, 'Breaking the hierarchy of galaxy formation', *MNRAS* 370, 645.
- Brotherton, M., de Breuck, C. & Schaefer, J. 2006, 'Spectropolarimetry of pks 0040-005 and the orientation of broad absorption line quasars', *MNRAS* 372, L58.
- Brotherton, M. S., van Breugel, W., Smith, R. J., Boyle, B. J., Shanks, T., Croom, S. M., Miller, L. & Becker, R. H. 1998, 'Discovery of radio-loud broad absorption line quasars using ultraviolet excess and deep radio selection', *ApJ* 505, L7.
- Brüggen, M. & Kaiser, C. R. 2002, 'Hot bubbles from active galactic nuclei as a heat source in cooling-flow clusters', *Nature* 418, 301.
- Castander, F. J. 1998, 'The sloan digital sky survey', *Ap&SS* 263, 91.
- Castor, J. I., Abbott, D. C. & Klein, R. I. 1975, 'Radiation-driven winds in of stars', *ApJ* 195, 157.
- Cecil, G., Bland, J. & Tully, R. B. 1990, 'Imaging spectrophotometry of ionized gas in NGC 1068. I - Kinematics of the narrow-line region', *ApJ* 355, 70.
- Chelouche, D. & Netzer, H. 2001, 'Radiation pressure acceleration by x-rays in active galactic nuclei', *MNRAS* 326, 916.
- Churchill, C. W., Schneider, D. P., Schmidt, M. & Gunn, J. E. 1999, 'An unusual "mini-bal" quasar at $z=4.59$ ', *AJ* 117, 2573.
- Code, A. D., Meade, M. R., Anderson, C. M., Nordsieck, K. H., Clayton, G. C., Whitney, B. A., Magalhaes, A. M., Babler, B., Bjorkman, K. S., Schulte-Ladbeck, R. E. & Taylor, M. 1993, 'The first ultraviolet spectropolarimetric study of ngc 1068', *ApJ* 403, L63.
- Cole et al. 2001, 'The 2df galaxy redshift survey: near-infrared galaxy luminosity functions', *MNRAS* 326, 255.
- Cole, S., Lacey, C. G., Baugh, C. M. & Frenk, C. S. 2000, 'Hierarchical galaxy formation', *MNRAS* 319, 168.
- Cottis, C. E., Goad, M. R., Knigge, C. & Scaringi, S. 2010, 'Searching for the signature of radiative line driving: on the absence of $\text{Ly}\alpha$ -NV line-locking features in a large sample of BALQSOs', *MNRAS* 406, 2094.
- Crenshaw, D. M., Kraemer, S. B., Schmitt, H. R., Kaastra, J. S., Arav, N., Gabel, J. R. & Korista, K. T. 2009, 'Mass outflow in the seyfert 1 galaxy ngc 5548', *ApJ* 698, 281.
- de Kool, M., Arav, N., Becker, R. H., Gregg, M. D., White, R. L., Laurent-Muehleisen, S. A., Price, T. & Korista, K. T. 2001, 'Keck hires observations of the qso first j104459.6+365605: Evidence for a large-scale outflow', *ApJ* 548, 609.
- de Kool, M., Becker, R. H., Gregg, M. D., White, R. L. & Arav, N. 2002a, 'Intrinsic absorption in the qso first j121442.3+280329', *ApJ* 567, 58.
- de Kool, M., Korista, K. T. & Arav, N. 2002b, 'The effects of inhomogeneous absorbers on the formation of intrinsic quasar absorption lines', *ApJ* 580, 54.

- Di Matteo, T., Springel, V. & Hernquist, L. 2005, 'Energy input from quasars regulates the growth and activity of black holes and their host galaxies', *Nature* 433, 604.
- Dunn, J. P., Bautista, M., Arav, N., Moe, M., Korista, K., Costantini, E., Benn, C., Ellison, S. & Edmonds, D. 2010, 'The quasar outflow contribution to agn feedback: Vlt measurements of sdss j0318-0600', *ApJ* 709, 611.
- Edge, D. O., Shakeshaft, J. R., McAdam, W. B., Baldwin, J. E. & Archer, S. 1959, 'A survey of radio sources at a frequency of 159 mc/s.', *MmRAS* 68, 37.
- Elvis et al. 1994, 'Atlas of quasar energy distributions', *ApJS* 95, 1.
- Elvis, M. 2000, 'A structure for quasars', *ApJ* 545, 63.
- Emmering, R. T., Blandford, R. D. & Shlosman, I. 1992, 'Magnetic acceleration of broad emission-line clouds in active galactic nuclei', *ApJ* 385, 460.
- Espey, B. R. & Junkkarinen, V. T. 1993, Velocity shifts and emission line studies of redshift 2 qsos, in 'Bulletin of the American Astronomical Society', Vol. 25 of *Bulletin of the American Astronomical Society*, p. 794.
- Fanaroff, B. L. & Riley, J. M. 1974, 'The morphology of extragalactic radio sources of high and low luminosity', *MNRAS* 167, 31P.
- Ferland, G. J., Korista, K. T., Verner, D. A., Ferguson, J. W., Kingdon, J. B. & Verner, E. M. 1998, 'Cloudy 90: Numerical simulation of plasmas and their spectra', *PASP* 110, 761.
- Ferland, G. J., Peterson, B. M., Horne, K., Welsh, W. F. & Nahar, S. N. 1992, 'Anisotropic line emission and the geometry of the broad-line region in active galactic nuclei', *ApJ* 387, 95.
- Ferrarese, L. & Merritt, D. 2000, 'A fundamental relation between supermassive black holes and their host galaxies', *ApJ* 539, L9.
- Filippenko, A. V. 1982, 'The importance of atmospheric differential refraction in spectrophotometry', *PASP* 94, 715.
- Filippenko, A. V., Ho, L. C. & Sargent, W. L. W. 1993, 'Hst observations of ngc 4395, the least luminous seyfert 1 nucleus - evidence against the starburst hypothesis for broad-lined active galactic nuclei', *ApJ* 410, L75.
- Ganguly, R., Eracleous, M., Charlton, J. C. & Churchill, C. W. 1999, 'Intrinsic narrow absorption lines in keck hires spectra of a sample of six quasars', *AJ* 117, 2594.
- Gebhardt et al. 2000, 'A relationship between nuclear black hole mass and galaxy velocity dispersion', *ApJ* 539, L13.
- George, I. M. & Fabian, A. C. 1991, 'X-ray reflection from cold matter in active galactic nuclei and x-ray binaries', *MNRAS* 249, 352.
- Gibson et al. 2009a, 'A catalog of broad absorption line quasars in sloan digital sky survey data release 5', *ApJ* 692, 758.
- Gibson, R. R., Brandt, W. N., Gallagher, S. C. & Schneider, D. P. 2009b, 'X-ray insights into the physics of mini-bal quasar outflows', *ApJ* 696, 924.
- Giustini, M., Cappi, M. & Vignali, C. 2008, 'On the absorption of x-ray bright broad absorption line quasars', *A&A* 491, 425.
- Goad, M. & Koratkar, A. 1998, 'Broad emission line variability as a constraint upon the physical conditions within the broad emission line region of ngc 5548', *ApJ* 495, 718.
- Green, A. R., McHardy, I. M. & Lehto, H. J. 1993, 'On the nature of rapid x-ray variability in active galactic nuclei', *MNRAS* 265, 664.

- Green, P. J. & Mathur, S. 1996, 'Broad absorption line quasars observed by the rosat pspc', *ApJ* 462, 637.
- Guilbert, P. W. & Rees, M. J. 1988, 'cold' material in non-thermal sources', *MNRAS* 233, 475.
- Haardt, F. & Maraschi, L. 1991, 'A two-phase model for the x-ray emission from seyfert galaxies', *ApJ* 380, L51.
- Hall et al., P. B. 2002, 'Unusual broad absorption line quasars from the sloan digital sky survey', *ApJS* 141, 267.
- Hamann, F. 1997, 'Metal abundances and ionization in quasar intrinsic absorbers', *ApJS* 109, 279.
- Hamann, F., Kaplan, K. F., Rodríguez Hidalgo, P., Prochaska, J. X. & Herbert-Fort, S. 2008, 'Emergence of a quasar outflow', *MNRAS* 391, L39.
- Kaiser, M. E., Bradley, II, L. D., Hutchings, J. B., Crenshaw, D. M., Gull, T. R., Kraemer, S. B., Nelson, C. H., Ruiz, J. & Weistrop, D. 2000, 'The Resolved Narrow-Line Region in NGC 4151', *ApJ* 528, 260.
- Kaspi, S., Maoz, D., Netzer, H., Peterson, B. M., Vestergaard, M. & Jannuzi, B. T. 2005, 'The relationship between luminosity and broad-line region size in active galactic nuclei', *ApJ* 629, 61.
- Kaspi, S., Smith, P. S., Netzer, H., Maoz, D., Jannuzi, B. T. & Giveon, U. 2000, 'Reverberation measurements for 17 quasars and the size-mass-luminosity relations in active galactic nuclei', *ApJ* 533, 631.
- Kauffmann, G., Colberg, J. M., Diaferio, A. & White, S. D. M. 1999, 'Clustering of galaxies in a hierarchical universe - i. methods and results at $z=0$ ', *MNRAS* 303, 188.
- Keel, W. C. 1983, 'Spectroscopic evidence for activity in the nuclei of normal spiral galaxies', *ApJ* 269, 466.
- Khachikian, E. Y. & Weedman, D. W. 1974, 'An atlas of seyfert galaxies', *ApJ* 192, 581.
- King, A. R. 2010, 'Black hole outflows', *MNRAS* 402, 1516.
- Kniffen et al. 1993, 'Time variability in the gamma-ray emission of 3c 279', *ApJ* 411, 133.
- Knigge, C., Scaringi, S., Goad, M. R. & Cottis, C. E. 2008, 'The intrinsic fraction of broad-absorption line quasars', *MNRAS* 386, 1426.
- Konigl, A. & Kartje, J. F. 1994, 'Disk-driven hydromagnetic winds as a key ingredient of active galactic nuclei unification schemes', *ApJ* 434, 446.
- Korista, K. T., Voit, G. M., Morris, S. L. & Weymann, R. J. 1993, 'Double troughs in broad absorption line quasars and ly-alpha-n v line-locking', *ApJS* 88, 357.
- Lawrence, A. & Elvis, M. 1982, 'Obscuration and the various kinds of seyfert galaxies', *ApJ* 256, 410.
- Lightman, A. P. & White, T. R. 1988, 'Effects of cold matter in active galactic nuclei - a broad hump in the x-ray spectra', *ApJ* 335, 57.
- Lundgren, B. F., Wilhite, B. C., Brunner, R. J., Hall, P. B., Schneider, D. P., York, D. G., Vanden Berk, D. E. & Brinkmann, J. 2007, 'Broad absorption line variability in repeat quasar observations from the sloan digital sky survey', *ApJ* 656, 73.
- Mathews, W. G. & Ferland, G. J. 1987, 'What heats the hot phase in active nuclei?', *ApJ* 323, 456.
- Mathur, S., Elvis, M. & Wilkes, B. 1999, 'Multiple velocity components in the c iv absorption line of ngc 5548', *ApJ* 519, 605.
- McLure, R. J. & Dunlop, J. S. 2004, 'The cosmological evolution of quasar black hole masses', *MNRAS* 352, 1390.

- Miller, J. S., Goodrich, R. W. & Mathews, W. G. 1991, 'Multidirectional views of the active nucleus of ngc 1068', *ApJ* 378, 47.
- Murray, N., Chiang, J., Grossman, S. A. & Voit, G. M. 1994, Dynamics, Shielding and Line Formation in Accretion Disk Winds from Active Galactic Nuclei, in 'Bulletin of the American Astronomical Society', Vol. 26 of *Bulletin of the American Astronomical Society*, p. 1369.
- Murray, N., Chiang, J., Grossman, S. A. & Voit, G. M. 1995, 'Accretion disk winds from active galactic nuclei', *ApJ* 451, 498.
- Narayanan, D., Hamann, F., Barlow, T., Burbidge, E. M., Cohen, R. D., Junkkarinen, V. & Lyons, R. 2004, 'Variability tests for intrinsic absorption lines in quasar spectra', *ApJ* 601, 715.
- Netzer, H. & Peterson, B. M. 1997, Reverberation mapping and the physics of active galactic nuclei, in D. Maoz, A. Sternberg, & E. M. Leibowitz, ed., 'Astronomical Time Series', Vol. 218 of *Astrophysics and Space Science Library*, p. 85.
- North, M., Knigge, C. & Goad, M. 2006, 'A new sample of broad absorption-line quasars exhibiting the ghost of lyman alpha', *MNRAS* 365, 1057.
- O'Brien, P. T., Gondhalekar, P. M. & Wilson, R. 1988, 'The ultraviolet continuum of quasars - part two - continuum variability', *MNRAS* 233, 845.
- Ogle, P. M., Cohen, M. H., Miller, J. S., Tran, H. D., Goodrich, R. W. & Martel, A. R. 1999, 'Polarization of broad absorption line qsos. i. a spectropolarimetric atlas', *ApJS* 125, 1.
- Onken, C. A., Ferrarese, L., Merritt, D., Peterson, B. M., Pogge, R. W., Vestergaard, M. & Wandel, A. 2004, 'Supermassive black holes in active galactic nuclei. ii. calibration of the black hole mass-velocity dispersion relationship for active galactic nuclei', *ApJ* 615, 645.
- Osterbrock, D. E. 1978, 'Observational model of the ionized gas in seyfert and radio-galaxy nuclei', *Proceedings of the National Academy of Science* 75, 540.
- Padovani, P., Ghisellini, G., Fabian, A. C. & Celotti, A. 1993, 'Radio-loud agn and the extragalactic gamma-ray background', *MNRAS* 260, L21.
- Pei, Y. C. 1992, 'Interstellar dust from the milky way to the magellanic clouds', *ApJ* 395, 130.
- Percival et al., W. J. 2010, 'Baryon acoustic oscillations in the sloan digital sky survey data release 7 galaxy sample', *MNRAS* 401, 2148.
- Peterson, B. M. 1993, 'Reverberation mapping of active galactic nuclei', *PASP* 105, 247.
- Peterson, B. M. 1997, *An Introduction to Active Galactic Nuclei*, Cambridge, New York Cambridge University Press.
- Pounds, K. A., King, A. R., Page, K. L. & O'Brien, P. T. 2003b, 'Evidence of a high-velocity ionized outflow in a second narrow-line quasar pg 0844+349', *MNRAS* 346, 1025.
- Pounds, K. A. & Page, K. L. 2006, 'Confirming the high velocity outflow in pg 1211+143', *MNRAS* 372, 1275.
- Pounds, K. A. & Reeves, J. N. 2009, 'Quantifying the fast outflow in the luminous seyfert galaxy pg1211+143', *MNRAS* 397, 249.
- Pounds, K. A., Reeves, J. N., King, A. R., Page, K. L., O'Brien, P. T. & Turner, M. J. L. 2003a, 'A high-velocity ionized outflow and xuv photosphere in the narrow emission line quasar pg1211+143', *MNRAS* 345, 705.
- Pounds, K. A., Turner, T. J. & Warwick, R. S. 1986, 'Rapid x-ray variability of the seyfert galaxy mcg-6-30-15', *MNRAS* 221, 7P.

- Pringle, J. E. & Rees, M. J. 1972, 'Accretion disc models for compact x-ray sources', *A&A* 21, 1.
- Proga, D. 2007, Theory of winds in agns, in L. C. Ho & J.-W. Wang, ed., 'The Central Engine of Active Galactic Nuclei', Vol. 373 of *Astronomical Society of the Pacific Conference Series*, p. 267.
- Proga, D., Stone, J. M. & Kallman, T. R. 2000, 'Dynamics of line-driven disk winds in active galactic nuclei', *ApJ* 543, 686.
- Rafferty, D. A., McNamara, B. R., Nulsen, P. E. J. & Wise, M. W. 2006, 'The feedback-regulated growth of black holes and bulges through gas accretion and starbursts in cluster central dominant galaxies', *ApJ* 652, 216.
- Reichard et al. 2003a, 'A catalogue of broad absorption line quasars from the sloan digital sky survey early data release', *AJ* 125, 1711.
- Reichard et al. 2003b, 'Continuum and emission-line properties of broad absorption line quasars', *AJ* 126, 2594.
- Reid, M. J., Menten, K. M., Genzel, R., Ott, T., Schödel, R. & Brunthaler, A. 2003, 'The position, motion, and mass of sgr a*', *Astronomische Nachrichten Supplement* 324, 505.
- Reynolds, C. S. 1996, Time variability of broad absorption-line QSO's, PhD thesis, Univ. of Cambridge.
- Richards et.al 2002, 'Spectroscopic target selection in the sloan digital sky survey: The quasar sample', *AJ* 123, 2945.
- Riffel, R. A., Storchi-Bergmann, T. & McGregor, P. J. 2009, 'The dusty nuclear torus in ngc 4151: Constraints from gemini near-infrared integral field spectrograph observations', *ApJ* 698, 1767.
- Robinson, A., Axon, D. J. & Smith, J. 2003, Spectropolarimetry and the geometry of type 1 seyfert nuclei, in E. Perez, R. M. Gonzalez Delgado, & G. Tenorio-Tagle, ed., 'Star Formation Through Time', Vol. 297 of *Astronomical Society of the Pacific Conference Series*, p. 393.
- Ruszkowski, M. & Begelman, M. C. 2002, 'Heating, conduction, and minimum temperatures in cooling flows', *ApJ* 581, 223.
- Sánchez, A. G., Crocce, M., Cabré, A., Baugh, C. M. & Gaztañaga, E. 2009, 'Cosmological parameter constraints from sdss luminous red galaxies: a new treatment of large-scale clustering', *MNRAS* 400, 1643.
- Sanders, D. B., Phinney, E. S., Neugebauer, G., Soifer, B. T. & Matthews, K. 1989, 'Continuum energy distribution of quasars - Shapes and origins', *ApJ* 347, 29.
- Sargent, W. L. W., Steidel, C. C. & Boksenberg, A. 1988, 'Mg ii absorption in the spectra of high and low redshift qos', *ApJ* 334, 22.
- Savage, B. D. & Sembach, K. R. (1991), 'The analysis of apparent optical depth profiles for interstellar absorption lines', *ApJ* 379, 245.
- Scannapieco, E., Silk, J. & Bouwens, R. 2005, 'Agn feedback causes downsizing', *ApJ* 635, L13.
- Scaringi, S., Cottis, C., Knigge, C. & Goad, M. 2009, 'Classifying broad absorption line quasars: Metrics, issues and a new catalogue constructed from sdss dr5', *MNRAS* 399, 2231.
- Schmidt, G. D. & Hines, D. C. 1999, 'The polarization of broad absorption line qos', *ApJ* 512, 125.
- Schmidt, M. (1963), '3c 273 : A star-like object with large red-shift', *Nature* 197, 1040.
- Schneider et al. 2005, 'The sloan digital sky survey quasar catalog. iii. third data release', *AJ* 130, 367.
- Schneider et al. 2007, 'The sloan digital sky survey quasar catalog. iv. fifth data release', *AJ* 134, 102.
- Scoville et al. 2007, 'The cosmic evolution survey (cosmos): Overview', *ApJS* 172, 1.

- Seyfert, C. K. 1943, 'Nuclear emission in spiral nebulae.', *ApJ* 97, 28.
- Shankar, F., Dai, X. & Sivakoff, G. R. 2008, 'Dependence of the broad absorption line quasar fraction on radio luminosity', *ApJ* 687, 859.
- Shen, Z., Lo, K. Y., Liang, M., Ho, P. T. P. & Zhao, J. 2005, 'A size of ~ 1 au for the radio source sgr a* at the centre of the milky way', *Nature* 438, 62.
- Shlosman, I., Begelman, M. C. & Frank, J. 1990, 'The fuelling of active galactic nuclei', *Nature* 345, 679.
- Shlosman, I., Vitello, P. A. & Shaviv, G. 1985, 'Active galactic nuclei - internal dynamics and formation of emission clouds', *ApJ* 294, 96.
- Shull, J. M. & Sachs, E. R. 1993, 'Variable c iv absorption in the seyfert galaxy ngc 5548: A connection to broad absorption line quasi-stellar objects?', *ApJ* 416, 536.
- Spitzer, L. 1978, *Physical processes in the interstellar medium*, New York Wiley-Interscience.
- Sprayberry, D. & Foltz, C. B. 1992, 'Extinction in low-ionization broad absorption line quasi-stellar objects', *ApJ* 390, 39.
- Springel, V., Di Matteo, T. & Hernquist, L. 2005, 'Black holes in galaxy mergers: The formation of red elliptical galaxies', *ApJ* 620, L79.
- Stoche, J., Morris, S., Weymann, R. & Foltz, C. 1992, 'The radio properties of the broad-absorption-line qos', *ApJ* 396, 487.
- Telfer, R. C., Kriss, G. A., Zheng, W., Davidsen, A. F. & Green, R. F. 1998, 'The very highly ionized broad absorption line system of the qso sbs 1542+541', *ApJ* 509, 132.
- Tremaine et al. 2002, 'The slope of the black hole mass versus velocity dispersion correlation', *ApJ* 574, 740.
- Trump et al. 2006, 'A catalog of broad absorption line quasars from the sloan digital sky survey third data release', *ApJS* 165, 1.
- Turnshek, D. 1984, 'Properties of the broad absorption-line qos', *ApJ* 280, 51.
- Ulrich, M. 1989, 'Intermediate resolution spectra of quasars with z of greater than 2', *A&A* 220, 71.
- Urry, C. M. & Padovani, P. 1995, 'Unified schemes for radio-loud active galactic nuclei', *PASP* 107, 803.
- Valdes, F. 1988, The iraf ccd reduction package - ccdred, in L. B. Robinson, ed., 'Instrumentation for Ground-Based Optical Astronomy', p. 417.
- Vanden Berk et al. 2001, 'Composite quasar spectra from the sloan digital sky survey', *AJ* 122, 549.
- Vilkoviskij, E. Y. & Irwin, M. J. 2001, 'The spectrum of bal qso q1303+308: intrinsic variability and line-locking stability', *MNRAS* 321, 4.
- Wandel, A. 1999, 'The black hole-to-bulge mass relation in active galactic nuclei', *ApJ* 519, L39.
- Warner, C., Hamann, F. & Dietrich, M. 2004, 'Active galactic nucleus emission-line properties versus the eddington ratio', *ApJ* 608, 136.
- Weymann, R. J., Morris, S. L., Foltz, C. B. & Hewett, P. C. 1991, 'Comparisons of the emission-line and continuum properties of broad absorption line and normal quasi-stellar objects', *ApJ* 373, 23.
- Wilkes, B. J. 1984, 'Studies of broad emission line profiles in qso. i - observed, high-resolution profiles', *MNRAS* 207, 73.
- Wilkes, B. J., Tananbaum, H., Worrall, D. M., Avni, Y., Oey, M. S. & Flanagan, J. 1994, 'The einstein database of ipc x-ray observations of optically selected and radio-selected quasars, 1.', *ApJS* 92, 53.

- York, D. G., Dopita, M., Green, R. & Bechtold, J. 1986, 'On the origin of some qso absorption lines', *ApJ* 311, 610.
- York, D. G., Yanny, B., Crotts, A., Carilli, C., Garrison, E. & Matheson, L. 1991, 'An inhomogeneous reference catalogue of identified intervening heavy element systems in spectra of qos', *MNRAS* 250, 24.
- York et al., D. G. 2000, 'The sloan digital sky survey: Technical summary', *AJ* 120, 1579.
- Zdziarski, A. A., Ghisellini, G., George, I. M., Fabian, A. C., Svensson, R. & Done, C. 1990, 'Electron-positron pairs, compton reflection, and the x-ray spectra of active galactic nuclei', *ApJ* 363, L1.
- Zheng, W., Kriss, G. A., Telfer, R. C., Grimes, J. P. & Davidsen, A. F. 1997, 'A composite hst spectrum of quasars', *ApJ* 475, 469.